

AN INVESTIGATION OF COMPRESSED AIR ENERGY STORAGE METHODS

by

BHARATH KANTHARAJ

Thesis submitted to the University of Nottingham for the degree of Doctor of Philosophy

May 2019

Abstract

This thesis broadly concerns the analysis of air storage methods within Compressed Air Energy Storage (CAES) systems. In a typical CAES system, pressurised air generated by electrically driven compressors is first stored in appropriate containments. During times of need, energy from the high-pressure air is recovered by withdrawing it from the containment and subsequently expanding it in appropriate machinery.

Since the most established method of air storage for commercial CAES applications today is in underground salt caverns, the thesis begins by analysing this technology. In particular, the thesis focuses on formulating a loosely coupled thermomechanical finite element model to predict the response of such caverns subjected to high-frequency cycling of compressed air. It is found that whilst the temperature variations are confined to a small region near the wall of the cavern, its effect on the resulting stress field is significant, especially when the rate of change of temperature is negative causing the resulting stresses to be tensile in nature. The structural stability of the cavern is investigated using two separate failure criteria which suggest that when the internal air pressure is minimum and change in temperature is maximum, the cavern is more susceptible to failure.

Recognising the fact that underground salt caverns are geologically constrained and thus might present an obstacle to widespread CAES deployment, two novel air storage methods have been proposed.

The first is a hybrid compressed air-liquid air energy storage system whose thermodynamic effectiveness is analysed. In this system, the energy storage capacity of compressed air is extended by supplementing the system with energy dense, geologically unconstrained, liquid air storage. The notional system consists of a compressed air store, liquid air store and associated machinery to transform between the two states of air. It is found that a maximum roundtrip storage efficiency of approximately 50 [%] could be achieved, where the roundtrip efficiency refers to the overall performance of converting compressed air to liquid air and back, but before conversion to and from electricity.

The second is a rigid underwater containment for storing compressed air, whose structural behaviour during the transaction of pressurised air is investigated. Using the finite element method, preliminary analysis is conducted on rigid wall vessels, where it is shown that non-trivial bending loads exist in the shell of the containment. Past research on flexible wall vessels is documented and contrasted with rigid wall vessels. Underwater environments offer significant advantages to a CAES system in terms of reduced load carrying requirements of the vessel due to the natural hydrostatic pressure restraint, and constant pressure operation which in turn enables more efficient power recovery. However, it is noted that the manufacturing and deployment of underwater vessels play a crucial role, especially at large scales.

Since the air storage options investigated are diverse in terms of geographical locations, scale of system, application landscape and technological maturity, a short chapter investigates the capital cost of these air storage systems. Both existing cost data as well as bottom-up estimation methods using cost correlations are employed in deriving the potential total and specific (per unit of stored exergy) costs. It is found that the underground air storage option is the most competitive at £9/kWh, underwater storage option (in rigid vessels) ranks second at £58/kWh and the hybrid storage option is the least competitive at £342/kWh. It is worth noting, however, that both the hybrid and underwater air storage options are novel and their competitiveness can be expected to improve as their technology readiness levels improve. Furthermore, the hybrid air storage option, whilst relatively unattractive on cost, is the least geologically-constrained option and intended for small-to-medium scale applications. Therefore, some parties (e.g. remote microgrids) may be willing to pay a premium on this system in exchange for flexibility in system locatability and scale.

Finally, techno-economic and financial analysis of energy storage systems coupled with renewable generators is carried out to gain insight into the commercial viability of a CAES system participating in the energy market today. A rolling-planning optimal scheduling algorithm is developed to maximise profits of a wind power generator coupled with an

underground CAES system (since it offers the least cost of storage) from its participation in the wholesale energy market. Various technical parameters are considered in the problem formulation, including the facility to incorporate energy leakage and energy capacity degradation, all within a purely linear optimisation framework. Whilst the proposed wind-CAES system does not produce a positive return on investment today, it is observed that managing the imbalance of the wind generator captures significant value, and stacking revenue sources increases the overall short-term revenue of the system. Furthermore, it is found that managing the imbalance of the renewable generator also reduces the cycling, or wear and tear, of the energy storage system, thereby prolonging its lifetime.

Acknowledgements

It all started in an undergraduate lecture room in 2011, when Prof. Seamus Garvey's talk on direct air compression wind turbines inspired my interest in energy storage. I would therefore like to thank my supervisor, Prof. Garvey, for providing me with an opportunity to work with him, and for his expertise and guidance throughout the course of the PhD. I would also like to thank Dr. Jon McKechnie for his invaluable feedback at my progression assessments.

Special thanks go to my advisors Dr. Andrew Pimm and Dr. Vincenzo Trovato for not only educating me on energy storage, electricity systems and the wider field of energy, but also for providing specific advice on, and help with, various topics within my thesis.

I also wish to thank my examiners Prof. Win Rampen and Dr. David Branson for their invaluable advice and suggestions, which have improved this thesis by a great deal.

Thank you Appa, Amma and Rajath for your unconditional love and support in all its forms. This thesis would not have existed without your help, constant encouragement and patience. Thank you, also, Eve and Ékalavya for bearing with me.

To my family

Contents

Abstract ii

Acknowledgements v

Contents vii

List of Tables ix

List of Figures xi

Nomenclature xv

1 Introduction 1
- 1.1 Context . . . 1
- 1.2 Thesis objectives . . . 4
- 1.3 Thesis layout . . . 4

2 Background 9
- 2.1 Introduction . . . 9
- 2.2 Basic principles of CAES . . . 12
- 2.3 System design classes in CAES . . . 16
- 2.4 Air storage reservoirs for CAES . . . 23
- 2.5 Conclusions . . . 27

3 Compressed air storage in salt caverns 29
- 3.1 Introduction . . . 29
- 3.2 Cavern thermodynamics and heat transfer . . . 33
- 3.3 Constitutive model of rock salt . . . 37
- 3.4 Cavern stability criteria . . . 42
- 3.5 Finite Element Analysis . . . 45
- 3.6 Results and discussion . . . 56
- 3.7 Conclusions . . . 71

4 Compressed air storage with liquid air capacity extension 75
4.1 Introduction . . . 75
4.2 Overview of liquid air energy storage . . . 77
4.3 Thermodynamic analysis of the ideal system . . . 82
4.4 Modelling system components . . . 86
4.5 A practical implementation . . . 94
4.6 Results and discussion . . . 99
4.7 Conclusions . . . 113

5 Flexible and rigid vessels for underwater compressed air storage 115
5.1 Introduction . . . 115
5.2 Underwater CAES . . . 117
5.3 Underwater pumped hydro storage . . . 132
5.4 Discussion and conclusions . . . 136

6 Cost comparison of compressed air storage options 141
6.1 Introduction and overall approach . . . 141
6.2 Cost modelling of system components . . . 143
6.3 Results and discussion . . . 147
6.4 Conclusions . . . 155

7 Value of energy storage behind-the-meter with renewable generators 157
7.1 Introduction and context . . . 157
7.2 Problem description . . . 162
7.3 Scenario generation methodology and energy storage model . . . 171
7.4 Optimisation model . . . 178
7.5 Financial model . . . 181
7.6 Results and discussion . . . 182
7.7 Conclusions . . . 192

8 Conclusions and future work 195
8.1 Thesis summary . . . 195
8.2 Summary of contributions to engineering science . . . 196
8.3 Key chapter conclusions . . . 196
8.4 Suggested future work . . . 199

Bibliography 201

List of Tables

3.1 Material properties of rock salt 41
3.2 Material constants used in the dilation criteria 44
3.3 System parameters used in the present analysis 57

4.1 System parameters for the CAES-LAES system 101
4.2 Thermodynamic performance summary of the CAES-LAES system 107

5.1 Rigid vessels in underwater CAES and PHS systems 136

6.1 Cavern cost parameters 144
6.2 Aboveground pressure vessel cost parameters 145
6.3 Compressor and expander cost parameters 145
6.4 Heat exchanger cost parameters 146
6.5 Cost coefficients for the hybrid compressed air-liquid air storage system . . 149
6.6 Construction cost parameters for corrosion resistant concrete [203] 151
6.7 Absolute and specific costs of exergy storage in air underground, hybridised with liquid air, and rigid underwater containers 153

7.1 Parameters for the renewable energy storage system 184

List of Figures

1.1 Proportion of 2016 UK electricity generation by fuel type 2

2.1 Schematic for D-CAES plants 17
2.2 Schematic of the Huntorf plant compression/storage/expansion process . . . 18
2.3 Schematic of the McIntosh plant compression/storage/expansion process . . 19
2.4 Schematic for AA-CAES plants 19
2.5 Exergy stored per unit volume of air compressed in an ideal CAES process 21
2.6 Schematic for an isochoric air storage reservoir 24
2.7 Schematic for a fixed volume isobaric air storage reservoir 25
2.8 Estimated capital cost split for a typical CAES plant 26

3.1 A schematic of the idealised cavern shape with air injection and withdrawal, and heat transfer across the walls 33
3.2 Regions of dilatant and compressible behaviour of rock salt 38
3.3 Schematic of the axisymmetric cavern and rock salt geometry with applied loads 46
3.4 Schematic of the eight-noded quadrilateral finite element 47
3.5 Shape functions of a corner node and mid-side node in an eight-noded quadrilateral finite element 47
3.6 The finite element mesh of the structure 48
3.7 Mass flow rate characteristics of Huntorf plant 51
3.8 Measured and simulated pressure and temperature variation for Huntorf salt cavern 52
3.9 Variation of viscosity with shear rate for creeping behaviour of salt 54
3.10 The daily compressed air charge-discharge cycle used in this study 57
3.11 Thermodynamic response in the first charge-discharge cycle 59
3.12 Temperature variation of air and the layers of rock 60
3.13 Temperature variation near the cavern wall 61
3.14 Thermodynamic response over 100 charge-discharge cycles 62
3.15 Displacement of the rock salt structure 64
3.16 Factor of Safety (FoS) contour plot for the DV dilatancy criterion 66
3.17 Factor of Safety (FoS) contour plot for the RD dilatancy criterion 67
3.18 Variation of principal stress with time in the cavern wall 69
3.19 Sensitivity of FoS to cavern geometry 70

4.1 Schematic of Linde-Hampson air liquefaction cycle 77

4.2 Schematic of an ideal LAES cycle . . . 78
4.3 The liquid air energy storage cycle proposed by E. M. Smith . . . 79
4.4 Highview Power Storage pilot plant . . . 81
4.5 Energy flows in the CAES-LAES system . . . 83
4.6 Schematic of the ideal CAES-LAES system . . . 84
4.7 Relative humidity of air . . . 87
4.8 Water holding capacity of humid air . . . 88
4.9 Schematic of a two-stream counter-current heat exchanger . . . 89
4.10 Schematic of a multi-stream counter-current heat exchanger with N hot stream and M cold streams . . . 91
4.11 Forward conversion mechanism of the CAES-LAES system . . . 96
4.12 Multi-stage Expansion with Heat Exchange in parallel ($MEHX_p$) . . . 97
4.13 The thermodynamic state of the forward conversion system based on parameters defined in the case study . . . 103
4.14 Heat exchanger composite curves . . . 105
4.15 Distribution of component exergy loss in forward conversion system . . . 109
4.16 Sensitivity of exergy loss in forward conversion process to number of stages of expansion . . . 111
4.17 Sensitivity of exergy loss in forward conversion process to starting compressed air pressure . . . 112

5.1 Recoverable energy from an underwater compressed air storage reservoir . . . 118
5.2 Energy Bag prototypes . . . 120
5.3 Energy Bag with single point of anchorage . . . 122
5.4 Deformed shapes of an Energy Bag with single point of anchorage . . . 123
5.5 Energy Bag with wide base radius and sealed base . . . 123
5.6 Energy Bag with wide base radius and unsealed base . . . 124
5.7 Pressure-volume curves for Energy Bags with sealed and unsealed base . . . 125
5.8 Pressure-volume curves for Energy Bags with sealed base . . . 125
5.9 A rigid underwater vessel for CAES . . . 127
5.10 Rigid underwater vessels used by Hydrostor . . . 128
5.11 Schematic of an axisymmetric underwater rigid vessel geometry . . . 130
5.12 Stress resultants in an underwater rigid vessel with non-uniform internal and external hydrostatic pressure . . . 132
5.13 Stress resultants in an underwater rigid vessel completely filled with compressed air . . . 133
5.14 Variation of maximum and minimum principal stresses in an underwater rigid vessel with fill level of compressed air . . . 133
5.15 Underwater pumped hydro storage system proposed by Slocum et al.[138] . . . 134
5.16 Underwater pumped hydro storage system proposed by Puchta et al.[139] . . . 134
5.17 Deployment mechanism for rigid vessels . . . 138
5.18 Deployment mechanism for flexible vessels . . . 139

6.1 Component and total cost of the hybrid compressed air-liquid air storage system . . . 150

7.1 Schematic of a behind-the-meter renewable energy storage system 163
7.2 Capacity Market de-rating factors with respect to the asset's discharge duration 166
7.3 Strategies for managing the imbalance of a renewable generator 168
7.4 Illustration of the rolling-planning optimisation framework 170
7.5 Empirical CDFs for normalised values of wind power, wholesale energy and system imbalance prices 172
7.6 Sorted values of wind power output across various statistically similar scenarios 173
7.7 Demonstration of variability in values between statistically similar scenarios 173
7.8 Demonstration of the time-increasing nature of wind power forecast errors . 175
7.9 Evolution of State of Charge in an energy storage unit 177
7.10 Cycling performance of lithium titanate hydrates in lithium ion batteriess . 178
7.11 Short-term revenue distribution for the renewable generator alone 184
7.12 Short-term revenue distribution for the renewable energy storage system . . 186
7.13 Volatility of system imbalance prices relative to the wholesale energy prices in the GB market for the year 2015-16 187
7.14 Optimal policy of the renewable energy storage system in a typical day . . . 188
7.15 Cycling CAES 189
7.16 Waterfall plot of NPV cash-flows 190
7.17 Short-term revenue distributions with increased frequency of wind power forecast update 191
7.18 Distribution of NPV across statistically similar scenarios 193

Nomenclature

Acronyms and initialisms

HVAC	Heating Ventilation and Air Conditioning
HVDC	High Voltage Direct Current
CAES	Compressed Air Energy Storage
LAES	Liquid Air Energy Storage
FoS	Factor of Safety
MEHXp	Multi-stage Expansion with Heat Exchange in parallel
MCHXp	Multi-stage Compression with Heat Exchange in parallel
PC	Pre-cooler
AH	After heater
RSO	Renewable Site Operator
SP	Settlement Period
RESS	Renewable Energy Storage System
SoC	State of Charge
DoD	Depth of Discharge
NPV	Net Present Value
IRR	Internal Rate of Return
FPN	Final Physical Notification
SO	System Operator
GC	Gate Closure
NIV	Net Imbalance Volume
BM	Balancing Mechanism

Symbols

P	Pressure (Chapters 2 and 3) or power (Chapter 7)
V	Volume
m	Mass
$\dot{m}$	Mass flow rate
R_{air}	Specific gas constant for air
T	Temperature
C_{p}	Specific heat capacity at constant pressure
C_{v}	Specific heat capacity at constant volume
γ	Ratio of C_{p} to C_{v} (Chapters 2, 3 and 4) or self-discharge parameter (Chapter 7)
C	Heat capacity (Chapter 3) or compressor (Chapter 4)
W	Work
η	Efficiency
$\eta_{\text{th-el}}$	Conversion efficiency of thermal to electrical energy
E	Energy (Chapters 2 and 7) or expander (Chapter 4)
ρ	Mass density
u	Specific internal energy
h	Specific enthalpy
s	Specific entropy
$\dot{Q}$	Rate of heat transfer
$\dot{Q}''$	Heat flux
κ	Thermal expansion coefficient
α	Heat transfer coefficient
k	Thermal conductivity
$\boldsymbol{\varepsilon}$	Strain tensor
$\boldsymbol{\sigma}$	Stress tensor
$\boldsymbol{\sigma}_{\text{D}}$	Stress deviator tensor
$\boldsymbol{C}$	Elastic stiffness tensor
Y	Young's modulus
ν	Poisson's ratio
f_{dilation}	Rock salt dilation function

d_{skin}	Skin depth
$\boldsymbol{M}$	Mass matrix
$\boldsymbol{K}$	Thermal conductance or stiffness matrix
$\boldsymbol{U}$	Nodal displacement vector
$\boldsymbol{T}$	Nodal temperature vector
$\dot{\boldsymbol{T}}$	Derivative of the nodal temperature vector
$\boldsymbol{F}$	Nodal force vector
$\boldsymbol{H}$	Shape function matrix
$\boldsymbol{B}$	Strain-displacement transformation matrix
$\dot{B}$	Flow exergy
U	Thermal conductance
A	Surface area
g	Acceleration due to gravity
f_{buoyancy}	Buoyancy force
r	Radius (Chapter 5) or cost of capital (Chapter 7)
W	Wind power output
λ	Half-hourly energy prices
S	State of charge of the energy store
τ	Self-discharge time constant of the energy store
σ	Standard deviation
μ	Mean
N_{c}	Number of charge/discharge cycles of the energy store

Common subscripts and superscripts

ref	Refrigerant
iso	Isothermal
isen	Isentropic
D-CAES	Diabatic-CAES
el	Electrical
th	Thermal
me	Mechanical

cav	Cavern
rock	Rock salt
0	Initial state / datum
pri	Primary
sec	Secondary
A	Actual
C	Compression (Chapter 4) or charge (Chapter 7)
D	Discharge
E	Expansion
F	Forecasted
G	Transmission network grid connection
2p	Two-phase
l	Liquid

Chapter 1

Introduction

1.1 Context

Climate change, arguably the most important global issue of the present century, has significant long-term negative impacts across several sectors including energy, water and food. There is strong scientific evidence that anthropogenic greenhouse gas emissions are responsible for a large proportion of the rise in global average temperatures over the last century [1]. The electricity sector is a major contributor to climate change owing to emissions of anthropogenic greenhouse gas, mainly stemming from the burning of fossil fuels. In the UK, the electricity sector accounted for 21 [%] of total CO_2 emissions in 2016 [2]. Therefore, it is no surprise that there is concerted effort from groups across the globe to reform the electricity sector, with particular focus on sources of low-carbon generation such as wind, solar and nuclear energies [3].

The European Union, within the 2008 European Commission directive [4], has set legally binding targets to reduce greenhouse gas emissions as well as increase the share of renewable energy sources on the electricity network. This has proven effective to some degree: in the UK, for instance, greenhouse gas emissions have decreased by 38 [%] based on 1990 levels, and the proportion of renewable energy sources on the grid has steadily increased in

parallel[5]. As shown in Fig. 1.1, electricity generation from renewable sources accounted for nearly 25 [%] of the total production in 2016. However, further increase in the share renewable generation sources may exceed the uptake capacity of the current electrical infrastructure, and may destabilise the power system[6].

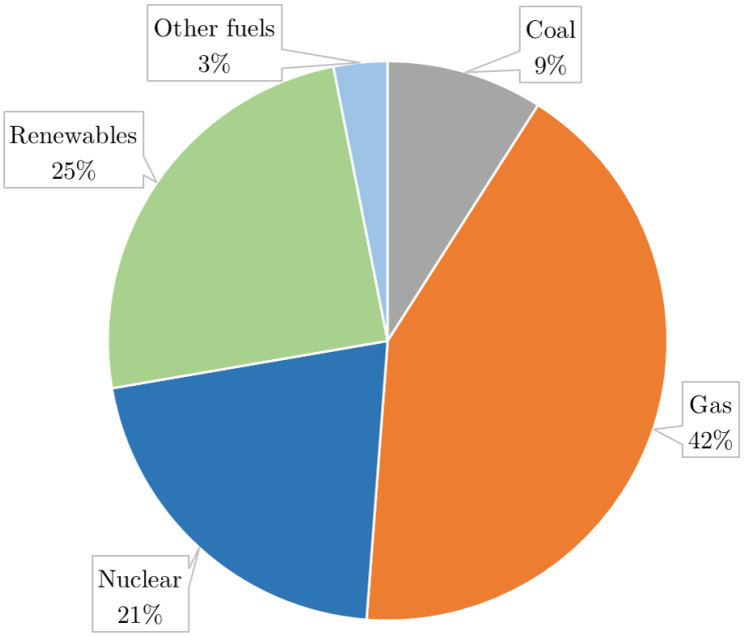


FIGURE 1.1: Proportion of 2016 UK electricity generation by fuel type

The issue of system security is magnified in the UK where wind energy, after biomass, represents the largest source of renewable energy with significant growth expected in the future[2]. Most wind turbines, unlike conventional generators, cannot naturally deploy the kinetic energy stored in the rotating masses[7], and therefore cannot support the inertial response of the power system. This can negatively impact power system operation as reduced inertia may cause large swathes of the national demand to automatically disconnect, leading to system shut down[8]. With the UK energy mix landscape set to undergo significant change in the coming decade due to the retiring of all but one nuclear plant[9], increased deployment of renewable energy sources for decarbonising the electricity sector at affordable cost levels whilst maintaining system security will be challenging. Therefore, the design and procurement of suitable additional services called *ancillary services* by the

system operator of a national or regional electrical transmission network becomes necessary to alleviate the system security issues brought forth by the increased grid integration of renewable energy sources.

Ancillary services are traditionally delivered via part-loaded conventional (fossil fuel based) generators. However, maintaining status quo in the provision of these services will not only lead to higher system costs owing to part-load operation of conventional generators, but also create hurdles in achieving grid decarbonisation. Therefore, an enormous degree of academic and industry research is focused on technologies that can act as alternative sources of flexibility for power system operation and security. These technologies belong to the broader concept of the *Smart Grid* [10], and include:

- 'Generation-side' technologies such as synchronous generators to provide control of system inertia and frequency [11]
- 'Demand-side' technologies – which encompass commercial and domestic appliances – such as HVAC, refrigeration units, etc., to provide frequency control and reserve capacity when aggregated [12]
- Energy storage technologies which can both generate and consume power to provide various system services [13], as well as integrate with renewable energy sources in unique ways [14]
- Power transmission technologies such as HVDC [11]

It is important to note that no single technology category will be able to provide the full set of flexibility services necessary for efficient operation of the power system. The interplay between the various sources of flexibility from the whole system perspective subject to the power generation mix, which helps to understand the dynamics between the different technologies, is the subject of ongoing research [15]. This thesis focuses on energy storage; specifically, it investigates the engineering and economic aspects of selected Compressed Air Energy Storage (CAES) designs, the results and conclusions of which can ultimately

aid further research and development of the technologies, with associated regulatory and policy framework to enable the transition to a future low-carbon power system.

1.2 Thesis objectives

This thesis is focused on the engineering analysis of three compressed air storage options used within CAES designs and economic analysis of a CAES system integrated with a renewable power generator.

The objectives are to:

1. Create a coupled thermomechanical model to predict the mechanical response and structural stability of an underground salt cavern subjected to high-frequency cyclical transactions of compressed air
2. Consider and analyse two alternative, novel, compressed air storage methods proposed in this thesis that aim to improve the overall system performance relative to the conventional, underground, method
3. Conduct preliminary cost analysis of the three air storage methods investigated herein
4. Develop a flexible optimisation tool to evaluate the economic and financial performance of CAES integrated with a renewable power generator, considering in detail the various characteristics of the storage system, renewable power generator and energy market bidding strategy

1.3 Thesis layout

The thesis comprises eight chapters including the introduction.

Background

Chapter 2 presents an overview of the historical development of CAES, the various modes of system operation including the governing thermodynamics, a comparison of different air storage reservoirs, and concludes by discussing plant performance metrics and the integration potential with sources of power generation and demand.

Compressed air storage in salt caverns

Chapter 3 investigates the stability of an underground salt cavern owing to the high-frequency cyclical transactions of compressed air into and out of the storage containment. Finite element analysis is used to model the thermomechanical cyclic loading and obtain the mechanical response of the cavern, to then inform the design of the air storage reservoir.

A version of this chapter is published as B. Kantharaj, S. Garvey and A. Pimm, "Thermodynamic modelling of underground salt caverns for compressed air energy storage", *Proceedings of the Offshore Energy Storage Symposium, OSES 2015*, Edinburgh, UK, 1-3 July 2015.

Compressed air storage with liquid air capacity extension

Chapter 4 considers an engineering alternative to the conventional CAES system. It evaluates the thermodynamic performance of a novel hybrid compressed air-liquid air energy storage system aimed at enhancing the effectiveness of an aboveground CAES design. Starting with fundamental thermodynamic analysis of an ideal system configuration, a possible practical arrangement of components is proposed, with the objective of arriving at an estimate of the roundtrip efficiency of the system and other thermodynamic trends that will aid eventual system design.

A version of this chapter is published as B. Kantharaj, S. Garvey and A. Pimm, "Compressed air energy storage with liquid air capacity extension", *Applied Energy*, **157**, 152-164, 2015.

Analysis of flexible and rigid vessels for underwater Compressed air storage

Chapter 5 considers another alternative to conventional CAES design – underwater, or deep sea, CAES. First, the motivations for underwater CAES are discussed. Then, a brief analysis of the structural behaviour of rigid wall air storage reservoirs is performed, by building on previous research on flexible fabric structures used as underwater storage vessels and employing the finite element tool developed in Chapter 3. Underwater pumped hydroelectric storage is also considered and compared with its CAES counterpart.

A version of this chapter is published as B. Kantharaj, S. Garvey and A. Pimm, "Flexible versus rigid containments for underwater compressed air energy storage", *Proceedings of the Offshore Energy Storage Symposium, OSES 2016*, Valletta, Malta, 13-15 July 2016.

Cost comparison of underground, hybrid and underwater compressed air storage options

Chapter 6 broadens the scope of the thesis by considering the economics of the three air storage options investigated in the previous chapters. Based on historical cost survey data as well as bottom-up methods, capital cost models are built and the total upfront costs of each air storage option is estimated.

Value of energy storage integrated behind-the-meter with renewable generators

Chapter 7 further extends the economic appraisal by integrating a CAES system with a renewable generator and optimising its operation in the energy market for maximum financial returns from the view point of the renewable site operator or developer. It should be noted that the cheapest of the three air storage options as determined in Chapter 6 is considered for the analysis here[1]. A straightforward methodology is developed for the business case analysis of an underground CAES system connected behind the energy meter with a renewable generator. A purely linear optimisation framework is developed, and executed on a rolling-plan basis, with the energy storage model considering the effects of both self-discharge and capacity degradation. The tool developed as part of this study is flexible and can easily be modified to accommodate various other technologies and system configurations.

Conclusions and future work

Chapter 8 reflects on the analysis performed and results found in the thesis, and describes future work that may be carried out to draw further insights.

[1]Since only costs of air storage are addressed in this thesis, other component costs (power conversion system, balance of plant, installation, etc.) are taken from the literature.

Chapter 2

Background

2.1 Introduction

Compressed air is widely used as an energy carrier in various industries such as manufacturing, food processing, etc., where it is usually generated by employing electrically driven compression machinery. In the UK, air compression consumes around 10 [TWh] of electricity each year, which accounts for 3 [%] of all electrical demand [16]. As noted by Kitchener [17], if all compressors were a country, they would have the same electrical demand as Italy, Spain and Turkey combined.

Whilst the first instance of using compressed air as an energy storage medium can be traced back to the patent *Means for storing fluids for power generation* by Gay [18], the practical implementation of this concept gained momentum in early 1970s when nuclear and coal plant were introduced into the power generation mix. This generated enough economic incentive for electrical energy storage by means of power price arbitrage.

The first CAES plant in the world, of 321 [MW]/2 [h] capacity, was built in 1969 in Huntorf (Germany) by the utility Nordwestdeutsche Kraftwerke, now owned by E.ON, to provide black start capability and reserve capacity to the northern German electrical grid [19]. The second CAES plant, of 110 [MW]/26 [h] capacity, was built in 1991 in McIntosh (Alabama,

US), now owned by PowerSouth Energy Cooperative. However, these plants combust natural gas to supply heat to the cool, high-pressure air before it is expanded to recover power[1]. Driven by the need to reduce greenhouse gas emissions, several academic and industrial groups have led intense research and development efforts both in Europe and the US to investigate advanced CAES technologies – so-called Advanced Adiabatic CAES (AA-CAES) systems – focused on the addition of thermal energy storage for minimising or eliminating natural gas/fossil fuel use present in conventional designs (such as Huntorf and McIntosh plants). While no such AA-CAES projects have come into commercial fruition as yet, a summary of noteworthy attempts and trials is as follows.

The ADELE (2010-2012) and ADELE-ING (2013-2017) projects were led by RWE Power, General Electric, Zublin AG and DLR in Germany [20;21]. The ADELE project focused on technical feasibility and system component development – most importantly air compressors capable of withstanding high-temperatures, suitable materials for thermal energy storage with considerations on thermomechanical stresses and resulting limitations on bearings and lubrication [22]. The follow-up ADELE-ING project aimed at performing detailed engineering design of the AA-CAES plant for pilot demonstration and testing. However, it was reported in 2017 [23] that efforts were abandoned due to both technical difficulties with minimising costs of specialised compression/expansion equipment and thermal energy storage system, coupled with poor projected financial returns from wholesale market trading activities.

The Iowa Stored Energy Park project spearheaded by the Iowa Association of Municipal Utilities intended to build, by 2015, a 270 [MW]/16 [h] CAES plant co-located with 75-100 [MW] of wind capacity [24]. The project was discontinued in 2011 [25] after studies concluded that the aquifer would not have provided the air flow rates required for the intended sizing of the power conversion system.

The Norton Energy Storage project was announced in 2009 by First Energy Generation Corp [26]. The project was discontinued in 2013 due to "low power prices and insufficient

[1] See § 2.3.1.

demand" [27].

Several start-ups such as US-based LightSail Energy, General Compression, SustainX, and France-based Airthium aim(ed) to develop and commercially deploy near-isothermal CAES systems. The near-isothermal effect was achieved by employing reversible reciprocating piston machines (e.g. hydraulic linear actuators and pumps/motors) and motor/generator units. Most notably, General Compression in partnership with ConocoPhillips trialled, in 2010, a 2 [MW]/150 [h] CAES system co-located with onshore wind in Gaines, Texas [28]. The air compression system was powered by wind and high pressure air was subsequently stored in a salt cavern. General Compression achieved the near-isothermal effect by using a pond of water located in proximity to the plant to transfer the heat to and from the air during compression and expansion, respectively; the water pond therefore acted as both the heat sink and the heat source.

The concepts of LightSail Energy and SustainX on the other hand involved spraying a fine mist of water in to the compression/expansion cylinders to absorb the 'heat of compression' [29;30]. Whilst the water spray-injected compression is an interesting idea, moisture in compressed air can lead to material corrosion and build-up of deposits if mixed with residual dust or oil in the machine, thereby increasing pressure losses in air transportation pipes. Possibly beset by these problems, LightSail Energy was put into liquidation in 2017 [32] and SustainX merged with General Compression in 2015 [33].

Airthium claimed to have developed an electromagnetic compressor capable of achieving high efficiencies [34]; however, Airthium has not reported any progress to date apart from the development of a 10 [W] prototype of the compressor [35].

Whilst it is not clear what specific challenges were encountered by these companies, the fact remains that for near-isothermal CAES systems the most significant challenge is enabling compression/expansion processes that are slow enough to minimise irreversibility (i.e. the temperature difference between the air being compressed or expanded and the

environment) but fast enough to have practical relevance and economic advantage to industry[2].

It is worth noting that to date, the Huntorf and McIntosh plants are the only CAES systems proven at utility scale. For a more detailed history of the technology, the reader is referred to the article by Budt et al.[19].

In the following, some basics of CAES covering the thermodynamics of compression and expansion, the importance of heat management in CAES, options for air storage, their location as well as the broad system design classes are described.

2.2 Basic principles of CAES

Generally, CAES systems operate to fill up the air storage reservoir by absorbing electricity when the cost of energy is low (i.e., charging), and emptying the storage reservoir to produce electricity when the cost of energy is high (i.e., discharging).

During charging, a compression device is driven by electricity to feed compressed air into a reservoir. Raising the pressure of the air also raises its temperature, i.e., compressing the air makes it hot. This 'heat of compression' may be discarded to the environment or stored before the air is passed into its containment.

During discharging, compressed air is withdrawn from the reservoir, heated and expanded in appropriate machinery to recover power. Conceptually, the expansion process mirrors the compression process in that the temperature of the air decreases with the reduction in pressure. It is therefore crucial to feed the air with sufficient thermal energy prior to its expansion, as failure to do so in practical systems will result in the freezing of any moisture content present in the air, potentially causing damage to the expansion device.

[2]It is worth noting that the heat stored in near-isothermal AA-CAES systems has zero (or nearly zero) exergy because all of the heat content is at (or very close to) ambient temperature; in other words, the heat is of low grade. By contrast, AA-CAES systems such as that proposed by ADELE employs adiabatic compression, and could therefore store more exergy in air as well as high-grade heat. See § 2.3.2 for more detail.

It is possible to expand the air to sub-ambient temperatures so that the cold energy can be extracted to then satisfy some cooling demand (e.g. at data centres), but this is not explored in the present thesis.

2.2.1 Governing thermodynamics

In this thesis, all analysis except that in Chapter 4 assumes that the air obeys the ideal gas law. Furthermore, the air is assumed to be completely dry. Again, Chapter 4 devotes a section on the effect of moisture on the thermodynamic properties of air. In the following, some equations governing the thermodynamics of CAES systems are described, which also assume the ideality of air behaviour.

The ideal gas law is[31]:

$$P_{\text{air}}\, V_{\text{air}} = m_{\text{air}}\, R_{\text{air}}\, T_{\text{air}} \tag{2.1}$$

where P_{air} is the pressure of air, V_{air} is the closed volume containing air, m_{air} is the mass of air in volume V_{air}, R_{air} is the specific gas constant for air, and T_{air} is the temperature of the bulk air.

When air is compressed or expanded adiabatically, the relationship between the temperature and pressure before the process to that after the process is given by[31]:

$$P_{1,\text{air}}\, V_{1,\text{air}}^{\gamma} = P_{2,\text{air}}\, V_{2,\text{air}}^{\gamma} \tag{2.2}$$

where the subscripts 1 and 2 refer to the state of the air before and after the process, respectively, and where γ is the ratio of the specific heat capacities of the fluid at constant pressure and constant volume.

Equation (2.2) expressed in terms of pressure and temperature becomes:

$$\frac{T_{2,\text{air}}}{T_{1,\text{air}}} = \left(\frac{P_{2,\text{air}}}{P_{1,\text{air}}}\right)^{\frac{\gamma-1}{\gamma}} \tag{2.3}$$

For a compression pressure ratio $\left(\frac{P_{2,\text{air}}}{P_{1,\text{air}}}\right) = 25$, e.g. from atmospheric pressure to around 25 [bar], single-stage compression of air starting at 20 [C] (293 [K]) will reach a final temperature of 462 [C] (735 [K]), equal to a temperature rise of 442 [C].

The work input to the compressor for this adiabatic compression process, where no net heat exchange with the surrounding, is given by [31]:

$$W_{\text{adiabatic}} = P_{1,\text{air}}\, V_{1,\text{air}}\, \gamma\, \frac{\left(\left(\frac{P_{2,\text{air}}}{P_{1,\text{air}}}\right)^{\frac{\gamma-1}{\gamma}} - 1\right)}{\gamma - 1} \tag{2.4}$$

The same pressure ratio can be achieved for instance via two-stage compression with intercooling after the first stage. Assuming equal pressure ratios between the compression stages, each stage will have a pressure ratio of $\sqrt{25} = 5$. The temperature rise in this case will be 126 [C]. Therefore, increasing the number of compression stages will reduce the rise in air temperature and the quality of thermal energy available for capture. However, it also has the effect of reducing the work input to air compression, which may be the objective in some processes.

If the number of compression stages is chosen to be arbitrarily large, the temperature of the air will remain nearly constant throughout, approximating an isothermal process. The work required to carry out the compression process in this case is given by [31]:

$$W_{\text{isothermal}} = P_{1,\text{air}}\, V_{1,\text{air}}\, \log\left(\frac{P_{2,\text{air}}}{P_{1,\text{air}}}\right) \tag{2.5}$$

It should be noted that the product $P_{1,\text{air}}\, V_{1,\text{air}}$ in equations 2.4 and 2.5 is equal to $P_{2,\text{air}}\, V_{2,\text{air}}$ as the temperature of the air remains constant.

The isothermal and adiabatic compression/expansion processes are thermodynamic ideals. Practical systems operate somewhere in between these two ideals, tending to one or the other, depending on the thermal conductivity of the system boundary and the speed of the compression/expansion process. A quick process without heat exchange may approximate adiabatic behaviour, whereas a slow process with little change in fluid temperature

may approximate isothermal behaviour. Nevertheless, the above equations are useful in determining the bounds for the work that can be extracted from the air store (cf. Chapter 5).

2.2.2 System performance metrics

Estimating the electrical roundtrip efficiency of CAES designs requires great care. Diabatic systems, for instance, combust natural gas to heat up the air prior to expansion. Therefore, energy is supplied to the system from both electricity and heat, whereas energy is extracted as electricity only. Data published by BINE Information Service [36] state that to produce 1 [kWh] output of electrical energy at Huntorf CAES plant requires 0.8 [kWh] input of electrical energy and 1.6 [kWh] of natural gas. At McIntosh CAES plant, electrical output of 1 [kWh] requires electrical input of 0.69 [kWh] and thermal input of 1.17 [kWh].

There exist two approaches to calculating the roundtrip efficiency of diabatic CAES systems. The first – and the most widely used in existing literature – is a simple ratio of input and output energy:

$$\eta_{\text{D-CAES,energy}} = \frac{E_{\text{output,el}}}{E_{\text{input,el}} + E_{\text{input,th}}} \tag{2.6}$$

The second is a ratio of *valuable* input and output energy, or exergy:

$$\eta_{\text{D-CAES,exergy}} = \frac{E_{\text{output,el}}}{E_{\text{input,el}} + \eta_{\text{th-el}}\, E_{\text{input,th}}} \tag{2.7}$$

The denominator of (2.6) implies equivalence between electrical and thermal energies. However, unlike electrical energy, not all thermal energy is useful. Gas-fired technologies such as open-cycle or closed-cycle gas turbine can convert about 60 [%] of input thermal energy into electricity. Furthermore, since diabatic systems are a combination of storage and generation plant, efficiency measures based on energy may be misleading when comparing diabatic designs with other 'pure' storage technologies such as pumped hydroelectric storage, battery storage, etc.

To estimate the useful thermal energy, or exergy, we may scale the thermal input, $E_{\text{input,th}}$, by a reference efficiency factor, $\eta_{\text{th-el}}$, to represent the conversion of thermal energy to electrical energy. This is shown in (2.7). Efficiency values obtained from (2.6) may be useful in comparing the performance of various diabatic designs. However, comparison with other storage technologies is more representative with (2.7).

Using (2.6), $\eta_{\text{D-CAES,energy}}$ for Huntorf and McIntosh plants are approximately 42 [%] and 54 [%], respectively. Using (2.7), and assuming $\eta_{\text{th-el}} = 60$ [%], $\eta_{\text{D-CAES,exergy}}$ for Huntorf and McIntosh plants are approximately 57 [%] and 72 [%], respectively.

2.2.3 Integration with power generation or demand

Several researchers have proposed the direct integration of CAES with sources of power generation or demand, mainly driven by the need for minimising energy conversions, i.e., losses. For instance, Ingersoll and Marcus [37] and Garvey [38] propose the integration of air compression with wind turbines, Sieber [39] with wave energy, and Fumio [40] and Southcombe [41] with tidal energy. Similarly, industrial air compression accounts for a significant proportion of electrical demand as discussed earlier, and this offers direct integration possibilities with storage of air and creates savings in capital costs of power conversion devices. These designs are out of scope of the present thesis and are not explored further.

2.3 System design classes in CAES

CAES is not one technology; it represents a broad array of technologies with several choices for configuring its system components comprising, most importantly, equipment for fluid compression and expansion, heat exchange, compressed air storage and thermal energy storage. As seen in § 2.2, the management and storage of thermal energy, although not explored in this thesis, play critical roles in enhancing the effectiveness of CAES systems.

The various designs of CAES systems may be classified within two categories:

- Diabatic systems, which use an *external* source of heat prior to recovering power from compressed air, and
- Adiabatic systems, which do not use an external source of heat before power recovery

2.3.1 Diabatic designs

The existing grid-scale CAES plants – 321 [MW]/2 [h] plant in Huntorf, Germany, owned by E.ON Kraftwerke, and 110 [MW]/26 [h] plant in McIntosh, Alabama, USA, owned by PowerSouth Energy Cooperative – are examples of diabatic design implementation. As discussed earlier, diabatic CAES systems are a combination of storage and generation plant, and external heat is supplied by combusting the air with natural gas after the air is withdrawn from the cavern. The plants also employ the isochoric air storage mechanism in large underground salt caverns. A general schematic of diabatic CAES plants is shown in Fig. 2.1.

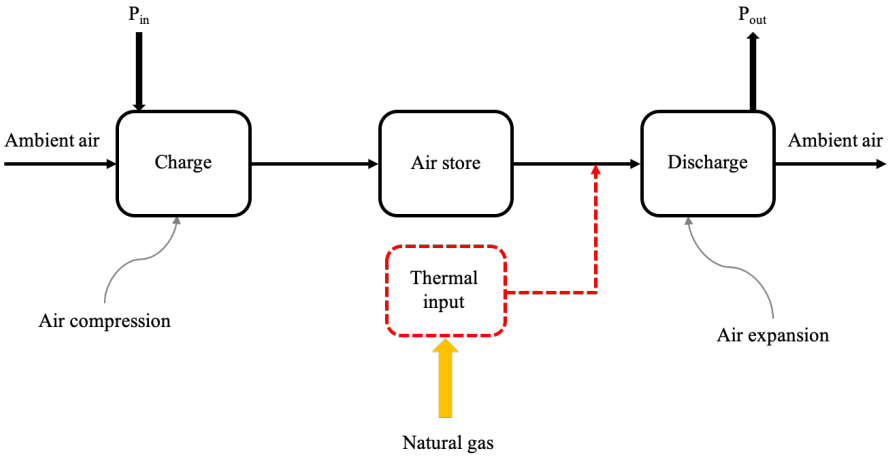


FIGURE 2.1: Schematic for D-CAES plants

A simplified process schematic of the Huntorf plant is shown in Fig. 2.2 [44]. The air is compressed to a maximum pressure of 72 [bar] in two stages with intercooling between the stages. The heat is discarded to the environment. It is cooled again before sending it to the storage reservoir. The compressed air is stored in two solution mined salt caverns with a total storage volume of 310,000 [m^3]. The caverns cycle between 42 [bar] and 72 [bar].

During power recovery, the air from the cavern is throttled to around 42 [bar] before entering being combusted with natural gas and expanded in two-stages with reheating between the stages. The exhaust of the expansion process is at atmospheric pressure and 480 [C]. All exergy contained in this heat is unused. The plant offers black start, frequency regulation and reactive power services to the local grid [19].

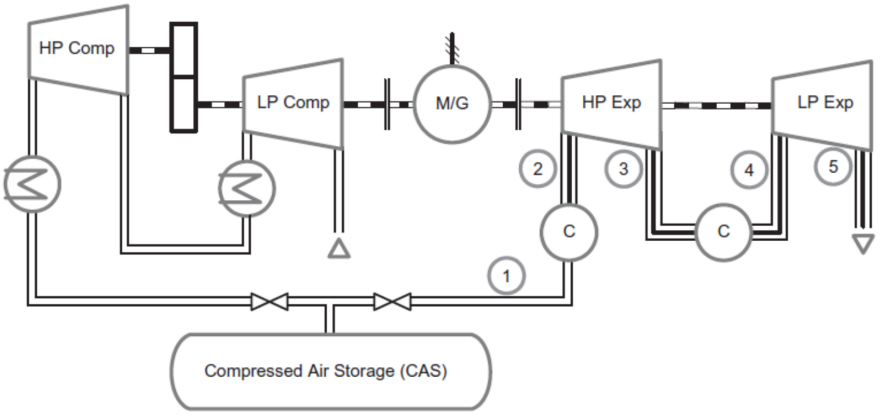


FIGURE 2.2: Schematic of the Huntorf plant compression/storage/expansion process. Adapted from Wolf [44]

The simplified process schematic of the McIntosh plant is shown in Fig. 2.3 [44]. The basic single-shaft arrangement of the motor/generator is similar to the Huntorf plant. However, a single salt cavern of 538,000 [m^3] volume is used to store the air. The main difference between the two plants is that the McIntosh plant recovers some of the exhaust heat via a recuperator to pre-heat the compressed air exiting the cavern. This minimises the amount of natural gas used for combustion. In contrast to the Huntorf plant, where black start capability and reserve power were the focus, the McIntosh plant was designed to shift energy on weekly timescales [19].

2.3.2 Adiabatic designs

The term "adiabatic CAES" is perhaps misleading because the word "adiabatic" has a precise thermodynamic definition. In the context of CAES, "adiabatic CAES" implies that the overall process (charging, storage and discharging) does not use a net external source of heat to aid with recovery of power from high-pressure air. Most authors specifically use

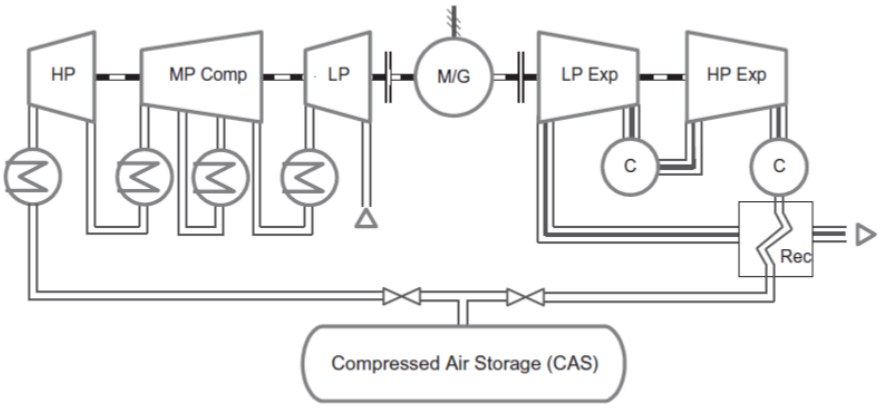


FIGURE 2.3: Schematic of the McIntosh plant compression/storage/expansion process. Adapted from Wolf[44]

this term to describe CAES systems without the use of fossil fuels to supply heat during expansion of air. Therefore, CAES systems in this design class integrate thermal energy storage to capture the heat generated during air compression and feed it back for reheating during air expansion. A general schematic of adiabatic CAES plants is shown in Fig. 2.4.

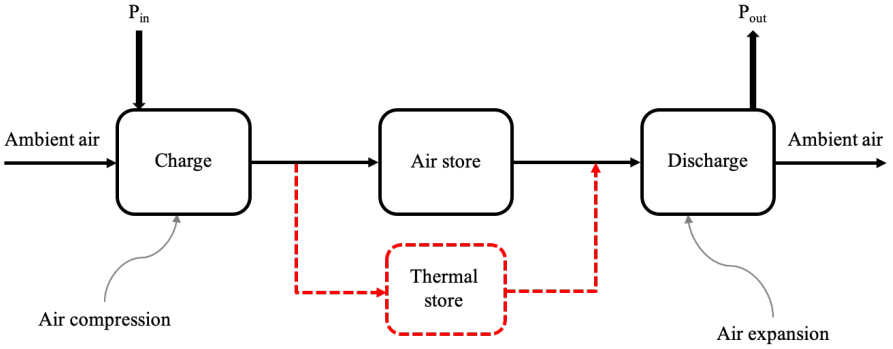


FIGURE 2.4: Schematic for AA-CAES plants

In general, adiabatic CAES systems are classified based on the type of compression and expansion processes employed: near-isothermal and adiabatic (where the latter now refers to the thermodynamic meaning of compression/expansion).

Isothermal compression (expansion) processes reject (absorb) heat to (from) a large heat sink (source) at, or close to, ambient temperature. Near-isothermal compression, for instance, involves maximising reversibility by minimising the temperature differences between the compressor driving the flow of heat to the environment. In practice, this is

achieved with several stages of compression and high-efficiency inter-cooling in between. A large body of water or the environment itself acts as the heat store (i.e. sink) for the low-temperature heat, which can later be used to prevent the air from cooling during expansion.

On the other hand, adiabatic CAES system designs use one or a few stage(s) of air compression. This raises the temperature of the air substantially compared with the near-isothermal variant. The heat associated with the high-temperature compressed air can be stored, and the cooler compressed air then sent to the air reservoir. The stored heat can be reused before the high-pressure air enters the expansion device.

The CAES system designs described above are not without challenges – the major ones were discussed earlier in §2.1. However, employing thermal energy storage can be beneficial to CAES systems, and the following will demonstrate how.

Assuming ideal gas behaviour, the compression of a given mass of air with subsequent cooling to reach its initial temperature results in the ejection of a quantity of heat that is identical to the net compression work. Whilst electrical energy is completely useful – indicating that mechanical work is also completely useful – not all heat is as valuable as work, because its value is dependent on fluid temperature. *Exergy* quantifies the amount of useful work that can be extracted from a system by allowing it to reach equilibrium with the surrounding environment. For an ideal gas, the exergy is given by:

$$B_{\text{ideal}} = m \left[C_p \left(T - T_0\right) - T_0 \left(C_p \ln\left(\frac{T}{T_0}\right) - R_{\text{air}} \ln\left(\frac{P}{P_0}\right)\right)\right] \tag{2.8}$$

Here, B_{ideal} is the exergy of the fluid which depends on the mass of the fluid, m, the specific heat of the fluid, C_p, the pressure, P, and temperature, T, of the fluid, the specific gas constant of the fluid, R_{air}, and the reference pressure, P_0, and reference temperature, T_0.

The exergy associated with the heat is zero if the fluid carrying that heat is at ambient or the reference temperature, and approaches the value of the heat at very high fluid temperatures. Thus, heat captured during near-isothermal compression has little exergy since the surrounding environment contains an infinite amount of heat at the same temperature. However, heat captured during adiabatic compression can contain substantial amounts of exergy at large enough temperatures.

If the adiabatic CAES system is ideal and reversible, i.e., the thermodynamic processes in the considered system employ ideally-behaving fluids and the system components are devoid of exergy losses, then the temperature at which the heat is stored (and indeed the pressure at which the air is stored) does not impact the system efficiency. However, low air storage pressures and the means by which the heat is stored (if thermal storage is employed) have a direct impact on the *economics* of the adiabatic CAES system. This is illustrated in Fig. 2.5, where the exergy per unit volume of air compressed is shown for various air storage pressures.

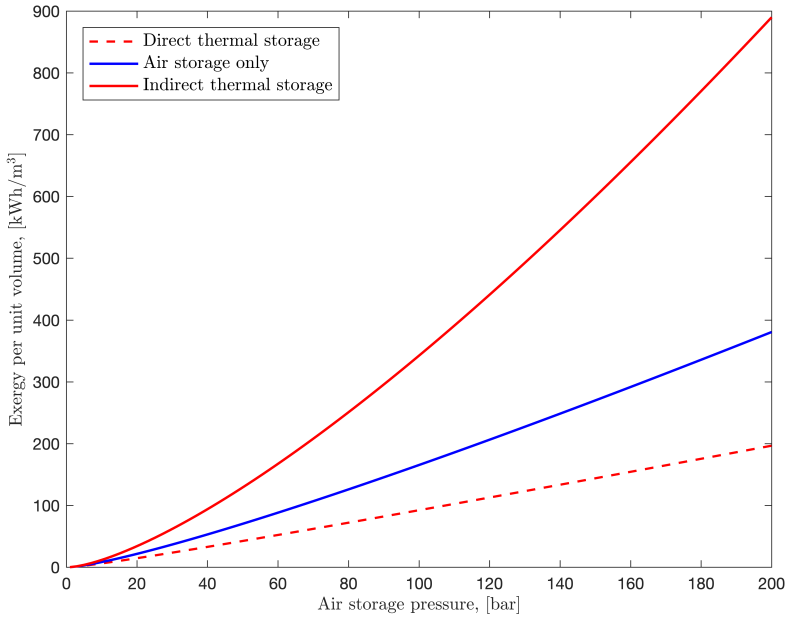


FIGURE 2.5: Exergy stored per unit volume of air compressed, with/without thermal energy storage, in an ideal CAES process

If all of the exergy is stored in pressurised air (i.e. the exergy in heat is zero), then the blue line (labelled *Air storage only*) shows how volumetric exergy varies with the final pressure of the compressed air. At low pressures, relative larger air storage reservoirs are required to store a given amount of exergy. It is therefore important to maximise the storage pressure of the air store to limit its size and costs.

If heat is also stored, then it is important to decide whether to embed the heat store within the air store or dedicate a separate thermal energy store external to the air store [45]. Storing heat within the air store enables effective heat transfer due to the large contact area between the air and the thermal storage media. However, the pressure vessel will not only be required to withstand high pressures and temperatures cyclically, but also require larger air stores compared to storing exergy in air only. This is relatively worse, economically, versus exergy storage in air only, as demonstrated by the dashed red line (labelled *Direct thermal storage*).

The most attractive option, from the perspective of the costs of the air storage reservoir, is to store the heat in a separate container as this further limits the size of the air storage reservoir (versus exergy storage in air only). This is demonstrated by the solid red line (labelled *Indirect thermal storage*). At larger pressures, thermal energy storage accounts for larger proportions of the total exergy stored in both the heat and the air. Therefore, compressors that minimise heat loss to the environment are required. This is different from conventional industrial compressors where the objective is to minimise work input for a given final pressure. This inevitably involves discarding heat at every available opportunity as relatively hot air requires more compression work.

Highly efficient heat exchangers are also required to capture heat from (return heat to) the compression inter-cooling process (the expansion inter-heating process). Therefore, the temperature difference between the air and the heat transfer medium must be minimised whilst maintaining minimal pressure losses.

It should be noted that this discussion does not consider the mass, and thus the costs,

of the thermal energy store, which depends on the heat capacity of the storage material. Furthermore, there are are several design and operational aspects to consider. The ADELE and ADELE-ING projects, which investigated packed-bed regenerators, dealt with inventory arrangement for the regenerators, thermomechanical cyclic loads (thermal ratcheting), selection of suitable low-cost thermal storage material, pressure losses within the store and finally experimental validation. Challenges with the development of specialised compressors, reduction of costs of thermal storage to expected levels, compounded by weak wholesale energy price signals propelled the ADELE-ING team to recommend partially adiabatic schemes that co-fire natural gas and/or integrate power-to-heat from excess electricity.

In all practical applications involving processes such as heat exchange, compression/expansion, mixing of fluids, etc., system irreversibilities occur and exergy is destroyed as a result. Therefore the attractiveness of adiabatic CAES systems depends on a trade-off between maximising reversibility and minimising costs of the compressed air and thermal storage systems.

2.4 Air storage reservoirs for CAES

A key component of any CAES system is the compressed air storage reservoir, as it not only contributes to a large proportion of recoverable energy depending on how it is operated, but can also account for significant capital expenditure. This section is therefore devoted to the basic operation mechanisms of the air store as well as their locatability.

In practical systems, the storage of high-pressure air is deployed in stores that exhibit one of two fundamentally different characteristics. One is constant volume, or *isochoric*, air storage where the volume occupied by the air in the vessel remains nearly constant relative to the total mass of stored air. This is an approximation of real behaviour where the change in volume of stored air between the maximum and minimum pressures is often so small that it is ignored. The other is constant pressure, or *isobaric*, air storage where

the pressure inside the vessel is insensitive to the total mass of stored air and thus remains nearly constant. This is also an approximation of real behaviour where pressure variation within the store is negligible.

2.4.1 Isochoric mechanism

Isochoric air stores are fixed volume containers which have conduits to transact the air, as illustrated in Fig. 2.6. Underground salt caverns employed in existing CAES plants and aboveground steel tank-based air storage are examples of isochoric stores.

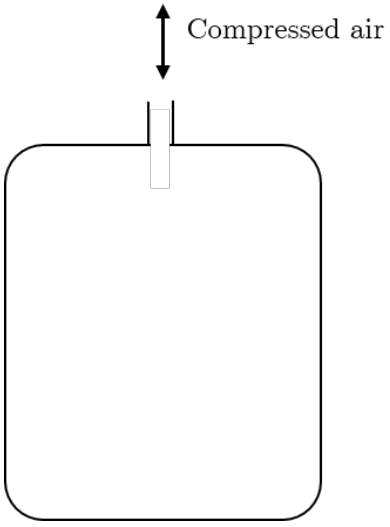


FIGURE 2.6: Schematic for an isochoric air storage reservoir

Both the pressure and temperature vary with the fill level of compressed air within the store, indicating that the resulting mechanical response is affected by both applied pressure and temperature changes in the store material. This is a complex issue, and is explored in Chapter 3.

In some CAES designs employing isochoric stores, as is the case with existing CAES plants, pressure of the air is reduced by throttling after exiting the cavern to the rated pressure of the expansion device. This results in a reduction of the useful energy that could be recovered. A remedy for avoiding throttling losses is to use variable pressure expansion

devices for power recovery. However, these devices are more complex which translates into higher capital costs.

2.4.2 Isobaric mechanism

Isobaric air stores enable near-constant pressure operation. One way of achieving this is by displacing the air contained within the fixed volume compressed air container with a fluid (e.g. water, oil), as shown in Fig. 2.7.

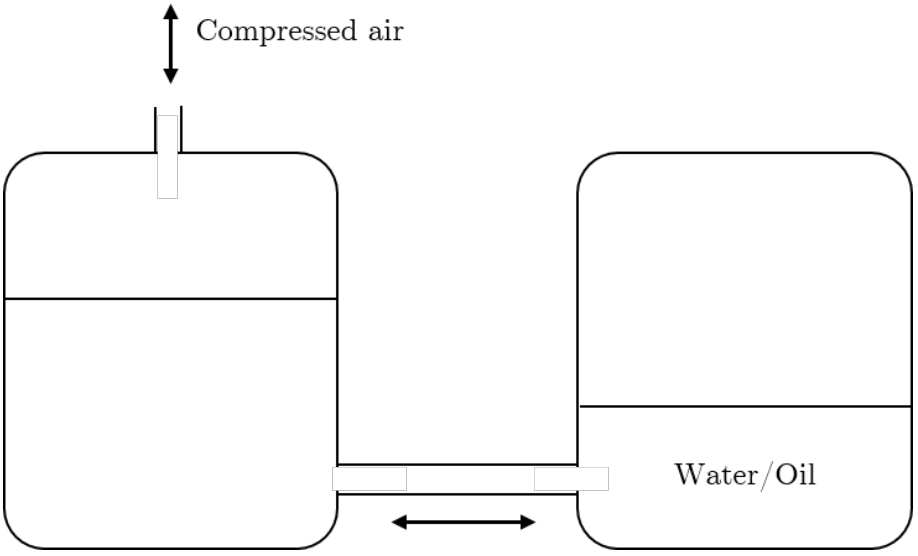


FIGURE 2.7: Schematic for a fixed volume isobaric air storage reservoir

This is advantageous because the system operation can be optimised for a unique design point due to the near identical pressure rating for compression and expansion machinery. Unlike isochoric containers, isobaric containers do not involve temperature fluctuations and therefore typically experience relatively lower stress variations. Furthermore, the amount of recoverable energy in this mechanism is relatively higher since throttling of high-pressure air is non-existent.

The isobaric mechanism can also be achieved by exploiting naturally occurring phenomena such as the high pressure environment in deep sea by employing either flexible containers that change their shape to enable near-constant pressure operation or rigid containers

which allow fluid displacement similar to Fig. 2.7. Analysis of fixed shape underwater structures for compressed air storage is the subject of Chapter 5.

2.4.3 Locations for the air stores

Air stores for CAES systems can be located above-ground (e.g. steel tanks), underground (e.g. salt caverns) or underwater (e.g. flexible fabric structures). Above-ground storage of compressed air in steel tanks is a mature technology, with an enormous supply chain. However, it is relatively more expensive than its underground or underwater counterparts. The capital costs of tank-based storage is directly proportional to the storage volume and the differential pressure between the air and the environment [42], which prevents the widespread deployment of these stores, especially at grid scale.

Underground and underwater storage of compressed air are characterised by high fixed costs (e.g. drilling a hole to form a cavern, see Fig. 2.8), but the marginal cost of extending the storage volume further can be significantly small. See § 3.6 for more detail.

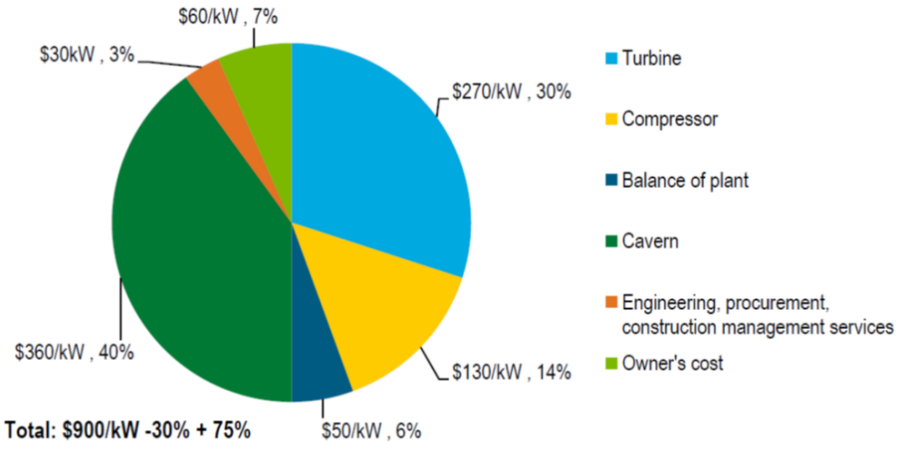


FIGURE 2.8: Estimated capital cost split for a typical CAES plant. Adapted from Black and Veatch [43]

2.5 Conclusions

This chapter has presented an overview of various aspects of CAES systems. In particular, it has highlighted that CAES represents a broad class of technologies, with options for the type of system components used and their locations. Previous discussion in this chapter has also highlighted the important role of thermal energy management in a CAES system. However, thermal energy storage is a vast topic which can be employed as a standalone energy storage alternative, or can be used in conjunction with other storage technologies (such as CAES). Whilst thermal energy storage must form part of any appraisal comprising a whole CAES system – i.e. compression/expansion systems, air store, heat exchangers and other auxiliary components – this thesis is focused on the air storage containment following from the fact that a central component of any CAES plant is the air storage reservoir and its operation mechanism. Therefore, the thesis:

- explores and formulates a methodology for investigating the structural integrity of salt cavern air stores used in large-scale CAES systems
- proposes and investigates the thermodynamic effectiveness of a novel energy storage system by hybridising compressed air storage with liquid air storage
- undertakes preliminary analysis into whether rigid containments are suitable for underwater compressed air storage
- compares the cost of storing air underground in a salt cavern, aboveground in a hybrid compressed air-liquid air storage system, and underwater in a rigid concrete containment, and
- investigates the financial returns of a CAES system operating in the UK energy market

Chapter 3

Compressed air energy storage in salt caverns

3.1 Introduction

Grid scale CAES, usually rated at several hundreds of MW of electrical output delivered over relatively long durations of a few hours to a few days, requires large volumes of pressurised air to be stored. Underground geological formations, such as salt caverns, hard rock caverns and porous aquifers, are all candidates for storing large amounts of air needed for grid scale CAES plants. Indeed, the industry is very well-accustomed to storing large volumes of natural gas and hydrogen in salt caverns. Although salt caverns have been widely used for underground gas storage, underground gas storage capacity in suitable salt deposits are a small fraction of that potentially available via hard rock caverns or aquifers around the globe. However, salt caverns possess two key advantages over hard rock caverns or aquifers making them the prime candidate for parties pursuing large-scale CAES:

- Salt rock has very low permeability which makes them virtually air- or gas-tight: values of around 10^{-22} to 10^{-20} [m^2] have been reported [48]. In the context of CAES, this ensures minimal loss of stored energy through leakage of pressurised air.

- Salt caverns enable relatively high air injection and withdrawal rates compared to the working air capacity (i.e. air that is not 'cushion gas'[1]) with the only limiting factor being the dehydration capability of the air handling equipment at the surface [49;50]. In the context of CAES, this allows the utilisation of compression and expansion units with high power ratings.

It is worth noting that there have been some experimental studies to date on rock caverns for compressed air storage. In Japan, two former mines were converted into rock caverns and tested for air tightness. One of the caverns was located 450 [m] below ground surface with storage volume of around 1,600 [m^3] [51]. Furthermore, the cavern was lined with reinforced concrete and a rubber sheet. However, a leakage rate of around 0.5 [%] by volume per day was observed due to cracks that arose in the concrete lining and rubber sheet. The second cavern, in this case unlined, was located 1,000 [m] deep with storage volume of around 200 [m^3]. The leakage rate observed was much more drastic – a 60 [bar] pressurised cavern reduced to ambient pressure in a mere 5 hour time-interval [52].

The Iowa Stored Energy Park project planned on constructing a 270 [MW] / 16 [h] CAES plant with air storage in an aquifer. However, the project was discontinued after several years of feasibility studies concluded that relatively low air flow rates in the aquifer (negatively impacting system power output) combined with low realised aquifer permeability (negatively impacting total air storage capacity) would have rendered the plant uneconomic [25].

Due to these issues, commercial CAES ventures based on rock cavern or aquifer based storage have to date been unsuccessful.

[1] This is the gas that must remain in the isochoric vessel when cycled between the maximum and minimum pressures to provide structural stability to the cavern and prevent its roof from spalling

Storing compressed air in salt caverns for the purpose of recovering power at a later time is not straightforward: Unlike long-term (e.g. seasonal) storage of natural gas in salt caverns, frequent (e.g. hourly or daily) cycling of compressed air causes significant temperature and pressure variations inside the cavern volume, which affect the material behaviour of the surrounding rock salt. These fluctuations are sensitive to cavern geometry and compressed air cycling characteristics. The changes in rock temperature, resulting from air temperature fluctuations, induces additional stresses around the cavern [53;54;55]. It becomes important, therefore, to assess the stability of the cavern due to the high-frequency cyclic thermomechanical loads that arise. This informs the design of the air storage reservoir, which is a crucial component of any compressed air based plant.

The usage of salt caverns for natural gas storage and its potential to contain nuclear waste motivated several parties to investigate the long-term behaviour of salt caverns operating at near-constant internal pressures with negligible changes in gas and rock temperatures. A large subset of that research deals with the tightness of rock salt for long-duration natural gas storage and seepage of gas [56;57], and the development of criteria to predict long-term structural integrity of rock salt [58;59;60;61].

Several researchers have also investigated the thermodynamics of salt caverns transacting compressed air. The thermodynamic response of air within the cavern volume was first modelled by Langham [62] by considering a horizontal hard rock tunnel with daily cycling of compressed air. Assuming the rock to be homogeneous, a one-dimensional radial model was developed considering air leakage from the cavern and heat conduction within the rock; subsequently, the dependence of temperature variations on material properties and the cavern inner radius was demonstrated. Raju and Khaitan [63] and Kushnir et al. [64] outline an analytical approach to model the thermodynamic response of the air and surrounding rock; whilst Raju and Khaitan adopt a simplified approach by considering the cavern wall temperature to be constant, Kushnir et al. remove this constraint. Their analyses show that material properties of the rock, heat transfer between the air and rock particles, and air injection temperature all significantly affect temperature and pressure variations in the

cavern. The details of the Huntorf and McIntosh salt cavern thermodynamic models are proprietary. However, a brief description of the Huntorf model along with measurements of air temperature and pressure data from trial plant runs are provided in Quast and Crotogino[65], whereas the McIntosh model is described in Nakhamkin et al.[66].

This chapter develops a methodology to investigate the mechanical response and structural stability of rock salt due to the combined thermomechanical cyclic loading in an underground compressed air storage system. In the first instance, the thermodynamic response of air in the cavern volume as well as the surrounding rock with respect to time is obtained using the laws of thermodynamics. Using the thermodynamic response as part of the boundary conditions on the rock salt structure, the mechanical response for cyclic loading is evaluated by employing an uncoupled thermoelastic material behaviour model. The thermodynamic and mechanical responses are obtained by discretising the governing equations and solving them numerically by the finite element method. As far as the author is aware, this is the first attempt at coupling the thermal and mechanical response models of a salt cavern structure transacting a compressed gas in the public domain. Moreover, it is important to note that only the storage containment of a typical large-scale CAES facility, i.e. the salt cavern, has been investigated. Power conversion machinery that generate compressed air and recover power through suitable heat exchange elements are not part of this study.

We begin by formulating the equations governing cavern thermodynamics, heat transfer between the air and cavern walls, and heat transfer through the surrounding rock particles. Next, the general behaviour of rock salt under applied loads and the thermoelastic constitutive material model is discussed briefly. This is followed by discussion on material failure and stability criteria chosen for the present analysis. Then, the finite element model employed in this work is outlined with associated governing equations. Finally, for user defined cavern geometry and cyclic air transaction characteristics, the thermodynamic and mechanical responses are presented and discussed, and some conclusions are drawn.

3.2 Cavern thermodynamics and heat transfer

The high-frequency cyclical transactions of compressed air into and out of the cavern result in the dynamic transfer of mass and energy across the system boundary. To predict the changes in temperature and pressure of air inside the cavern, and model the process of heat transfer between the air and surrounding rock brought about by these changes, we employ the laws of thermodynamics, along with appropriate simplification rules. The evaluation of the aforementioned quantities facilitate the estimation of mechanical response of the rock salt.

We begin by considering an idealised cavern, shown schematically in Fig. 3.1, whose enclosure forms the control volume for the thermodynamic problem. As shown, the shape approximates a vertical cavern by considering a cylindrical body with hemispherical end-caps. Typical gas storage caverns in existence are vertical in nature [67] with an aspect ratio of about 1:6 (i.e. unit width to unit height) [68] as this provides for a structurally stable roof span. Moreover, the existing CAES plants in Huntorf and McIntosh both employ vertical salt caverns approximating the shape shown in Fig. 3.1.

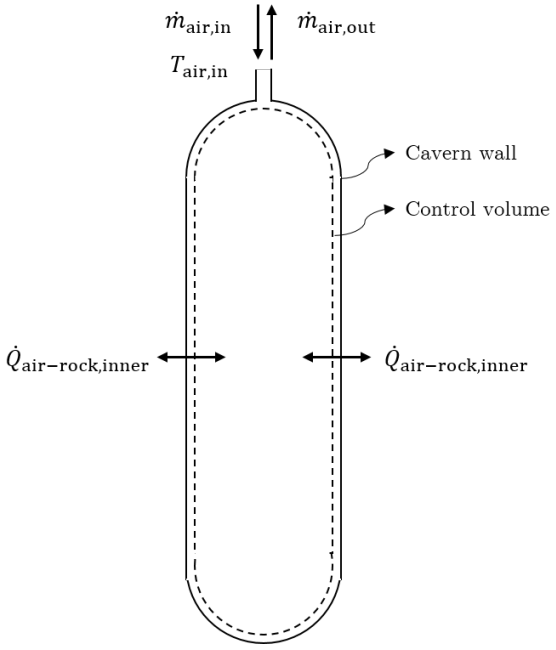


FIGURE 3.1: A schematic of the idealised cavern shape with air injection and withdrawal, and heat transfer across the walls

The transaction of air is a binary process; namely, air is either injected into or withdrawn from the cavern using a single pipe or conduit located at one end of the cavern. It is assumed that the air is injected at a known constant mass flow rate of $\dot{m}_{\text{air,in}}$ and temperature $T_{\text{air,in}}$, and withdrawn at a known constant mass flow rate of $\dot{m}_{\text{air,out}}$, as shown in the schematic. It is also assumed that the change in cavern volume, and its effect on the changes in temperature and pressure inside the containment, is negligibly small; thus, for all practical purposes the cavern volume remains constant [69]. Furthermore, the temperature and pressure of air inside the cavern volume are assumed to be uniform, since the rate of change of these quantities with respect to time are relatively small [69;70]. Finally, it should be noted that the properties of air are calculated from the governing equations of an ideal gas.

3.2.1 Cavern thermodynamics

For a cavern of volume V_{cav} which undergoes compression and decompression cycles with air of density ρ_{air}, a balance of mass transfer is given by (3.1):

$$V_{\text{cav}} \frac{\mathrm{d}\rho_{\text{air}}}{\mathrm{d}t} = \dot{m}_{\text{air,in}} - \dot{m}_{\text{air,out}} \tag{3.1}$$

Similarly, a balance of heat transfer is given by (3.2), where $\dot{Q}_{\text{air-rock,inner}}$ is the rate of heat transfer between the air and the inner wall of the cavern.

$$V_{\text{cav}} \left(\frac{\mathrm{d}u_{\text{air}}}{\mathrm{d}t} \rho_{\text{air}} + u_{\text{air}} \frac{\mathrm{d}\rho_{\text{air}}}{\mathrm{d}t} \right) = \dot{m}_{\text{air,in}} h_{\text{air,in}} - \dot{m}_{\text{air,out}} h_{\text{air,out}} + \dot{Q}_{\text{air-rock,inner}} \tag{3.2}$$

The specific internal energy u_{air} and specific enthalpy h_{air} of air are given by (3.3) and (3.4), respectively. Here, $C_{\text{p,air}}$ and $C_{\text{v,air}}$ are the specific heat capacities of air at constant pressure and constant volume, respectively, and are assumed to be independent of temperature. R_{air} is the specific gas constant for air.

$$u_{\text{air}} = h_{\text{air}} - R_{\text{air}} T_{\text{air}} \tag{3.3}$$

$$h_{\text{air}} = C_{\text{p,air}}\, T_{\text{air}} - C_{\text{v,air}}\, T_0 \tag{3.4}$$

The relationship between the pressure and temperature of air inside the cavern is given by (3.5):

$$P_{\text{air}} = \rho_{\text{air}}\, R_{\text{air}}\, T_{\text{air}} \tag{3.5}$$

Using (3.3), (3.4) and its derivatives, and substituting them in (3.2), a simplified ordinary differential equation in T_{air} is obtained. This is shown in (3.6):

$$V_{\text{cav}}\, \rho_{\text{air}}\, C_{\text{v,air}}\, \frac{\mathrm{d}T_{\text{air}}}{\mathrm{d}t} = \dot{m}_{\text{air,in}}\, (C_{\text{p,air}}\, T_{\text{air,in}} - C_{\text{v,air}}\, T_{\text{air}}) - \dot{m}_{\text{air,out}}\, R_{\text{air}}\, T_{\text{air}} + \dot{Q}_{\text{air-rock,inner}} \tag{3.6}$$

Together with the equations describing heat transfer mechanisms in the rock and the air-to-rock interface, (3.6) is solved numerically to predict the thermodynamic response.

3.2.2 Heat transfer mechanism

The variation in air temperature within the cavern causes changes in temperature of the surrounding rock. Thus, the resulting transfer of heat between the air and the cavern surface as well as within the rock particles may be modelled as a combination of two processes:

- Convective heat transfer between the bulk air and the inner wall of the cavern
- Conductive heat transfer within the rock

Denoting the temperature of rock particles on the innermost layer by $T_{\text{rock,inner}}$, and the cross-sectional area for the particles on the inner surface of the cavern by $A_{\text{rock,inner}}$, the rate of heat transfer between the air and cavern wall is given by (3.7):

$$\dot{Q}_{\text{air-rock,inner}} = \kappa_{\text{air-rock,inner}}\, A_{\text{rock,inner}}\, (T_{\text{rock,inner}} - T_{\text{air}}) \tag{3.7}$$

where $\kappa_{\text{air-rock,inner}}$ is the heat transfer coefficient. In the present work, the heat transfer coefficient is assumed to be a system parameter, and a constant mean value is assigned. As discussed in Kushnir et al.[64], the heat transfer coefficient depends on various factors such as the geometry of the cavern, pressure- and temperature-dependent air properties, the flow velocity of the air, and the temperature difference between the air and the inner wall. However, in-situ measurements required for the development of an accurate heat transfer coefficient correlation are difficult to obtain[63]. Therefore, the constant value heat transfer coefficient approach can be reasonably justified.

For a homogeneous, isotropic material of constant thermal conductivity k, Fourier's law of heat conduction, shown in (3.8), describes the relationship between the heat flux (i.e. the ratio of heat transfer rate to the cross-sectional area across which the heat flows), $\dot{Q}''_{\text{1D}}$, and the temperature differential, $\mathrm{d}T$, over a differential thickness, $\mathrm{d}x$, in the direction of the heat flow.

$$\dot{Q}''_{\text{1D}} = -k \frac{\mathrm{d}T}{\mathrm{d}x} \tag{3.8}$$

More generally, (3.8) is expressed in its multidimensional form, given by (3.9), where $\dot{Q}''$ is the heat flux vector, and ∇T is the temperature gradient vector.

$$\dot{Q}'' = -k \nabla T \tag{3.9}$$

By using (3.9), and applying conservation of thermal energy on a differential volume element in the rock, the solution to the heat conduction problem in rock salt particles may be formulated as a differential equation in rock salt temperature, T_{rock}. This results in the well-known heat conduction equation, shown in (3.10):

$$\rho_{\text{rock}} C_{\text{rock}} \frac{\mathrm{d}T_{\text{rock}}}{\mathrm{d}t} = k_{\text{rock}} \nabla^2 T_{\text{rock}} \tag{3.10}$$

The convective heat transfer rate on the inner wall of the cavern, (3.7) is a boundary condition on the heat conduction equation, (3.10). This is implemented as shown in

(3.11):

$$k_{\text{rock}} \nabla T_{\text{rock}} = \alpha_{\text{air-rock,inner}} \left(T_{\text{rock,inner}} - T_{\text{air}}\right) \tag{3.11}$$

In addition, the constraint that the temperature of the rock particles on the outermost boundary is constant and equal to ambient environment temperature, is also enforced. This is given by (3.12):

$$T_{\text{rock,outer}} = T_0 \tag{3.12}$$

For a given charge-discharge cycling pattern of compressed air, simulation of the air temperature variation within the cavern as well as the temperature change in rock particles is achieved by coupling (3.6) with (3.10), considering (3.7) and (3.12) as boundary conditions. Once the simulated temperature fluctuations are obtained, air pressure variation within the cavern is estimated using (3.5). The implementation of this model within a finite element scheme is described in § 3.5.1.

3.3 Constitutive model of rock salt

Rock salt, or polycrystalline halite rock, comprises crystal grains of sodium chloride, with impurities and fluids confined in grain boundaries[71]. The mechanical response of rock salt depends on the nature of applied loads; cyclic or constant pressure loads, thermal loads, etc.. Whilst there are various types of rock salt with differing material properties, experimental investigations have shown that, in general, the stress field due to the applied loads contains within it a boundary where a marked deviation occurs in material response. Specifically, there exist regions of *compressible* behaviour, where deviatoric stresses are relatively lower than confining stresses, and *dilatant* behaviour, where deviatoric stresses are higher[72]. This is shown in Fig. 3.2, where compressible behaviour is observed in the area below curve C, and dilatant behaviour is observed in the area between curves A and B.

The shear stresses in rock salt lead to a time-dependent ductile deformation observed in the compressible region, indicated in Fig. 3.2, where the sodium chloride grains experience

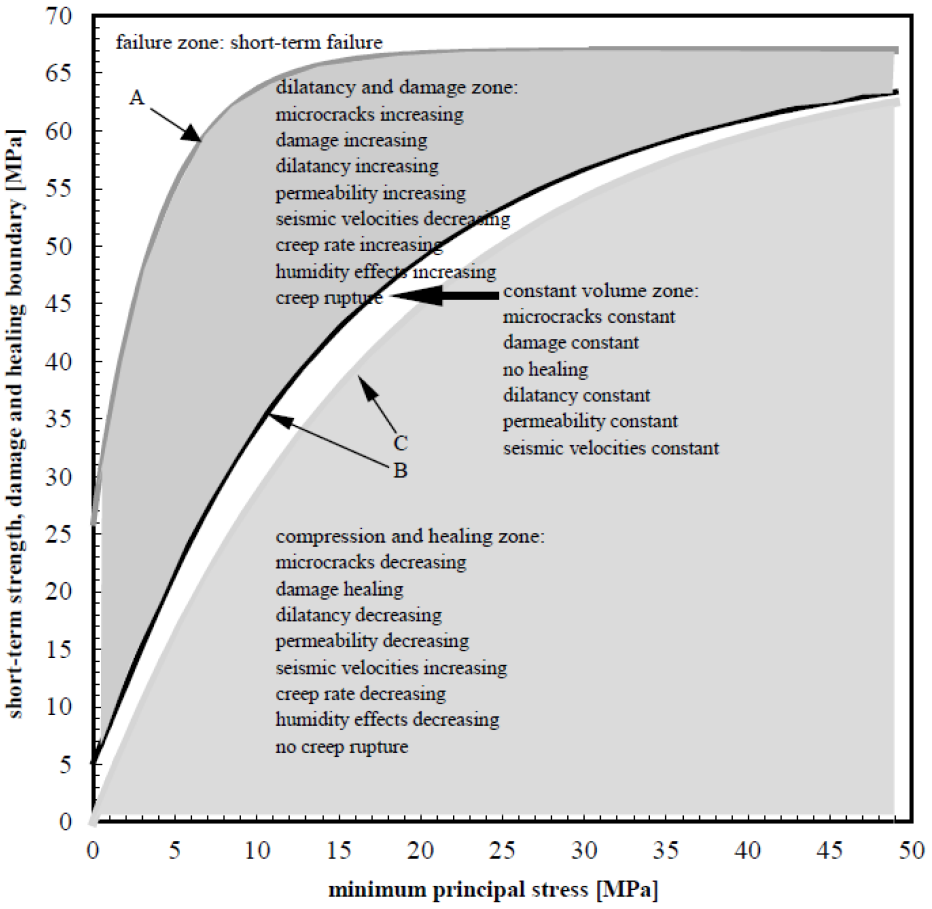


FIGURE 3.2: Regions of dilatant and compressible behaviour of rock salt. Adapted from Hou[72]

a change in volume without a change in shape or orientation. This deformation, called *creeping*, depends on the magnitude of the pressure load as well as the ambient temperature, is devoid of macroscopic fracture and, therefore, does not lead to material rupture or fatigue failure[73]. However, the shear stresses can surpass the strength of rock salt when, for instance, the cavern internal pressure is cycled at relatively low values or when large thermal stresses are induced due to temperature changes in the rock. The resulting deformation, called *dilation*, causes rock salt to microfracture and causes its volume to increase irreversibly. This occurs in the dilatant region in Fig. 3.2. The microfracturing of the grains of salt is characterised by a reduction in its resistance to shear stress, an increase in permeability and fatigue failure[73].

The temperature changes in the rocks due to frequent cycling of air in the cavern causes

the rock particles to deform in a way that changes its volume but not its shape. These volumetric strains contribute to the overall state of stress [54], and therefore, the thermally induced expansions and contractions in the rocks are taken into account. Although material properties of rock salt are a function of temperature, relatively high temperatures (in the order of 200 [C]) are necessary for observable changes. Thus, material properties are assumed to be independent of temperature in the present work.

We model the response of rock salt via the classical uncoupled theory of thermoelasticity, whereby the effect on the temperature field due to changes in deformation of the material is neglected; in other words, the temperatures of rock particles do not change due to the stresses that arise [74]. Furthermore, we consider the salt to be homogeneous, isotropic and materially linear in behaviour.

The creeping behaviour of rock salt, the effect of rock temperature on the rate of creeping, and rate dependent volumetric dilation and compression are important aspects of any salt response model. Although the numerical assessment on the dynamic behaviour of salt presented in § 3.5.2 demonstrates that for the chosen cycling pattern the creeping behaviour of rock salt plays a significant role, we choose not to model this aspect. Our goal here is to develop a tool that quickly performs a first evaluation of the structural integrity of an underground containment which transacts compressed air and possesses the general characteristics of rock salt. However, the detailed design of salt caverns must account for behaviours specific to the type of salt considered; laboratory testing of salt specimens can help identify parameters associated with these behaviours, which can then be used to extrapolate the response of the material under complex loading conditions. Accurate material modelling of rock salt is a vast topic in itself and extensions to the proposed model can form part of further research.

Assuming small deformations, and applying the principle of strain superposition, the total strain tensor, $\boldsymbol{\varepsilon}$, arising at a point in the material is defined as the sum of the elastic (mechanical) strain tensor, $\boldsymbol{\varepsilon}^{\mathrm{me}}$, induced by the stresses, and the thermal strain tensor, $\boldsymbol{\varepsilon}^{\mathrm{th}}$, induced by the expansion or contraction of the material due to changes in temperature

at that point[74]. This is shown below:

$$\boldsymbol{\varepsilon} \coloneqq \boldsymbol{\varepsilon}^{\mathrm{me}} + \boldsymbol{\varepsilon}^{\mathrm{th}} \tag{3.13}$$

The strain tensor, $\boldsymbol{\varepsilon}$, for a three-dimensional body consists of six independent components[75]; namely, three normal strains, ε_{11}, ε_{22}, ε_{33}, and three shear strains, ε_{12}, ε_{23}, ε_{31}. This is shown in (3.14), where u, v and w are displacements of the body in the x, y and z directions, respectively.

$$\begin{gathered}
\boldsymbol{\varepsilon} = \begin{bmatrix} \varepsilon_{11} & \varepsilon_{12} & \varepsilon_{31} \\ \varepsilon_{12} & \varepsilon_{22} & \varepsilon_{23} \\ \varepsilon_{31} & \varepsilon_{23} & \varepsilon_{33} \end{bmatrix} \\
\varepsilon_{11} = \frac{\partial u}{\partial x} \quad \varepsilon_{22} = \frac{\partial v}{\partial y} \quad \varepsilon_{33} = \frac{\partial w}{\partial z} \\
\varepsilon_{12} = 0.5\left(\frac{\partial u}{\partial y} + \frac{\partial v}{\partial x}\right) \quad \varepsilon_{23} = 0.5\left(\frac{\partial u}{\partial z} + \frac{\partial w}{\partial x}\right) \quad \varepsilon_{31} = 0.5\left(\frac{\partial v}{\partial z} + \frac{\partial w}{\partial y}\right)
\end{gathered} \tag{3.14}$$

The thermal strain tensor, $\boldsymbol{\varepsilon}^{\mathrm{th}}$, which depends on the thermal expansion coefficient of the material (α_{rock}) and the change in temperature (ΔT_{rock}), also consists of six components; the normal strains, $\varepsilon_{11}^{\mathrm{th}}$, $\varepsilon_{22}^{\mathrm{th}}$, $\varepsilon_{33}^{\mathrm{th}}$, and the shear strains, $\varepsilon_{12}^{\mathrm{th}}$, $\varepsilon_{23}^{\mathrm{th}}$, $\varepsilon_{31}^{\mathrm{th}}$. Since the thermal strains are volumetric in nature, its shear components are all zero. This is shown in (3.15). It should be noted that the thermal expansion coefficient is assumed to be constant in this work.

$$\begin{gathered}
\boldsymbol{\varepsilon}^{\mathrm{th}} = \begin{bmatrix} \varepsilon_{11}^{\mathrm{th}} & \varepsilon_{12}^{\mathrm{th}} & \varepsilon_{31}^{\mathrm{th}} \\ \varepsilon_{12}^{\mathrm{th}} & \varepsilon_{22}^{\mathrm{th}} & \varepsilon_{23}^{\mathrm{th}} \\ \varepsilon_{31}^{\mathrm{th}} & \varepsilon_{23}^{\mathrm{th}} & \varepsilon_{33}^{\mathrm{th}} \end{bmatrix} \\
\varepsilon_{11}^{\mathrm{th}} = \varepsilon_{22}^{\mathrm{th}} = \varepsilon_{33}^{\mathrm{th}} = \alpha_{\mathrm{rock}} \Delta T_{\mathrm{rock}} \\
\varepsilon_{12}^{\mathrm{th}} = \varepsilon_{23}^{\mathrm{th}} = \varepsilon_{31}^{\mathrm{th}} = 0
\end{gathered} \tag{3.15}$$

The mechanical response of the rock, i.e., the stress tensor at each point in the material, $\boldsymbol{\sigma}^{\mathrm{me}}$, is then given by the generalised Hooke's law, shown in (3.16) [76].

$$\boldsymbol{\sigma}^{\mathrm{me}} = \mathbf{C}\left(\boldsymbol{\varepsilon} - \boldsymbol{\varepsilon}^{\mathrm{th}}\right) \tag{3.16}$$

$\mathbf{C}$ represents the elastic stiffness tensor, which for an isotropic, linear elastic material has the form shown in (3.17).

$$\mathbf{C} = \begin{bmatrix} \lambda_{\mathrm{L}} + 2\,\mu_{\mathrm{L}} & \lambda_{\mathrm{L}} & \lambda_{\mathrm{L}} & 0 & 0 & 0 \\ \lambda_{\mathrm{L}} & \lambda_{\mathrm{L}} + 2\,\mu_{\mathrm{L}} & \lambda_{\mathrm{L}} & 0 & 0 & 0 \\ \lambda_{\mathrm{L}} & \lambda_{\mathrm{L}} & \lambda_{\mathrm{L}} + 2\,\mu_{\mathrm{L}} & 0 & 0 & 0 \\ 0 & 0 & 0 & \mu_{\mathrm{L}} & 0 & 0 \\ 0 & 0 & 0 & 0 & \mu_{\mathrm{L}} & 0 \\ 0 & 0 & 0 & 0 & 0 & \mu_{\mathrm{L}} \end{bmatrix} \tag{3.17}$$

Here, λ_{L} and μ_{L} are the elastic Lamé parameters [76], shown in (3.18) and (3.19), which are derived from material properties: Young's modulus, Y, and Poisson's ratio, ν.

$$\lambda_{\mathrm{L}} = \frac{Y\,\nu}{(1+\nu)\,(1-2\,\nu)} \tag{3.18}$$

$$\mu_{\mathrm{L}} = \frac{Y}{2\,(1+\nu)} \tag{3.19}$$

The material properties of rock salt considered in this study are listed in Table 3.1.

TABLE 3.1: Material properties of rock salt

Young's modulus, Y	25 [GPa]
Poisson's ratio, ν	0.3 [-]
Density of rock salt, ρ_{rock}	2000 [kg/m^3]
Specific heat capacity of rock salt, C_{rock}	1000 [J/kg K]
Thermal conductivity of rock salt, k_{rock}	6 [W/m K]
Thermal expansion coefficient of rock salt, α'_{rock}	1×10^{-5} [K^{-1}]

3.4 Cavern stability criteria

In general, failure of a material occurs when the magnitudes of stresses surpass the allowable normal or shear strengths of that material. From the perspective of structural design and integrity, it is therefore useful to evaluate the maximum normal and shear stresses, or principal stresses, for a given state of stress at a point. We shall concern ourselves with only the magnitudes of principal stresses in the present application.

In a similar vein, it is also useful to evaluate certain *invariants* of the stress and stress deviator tensors at a point. Invariants are quantities based on sums and products of the components of a tensor, which remain constant regardless of the coordinate system chosen for the structural analysis. It should be noted that the stress tensor is given by (3.16), and the stress deviator tensor, $\boldsymbol{\sigma}_{\mathrm{D}}^{\mathrm{me}}$, is given by (3.20), where $\mathrm{tr}\,(\boldsymbol{\sigma}^{\mathrm{me}})$ is the sum of diagonal elements of the stress tensor, and $\mathbf{I}$ is the identity matrix.

$$\boldsymbol{\sigma}_{\mathrm{D}}^{\mathrm{me}} = \boldsymbol{\sigma}^{\mathrm{me}} - \frac{1}{3}\,\mathrm{tr}\,(\boldsymbol{\sigma}^{\mathrm{me}})\,\mathbf{I} \tag{3.20}$$

We shall consider those invariants most often used in material failure analysis: the first invariant of the stress tensor, I_1, shown in (3.21), and the second and third invariants of the stress deviator tensor, J_2 and J_3, shown in (3.22)-(3.23), respectively. Further details about the evaluation procedure of these quantities can be found in Reddy [76].

$$I_1 = \mathrm{tr}\,[\boldsymbol{\sigma}^{\mathrm{me}}] \tag{3.21}$$

$$J_2 = \frac{1}{2}\left[(\mathrm{tr}\,[\boldsymbol{\sigma}_{\mathrm{D}}^{\mathrm{me}}])^2 - \mathrm{tr}\left([\boldsymbol{\sigma}_{\mathrm{D}}^{\mathrm{me}}]^2\right)\right] \tag{3.22}$$

$$J_3 = \det\,[\boldsymbol{\sigma}_{\mathrm{D}}^{\mathrm{me}}] \tag{3.23}$$

Rock salt possesses relatively poor tensile strength; therefore, if the principal stresses are positive at any location in the rock mass, it may indicate the onset of failure. Therefore, the condition that the maximum and minimum principal stresses in the rock be compressive, especially in the vicinity of the cavern wall, forms our first stability criterion.

The second stability criterion is concerned with the dilation of rock salt. The microfracturing of salt grains, discussed in § 3.3, can have a detrimental effect on the storage containment: if the state of stress around the cavern causes the shear stresses to surpass the strength of rock salt for prolonged periods, spalling of the cavern roof and wall can occur, which ultimately leads to a loss of structural integrity of the cavern. It is important, therefore, to translate the stress field in the rocks to quantities that help identify the onset of failure.

Whilst there exist several stress invariant-based formulae for evaluating the potential for salt microfracture or dilatant behaviour, two in particular are chosen for the present analysis:

- Desai and Varadarajan[58] conducted laboratory tests on rock salt from the Salado formation in New Mexico to develop a general, simplified, constitutive model of the material. The goal of the tests was the identification and determination of parameters by considering the effects of confining pressures and deviatoric stress on the strength of rock salt, to then describe its behaviour under more complex loading conditions. Their formulation of the dilation function to describe rock salt failure behaviour is shown in (3.24), which we shall refer to as the *DV criterion*.

$$f_{\text{dilation}} = \left[\left(1 - \frac{2}{n}\right) \gamma_1 I_1^2 \left(e^{\beta_1 I_1} - \beta \cos(3\theta)\right)^m\right]^{1/2} \tag{3.24}$$

  where I_1 is the first invariant of the stress tensor, θ is the Lode angle calculated as shown in (3.25)[76], and β, β_1, γ_1, m and n are material parameters.

$$\theta = \frac{1}{3} \cos^{-1}\left(\frac{J_3}{2}\left(\frac{3}{J_2}\right)^{3/2}\right) \tag{3.25}$$

- DeVries et al. of RESPEC[61] sought to improve upon existing criteria for describing salt failure behaviour. Laboratory tests were conducted on rock salt specimens from Cauyta in Schuyler County, New York, which considered not only the effects of mean stress, shear stress and the Lode angle, but also pore pressure, temperature and Lode

angle, on the strength of rock salt. RESPEC's formulation of the dilation function is shown in (3.26), which we shall refer to as the *RD criterion*.

$$f_{\text{dilation}} = \frac{D_1 \left(\frac{|I_1|}{\sigma_0}\right)^{m'} + T_0'}{\sqrt{3}\,\cos(\theta) - D_2\,\sin(\theta)} \tag{3.26}$$

where I_1 is the first invariant of the stress tensor, σ_0 is a dimensional stress-based constant, T_0' is the unconfined tensile strength of salt, θ is the Lode angle, D_1 and D_2 are material constants, and m' is a power term no greater than 1.

Two measures of Factor of Safety (FoS), FoS_{DV} and FoS_{RD}, are then defined for both the DV and RD criteria, respectively. FoS is a dimensionless quantity which compares the magnitudes of mean stresses relative to shear stresses at various locations in the material. In the present work, FoS indicates the onset of salt failure; namely, the likelihood of salt microfracture and dilation. For values of FoS less than 1, failure is said to occur. It is in general given by (3.27).

$$\text{FoS} \coloneqq \frac{f_{\text{dilation}}}{\sqrt{J_2}} \tag{3.27}$$

The material constants used in the two dilation criteria are listed in Table 3.2.

TABLE 3.2: Material constants used in the DV and RD dilation criteria, adapted from Desai and Varadarajan[58] and DeVries et al.[61], respectively

DV criterion		**RD criterion**	
β	0.995	σ_0	20.57 [MPa]
β_1	4.8×10^{-3} [MPa^{-1}]	T_0'	1.95 [MPa]
γ_1	0.11	D_1	0.773 [MPa]
m	-0.5	D_1	0.524
n	3	m'	0.693

3.5 Finite Element Analysis

In this section, the complete thermomechanical cyclic loading problem is implemented using finite element analysis. Whilst any standard textbook on the finite element method will contain the steps described here in more detail, a brief commentary on the method including key relations used in this work is nevertheless provided to justify the assumptions made, and for the sake of clarity.

We start by defining the dimensions and loading conditions of a single isolated salt cavern and the surrounding rock. Since the idealised geometry as well as loading conditions on the cavern and surrounding rock are symmetrical about an axis, only one-half of a diametral cross-section of the structure is analysed; this is shown in Fig. 3.3. As observed in the schematic, the cavern geometry is considered (initially) to be a cylinder with hemispherical shells at the roof and floor of the reservoir. The height of the cylinder is 150 [m], and the inner radius of the cylinder and hemispherical shells is 15 [m]. The rock salt boundary stretches out to 100 [m] to the right of the cavern, and 85 [m] above and below the ends of the cavern. Compressed air exerts pressure on the inner wall of the cavern, and the associated air temperature exerts thermal loads in the rocks in terms of temperature changes. At the right-side boundary of the assemblage a uniformly increasing geostatic pressure load is applied, and at the top-side boundary an overburden traction load is applied to consider additional rock material above the region of interest. The movement of the bottom of the structure is constrained in the vertical direction. The dimensions of this outer boundary are chosen such that the rock particles in this region are far enough from the highly thermomechanically 'active' region near the cavern wall.

The essence of finite element analysis lies in approximating a continuous body using information at discrete locations or *elements*, with the *nodal points* interconnecting the elements at their boundaries. Interpolation of information within the elements is accomplished through interpolation, or *shape*, functions[77].

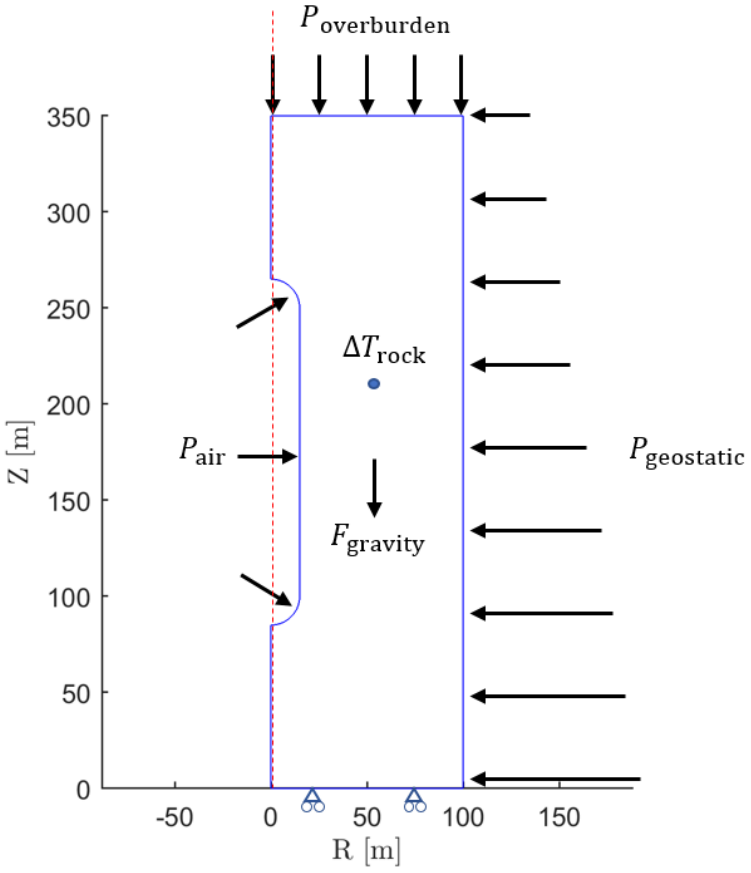


FIGURE 3.3: Schematic of the axisymmetric cavern and rock salt geometry with applied loads

The coordinate interpolations for a general two-dimensional element, with local coordinates X and Y located anywhere inside the element, are defined as shown in (3.28):

$$X = \sum_{\mathrm{i}=1}^{\mathrm{k}} h_{\mathrm{i}}\, x_{\mathrm{i}}$$
$$Y = \sum_{\mathrm{i}=1}^{\mathrm{k}} h_{\mathrm{i}}\, y_{\mathrm{i}} \tag{3.28}$$

where x_{i}, y_{i} $\forall\, i = \{1, \ldots, k\}$ are the k nodal point coordinates, and h_{i} are the unknown shape functions. The shape functions are defined in a *natural coordinate system*, with associated variables ξ and ζ, each bounded from -1 to $+1$, allowing the dimensions of the element to be normalised and the shape functions to be used for elements of arbitrary sizes. To determine the shape functions for the element, we use the property that $h_{\mathrm{i}}\,(\xi, \zeta)$ is equal

to 1 at node i and zero at all other nodes[77]. In the present application, the finite element structure is axisymmetric and is composed of eight-noded quadrilateral (two-dimensional) elements; a schematic in Fig. 3.4 illustrates this. The shape functions for a corner node and a mid-side node in an eight-noded quadrilateral element is shown in Fig. 3.5.

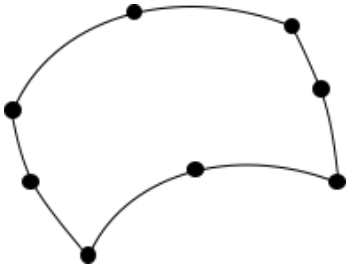


FIGURE 3.4: Schematic of the eight-noded quadrilateral finite element

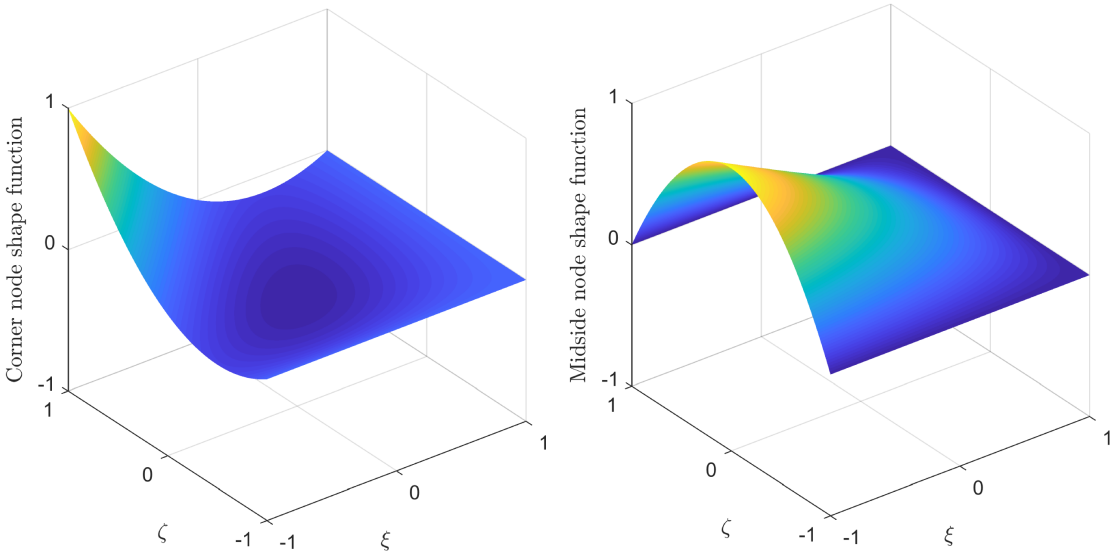


FIGURE 3.5: Shape functions of a corner node and mid-side node in an eight-noded quadrilateral finite element

The interpolation of nodal displacements U and V at any location within the element, in the X and Y directions, respectively – essential in obtaining the mechanical response of the structure – are determined as given by (3.29):

$$U = \sum_{\mathrm{i}=1}^{\mathrm{k}} h_{\mathrm{i}}\, u_{\mathrm{i}}$$
$$V = \sum_{\mathrm{i}=1}^{\mathrm{k}} h_{\mathrm{i}}\, v_{\mathrm{i}} \tag{3.29}$$

where u_i, v_i $\forall\, i = \{1, \ldots, k\}$ are the k nodal point displacements. Since the same shape functions are used as in the coordinate interpolation, this methodology is termed the isoparametric formulation. Extensive research and experience has shown that analyses performed using the isoparametric formulation of finite elements enables straightforward implementation and produce effective results [77].

In this work, the finite element structure comprises 3510 elements and 11097 nodal points. As observed in Fig. 3.6, the rock region in close proximity to the cavern wall consists of relatively more finite elements (i.e. it is finely divided) than the region beyond, to accurately model the temperature and stress gradients that arise. The temperature skin depth, shown in (3.30), is a useful measure in this regard: it is the distance into the rock where significant fluctuations in temperature are observed [64]; beyond this distance, the variations are minimal.

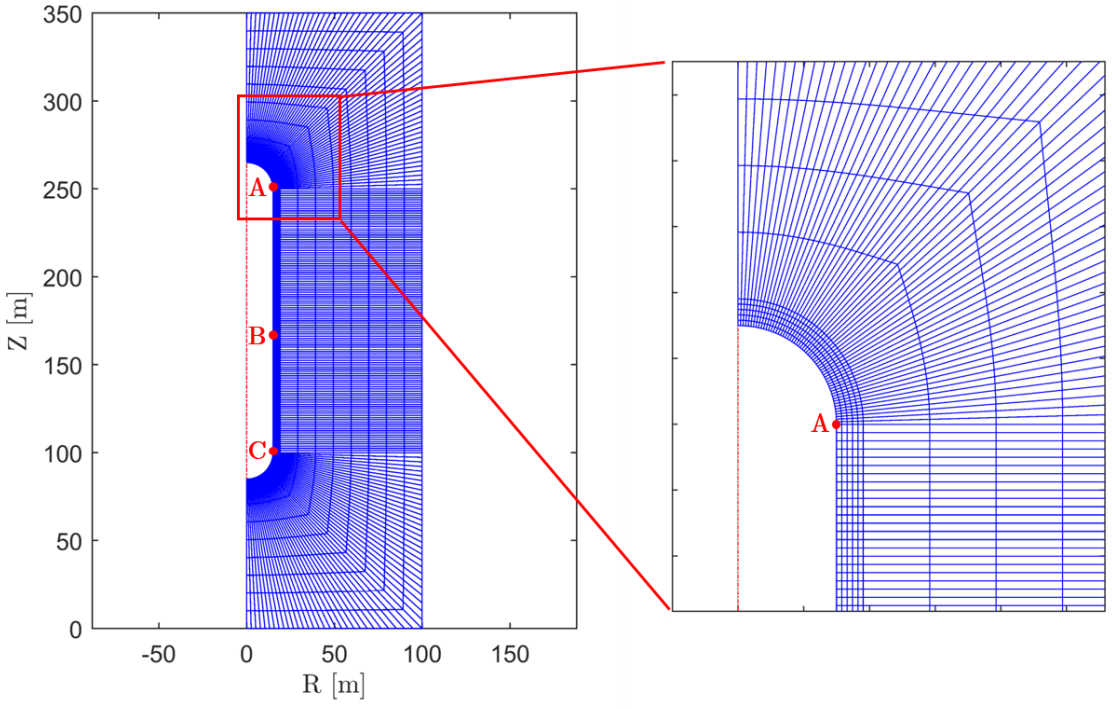


FIGURE 3.6: The finite element mesh of the structure with three points of interest, A, B and C, on the cavern wall. Inset shows magnified region where the area in close proximity to the cavern wall is finely subdivided than the area beyond

$$d_{\text{skin}} = \sqrt{\frac{k_{\text{rock}}\, t_{\text{cycle}}}{2\,\pi\,\rho_{\text{rock}}\, C_{\text{rock}}}} \tag{3.30}$$

It is easily seen that for constant material properties of the rock, the temperature skin depth increases with periodic or cycling time. In this work, the width of the finely divided region is chosen to be five times the skin depth.

3.5.1 Implementation of the thermodynamic response model

The finite element equations for a heat transfer problem, in general, may be expressed as shown in (3.31)[77]:

$$\left[\mathbf{M}^{\text{th}}\right]\left\{\dot{\mathbf{T}}\right\} + \left[\mathbf{K}^{\text{th}}\right]\left\{\mathbf{T}\right\} = \left\{\mathbf{F}^{\text{th}}\right\} \tag{3.31}$$

where $\left[\mathbf{M}^{\text{th}}\right]$ and $\left[\mathbf{K}^{\text{th}}\right]$ are the thermal mass matrix and thermal conductance matrix; $\left\{\mathbf{T}\right\}$ and $\left\{\dot{\mathbf{T}}\right\}$ are vectors of nodal temperatures and its first derivative with respect to time; and $\left\{\mathbf{F}^{\text{th}}\right\}$ is a vector of thermal forces.

To account for the coupling between the thermodynamics of air within the cavern volume, (3.6), and the heat conduction in rock salt, (3.10), along with the air-to-rock heat convection boundary condition at the cavern wall, (3.7), we may modify the finite element equations using (3.32).

$$\begin{bmatrix} \mathrm{M}^{\text{th}}_{\text{air}} & 0 \\ 0 & \left[\mathbf{M}^{\text{th}}_{\text{rock}}\right] \end{bmatrix} \begin{Bmatrix} \dot{\mathrm{T}}_{\text{air}} \\ \left\{\dot{\mathbf{T}}_{\text{rock}}\right\} \end{Bmatrix} + \begin{bmatrix} \sum \mathbf{K}^{\text{th}}_{\text{air-rock,inner}} & -\mathbf{K}^{\text{th}}_{\text{air-rock,inner}} \\ -\mathbf{K}^{\text{th}}_{\text{air-rock,inner}} & \left[\mathbf{K}^{\text{th}}_{\text{rock}}\right] + \mathbf{K}^{\text{th}}_{\text{air-rock,inner}} \end{bmatrix} \begin{Bmatrix} \mathbf{T}_{\text{air}} \\ \left\{\mathbf{T}_{\text{rock}}\right\} \end{Bmatrix} = \begin{Bmatrix} \mathrm{F}^{\text{th}}_{\text{air}} \\ 0 \end{Bmatrix} \tag{3.32}$$

Since the properties of air are assumed to be uniform within the cavern volume, the air may be considered as a single nodal point of the thermal finite element model. Thus, the thermal mass of air, $\mathrm{M}^{\text{th}}_{\text{air}}$, is calculated as (3.33):

$$\mathrm{M}^{\text{th}}_{\text{air}} = V_{\text{cav}}\, \rho_{\text{air}}\, C_{\text{v,air}} \tag{3.33}$$

The node of air is thermally connected to the nodes of rock on the inner surface of the cavern. The thermal conductance between the air and the cavern wall, $\mathbf{K}^{\text{th}}_{\text{air-rock}}$, evaluated as shown in (3.34), is a vector that quantifies the heat convection boundary condition. The quantity $\sum \mathbf{K}^{\text{th}}_{\text{air-rock,inner}}$ is the sum of all elements in $\mathbf{K}^{\text{th}}_{\text{air-rock}}$, and represents the overall thermal conductance between the air and the cavern wall.

$$\left\{\mathbf{K}^{\text{th}}_{\text{air-rock,inner}}\right\} = \sum_{\text{i}=1}^{N_{\text{ele}}} \int_{S} \alpha_{\text{air-rock,inner}} \left[\mathbf{H}^{\text{S}}\right]_{\text{i}} \, \text{d}S_{\text{i}} \tag{3.34}$$

$\left[\mathbf{M}^{\text{th}}_{\text{rock}}\right]$ and $\left[\mathbf{K}^{\text{th}}_{\text{rock}}\right]$ are the thermal mass and conductance matrices of the rock finite element assemblage, and are calculated as shown in (3.35) and (3.36), respectively.

$$\left[\mathbf{M}^{\text{th}}_{\text{rock}}\right] = \sum_{\text{i}=1}^{N_{\text{ele}}} \int_{V} \rho_{\text{rock}} \, C_{\text{rock}} \, [\mathbf{H}]^{\intercal}_{\text{i}} \, [\mathbf{H}]_{\text{i}} \, \text{d}V_{\text{i}} \tag{3.35}$$

$$\left[\mathbf{K}^{\text{th}}_{\text{rock}}\right] = \sum_{\text{i}=1}^{N_{\text{ele}}} \int_{V} k_{\text{rock}} \, [\mathbf{B}]^{\intercal}_{\text{i}} \, [\mathbf{B}]_{\text{i}} \, \text{d}V_{\text{i}} \tag{3.36}$$

The elements of $\mathbf{K}^{\text{th}}_{\text{air-rock,inner}}$ are then added to the appropriate entries (the surface nodes) in $\left[\mathbf{K}^{\text{th}}_{\text{rock}}\right]$ to complete the thermal connections.

The thermal force for air, $\text{F}^{\text{th}}_{\text{air}}$, is given by the heat transfer rate resulting from the charging-discharging characteristics of the system, as shown in (3.37).

$$\text{F}^{\text{th}}_{\text{air}} = \dot{m}_{\text{air,in}} \, (C_{\text{p,air}} \, T_{\text{air,in}} - C_{\text{v,air}} \, T_{\text{air}}) - \dot{m}_{\text{air,out}} \, R_{\text{air}} \, T_{\text{air}} \tag{3.37}$$

$[\mathbf{H}]$ is the matrix of shape functions of a finite element, $\left[\mathbf{H}^{\text{S}}\right]$ is the shape function matrix containing the surface coordinates of the element, and $[\mathbf{B}]$ is the strain-displacement transformation matrix obtained by differentiating and combining rows of $[\mathbf{H}]$. The volume and surface integrals are evaluated using Gauss numerical integration procedure (see for e.g. Bathe[77]).

The ordinary differential equation in (3.32) is solved numerically to yield temperature variation of the air and rock nodes with time, and the variation of air pressure with time,

which then form the boundary conditions to the mechanical response model.

The thermodynamic response model is validated against measured air temperature data from Huntorf plant within a typical daily cycle, drawn from Kushnir et al.[64] and from Quast and Crotogino[65]. For the mass flow characteristics shown in Fig. 3.7, the simulated variation of pressure and temperature of air within the cavern (solid red line) is shown against measured data (solid black line with markers) in Fig. 3.8. The initial temperature of the rock salt and the air within the cavern is approximately 40 [C], or 313 [K]; the air injection temperature is also assumed to be 313 [K], and the injection pressure to be 59 [bar]. It can be observed from the figure that predicted values are sufficiently close to measured values.

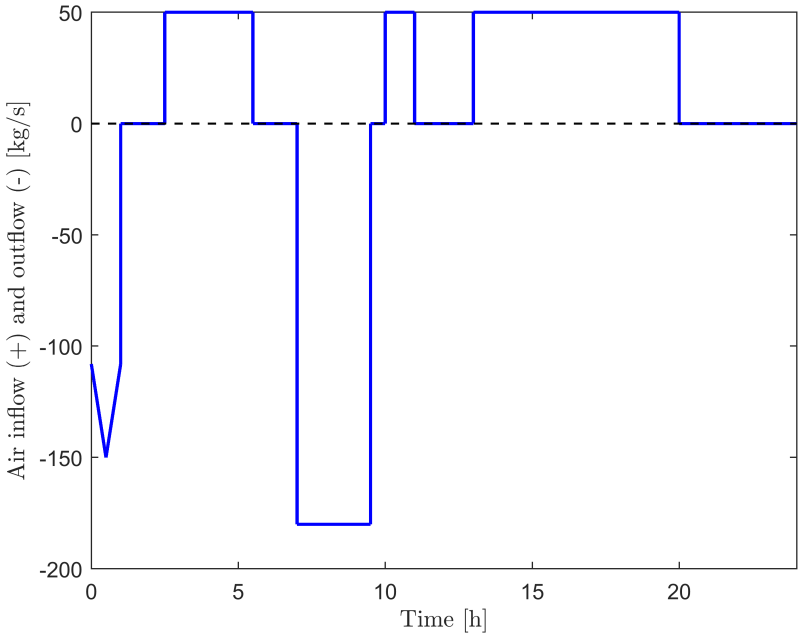
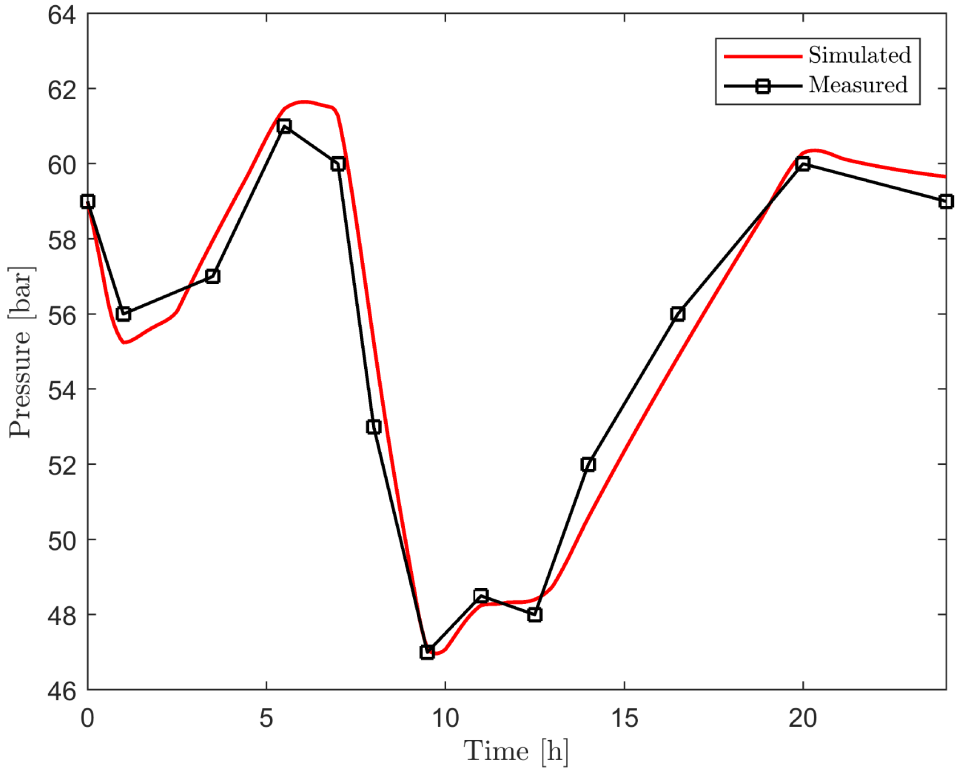


FIGURE 3.7: Typical daily cycle mass flow rate characteristics of Huntorf plant during the trial runs, adapted from Quast and Crotogino[65]

(a)



(b)

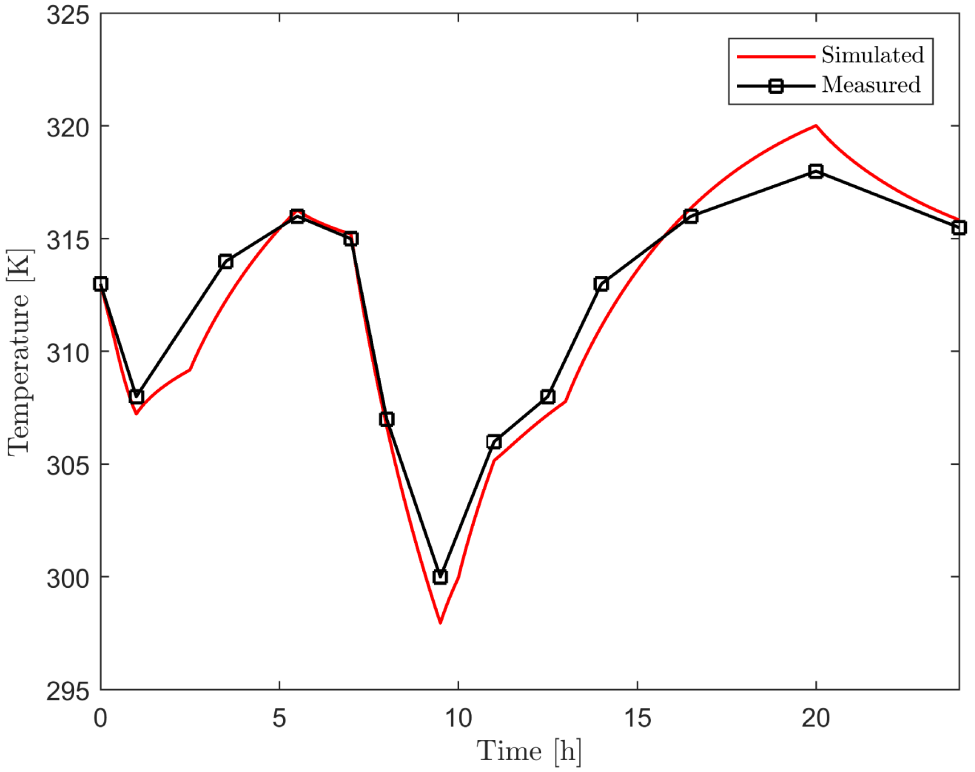


FIGURE 3.8: Measured and simulated (a) pressure variation of air and (b) temperature variation of air within a single salt cavern geometrically similar to the Huntorf salt caverns. Measured data from from Quast and Crotogino [65]

3.5.2 Implementation of the mechanical response model

The application of loads – cavern internal pressure, boundary tractions, gravity load, and temperature changes within the rock – causes the nodal points in the finite element assemblage to displace relative to each other. Since some of the loads are cyclic in nature, the applied forces are time-dependent, the mechanical response will be dynamic in nature and depends on rate of applied loads. In other words, the equation of motion, shown in (3.38), which considers acceleration-dependent inertia forces, in addition to the displacements of points within the structure, would need to be solved.

$[\mathbf{M}_{\text{rock}}]$ and $[\mathbf{K}_{\text{rock}}]$ are the mass and stiffness matrices of the rock salt finite element structure; $\left\{\hat{\ddot{\mathbf{U}}}_{\text{rock}}\right\}$ and $\left\{\hat{\mathbf{U}}_{\text{rock}}\right\}$ are the nodal acceleration and nodal displacement vectors (for the two-dimensions); and $\left\{\mathbf{F}_{\text{rock}}\right\}$ is the vector of equivalent forces.

$$[\mathbf{M}_{\text{rock}}] \left\{\hat{\ddot{\mathbf{U}}}_{\text{rock}}\right\} + [\mathbf{K}_{\text{rock}}] \left\{\hat{\mathbf{U}}_{\text{rock}}\right\} = \left\{\mathbf{F}_{\text{rock}}\right\} \tag{3.38}$$

In order to assess the significance of dynamic loading on the response of the structure, we solve the *eigenvalue problem*, shown in (3.39), to determine the natural frequencies of that structure. This results from the equation of motion for a body experiencing free vibration[77].

$$\left([\mathbf{K}_{\text{rock}}] - \omega_{\text{rock}}^2 \, [\mathbf{M}_{\text{rock}}]\right) \{\phi_{\text{rock}}\} = 0 \tag{3.39}$$

where ω_{rock} are the set of natural frequencies of the rock salt structure. These are obtained by setting the determinant of $\left([\mathbf{K}_{\text{rock}}] - \omega^2 \, [\mathbf{M}_{\text{rock}}]\right)$ to be equal to zero[77], which produces a set of discrete values for ω_{rock}.

It is found that the lowest, or fundamental, natural frequency of the finite element structure is approximately 2.1 [Hz], which is much larger than the frequency of daily compressed air cycling, $(24 \times 3600)^{-1}$ [Hz], or approximately 1.2×10^{-5} [Hz]. In other words, the thermomechanical cyclic loading may be considered to be applied relatively slowly so that the inertia forces can be neglected. This results in a quasi-static problem where the equation of motion is given by the static equilibrium of the structure, shown in (3.40), but

with time-dependent loading characteristics.

$$[\mathbf{K}_{\text{rock}}] \left\{\hat{\mathbf{U}}_{\text{rock}}\right\} = \left\{\mathbf{F}_{\text{rock}}\right\} \tag{3.40}$$

A similar eigenvalue appraisal is made on the creeping behaviour of rock salt. When the rock particles deform due to creeping, its response may be described by a viscoelastic constitutive model, which considers the viscosity of the material in addition to the elastic parameters[76]. An equivalent stiffness matrix, $[\mathbf{D}_{\text{rock}}]$, may then be constructed from (3.43) for the viscoelastically behaving material. We begin by setting the equivalent shear Lamé parameter of rock salt $\mu'_{\text{L}} = 10^{19}\,[\text{Pa s}]$, which is calculated from the curve representing the variation of viscosity with shear rate as shown in Fig. 3.9[78]. Below a certain value of strain rate (e.g. $10^{-12}\,[\text{s}^{-1}]$ for a salt grain size, d, of $5\,[\text{mm}]$), the viscosity is independent of the strain rate indicating the dominance of creeping behaviour. Assuming normal temperature operation, an average value across the three salt grain sizes for the creep dominant regions is calculated. By also assuming the Poisson's ratio $\nu'_{\text{rock}} = 0.49$, to represent nearly incompressible behaviour of rock salt during creeping, the equivalent Young's modulus, $E'\,[\text{Pa s}]$, is then calculated from (3.19).

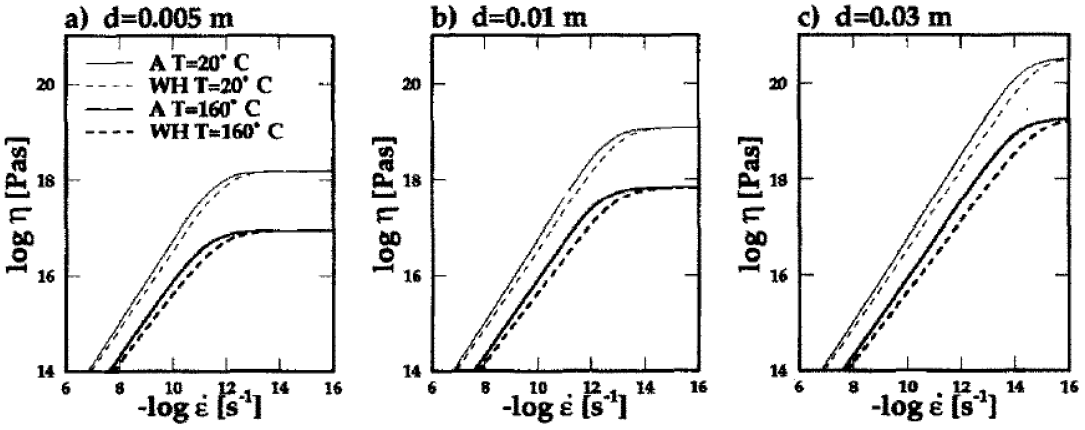


FIGURE 3.9: Variation of effective viscosity of rock salt with shear rate for creeping behaviour at normal and high operating temperatures, and across various grain sizes, d. Adapted from van Keken et al.[78]

The lowest natural frequency resulting from the eigenproblem involving the matrices $[\mathbf{K}_{\text{rock}}]$

and $[\mathbf{D}_{\text{rock}}]$ is approximately 8.6×10^{-6} [Hz]. In other words, creeping behaviour has a non-trivial impact on the material response of rock salt under daily cyclic loading conditions. The response is dynamic and is governed by the rate at which the material deforms. However, as discussed earlier, we do not explore this area further.

The overall forcing vector $\left\{\mathbf{F}_{\text{rock}}\right\}$ comprises forces due to cavern internal pressure and overburden pressure, $\left\{\mathbf{F}^{\text{S}}_{\text{rock}}\right\}$; gravity, $\left\{\mathbf{F}^{\text{G}}_{\text{rock}}\right\}$; and temperature changes in the rock, $\left\{\mathbf{F}^{\text{T}}_{\text{rock}}\right\}$, as shown in (3.41).

$$\left\{\mathbf{F}_{\text{rock}}\right\} = \left\{\mathbf{F}^{\text{S}}_{\text{rock}}\right\} + \left\{\mathbf{F}^{\text{G}}_{\text{rock}}\right\} + \left\{\mathbf{F}^{\text{T}}_{\text{rock}}\right\} \tag{3.41}$$

In the above, the mass and stiffness matrices are calculated for each local element as shown in (3.42) and (3.43), and then assembled to obtain values for the entire assemblage.

$$[\mathbf{M}_{\text{rock}}] = \sum_{\text{i}=1}^{N_{\text{ele}}} \int_{V} \rho_{\text{rock}} \, [\mathbf{H}]_{\text{i}}^{\intercal} \, [\mathbf{H}]_{\text{i}} \, \mathrm{d}V_{\text{i}} \tag{3.42}$$

$$[\mathbf{K}_{\text{rock}}] = \sum_{\text{i}=1}^{N_{\text{ele}}} \int_{V} [\mathbf{B}]_{\text{i}}^{\intercal} \, [\mathbf{C}_{\text{rock}}]_{\text{i}} \, [\mathbf{B}]_{\text{i}} \, \mathrm{d}V_{\text{i}} \tag{3.43}$$

The components of $\left\{\mathbf{F}_{\text{rock}}\right\}$ are calculated as shown in (3.44)-(3.46):

$$\left\{\mathbf{F}^{\text{S}}_{\text{rock}}\right\} = \sum_{\text{i}=1}^{N_{\text{ele}}} \int_{S} \left[\mathbf{H}^{\text{S}}\right]_{\text{i}} \left\{\mathbf{f}^{\text{S}}_{\text{rock}}\right\}_{\text{i}} \mathrm{d}S_{\text{i}} \tag{3.44}$$

$$\left\{\mathbf{F}^{\text{G}}_{\text{rock}}\right\} = \sum_{\text{i}=1}^{N_{\text{ele}}} \int_{V} [\mathbf{H}]_{\text{i}}^{\intercal} \left\{\mathbf{f}^{\text{G}}_{\text{rock}}\right\}_{\text{i}} \mathrm{d}V_{\text{i}} \tag{3.45}$$

$$\left\{\mathbf{F}^{\text{T}}_{\text{rock}}\right\} = \sum_{\text{i}=1}^{N_{\text{ele}}} \int_{V} [\mathbf{B}]_{\text{i}}^{\intercal} \, [\mathbf{C}_{\text{rock}}]_{\text{i}} \left\{\mathbf{f}^{\text{T}}_{\text{rock}}\right\}_{\text{i}} \mathrm{d}V_{\text{i}} \tag{3.46}$$

$\left\{\mathbf{f}^{\text{S}}_{\text{rock}}\right\}$, $\left\{\mathbf{f}^{\text{G}}_{\text{rock}}\right\}$ and $\left\{\mathbf{f}^{\text{T}}_{\text{rock}}\right\}$ are vectors containing the element traction, gravity and equivalent temperature forces, respectively; and $[\mathbf{C}_{\text{rock}}]$ is the element elastic stiffness, or stress-strain, matrix.

The vector of element strains is related to the corresponding displacements through the strain-displacement matrix, as shown in (3.47).

$$\left\{\boldsymbol{\varepsilon}_{\text{rock}}\right\}_{\text{i}} = [\mathbf{B}]_{\text{i}} \left\{\hat{\mathbf{U}}_{\text{rock}}\right\}_{\text{i}} \quad \forall\, i = \{1, \ldots, N_{\text{ele}}\} \tag{3.47}$$

This facilitates the evaluation of element stresses using (3.48), where $\left\{\boldsymbol{\varepsilon}^{\text{th}}_{\text{rock}}\right\}$ is the vector of element thermal strains.

$$\left\{\boldsymbol{\sigma}^{\text{me}}_{\text{rock}}\right\}_{\text{i}} = [\mathbf{C}_{\text{rock}}]_{\text{i}} \left(\left\{\boldsymbol{\varepsilon}_{\text{rock}}\right\}_{\text{i}} - \left\{\boldsymbol{\varepsilon}^{\text{th}}_{\text{rock}}\right\}_{\text{i}}\right) \quad \forall\, i = \{1, \ldots, N_{\text{ele}}\} \tag{3.48}$$

In the present application, the evaluation of element stresses means that the independent components of the stress tensor are extracted for each node in the finite element assemblage. Since the model is axisymmetric, the number of independent components in the strain, and hence the stress, tensor is reduced from six to four.

3.6 Results and discussion

The air compression-decompression mass flow characteristics chosen for the present analysis are shown in Fig. 3.10. A single cycle comprises 8 [h] of compressed air injection into the cavern at a mass flow rate of 108 [kg/s], followed by 4 [h] of downtime, followed by 2 [h] of withdrawal at 417 [kg/s], and 10 [h] of downtime. The injection and withdrawal mass flow rates and durations are based on Huntorf plant operation characteristics.

There exists a temperature gradient in the cavern which varies approximately linearly with depth as 0.03 [C/m] [79]. We neglect this variation and assume that the initial temperature of rock salt is uniform and equal to T_0.

We also do not model cavern excavation or leaching processes, whereby the geostatic pressure is incrementally decreased to that exerted by the brine solution on the inner cavern wall. The goal here is to investigate via suitable criteria the likely onset of failure

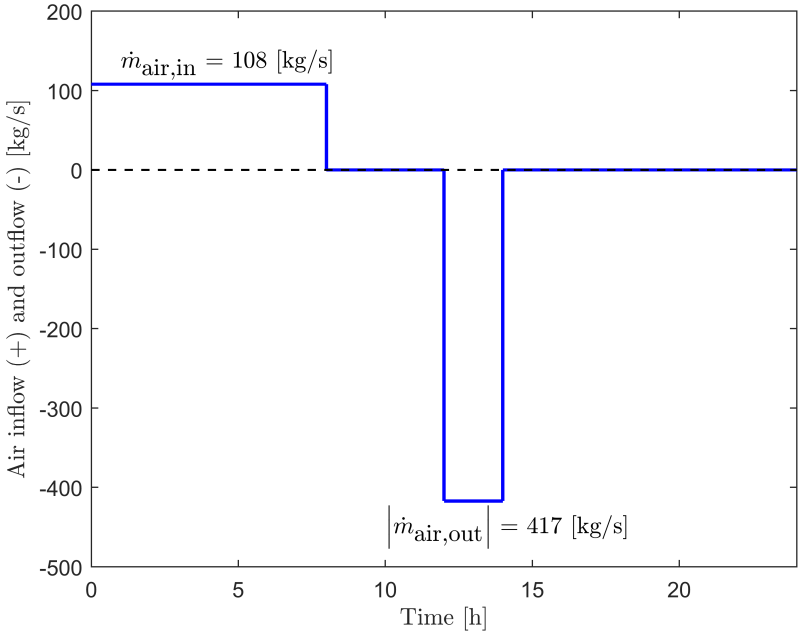


FIGURE 3.10: The daily compressed air charge-discharge cycle used in this study

due to thermomechanical cyclic loading, for which purpose a snapshot operation period is modelled.

The system parameters used in the simulations are shown in Table 3.3.

TABLE 3.3: System parameters used in the present analysis

Ambient pressure, P_{amb}	101325 [Pa]
Ambient temperature, T_{amb}	290 [K]
Initial temperature of rock salt and air in cavern volume, T_0	323 [K]
Specific heat capacity of air at constant pressure, $C_{\text{p,air}}$	1005 [J/kg K]
Specific gas constant of air, R_{air}	287 [J/kg K]
Air injection temperature, $T_{\text{air,in}}$	323 [K]
Air injection mass flow rate, $m_{\text{air,in}}$	108 [kg/s]
Air withdrawal mass flow rate, $m_{\text{air,out}}$	417 [kg/s]
Heat transfer coefficient between air and inner cavern wall, $\alpha_{\text{air-rock,inner}}$	90 [W/m^2 K]

The temperature and pressure variations are simulated for 100 daily cycles. The thermodynamic response of air within the cavern volume and the temperature variation of the cavern wall in the first cycle is shown in Fig. 3.11. For ease of interpretation, rock layers are identified by shortest horizontal distance (labelled d_{h} in the figure(s)) from the mid-point of the cavern axis of symmetry.

Injection of air during the charging phase increases its temperature in the cavern. The pressure also increases owing to an increase in the mass of air contained in the cavern. Immediately afterward, in the first idle phase, some cooling is observed due to heat transfer between the air and the cavern wall; consequently, the pressure and temperature of air decrease. This rate of reverse heat transfer increases during the discharge phase when air is withdrawn from the cavern. In the final idle phase, this trend is reversed once more.

The cavern wall temperature varies in tandem with that of air, owing to convective heat transfer at the walls, as observed in Fig. 3.11. This translates to temperature variations in the rock particles due to conductive heat transfer through the rock salt. Fig. 3.12 shows the temperature variation of the 'layers' of rock at progressively farther distances from the cavern wall. It is easily observed that amplitude of the cycles decreases rapidly with increasing distance, approaching zero at the outer boundary of the structure. In other words, the temperature of the outermost layer of rock remains constant and equal to the ambient, or ground, temperature; this is shown as a solid black line in Fig. 3.12.

The temperatures of nodal points along a horizontal distance at mid-cavern height is shown in Fig. 3.13. As observed in Fig. 3.13(a), the drop in temperature with increasing distance from the cavern wall is significant, indicating the relatively short temperature skin depth for the chosen cycling pattern ($\sim 1\,[\mathrm{m}]$). By contrast, the temperature variation at the end of a cycle contains within it a peak, as shown in Fig. 3.13(b). The temperature skin depth has progressed into the rock only very slighlty by the end of the hundredth cycle. This is because a typical salt cavern operates on significantly longer time-scales than the duration considered in the present analysis, and long-term simulations are necessary for achieving steady-state conditions. It should be noted, however, that higher air injection

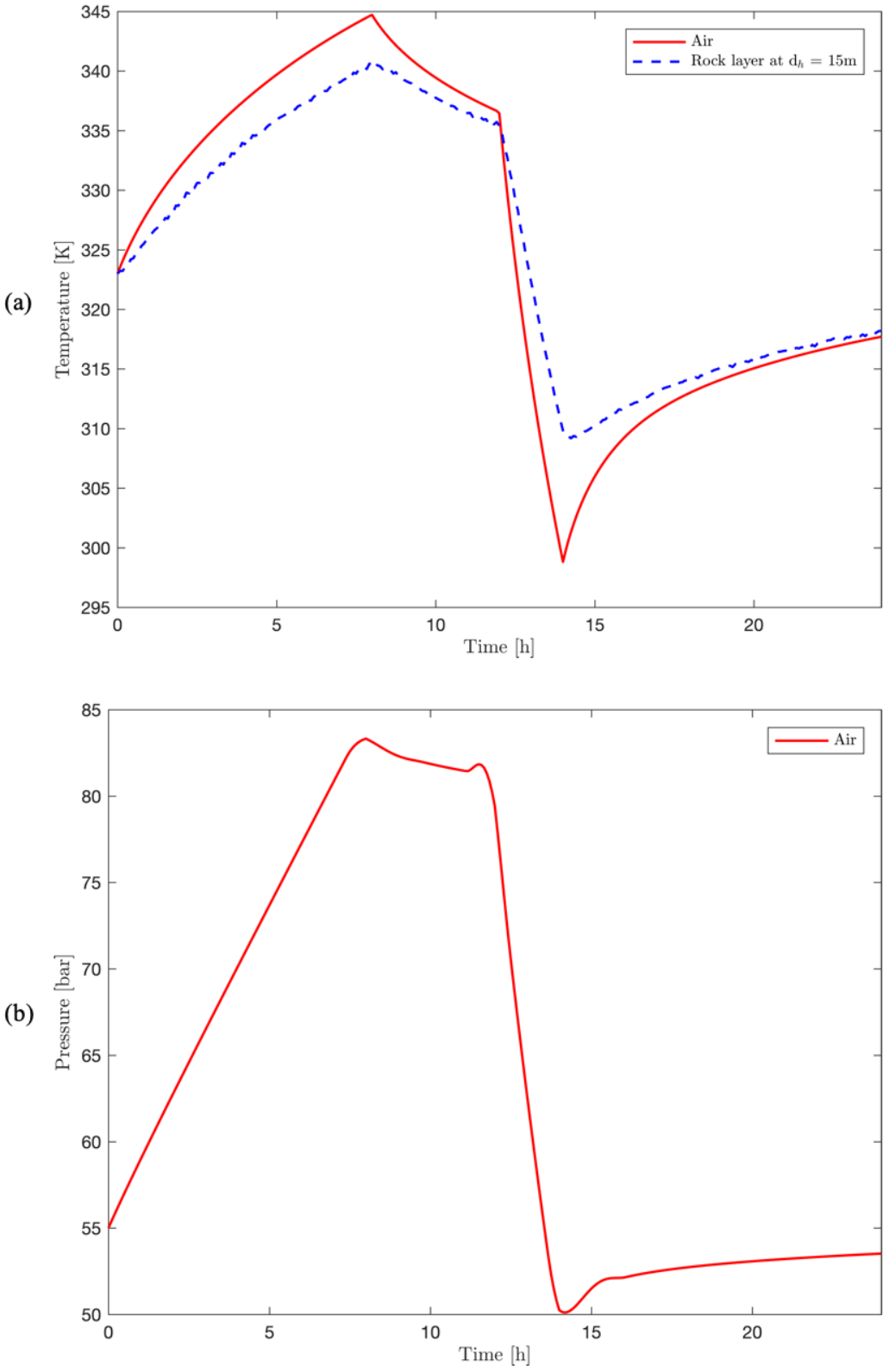


FIGURE 3.11: (a) Temperature variation of air and the inner cavern wall and (b) Pressure variation of air inside the cavern in the first charge-discharge cycle

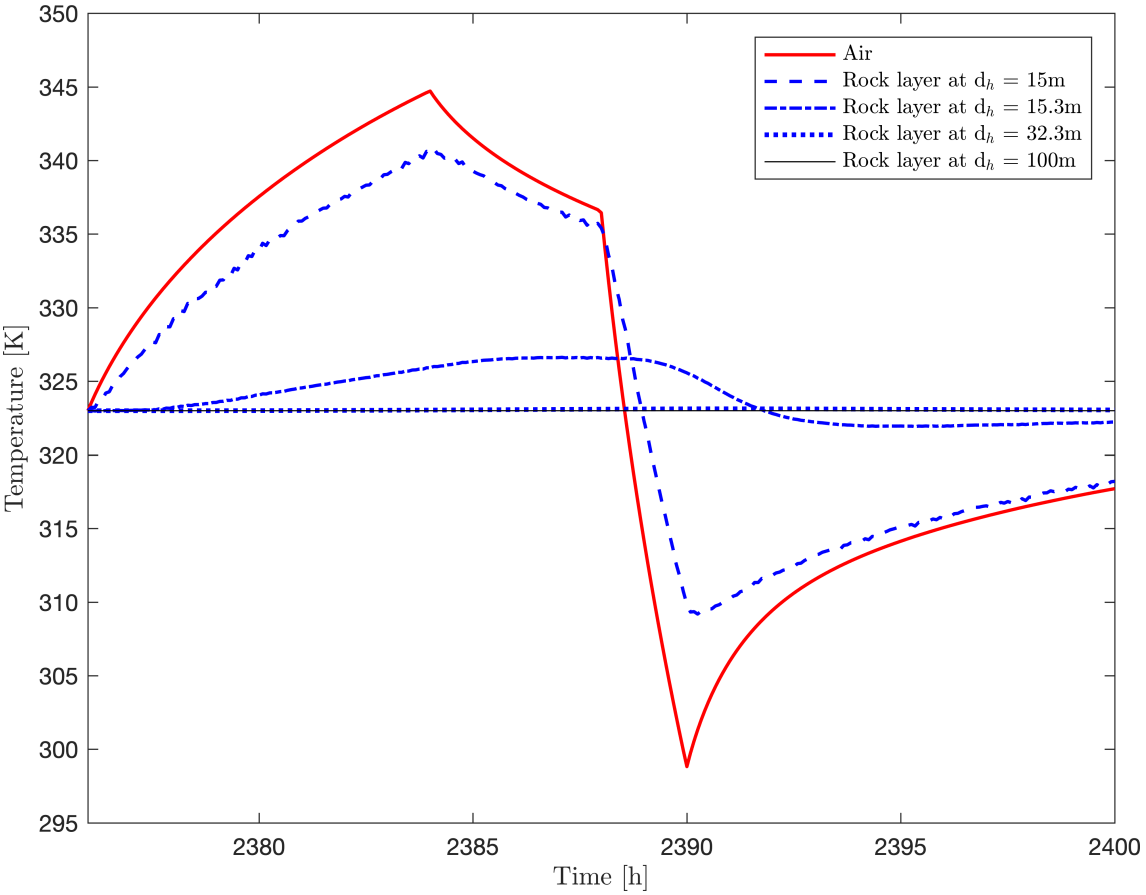


FIGURE 3.12: Temperature variation of air along with the layers of rock at some horizontal distances d_{h} from the cavern's (Y) axis of symmetry

temperatures would increase the average cycle temperature of the rock layers, thereby widening the skin depth. Furthermore, longer cycling time periods (e.g. one week) would also increase the temperature skin depth, as can be inferred from (3.30).

The simulated thermodynamic response of air and the inner cavern surface over 100 cycles is shown in Fig. 3.14. Although the mean temperature of the rocks increases, as evident from the figure, the heat build-up in the rocks would only cease over a sufficiently long time. In other words, true steady-state conditions would be reached only when the skin depth becomes large enough to reach the outer boundary of the cavern. In practice, however, the cavern would likely not operate over such long periods of time; therefore, a snapshot of 100 cycles is considered to gain insights into the thermomechanical response of the cavern. As noted in § 3.5.2, the thermodynamic response of the air and rock particles

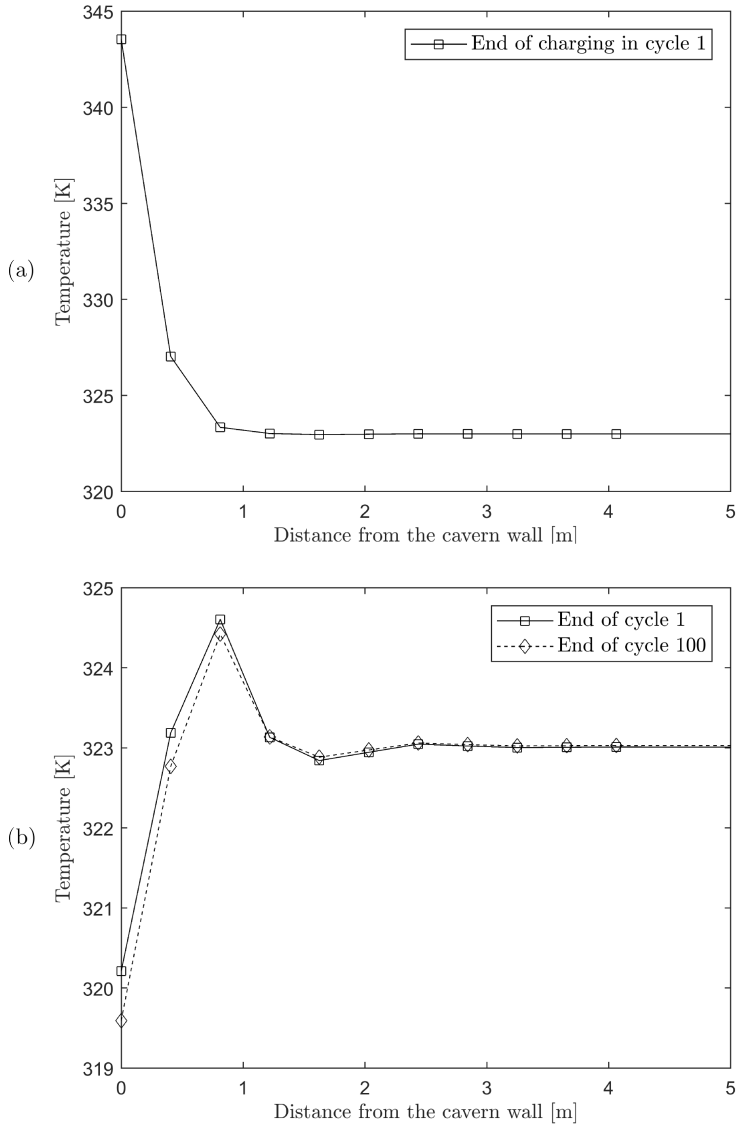


FIGURE 3.13: Temperature variation near the cavern wall (a) at the end of the charging phase in the first cycle and (b) at the end of the first and last cycles

at any instant in time forms, in part, the loading conditions on the cavern.

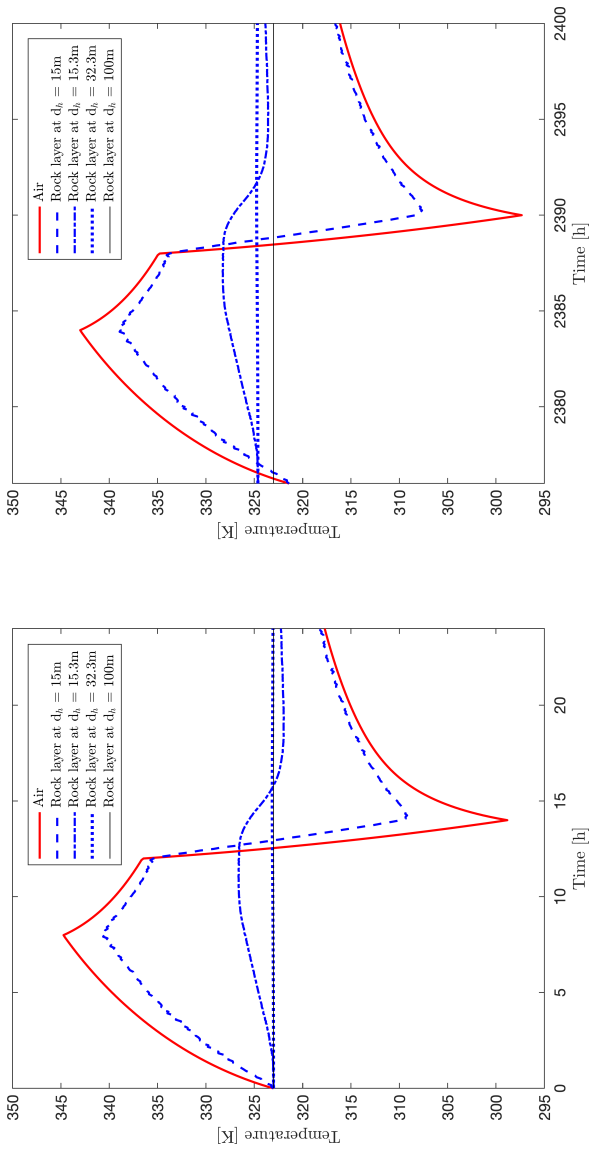


FIGURE 3.14: Temperature variation of air and rock layers at various horizontal distances into the cavern wall (a) in the first cycle and (b) in the 100^{th} cycle

The next step is to compute the displacements of nodal points due to the applied loads. The scaled displacements of the boundary of the structure just after the end of the charging phase (maximum temperature and pressure point) and discharging phase (minimum temperature and pressure point) in the hundredth cycle are shown in Fig. 3.15. The structure continuously 'expands' until the end of the charging phase due to increasing pressure load at the cavern walls and thermal loads due to temperature changes in the rock particles, at which time the relative displacement of each rock particle is maximum. At the end of the charging phase, the maximum horizontal and vertical displacements are 27.8 [mm] and 7.4 [mm], respectively, as shown in Fig. 3.15(a). This is followed by 'contraction' of the structure until the end of the discharging phase, when the relative displacement of each rock particle is minimum. Although the difference between the magnitudes of maximum displacements at the end of the charging and discharging phases are only slightly discernible, a significant difference is observed in the resulting stress fields.

A key requirement in the design of a cavern is the definition of loading conditions so that the resulting stress fields are in the compressible region (cf. Fig. 3.2); namely, FoS $\geq$ 1, as defined in (3.27). If the cavern is cycled at low pressures or subjected to large temperature changes, stresses around the cavern may be in the dilatancy region leading to unsafe operating regimes.

The state of stress in terms of the two dilatancy stability criteria, FoS_{DV} and FoS_{RD}, is plotted in Figs. 3.16 and 3.17, respectively. We shall focus on the thermodynamic extrema of the hundredth cycle, which are the instants in time at the end of the charging and discharging phases. As observed in Fig. 3.16(a), at the end of the charging phase when the confining pressure is greatest, $\text{FoS}_{\text{DV}} < 1$ in a small region towards the bottom of the cavern. In other words, the intersection of the hemispherical and cylindrical regions near the floor of the cavern has stress states which are in the dilatancy zone; thus, rock salt in this area may experience micro-fracture leading to long-term failure of the cavern. At the end of the discharging phase, as seen in Fig. 3.16(b), owing to lower cavern internal pressure and larger temperature changes in the rock particles, the DV criterion predicts

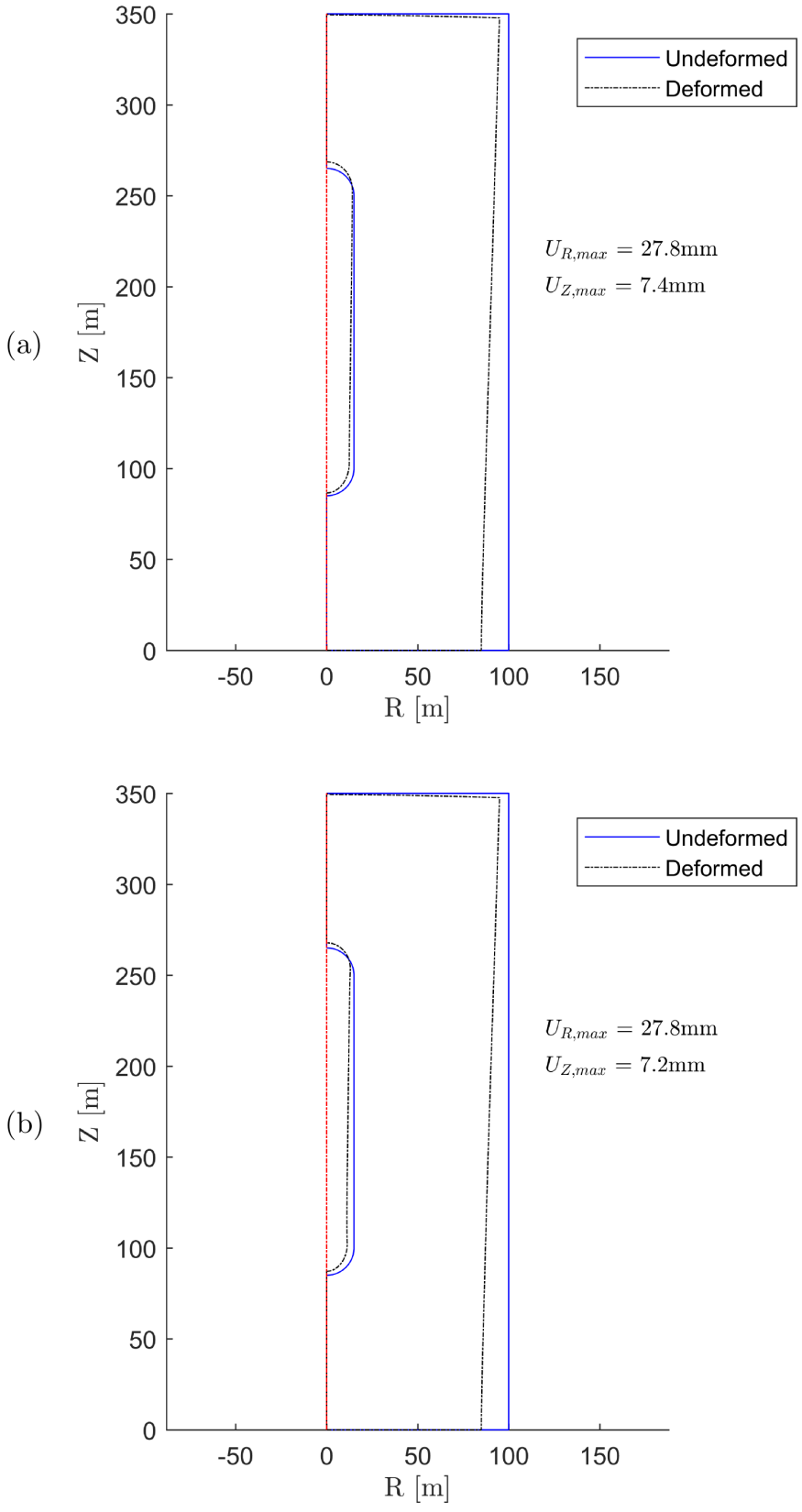


FIGURE 3.15: Displacement of the rock salt structure in the hundredth cycle at the end of the (a) charging phase and (b) discharging phase

the stress states of relatively more points in the vicinity of the cavern wall to be in the dilatancy zone.

On the other hand, whilst the contour plots of FoS_{RD} using the RD criterion as shown in Fig. 3.17 exhibit a similar trend as the DV criterion – namely, a higher risk of failure when the cavern is operating at low pressures and large temperature changes – a greater degree of failure is predicted by the RD criterion.

The observed differences in failure prediction may be attributed to several factors. The rock salt samples used for determining the material constants associated with the two formulations that extrapolate its mechanical behaviour are fundamentally different in composition, and hence demonstrate variability in response. The RD criterion considers more variables in the formulation of the failure criteria than the DV criterion; most importantly, the effect of thermal loads due to changes in temperature in the rock salt are taken into account. As discussed earlier, the RD criterion sought to improve salt failure prediction mechanisms; thus, one may consider this criterion to be the current state-of-the-art.

Finally, tensile stresses in the cavern walls negatively affect its mechanical stability. Thus, it is useful to look at the variation of maximum and minimum principal stresses with time: Fig. 3.18 shows this for points A, B and C highlighted in Fig. 3.6. Whilst the criterion is satisfied in the sense that none of the principal stress values are positive, it is easily observed that for point C near the cavern floor, shown in Fig. 3.18(a), the shear stresses are maximum. This indicates that rock particles around this region are more susceptible to failure, with the region of likelihood of failure decreasing as one moves from point C to A along the cavern wall, as observed from the FoS trends shown in Figs. 3.16 and 3.17.

The sensitivity of the results to cavern geometry was tested. First, the geometry of the cavern was parameterised by introducing two variables: (a) the ratio of inner radius of the top hemispherical shell (cavern roof) to that of the bottom hemispherical shell (cavern floor), $R^{\text{roof-radius}}_{\text{floor-radius}}$; and (b) the ratio of the height of the cavern to its mean radius, $R^{\text{height}}_{\text{mean-radius}}$. Over a space of appropriate values for the parameters, the mechanical response is obtained. The magnified FoS contour plots are shown in Fig. 3.19 for two cavern

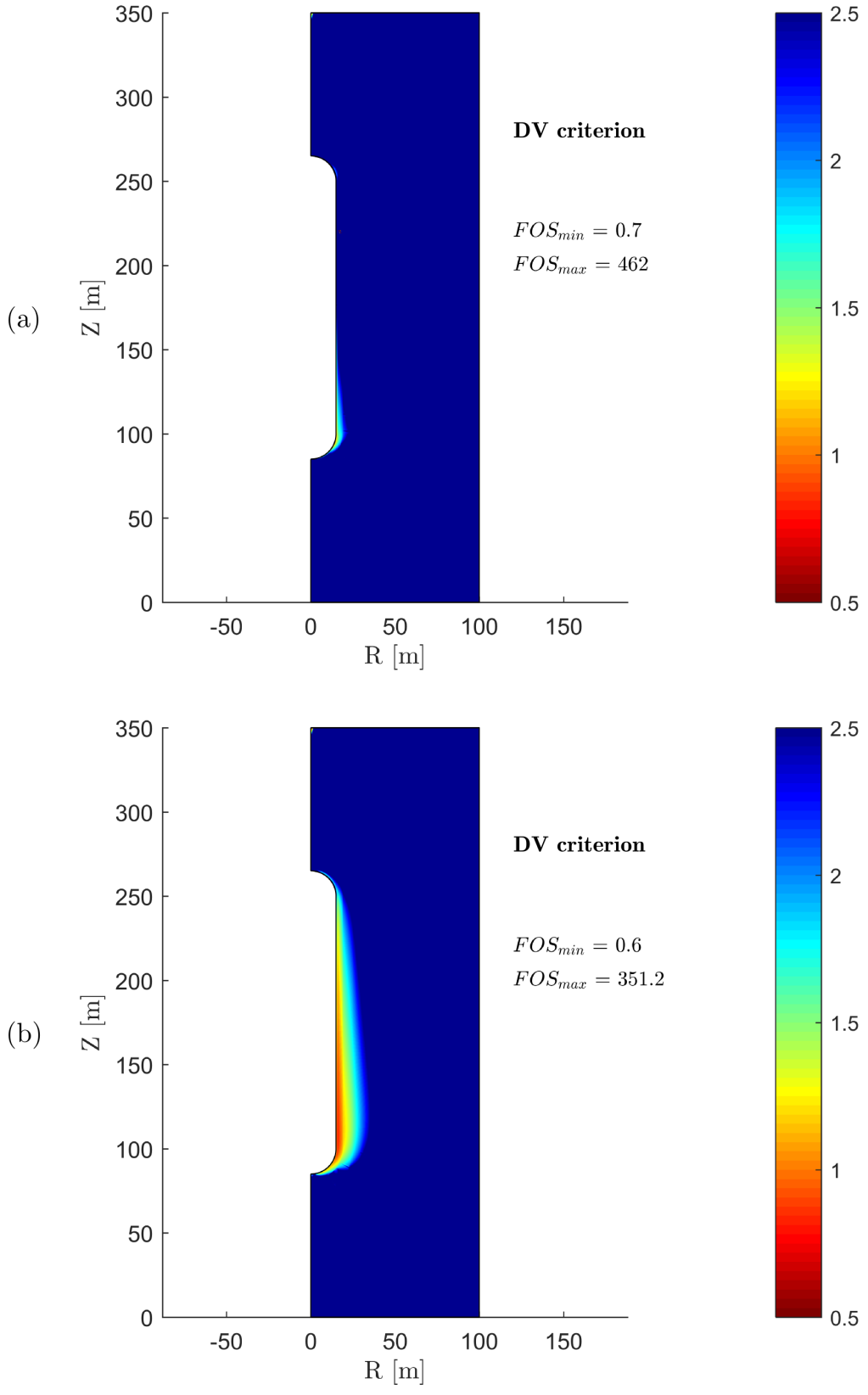


FIGURE 3.16: FoS plots, given by the DV criterion, in the hundredth cycle at the end of the (a) charging phase and (b) discharging phase

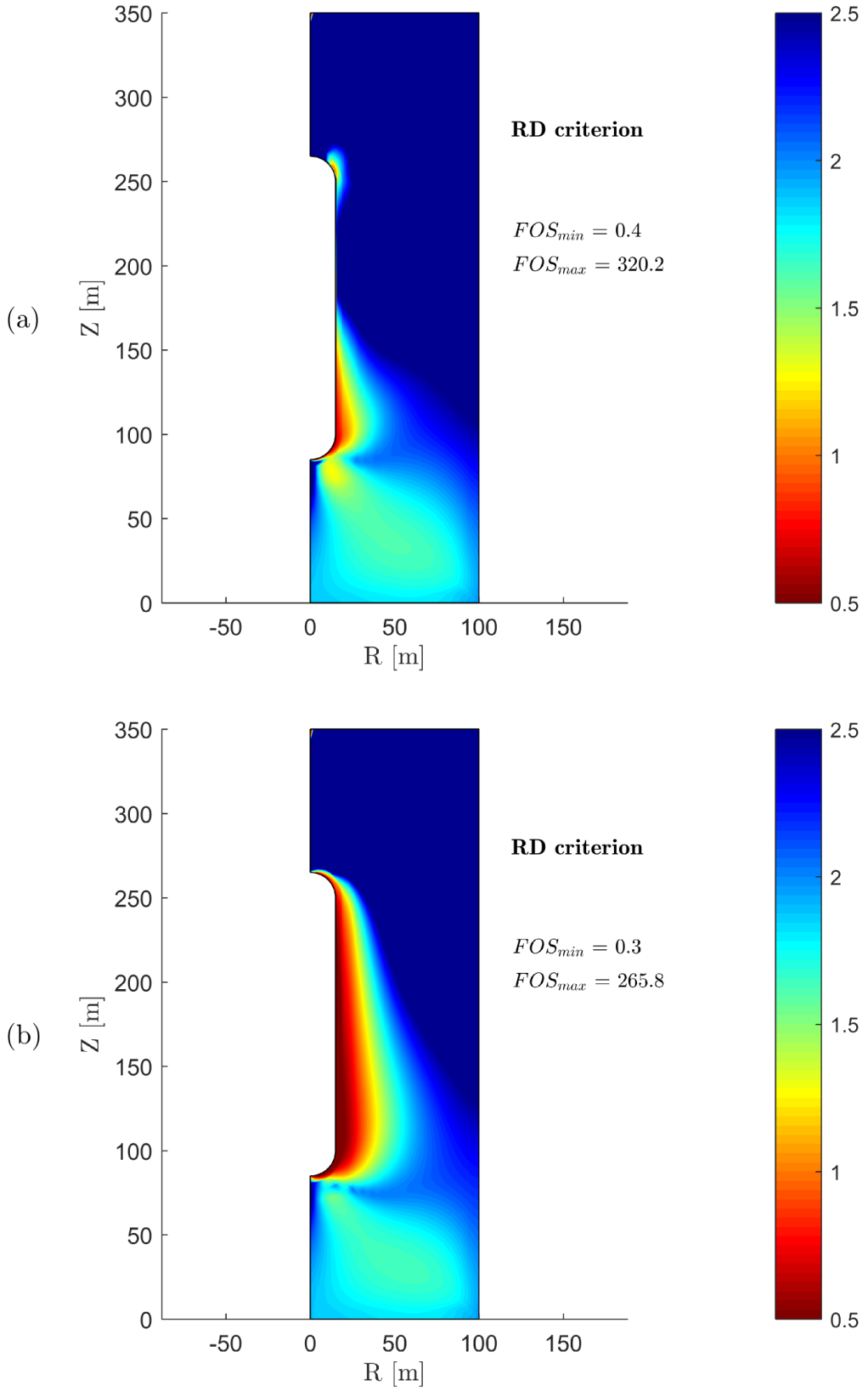


FIGURE 3.17: FoS plots, given by the RD criterion, in the hundredth cycle at the end of the (a) charging phase and (b) discharging phase

geometries: one with relatively smaller cavern height and larger roof radius, and the other with relatively larger cavern height and larger floor radius. For each geometry, the FoS values are plotted at the end of the charging and discharging phases. Although the geometries do not operate in safe regimes at all times, it is evident that the cavern with relatively smaller $R^{\text{height}}_{\text{mean-radius}}$ and larger $R^{\text{top-radius}}_{\text{bottom-radius}}$ performs better.

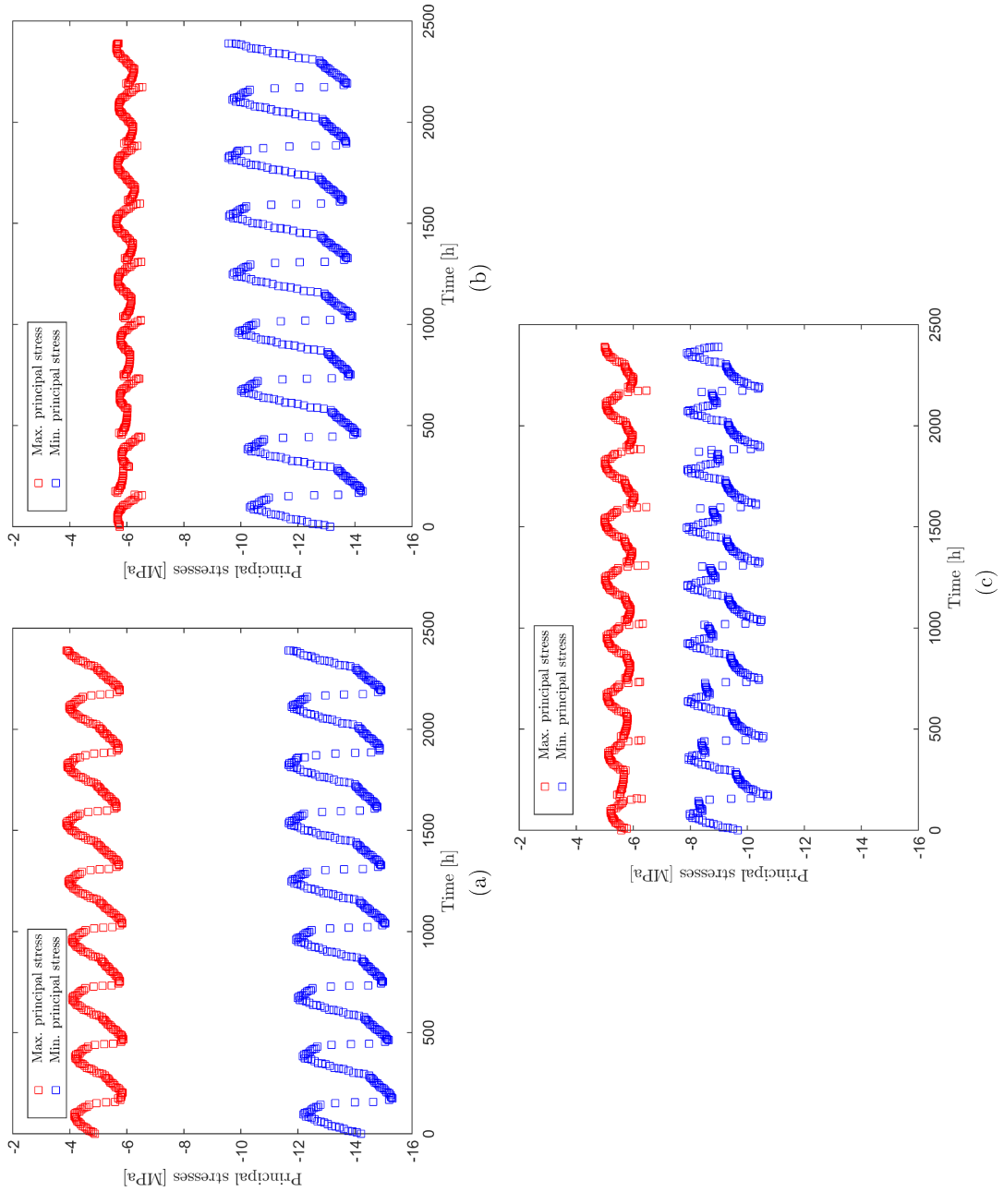


FIGURE 3.18: Variation of principal stresses with time in the cavern wall for (a) point C near the cavern floor, (b) point B at cavern mid-height and (c) point A near the cavern roof

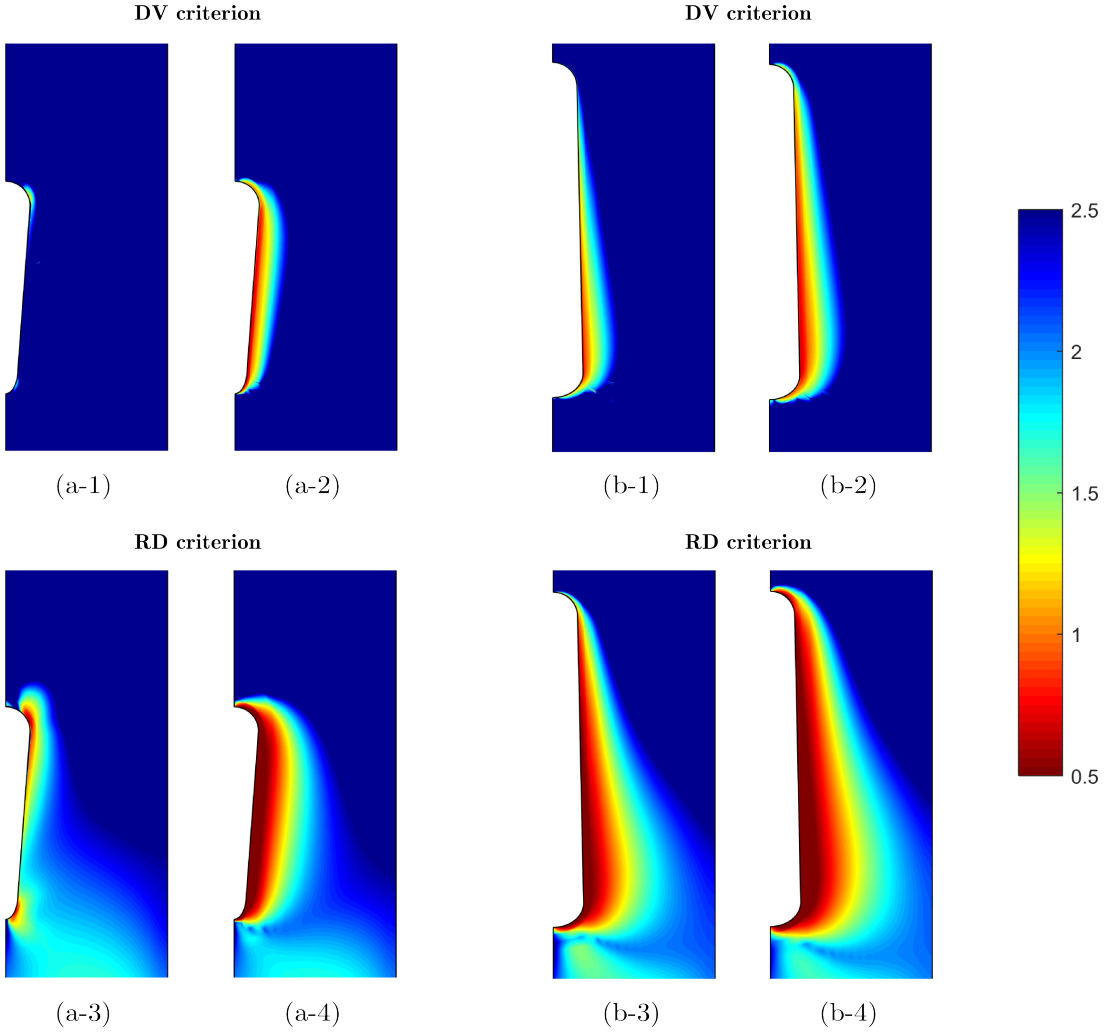


FIGURE 3.19: (a-1), (a-2), (a-3) and (a-4) show FoS for a cavern with a relatively larger value of $R^{\text{top-radius}}_{\text{bottom-radius}}$ and a relatively smaller value of $R^{\text{height}}_{\text{mean-radius}}$ than (b-1), (b-2), (b-3) and (b-4). Moreover: (a-1) and (b-1) represent FoS due to DV criterion at the end of the charging phase; (a-2) and (b-2) represent FoS due to DV criterion at the end of the discharging phase; (a-3) and (b-3) represent FoS due to RD criterion at the end of the charging phase; and (a-4) and (b-4) represent FoS due to RD criterion at the end of the discharging phase

3.7 Conclusions

This chapter has developed a methodology to predict the response of an underground salt cavern subjected to daily cycling of compressed air.

As discussed in § 3.1, due to extensive accumulated experience in industry, salt caverns are the preferred option for storing large volumes of compressed gases, such as compressed air for utility scale CAES plants. Salt caverns have a smaller footprint compared to pressure vessels on land[2], offer excellent air tightness characteristics compared to other underground storage options whilst also being the lowest cost option in terms of capital cost per unit of useful energy (i.e. exergy) stored, at around \$25-30/kWh[43;80]. More importantly, the cost of adding an incremental unit (i.e., marginal cost) of energy storage capacity in salt caverns is very low at around \$1-2/kWh[80]. This is because the costs associated with salt cavern construction are largely fixed – they are incurred in sourcing the rock drilling and salt mining equipment, drilling the bore hole (up to around 2,000 [m] below ground surface[53]) and cementing the bore hole from the ground surface to the top of the cavern (i.e. the casing-shoe). For a cavern that is solution mined, the only additional costs of extending the storage capacity are due to the costs of further leaching (set by volume of water used to shape the cavern) and labour for personnel operating the leaching equipment. It is therefore in the interests of the CAES plant operator to maximise the volume of salt cavern created, the upper limit on the amount of salt leached out being set only by surrounding geology.

Salt caverns are not ubiquitous, however, and this is therefore a major barrier to large-scale CAES plants being widely deployed. The issue has led some parties to investigate the suitability of hard rock caverns and aquifers for compressed air storage; however, apart from being higher cost (of construction and marginal capacity) than salt cavern based

[2]Underwater pressure vessels, the subject of Chapter 5, also leave behind a smaller onshore land footprint versus aboveground air pressure vessels. However, as seen in Chapter 6, underwater containments are at present more expensive per unit of useful energy stored compared to salt cavern-based compressed air storage

storage[80], there are operability concerns for rock cavern- and aquifer-based gas storage as discussed in § 3.1, and commercial implementations do not yet exist.

It is worth noting that the British Geological Survey conservatively estimated the availability of around 1.5 trillion m^3 of salt cavern storage volume in the UK alone[81] – equivalent to around 5 million Huntorf storage caverns. However, it is unclear whether all of this volume could be developed for commercial CAES use.

In general, the contribution of this chapter is the development of a tool to investigate the structural reliability of a salt cavern for high frequency cyclical air storage by way of combined thermomechanical analysis. In other words, the contents of this chapter could be useful to a project developer intending to use salt caverns to store gases, especially if it involves cyclical transactions at relatively high frequencies (e.g. one cycle per day) with fluctuations in pressure as well temperature. Whilst the operators of Huntorf and McIntosh CAES plants, and the developers of numerous other CAES plants that did not come to fruition, would have developed similar tools for reliability analysis, this thesis presents the first attempt in the public domain.

Conclusions specific to the analysis carried out in the previous sections are detailed below.

In the first instance, a quasi-static model predicts the thermodynamic response by coupling the heat and mass transfer equations in a cavern with appropriate boundary conditions. The computed temperature and pressure variation of air within the cavern volume, as well as temperature fluctuations in the rock particles, form the boundary conditions for evaluating the mechanical response of the rock salt structure. The relationship between material strains and the associated stresses is described by an uncoupled thermoelastic model. The equations contained within the material model are discretised using the finite element method which facilitates the numerical computation of the stress-fields.

The temperature skin depth is shown to be narrow; namely, the temperature fluctuations in the rock is confined to a small distance from the cavern wall. However, the resulting thermal loads contribute significantly to the overall stress field, especially when the rate

of change of temperature is negative causing the stresses to be tensile in nature. When the cavern operating pressure is minimum, the rate of temperature change is negative and maximum, thereby requiring extra care in the design of the cavern.

The structural stability is then investigated for the initial cavern geometry by calculating (a) the principal stresses at three locations along the cavern wall and (b) Factor of Safety (FoS) values for the rock particles. Whilst the principal stresses are not tensile for any of the considered 'high risk' locations, the deviatoric stresses are maximum near the floor of the cavern. The contour plots of FoS values, which measure the propensity of the rock particles to dilate, thereby setting them on a path to permanent failure, indicate that the regions along the cavern wall – especially near the floor – are operating in unsafe stress regimes even when the confining pressures are high and the change in temperature has not reached the maximum value. Two failure criteria, referred to here as the DV criterion and the RD criterion, are used to obtain the FoS values. It is observed that when the confining pressures are low and the change in temperature is maximum, the susceptibility of rock particles to failure is increased.

The sensitivity of the results to cavern geometry is then analysed. When using the DV criterion, for a cavern with smaller storage capacity, the FoS values indicate that the cavern operation is safe when its confining pressure is maximum within a cycle. However, the RD criterion for the same geometry and operating conditions indicates that regions around the cavern wall may fail. Thus, it is easily observed that not only the chosen system parameters (geometry, cycling characteristics, type of salt, etc.) can have a significant impact on the mechanical response of the cavern, but also the criteria that best represents failure for the application.

Chapter 4

Compressed air energy storage with liquid air capacity extension

4.1 Introduction

For CAES designs to be cost-effective, they must typically be employed at large scales, for instance, in underground salt caverns and aquifers. However, geological constraints prevent widespread deployment of this variant of CAES. An alternative approach that has been employed is aboveground storage of compressed air, for instance, in pressurised steel tanks; this scheme, however, can incur significant costs associated with storage. Moreover, conventional CAES designs are also disadvantaged by the fact that the power generation phase incorporates the burning of fossil-fuel. Thus, various newer strategies have been proposed to address these underlying issues, as discussed in Chapter 2.

This chapter introduces and evaluates a novel energy storage system aimed at addressing the effectiveness of an aboveground CAES system. The proposed system supplements compressed air storage with liquid air storage facilities primarily to extend the capacity of energy storage. Apart from the fact that liquid air is relatively a few thermodynamic-steps away from compressed air (the first step in producing liquid air/nitrogen is the

compression of atmospheric air), and that liquid air energy storage (LAES) has been considered a possible candidate for bulk storage of electrical energy, especially in the UK, there are several advantages to the proposed co-location:

- Liquid air, unlike compressed air, possesses high exergy density and can thus be compactly stored
- Liquid air is usually stored at near ambient pressures, precluding the need for relatively more expensive pressurised vessels
- Liquid air storage also has the strong advantage that it can be located almost anywhere

However, as discussed in the following sections, current LAES schemes do not offer high roundtrip efficiencies, and thus the present proposal attempts to exploit the different characteristics of CAES and LAES systems; namely, the relatively higher roundtrip efficiency of CAES and the lower cost per unit of energy storage capacity of LAES.

The system thus comprises a compressed air store of relatively lower energy storage capacity and a liquid air store of higher energy storage capacity, and associated machinery to transform between the two states of air. The low-frequency components of power are associated with large quantities of stored energy and are mainly handled by the conversion between liquid air and compressed air. The higher-frequency components of power are mainly handled by CAES alone. Thus, when electricity prices are low, and the compressed air tank is nearly full, electricity can still be drawn from the grid by converting some amount of compressed air into liquid air. Conversely, when electricity prices are high, and the compressed air tank is nearly empty, electricity can still be exported to the grid by converting liquid air back to compressed air, and then to electricity. Here, the liquid air is stored at atmospheric pressure.

We begin by considering, briefly, the historical development of LAES technologies and summarising the current state-of-the art in technology and costs. An analysis of the thermodynamically ideal hybrid energy storage system is then performed, before moving on

to the description of system component modelling and discussion on a possible practical arrangement of the hybrid storage system. Then, results of the practical system analysis are presented and discussed, and some conclusions are drawn. The scope of this chapter does not include economic analysis. The objective here is to arrive at an estimate of the roundtrip exergy efficiency of the novel hybrid energy storage system and other thermodynamic trends that are of interest for eventual system design.

4.2 Overview of liquid air energy storage

If one removes sufficient heat from an isolated mass of air, it will liquefy. At ambient pressure, air completely liquefies at around 79 [K] or −194 [C]. Liquefied air is a mixture of pure substances – mainly nitrogen, oxygen and the noble gases. A simple air liquefaction cycle, the Linde-Hampson cycle, which exploits the Joule-Thomson effect to produce liquid air is shown in Fig. 4.1. Liquid air can also be produced by mixing together pure liquid nitrogen and liquid oxygen, although large-scale commercial manufacturing schemes are currently non-existent [82].

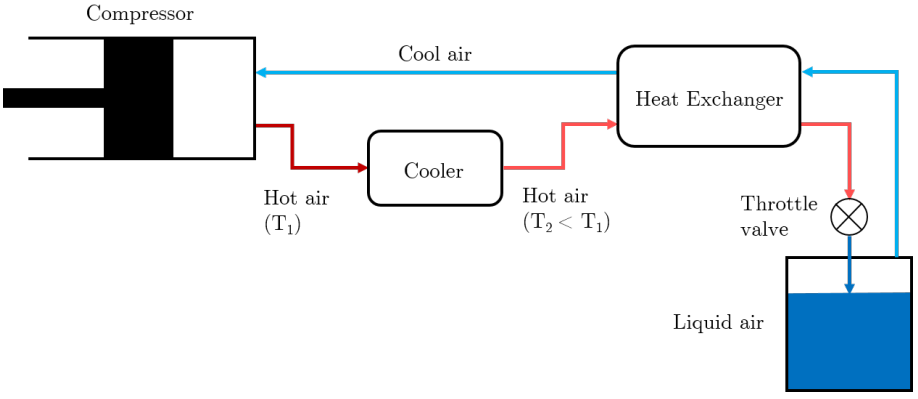


FIGURE 4.1: A simple air liquefaction cycle

Liquid air stores exergy by exploiting the temperature difference between two thermal reservoirs. Thus, LAES systems belong to the wider class of thermoelectric energy storage strategies. The ideal LAES cycle, which is depicted in Fig. 4.2, involves:

- Charging the liquid air store by employing electrically driven air liquefaction processes, with the liquid air being stored in thermally insulated tanks at near-ambient pressures
- Discharging the liquid air store, where power is recovered by first pressurising the liquid air, then supplying thermal energy to the fluid, and subsequently expanding to generate work output
- Recycling the thermal energy, where either exergy released during discharge is stored and used to minimise the liquefaction work during charging, or hot thermal energy released during charge is captured and used to boost the energy recovery efficiency, or both

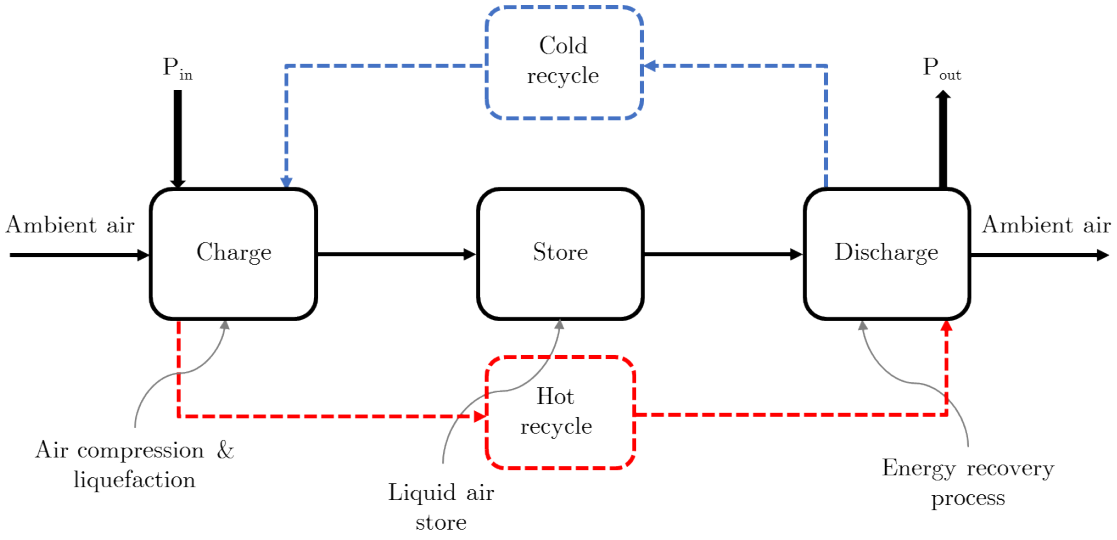


FIGURE 4.2: The ideal liquid air energy storage cycle

Practical LAES systems differ from each other in a wide variety of ways: from the complexity of the air liquefaction processes involved, to the methods of power recovery, to the methods of thermal energy recycle, to the design of thermal storage units. However, the use of energy dense liquid air as the storage medium, excellent geographical locatability of the relatively inexpensive liquid air storage tanks, the relative ease of integration with other energy systems (especially thermal energy systems), and the use of mature components are characteristics common across all LAES schemes.

The use of liquid air as a carrier of energy within the context of energy storage was first proposed by Smith in 1977 [83]; the concept is reproduced in Fig. 4.3. Smith proposed using adiabatic air compressors to transform ambient air at around 20 [C] to 50 [bar] and 775 [C] to feed the liquefaction process, with the heat of compression captured in a stainless steel containment as the air passes through. Energy is recovered by adiabatic expansion, with the heat of compression from the thermal store helping to boost the recovery efficiency. Whilst a roundtrip efficiency range of 62-72 [%] was quoted by Smith, the configuration required the system components to withstand temperatures between −200 [C] and 800 [C], pressures up to 80 [bar], and allow contact with both compressed air and liquid air. Components able to withstand stresses due to such intensive thermomechanical loading would inevitably be expensive in terms of both capital and operating costs.

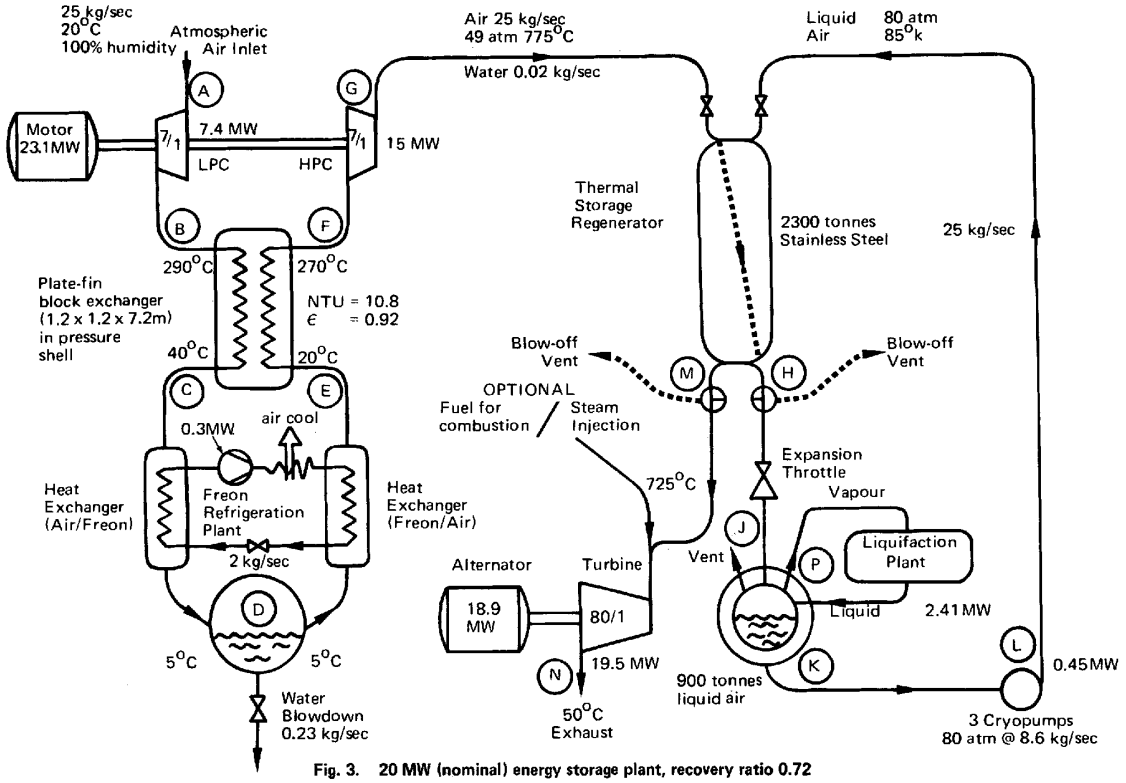


FIGURE 4.3: The liquid air energy storage scheme proposed by Smith [83]

Next, in the year 2000, Chino and Araki [84] proposed various LAES strategies with efficiencies similar to those reported by Smith. The focus of their efforts was the design of the thermal store, whereby a mass of concrete would contain an array of steel pipes within it,

to enable the smaller diameter pipes to bear the pressure loads and the concrete to store the thermal energy [85].

In the year 2005, UK-based Highview Power Storage along with University of Leeds re-started the work on LAES [86], which led to the development of a 350 [kW]/2.5 [MWh] pilot plant in 2009 [87], shown in Fig. 4.4. Highview Power Storage, unlike its predecessors, employed near-isothermal compression to feed compressed air into the liquefier. When power was recovered from the expansion of pressurised liquid air, cold thermal energy was also extracted and stored. The use of a separate heat transfer fluid to recover the cold enabled storage in a relatively cheaper non-pressurised thermal store; however, expected roundtrip efficiency for this scheme at scale was quoted as 50-60 [%], which is lower compared to earlier proposals.

A pivotal component in the Highview concept is the cold thermal storage unit. The *cold thermal recycle* helps to control not only the efficiency of the liquefaction unit, but also the roundtrip efficiency of the system. Foregoing cold energy recycle would significantly lower the effectiveness of the overall process. In its pilot plant, the cold store was made of a series of packed gravel beds filled with relatively small quartzite rock particles (sized by a 15 [mm] sieve). Ambient pressure air was used as the heat transfer fluid to capture the cold energy, stored at around -158 [C]. The roundtrip efficiency of the system was reported to be 8 [%] [88].

Furthermore, the pilot plant was subjected to simulated tests of two electricity grid-related services: the *Reserve* and *Response* trials, similar to the Short Term Operating Reserve service and the *PJM test*, respectively. More detail can be found in the paper by Morgan et al. [88].

The pilot plant testing unearthed several issues on the practical aspects of a LAES scheme. For instance, the expected longer start-up times for larger plant due to rotational inertia of turbomachinery, the dynamics of plant operation (especially the degradation of the thermal front), and the sensitivity of the roundtrip efficiency to charging and discharging pressures. However, the most significant issue was perhaps the stratification observed



FIGURE 4.4: The 350 [kW]/2.5 [MWh] LAES pilot plant from Highview Power Storage

within the liquid air storage tank. Nitrogen, by virtue of its lower boiling point relative to oxygen, boils off quicker as heat seeps through the tank over time, thus resulting in a liquid mixture richer in oxygen. This raised concerns around the potential for explosions or fire incidents if the oxygen-enriched liquid came into contact with, for instance, a hydrocarbon in the power conversion equipment. It was observed that the system components of the pilot plant required oxygen cleaning after a period of five to seven days of continuous liquid air storage, thus significantly lowering the expected longer-duration storage of liquid air for several weeks to months.

Highview Power Storage is currently engaged in demonstrating a 5 [MW]/15 [MWh] plant in collaboration with Viridor in Manchester, UK [89]. It should be noted that this demonstrator is a 'half-cycle' plant; namely, only the discharge cycle is put into function as the liquefaction of air is performed off-site and shipped in by tankers. This implies that the cold energy released during power recovery is stored in thermal containers only for demonstration purposes, since the opportunity for using this energy to reduce liquefaction work is absent [90].

Due to these efforts, the relatively high exergy density of liquid air and its potential as a clean transport fuel, there has been a surge in interest in liquid air based energy

systems[82;91], including press-releases by companies such as Air Products[92], and Linde and Hitachi[93].

Academic research on LAES systems is also being actively pursued. Ameel et al.[94] analyse a Linde liquefaction process combined with a Rankine cycle, and report that up to 43 [%] of the energy could be recovered from liquid air. Li et al.[95] propose a liquid air system coupled with natural gas-fuelled closed Brayton cycle, where the carbon dioxide produced is captured as dry ice. The roundtrip efficiency is reported to be 54 [%]. Helium circulates in this system without being consumed, and helps to control the temperature of the natural gas after combustion in an oxygen rich environment, prior to entering the gas turbine. Morgan et al.[96] analyse a system where a Rankine cycle is used to extract energy from liquid air, and also evaluate the levelised energy costs for a 20 [MW]/80 [MWh] installation. Li et al.[97] propose a scheme for integrating LAES with inflexible nuclear power to time-shift electrical energy, and report that roundtrip efficiencies greater than 70 [%] could be achieved by recovering thermal energy from the nuclear plant. However, it is worth noting that due to the liquid air tank stratification issues discussed earlier, safety concerns may prevent this configuration from being explored in practical settings.

Capital costs dominate for a LAES system, with the air liquefaction unit accounting for a large proportion of the costs. The cost of the cryogenic storage tank depends on its capacity; in terms of cost per rate of liquefaction, for a plant with 300 [tonne/day] capacity, £34k [1/tonne/day] is suggested, and for plant with 600 [tonne/day] capacity, £26k [1/tonne/day] is suggested[82;98].

4.3 Thermodynamic analysis of the ideal reversible system

An analysis of the hybrid system must rely on exergy as it helps to locate irreversibilities in individual components. Exergy is defined as the maximum amount work that can be extracted by allowing the system to come back into equilibrium with its ambient environment[99]. Neglecting kinetic and potential energy effects, and assuming chemical reactions

do not occur, the flow exergy of a stream of fluid relative to ambient conditions can be expressed as shown in (4.1):

$$\dot{B} = \dot{m}[(h - h_0) - T_0(s - s_0)] \tag{4.1}$$

Storing liquid air is storing exergy because as ambient heat is allowed back into that air, it will evaporate and do work. All pumped thermal electricity storage systems are implicitly exergy storage systems.

In the following, the configuration of an ideal reversible system is described and an exergy analysis is outlined. Based on the ideal system, considerable insight is gained into what features a practical system should have.

The proposed hybrid energy storage system has a compressed air store of relatively lower energy storage capacity and a liquid air store of higher energy storage capacity. These are arranged in series so that all energy transactions with the grid are carried out via the compressed air store; the liquid air store acts only as overflow capacity. This is shown schematically in Fig. 4.5.

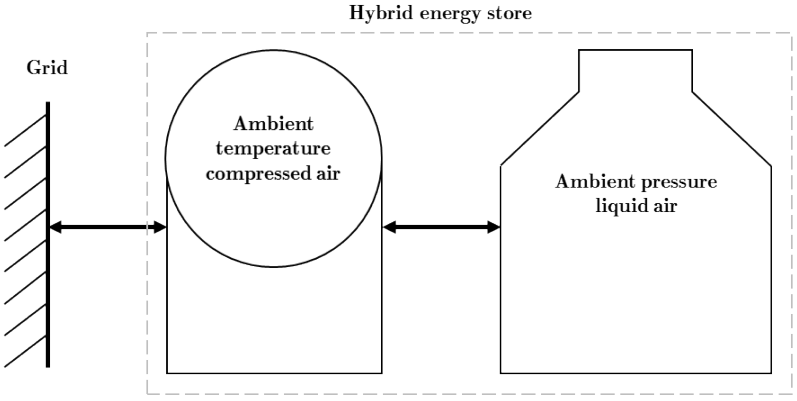


FIGURE 4.5: Flow of energy to and from the hybrid storage system

When electricity prices are low and the compressed air store is nearly full, compressed air is converted into liquid air and stored, so that more energy can be bought to additionally generate compressed air. We will describe this process as *forward conversion* (high-pressure air → liquid air). Conversely, when electricity prices are high, and the

compressed air store is nearly empty, liquid air is converted back into compressed air so that energy can then be restored to the grid. We will describe this process as *backward conversion* (liquid air → high-pressure air).

In the ideal system configuration shown in Fig. 4.6, there is no loss of exergy; namely, the flow exergy of ambient temperature compressed air is completely transformed into the flow exergy of ambient pressure liquid air during the forward conversion process. Similarly, the flow exergy of the liquid air is transformed back into the flow exergy of compressed air in the backward conversion process.

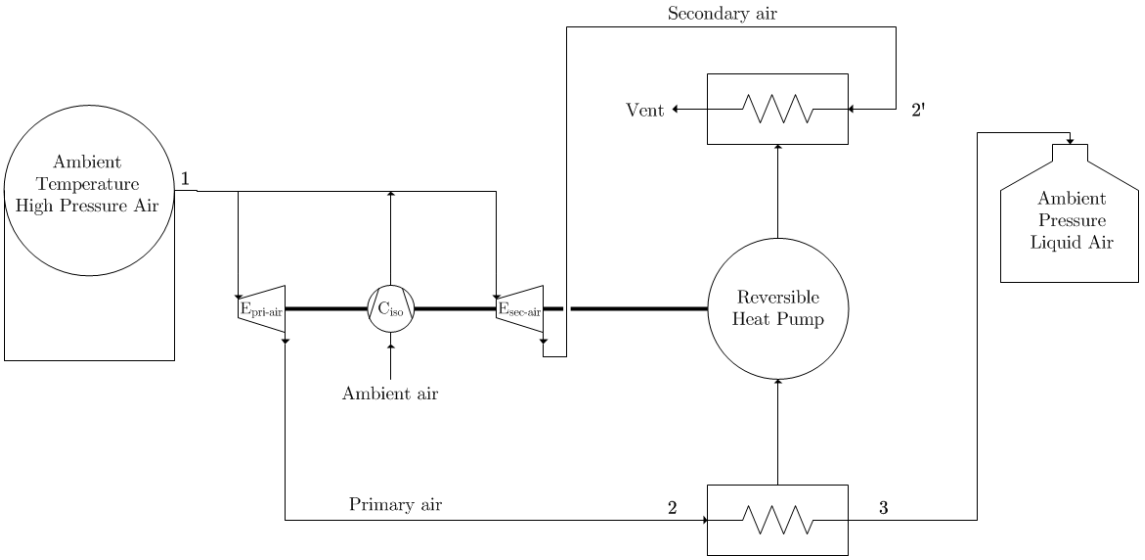


FIGURE 4.6: Ideal, reversible, hybrid energy storage system

For brevity in what follows, it is convenient to assign notation to some relevant temperatures:

$T_1 \coloneqq$ Atmospheric or ambient temperature [K]

$T_2 \coloneqq$ A temperature just above dew point for atmospheric air [K]

$T_3 \coloneqq$ A temperature just below bubble point for atmospheric air [K]

The forward conversion process is explained as follows. High-pressure air is drawn from the compressed air store in two different streams: *primary air* which is all ultimately converted into liquid form and *secondary air* whose exergy is exploited to provide additional cooling for the primary air. A straightforward exergy balance for the ideal system reveals the

required mass-flow ratio between primary and secondary air. Taking ambient temperature to be 290 [K], and assuming that the high pressure air is stored at 50 [bar], 1 [kg] of liquid air has the same flow exergy as approximately 2.2 [kg] of compressed air. In that case, the ratio of mass flow rates of air in the primary and secondary streams is 1:1.2.

The primary air stream begins at high pressure and temperature T_1. This air is expanded isentropically to atmospheric pressure via the expander E_{pri} so that its temperature reduces to T_2. The primary air at point *2* in Fig. 4.6 then passes through heat exchangers present on the cold side of a heat pump described separately in § 4.5. At point *3*, when sufficient heat has been removed from the primary air, it has become fully liquid with temperature T_3 and it can be stored at atmospheric pressure.

The secondary air stream also begins at the same high pressure and temperature T_1. This stream of air is expanded isentropically to atmospheric pressure via the expander E_{sec} to yield a stream of cool air which passes through a heat exchanger, on the hotter side of the heat pump, in order to draw heat from that heat pump. At point *2′*, the secondary air is also at temperature T_2. The latent heat of evaporation of liquid air is very much larger than the total heat required to raise air from T_2 to T_1. Moreover, the heat released from a heat pump on its hotter side will necessarily be larger than the heat drawn in on its colder side. Thus, it becomes obvious that the secondary air stream will not provide enough capacity for heat removal from the heat exchanger if the amount of secondary air suggested by a balance of exergy is used directly for cooling.

The isothermal compressor, C_{iso}, shown in Fig. 4.6 between E_{pri} and E_{sec} provides one means by which the notional system can be made fully reversible. By drawing some of the shaft power produced by E_{sec} to drive C_{iso}, the total mass flow rate of cooler ambient-pressure air exiting E_{sec} can be multiplied such that there is now sufficient thermal capacity to remove all heat from the heat pump with all air discharged being at ambient temperature. The heat pump in this system has an interesting configuration: temperatures on its hot-side range from T_2 to T_1 – close to 200 [K] for air that started at 50 [bar] prior to

expansion; by contrast, temperatures on its cold-side range from just T_3 to T_2 – typically ∼20 [K].

Since this is an ideal system, and all system components are lossless, the backward conversion process is obtained by simply reversing the direction of fluid flow relative to the forward conversion process.

4.4 Modelling system components

Before delving into a possible practical arrangement of the hybrid system, it is useful to describe the modelling methodology for the main components in the proposed system as well as the thermodynamic and transport properties of the fluids involved.

4.4.1 Fluid properties

Air functions as the energy carrier in the hybrid system. Thermodynamic properties of dry air are calculated from the formulation of Lemmon et al.[100], and the transport properties of dry air are calculated from Lemmon and Jacobsen[101].

It is important to note that whilst air is assumed to be completely dry in the present work, even industrial-grade air (used for instance in pharmaceutical and food-processing applications) will contain trace amounts of water vapour towards the end of the drying process. The actions of compressing humid air with subsequent cooling will result in the condensation of water vapour. The amount of water condensed depends strongly on the meteorological conditions. The relative humidity of air, which measures the actual content of water vapour in air as a proportion of the maximum amount that the air can contain, is dependent on temperature, as shown in Fig. 4.7. Moreover, the maximum amount of water vapour that a given mass of air can hold is itself a function of temperature and pressure of the air, as shown in Fig. 4.8. By way of example, if air at 1 [atm] and 290 [K], of 50 [%] relative humidity, is compressed to 10 [bar], and subsequently cooled to 290 [K],

$\sim$4.7 [g] of water vapour will condense for every 1 [kg] of air. Thus, adequate provisions must be made in the machinery involved to divert this by-product.

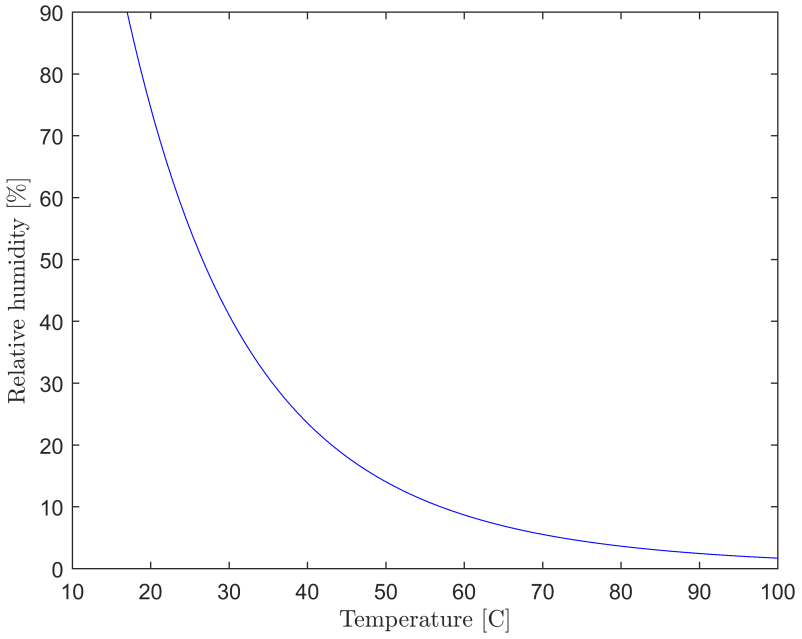


FIGURE 4.7: Variation of relative humidity of ambient pressure air with temperature

Conversely, direct cooling of the air to a temperature below its dew point also results in water vapour condensation. This already occurs naturally in nature by radiative cooling at night time resulting in the formation of dew on surfaces. However, active air cooling schemes are being pursued by many parties around the globe where there may be a shortage of freshwater sources or an alternative to the more conventional desalination techniques is desired [102]. These topics are not explored further here.

In the proposed hybrid system, ideally-behaving hydrogen is chosen to be the refrigerant, and its properties are calculated from the formulation of Leachman et al. [103]. The transport properties of hydrogen are calculated from Assael et al. [104].

4.4.2 Compressor and expander models

If the system considered is ideal in behaviour, its components are devoid of exergy losses. In that case, the compression and expansion of fluids are modelled as isentropic processes,

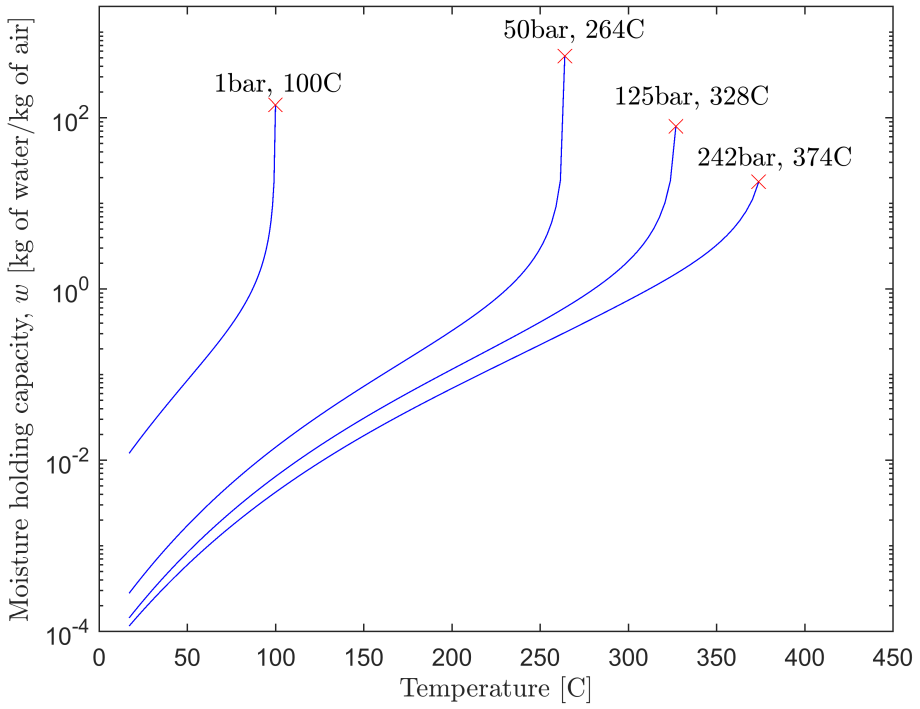


FIGURE 4.8: Water holding capacity of humid air as a function of air temperature and pressure

namely, the process of transformation of the state of fluids by compression or expansion is adiabatic as well as thermodynamically reversible.

If the fluid is considered to behave ideally, such as the refrigerant hydrogen in the proposed system, the temperature at the end of an isentropic compression or expansion process is given by (4.2), where it is assumed that the temperature and pressure of the fluid at the start, and its final pressure at the end, are known a priori.

$$T_{2,\text{isen}} = T_1 \left(\frac{P_1}{P_2} \right)^{\frac{(1-\gamma)}{\gamma}} \tag{4.2}$$

If the fluid operates outside the regime considered acceptable for ideal behaviour, as the air in the proposed system does, then the temperature at the end of an isentropic process is governed by (4.3); it is easily seen that the final process temperature in case of non-ideal fluid behaviour is not only a function of the starting temperature and pressure, and the

final pressure, but also the density of the fluid at the start.

$$T_{2,\text{isen}} = f\left(P_1, T_1, \rho_1, P_2\right) \tag{4.3}$$

For non-ideal system behaviour, determining temperatures at the outlet to the compressor or expander involves firstly calculating the ideal or isentropic outlet temperatures and subsequently applying a correction factor to evaluate the deviation from the ideal process. Here, isentropic efficiencies for the compression and expansion devices are used, and implemented as shown in (4.4) and (4.5), respectively.

$$T_2 = T_1 + \left(\eta_{\text{isen}}^{\text{C}}\right)^{-1}\left(T_{2,\text{isen}} - T_1\right) \tag{4.4}$$

$$T_2 = T_1 + \eta_{\text{isen}}^{\text{E}}\left(T_{2,\text{isen}} - T_1\right) \tag{4.5}$$

4.4.3 Heat exchanger model

Consider the generic two-stream counter-current heat exchanger shown in Fig. 4.9. A hot stream with constant mass flow rate, $\dot{m}_{\text{hot}}$, and constant specific heat capacity, $C_{\text{p,hot}}$, cools from inlet temperature $T_{\text{hot,in}}$ to $T_{\text{hot,out}}$, by exchanging heat with a cold stream of constant mass flow rate, $\dot{m}_{\text{cold}}$, and constant specific heat capacity, $C_{\text{p,cold}}$, with a corresponding rise in its temperature from $T_{\text{cold,in}}$ to $T_{\text{cold,out}}$. For simplicity, the model here is explained assuming constant specific heat capacities; however, in actual applications – and especially where phase change is involved as in the proposed hybrid system – heat capacities vary with temperature and pressure. This is addressed in the latter part of this section.

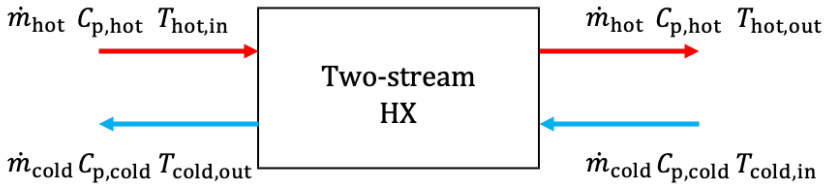


FIGURE 4.9: Schematic of a two-stream counter-current heat exchanger

To solve for the unknown decision variables (e.g. fluid temperatures), the heat exchange mechanism in Fig. 4.9 is formulated by the following two equations [REF]:

$$\dot{m}_{\text{hot}}\, C_{\text{p,hot}}\, (T_{\text{hot,in}} - T_{\text{hot,out}}) = \dot{m}_{\text{cold}}\, C_{\text{p,cold}}\, (T_{\text{cold,out}} - T_{\text{cold,in}}) \tag{4.6}$$

$$\dot{m}_{\text{hot}}\, C_{\text{p,hot}}\, (T_{\text{hot,in}} - T_{\text{hot,out}}) = U\, A\, \Delta T_{\text{LM}} \tag{4.7}$$

where equation (4.6) is the energy balance between the streams exchanging heat and equation (4.7) defines the relationship between the quantity of heat transferred, the heat transfer coefficient, U, heat transfer area, A, and the log mean temperature difference, ΔT_{LM}. This formulation is valid so long as the minimum temperature difference between the hot and cold streams (or the minimum approach temperature)[1], ΔT_{min}, defined below, is greater than zero to ensure (physical) feasibility of heat transfer.

$$\Delta T_{\text{min}} = \min\{T_{\text{hot,in}} - T_{\text{cold,out}}, T_{\text{hot,out}} - T_{\text{cold,in}}\} \tag{4.8}$$

For strictness, equation (4.8) must be accounted for explicitly within the heat exchange mechanism formulation. In practice, however, ΔT_{min} is usually set as a parameter and the solution of equations (4.6) and (4.7) are checked a-posteriori for any infeasibility, i.e., temperature cross-over of hot and cold streams.

Since the above formulation with two equations allows for only *two* unknowns, all other quantities must be known. If the unknowns are fluid temperatures, then – crucially – U and A must be known. Therefore, it becomes necessary to capture the implications of material properties and fluid dynamics on heat transfer, and design the heat exchanger to determine its heat transfer area; these tasks may be complex and even unnecessary at the initial stages of analysis and, thus, may lead to ineffective system design. As noted by Watson et al.[109], it is possible to circumvent this problem by including equation (4.8) within the formulation explicitly, and by setting ΔT_{min} as a parameter, which allows

[1] The minimum approach temperature is another measure of heat exchanger effectiveness. In liquefaction systems, where highly efficient heat exchangers are employed, minimum approach temperatures of 1 [K] are not uncommon.

for one more unknown. Conveniently, this unknown can be the product of U and A to characterise heat exchanger type and design. The analysis here, therefore, adopts this approach[2].

The proposed hybrid energy storage system involves the use of highly efficient heat exchangers with multiple hot and cold streams exchanging heat. This is to facilitate effective heat transfer between the refrigerant and the fluid undergoing phase change (such as air in the present work). There is a need, therefore, to not only model multi-stream heat exchangers (MSHX), but to also account for stream(s) undergoing phase change (e.g. compressed air to liquid air and back).

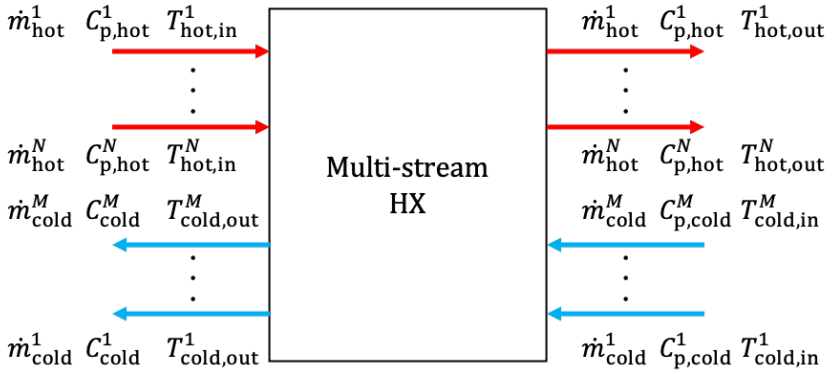


FIGURE 4.10: Schematic of a multi-stream counter-current heat exchanger with N hot stream and M cold streams

A typical MSHX is shown in Fig. 4.10 with N hot streams and M cold streams. Here, the modelling of MSHXs is based upon the recent work of Watson et al. [109;110], which extends the formulation of the two-stream heat exchanger model presented earlier. Therefore, the formulation: (a) assumes that the hot (cold) streams are co-directional with each other and flow in an opposite direction to the cold (hot) streams, and (b) ignores the internal geometric configuration of the heat exchanger, relying instead on the product of U and A to describe the heat exchanger's overall thermal conductance.

[2]There exists a further advantage to this approach: Generalised heat exchanger costs, by heat exchanger type, have been published normalised w.r.t. the product of U and A [202]. Therefore, detailed bottom-up component costing of heat exchangers can be avoided in the early stages of analysis, especially when system design is uncertain and evolving. This is relied upon in Chapter 6 for cost estimation of the hybrid storage system.

One of the core advantages of Watson et al.'s approach is the equation-oriented formulation, where a root-finding method like the Newton-Raphson alogrithm can be applied to solve for the unknowns. This is unlike all previous works on MSHX modelling where, for streams undergoing phase change, solutions to mixed-integer non-linear optimisation problems are necessary[110;112]. The reader is referred to the articles of Watson et al.[109;110], Kamath et al.[112] and Hasan et al.[107] for a detailed background on multi-stream heat exchanger modelling with/without phase change.

The analogous formulation for MSHX modelling, then, is as follows[109;110]:

$$\sum_{i \epsilon N} \dot{m}_{\text{hot},i}\, C_{\text{p,hot},i}\ (T_{\text{hot,in},i} - T_{\text{hot,out},i}) = \sum_{j \epsilon M} \dot{m}_{\text{cold},j}\, C_{\text{p,cold},j}\ (T_{\text{cold,out},j} - T_{\text{cold,in},j}) \quad (4.9)$$

$$UA = \sum_{d \epsilon D} \frac{H_{d+1} - H_d}{\Delta T_{\text{LM},d}} \quad (4.10)$$

$$\min_{p \epsilon P} \{\text{EP}_{M,p} - \text{EP}_{N,p}\} = 0 \quad (4.11)$$

where equation (4.9) is the heat balance equation, equation (4.10) is the overall conductance equation with UA as an unknown variable, and equation (4.11) is an extended 'pinch point' location function, as defined by Watson et al., to help locate the minimum approach temperature within the heat exchanger comprising multiple hot and cold streams.

P is the set of pinch point temperature candidates amongst all hot and cold streams. For each p belonging to P, the pinch point temperature is defined as follows:

$$T_p = \begin{cases} T_{\text{hot,in},i}, & \forall p = i \epsilon N \\ T_{\text{cold,in},j} + \Delta T_{\text{min}}, & \forall p = j \epsilon M \end{cases} \quad (4.12)$$

where ΔT_{min} is a parameter set by the user. The advanced pinch point location functions are, then, defined by the following for hot and cold streams, respectively:

$$\begin{aligned} \text{EP}_{N,p} = \sum_{i \epsilon N} \dot{m}_{\text{hot},i}\, C_{\text{p,hot},i}\ [&\max\{0, T_p - T_{\text{hot,out},i}\} - \max\{0, T_p - T_{\text{hot,in},i}\} \\ &- \max\{0, T_{\text{hot,min}} - T_p\} + \max\{0, T_p - T_{\text{hot,max}}\}] \end{aligned} \quad (4.13)$$

$$\begin{aligned}\mathrm{EP}_{M,p} = \sum_{i \epsilon N} \dot{m}_{\mathrm{cold},i}\, C_{\mathrm{p,cold},i}\ [&\max\{0, (T_p - \Delta T_{\min}) - T_{\mathrm{cold,in},j}\} \\ &- \max\{0, (T_p - \Delta T_{\min}) - T_{\mathrm{cold,out},j}\} + \max\{0, (T_p - \Delta T_{\min}) - T_{\mathrm{cold,max}}\} \\ &- \max\{0, T_{\mathrm{cold,min}} - (T_p - \Delta T_{\min})\}]\end{aligned} \tag{4.14}$$

where $T_{\mathrm{hot/cold,min/max}}$ are minimum and maximum temperatures of the hot and cold streams.

D is the set of end points of the hot and cold streams, where each d has an associated enthalpy H by virtue of temperatures $T_{\mathrm{hot},d}$ and $T_{\mathrm{cold},d}$. For each d belonging to D, the enthalpies are calculated by the fluid equations of state [113], and the log-mean temperature difference is defined as follows:

$$\Delta T_{\mathrm{LM},d} = \begin{cases} 0.5\ (\Delta T_d + \Delta T_{d+1})\,, & \text{if } \Delta T_d = \Delta T_{d+1} \\ \frac{\Delta T_{d+1} - \Delta T_{d+1}}{\log(\Delta T_{d+1}) - \log(\Delta T_d)}, & \text{otherwise} \end{cases} \tag{4.15}$$

with each ΔT_{d+1} being defined as:

$$\Delta T_d = \max\{\Delta T_{\min}, T_{\mathrm{hot}} - T_{\mathrm{cold}}\} \tag{4.16}$$

If any of the hot or cold streams changes its phase, then the most important modelling consideration is the estimation of the heat capacity flow rate (the product of mass flow and specific heat capacity) of the fluid undergoing phase change. The previous discussion implicitly assumed constant specific heat capacities or, in other words, linear temperature-enthalpy relationships. However, fluids changing phase undergo a very large change in enthalpy over very small or zero temperature changes[3]. As the fluid traverses the path from gaseous (liquid) to two-phase to liquid (gaseous) phases, the specific heat capacity of that fluid changes – dramatically so in the two-phase region. One must, therefore, account for the non-linearity in the change in enthalpy relative to temperature. To do this – as suggested by Watson et al. – each *physical* stream undergoing phase change is subdivided

[3] Air is a mixture (of pure components) and is modelled as such in the present work using CoolProp [113]. Therefore, it undergoes phase change over a temperature change of a little more than 2 [K].

into separate *non-physical* modelling segments to approximate non-linear temperature-enthalpy behaviour via several linear parts. In the simplest case, this means subdividing the temperature-enthalpy region into the superheated (above dew point temperature), two-phase (between dew point and bubble point temperatures), and subcooled (below bubble point temperature) regions[4]. Then, in each segment, the specific heat capacity is determined as the ratio of enthalpy differences to temperature differences. With this modification, the heat exchanger modelling equations described above can be applied to the individual segments to solve for the unknowns.

It should be noted that splitting this regime into more than three non-physical segments yields a better approximation of the temperature-enthalpy curve, but at the cost of more computation time for modelling. In the present work, three non-physical heat exchanger segments are chosen for the single physical stream of air undergoing liquefaction or re-gasification.

Finally, the following assumptions are also made:

- The heat exchanger units are operating in steady-state
- The pressure drop in the pipe work and heat exchanger units is negligible
- Axial heat conduction in the heat exchangers is negligible
- Fouling resistances are negligible (i.e. only resistance to heat flow in the pipe wall is considered)

4.5 A practical implementation

The discussion in § 4.3 highlighted the main components of the hybrid energy storage system; namely, the compressed air and the liquid air stores, reversible heat pump, and compression-expansion devices. Subsequently, in § 4.4, detailed modelling considerations

[4]The dew point and bubble point temperatures of air at 1 [atm] are 81.2 [K] and 78.9 [K], respectively.

for both real fluid behaviour and non-ideal component behaviour were introduced. In this section, the component-to-system link is established and analysed for both the forward and backward conversion processes. The objective is to determine the thermodynamic performance of a practical arrangement of the hybrid system by exergy analysis and understand the distribution of losses across the sub-system components.

4.5.1 Forward conversion process

The mechanism for the conversion of high-pressure air to liquid air in the proposed system is shown in Fig. 4.11. Two separate streams of air from the compressed air tank follows a series of thermodynamic processes resulting in the conversion of one (primary) stream of air to liquid air in its respective storage tank. Thus, the forward conversion process is essentially an air liquefaction unit which, in the present case, comprises a single-stage primary air expander, $E_{\text{pri,air}}$; a multi-stage secondary air expanders, $E_{\text{sec,air-1}}$ and $E_{\text{sec,air-2}}$; a 'near-isothermal' compressor for ambient air, $C_{\text{iso,air}}$; two multi-stream heat exchangers $\text{MSHX}_{\text{pri,air}}$ and $\text{MSHX}_{\text{sec,air}}$; a refrigerant compressor, C_{ref}; a single-stage refrigerant expander, $E_{\text{pri,ref-1}}$; followed by multi-stage refrigerant expanders with heat exchange, $E_{\text{sec,ref-1}}$, $E_{\text{sec,ref-2}}$ and $E_{\text{sec,ref-3}}$.

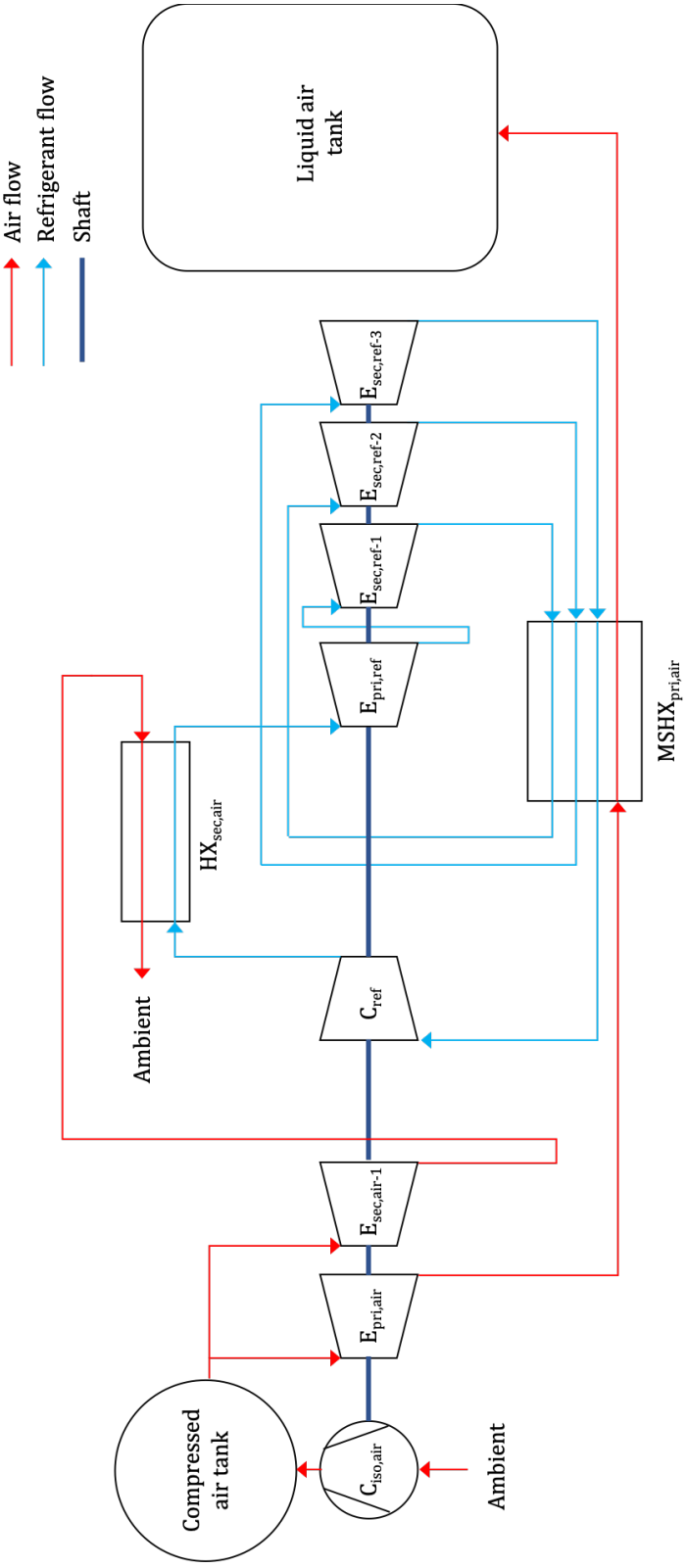


FIGURE 4.11: The forward conversion mechanism (compressed air → liquid air) of the hybrid energy store

The proposed system includes two MSHXs. At the top section of the heat pump, multiple streams of secondary air absorbs heat carried by a single stream of refrigerant at the top section of the heat pump; the secondary air itself is undergoing multi-stage of expansion, of equal pressure ratios, before passing through the heat exchanger. Similarly, at the bottom section of the heat pump, the refrigerant stream undergoes multi-stage expansion, also of equal pressure ratios, before passing through the heat exchanger, multiple times, to help liquefy the primary air stream.

In order to aid with explanation and presentation in Fig. 4.11, the process of multi-stage expansion with successive re-heating or -cooling is simplified by adopting a convention to represent a collection of these items. The abbreviation MEHX$_p$ is employed to mean a provision comprising *Multi-stage Expansion with Heat Exchange in parallel*; Fig. 4.12 clarifies this concept.

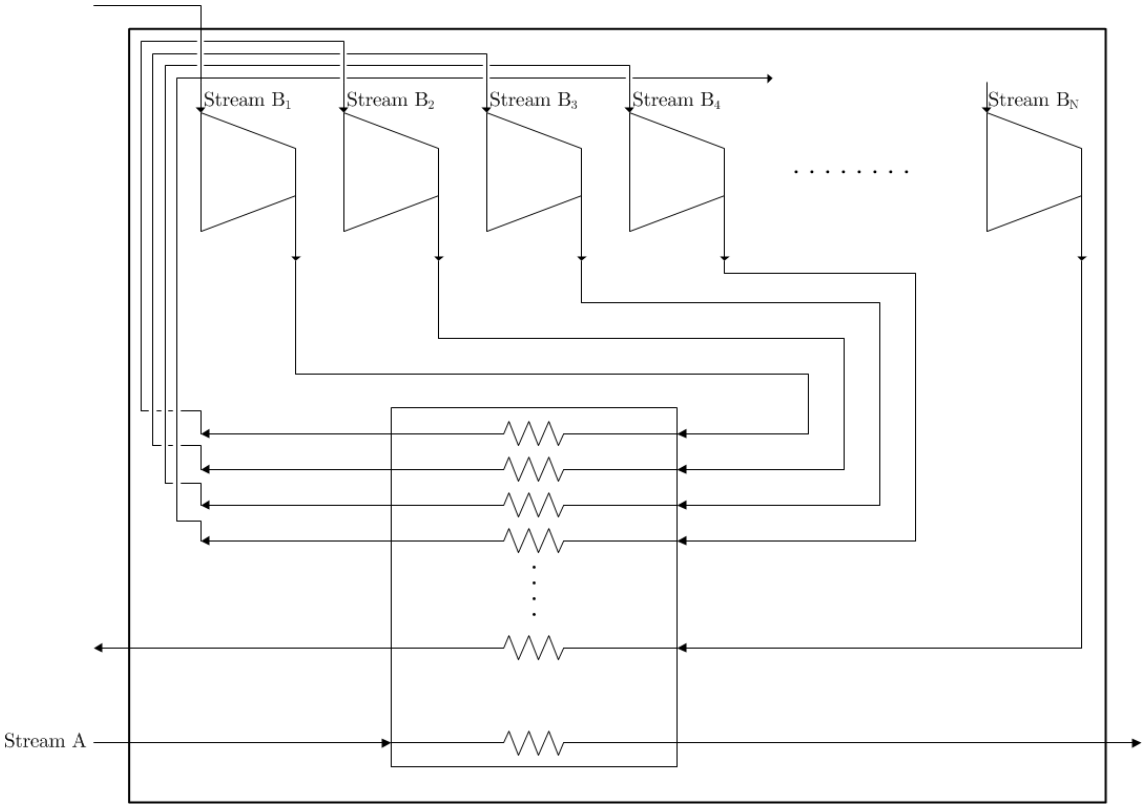


FIGURE 4.12: An MEHX$_p$ unit with N streams of one fluid exchanging heat with *1* stream of another fluid

In the present application, a single heat exchanger would have *one* fluid path carrying primary air (or refrigerant) at atmospheric pressure and N other fluid paths carrying the working fluid of the heat pump (or secondary air) at different pressures but spanning a similar range of temperatures. Thus, two MEHX$_p$ units have been considered – one with multiple refrigerant streams for exchanging heat associated with phase change of air (towards the bottom of Fig. 4.11), and the other with multiple secondary air streams for exchanging heat associated with the compressed refrigerant at the top part of Fig. 4.11.

Assuming, for the sake of argument, that an ideal gas as the operating fluid in a single MEHX$_p$ set is being expanded in equal pressure ratios, the temperature ratio across the MSHX will then be:

$$\frac{T_{\text{out}}}{T_{\text{in}}} = \left(\frac{P_{\text{in}}}{P_{\text{out}}}\right)^{\frac{N(1-\gamma)}{\gamma}} \tag{4.17}$$

For the heat-exchange element of a single MEHX$_p$ set to be thermodynamically reversible, one requirement is that the specific heat, C_{p}, of the working fluid being expanded should be independent of pressure. It is also necessary that the variation of C_{p} with temperature for one fluid should be in proportion to the variation of C_{p} with temperature for the other fluid. This cannot generally be achieved exactly with real fluids, as in the proposed system, but by deploying several MEHX$_p$ sets in series, one may approach full reversibility arbitrarily closely.

4.5.2 Backward conversion process

In the backward conversion process, all fluid flow directions (cf. Fig. 4.11) are reversed. Machinery functions are also reversed: the heat pump now operates as a heat engine, compressors (expanders) operate as expanders (compressors)[5], and MEHX$_p$ units operate as *Multi-stage Compression with Heat Exchange in parallel*, abbreviated as MCHX$_p$. Air from the atmosphere is drawn in by the multi-stage secondary air compressor, which initially passes through the secondary air MCHX$_p$. The multiple streams of secondary air reject heat into the refrigerant stream at the top-section of the heat engine, which in effect

[5]See § 4.6 .

provides the heating capacity for the transition of liquid air to cooler, gaseous air at the bottom-section of the heat engine, before compression to near-ambient temperature in the primary air compressor.

The primary air stream, which is cooled down to sub-bubble point at ambient pressure in the forward conversion process, is stored in a thermally insulated tank. With effective insulation, energy losses to the environment can be as low as 0.05% by volume/day [88]. In the analysis that follows, exergy losses by leakage is assumed to be negligible. In other words, the liquid air begins its (backward) conversion to compressed air at the temperature it achieved towards the end of the forward conversion process. In reality, this energy loss is non-negligible and the temperature of the liquid air rises from its storage temperature, with the effect being more pronounced the longer the duration of storage.

4.6 Results and discussion

The aim of this section is to report, and comment on, the thermodynamic performance results of the system presented in § 4.5. This is done in two parts:

- A notional system configuration, i.e., the arrangement of system components with the respective number of stages of expansion/compression/heat exchange, as presented in Fig. 4.11 is analysed for a given set of parameters. The performance of the backward conversion process is also summarised.
- The sensitivity of the thermodynamic performance to key system parameters is then analysed. The parameters considered for the sensitivity analysis are the starting pressure of compressed air in the tank, the number of stages of expansion (compression) in the forward (backward) conversion process and the maximum pressure ratio in the heat pump (engine)[6].

[6]Commentary is provided only on the forward conversion process as similar arguments also apply in the backward conversion process.

4.6.1 Case study

The parameters of the hybrid system in the present analysis are pressures of all fluids, mass flow of primary air, mass flow of refrigerant and the minimum approach temperature within the heat exchangers (i.e. the MSHX for primary air liquefaction and the two-stream heat exchanger for secondary air and refrigerant streams). The unknown variables are therefore the temperatures of the fluids, the thermal conductance (i.e. the product of the overall heat transfer coefficient and surface area) of the heat exchangers, and the mass flow of secondary air. Based on the governing equation(s) for each system component described in § 4.4, a 'residual' term for each of those equations is defined. Here, a residual is implied to be the difference between the two sides of an equation that is to be solved in order to obtain the unknown decision variables.

The 'whole system' model involving the governing equations of all system components and fluids is implemented in a MATLAB® runtime environment. The default built-in solver for a system of non-linear equations, *fsolve*, is used to solve for the unknown decision variables. This iterative solver minimises the sum of squares of residuals of the system of governing equations. Solving for the unknowns in the forward (and backward) conversion process takes approximately 19 minutes using a computing node of two 2.7GHz cores and 8GB of RAM. The relatively high computational time is primarily due to non-linearity present in the equations of state of real fluid properties and non-smoothness present in the equations of Watson et al.'s[109;110] multi-stream heat exchanger formulation.

For the case study, it is assumed that a flow of compressed air starting at 50 [bar] is converted to liquid air (and back) at atmospheric pressure. Another stream of air originating from the compressed air tank at the same pressure and temperature is diverted the top of a heat pump responsible for air liquefaction. The primary air stream undergoes single stage expansion before passing through a MSHX for liquefaction; similarly, the secondary air stream also undergoes single stage expansion. The refrigerant (or the working fluid), chosen to be hydrogen in the present system, undergoes multi-stage expansion and heat exchange to provide cooling for the primary air stream. Hydrogen is one of a select few of

fluid that remains gaseous air liquefaction temperatures. Moreover, it has excellent heat transfer characteristics and is available relatively cheaply for industrial applications. A noteworthy alternative is helium, which also has the same excellent, albeit slightly lower, thermophysical properties as hydrogen (thermal conductivity is 16% lower, whilst isobaric specific heat capacity is nearly 3 times lower). However, it is worth noting that helium is not corrosive like hydrogen and may prove a better alternative overall considering full system costing (which is out of scope of the present thesis).

The parameters used in the case study are listed in Table 4.1.

TABLE 4.1: Parameters for the overall system

System parameters for case study	
Ambient temperature	290 [K]
Ambient pressure	1 [atm] (1.01325 [bar])
Pressure of air in compressed air store	50 [bar]
Pressure at the top-section of the heat pump	55 [atm]
Temperature of air in compressed air store	290 [K]
Mass flow rate of primary air	1 [kg/s]
Compression ratio of C_{ref}	55
Expansion ratio of $E_{\text{pri,ref}}$	2.75
Number of stages in $E_{\text{sec,ref}}$	3
Number of streams in $\text{MSHX}_{\text{pri,air}}$	4
Isentropic efficiency of air expander sets	97 [%]
Isentropic efficiency of refrigerant expander sets	97 [%]
Isentropic efficiency of refrigerant compressor sets	95 [%]
Efficiency of near-isothermal air compressor	90 [%]
Conversion efficiency of compressed air to and from electricity	85 [%]
Mass low rate of refrigerant	0.33 [kg/s]

The results of the case study are shown in Fig. 4.13. The state of the fluid in terms of its mass flow, pressure and temperature is shown at each point of interest in the system. The

quantities obtained from the iterative solver are shown in green font, with the parameters shown in black font.

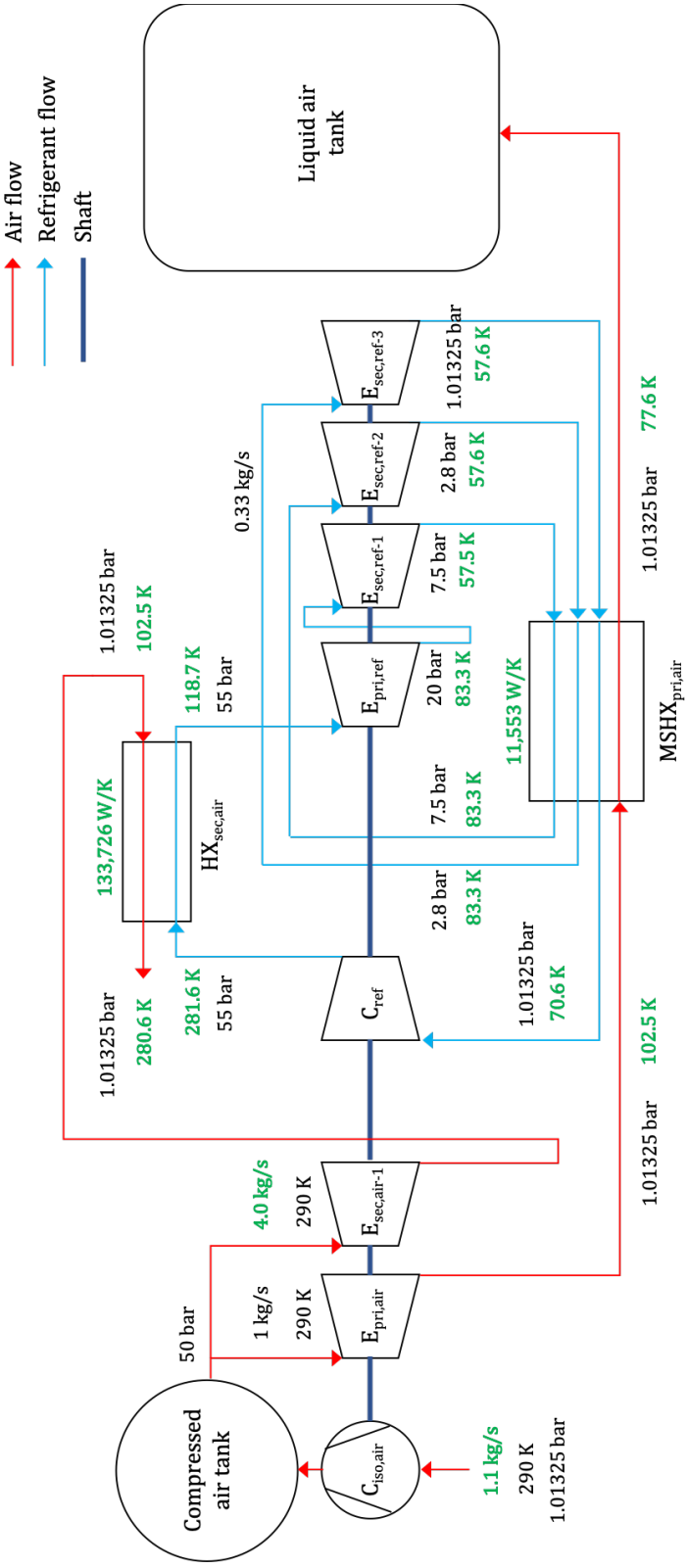


FIGURE 4.13: The thermodynamic state of the forward conversion system based on parameters defined in the case study

As seen from the figure, primary air at 50 [bar] and 290 [K] expands via single-stage expansion to around 103 [K], before passing through the MSHX at the bottom section of the heat pump to undergo liquefaction. As discussed earlier, during phase change the air releases (or absorbs) a large quantity of heat over very small ranges of temperature. Employing multiple streams of a refrigerant to help liquefy the air is an established industrial technique for achieving compact, efficient and economic heat exchange. In the present application, three streams of hydrogen absorb heat from primary air, before being compressed at around 71 [K] and 1 [atm] to around 282 [K] and 55 [atm]. Meanwhile, secondary air – also at 50 [bar] and 290 [K] – expands to around 103 [K] and absorbs heat from the hot refrigerant at the top section of the heat pump before being vented to the atmosphere at just below ambient temperature. The conversion process results in the primary air stream being liquefied to around 77 [K] at 1 [atm].

To gain insight into performance of the heat exchangers, composite curves are plotted in Fig. 4.14 for both the primary air MSHX and secondary air heat exchanger analysed as part of the case study. The construction of composite curves involves dividing the temperature axis into intervals based on the inlet and outlet temperatures of the various hot streams (red lines in the figure) and cold streams (blue lines) and then adding together enthalpy values of those hot and cold streams in each temperature interval. Fig. 4.14 therefore shows cumulative enthalpies against corresponding temperatures, resulting in one curve for the hot stream and one curve for the cold stream, regardless of the number of physical hot/cold streams present. For illustration, Fig. 4.14(b) shows the hot refrigerant stream cooling down from around 281 [K] to 120 [K], with the cooler secondary air stream, picking up the heat from around 100 [K] to 280 [K].

The hot and cold composite curves in the figure overlap each other horizontally indicating that all of the heat can be recovered. This is also the maximum amount of heat that could be recovered – if the curves did not overlap, then additional 'utilities' would be required to satisfy heating or cooling requirements. The horizontal overlap (distance) between the curves, therefore, defines the heat integration limit. Similarly, the economic limit is

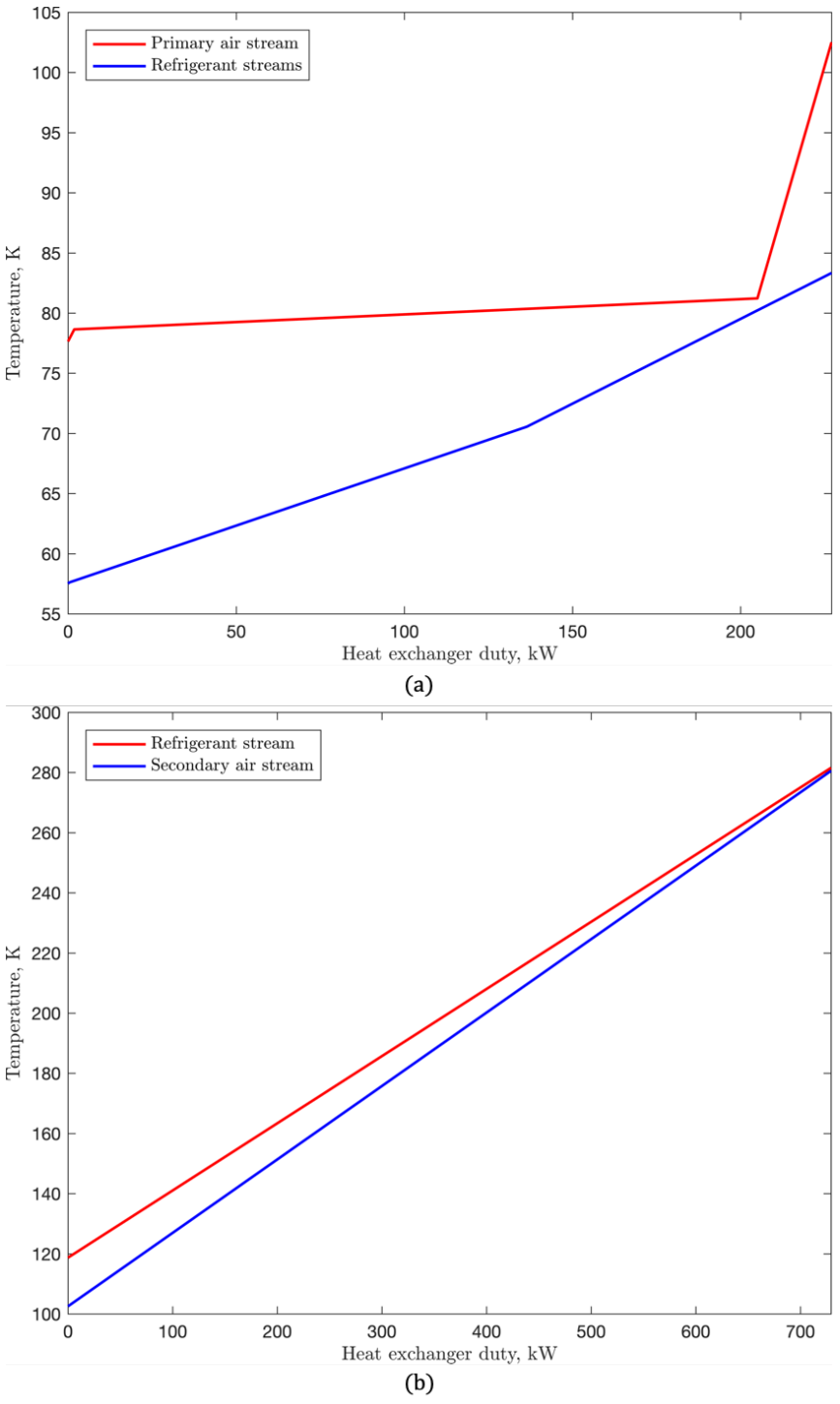


FIGURE 4.14: Composite curves of (a) the primary air MSHX and (b) the two-stream secondary air heat exchanger

reached when the vertical distance between the curves is equal to the minimum approach temperature, $\Delta T_{\min}$ (as the heat exchanger cannot bring the temperature of the streams any closer for the given heat exchanger type or cost spent), and the thermodynamic or physical limit is reached when the vertical distance between the curves is equal to zero. Therefore, a cross-over of the curves would indicate infeasible heat transfer.

It is therefore easily observed from Fig. 4.14 that the secondary air heat exchanger is of high effectiveness because the temperature difference between the hot and cold composite curves does not vary significantly across the range of enthalpy transactions. In other words, for the given minimum approach temperature and chosen mass flow rates of air and refrigerant, and their thermodynamic properties, the heat capacities are close to being balanced, thus leading to relatively low exergy losses.

On the other hand, as shown in Fig. 4.14(a), the temperature-enthalpy composite curve for the primary air MSHX is clearly non-linear. In particular, it is evident that a piece-wise linear function (three pieces) is used to approximate the cooling of the primary air from around 102 [K] to 77 [K]. Kinks on the curve are observed at the dew point and bubble point temperatures of the air (because the piece-wise linear function subdivides the segments at these temperatures), with a large specific heat capacity (i.e. the reciprocal of the slope of the curve) associated with a very small temperature range in the two-phase region. In the present case study, three non-physical segments were chosen to model the phase change of primary air; choosing more non-physical segments would make the hot composite curve smoother. even with a small minimum approach temperature, the primary air MSHX will have much larger exergy losses because the economic limit is reached somewhere within the heat exchanger, with the rest of the hot and cold profiles poorly matched in terms of heat capacities. Therefore, temperature difference along the length of the heat exchanger will be uneven and larger than that observed at the pinch point. This information can be used by a chemical process engineer to address key design considerations on the the type of fluids used, its mass flows, operating regimes, etc. Whilst this exercise is out of scope of the present thesis, sensitivity analysis presented later draws out noteworthy trends.

The exergy efficiency of the forward conversion process, measured as a simple ratio of output flow exergy to input flow exergy, is calculated as:

$$\eta_{\text{ex,F}} \coloneqq \frac{\dot{B}_{\text{LA}} + \dot{W}_{\text{net,out}}}{\dot{B}_{\text{CA}}} \tag{4.18}$$

Similarly, for the backward process, the exergy efficiency is defined as:

$$\eta_{\text{ex,B}} \coloneqq \frac{\dot{B}_{\text{CA}}}{\dot{B}_{\text{LA}} + \dot{W}_{\text{net,in}}} \tag{4.19}$$

The roundtrip efficiency of the hybrid storage system is then defined as the product of forward and backward conversion efficiencies. Table 4.2 summarises the performance of the forward and backward conversion processes. In the forward conversion process, any excess shaft power is used to drive a near-isothermal air compressor, $C_{\text{iso-air}}$, which sucks in air from ambient conditions and generates 'feedback' flow exergy of compressed air (cf. Fig. 4.11).

TABLE 4.2: Thermodynamic performance summary of the forward and backward conversion processes for air starting at 50 [bar]

Forward conversion process	
Temperature of liquefied air	77 [K]
Forward conversion efficiency	66 [%]
Backward conversion process	
Temperature of compressed air returned to store	286 [K]
Backward conversion efficiency	67 [%]
Roundtrip efficiency of the hybrid storage system only	44 [%]

It should be noted that the exergy efficiency measure defined above does not capture the actions of borrowing electricity from, and then returning it to, the grid. Those actions involve power conversion machinery before that energy is stored and released, and therefore incurs additional energy penalties.

It is useful to look at the distribution of exergy losses across system components to gain insight into where potential improvements could be made to enhance overall performance. To do this, we rely on calculations of flow exergy, which is determined using (4.1). The exergy loss in each component is then evaluated using (4.20):

$$\dot{B}_{\text{loss}} = \dot{B}_{\text{in}} - \dot{B}_{\text{out}} \tag{4.20}$$

For example, in a compression device, flow exergy contained in the fluid at the inlet to the compressor and the rate of work into the device constitute $\dot{B}_{\text{in}}$, whereas flow exergy at the outlet to the compressor constitutes $\dot{B}_{\text{out}}$. In a heat exchanger, stream(s) of fluid which release and absorb exergy have to be identified before calculating the losses as their difference.

The distribution of exergy losses across system components for the forward conversion system is shown in Fig. 4.15. It is easily observed that the three largest contributors to the overall exergy loss are the primary air MSHX, single-stage secondary air expander and the secondary air two-stream HX. The relatively high exergy loss in the primary air MSHX can be attributed to the fact that the minimum approach temperature is found inside the MSHX (see Fig. 4.14), implying that temperatures at the ends of the heat exchanger cannot be brought closer together any further. The secondary air expander is single stage, with a relatively high mass flow (ca. 4 [kg/s]) required to provide cooling for the hot refrigerant stream in the two-stream heat exchanger. Increasing the number of expansion stages (and therefore the number of heat exchanging streams) would be one way of reducing exergy losses in these machines. In a bid to explore this further, sensitivity analysis to key system parameters is performed in § 4.6.2.

The modelling is technology-agnostic in terms of the type of heat exchanger or compression/expansion machinery. However, for the purposes of costing heat exchangers – see Chapter 6 – its type must be specified (as costs are dependent on this). Therefore, wherever a two-stream counterflow heat exchanger is modelled, it will be assumed that this heat exchanger is of the finned shell-and-tube type. This heat exchanger type also has

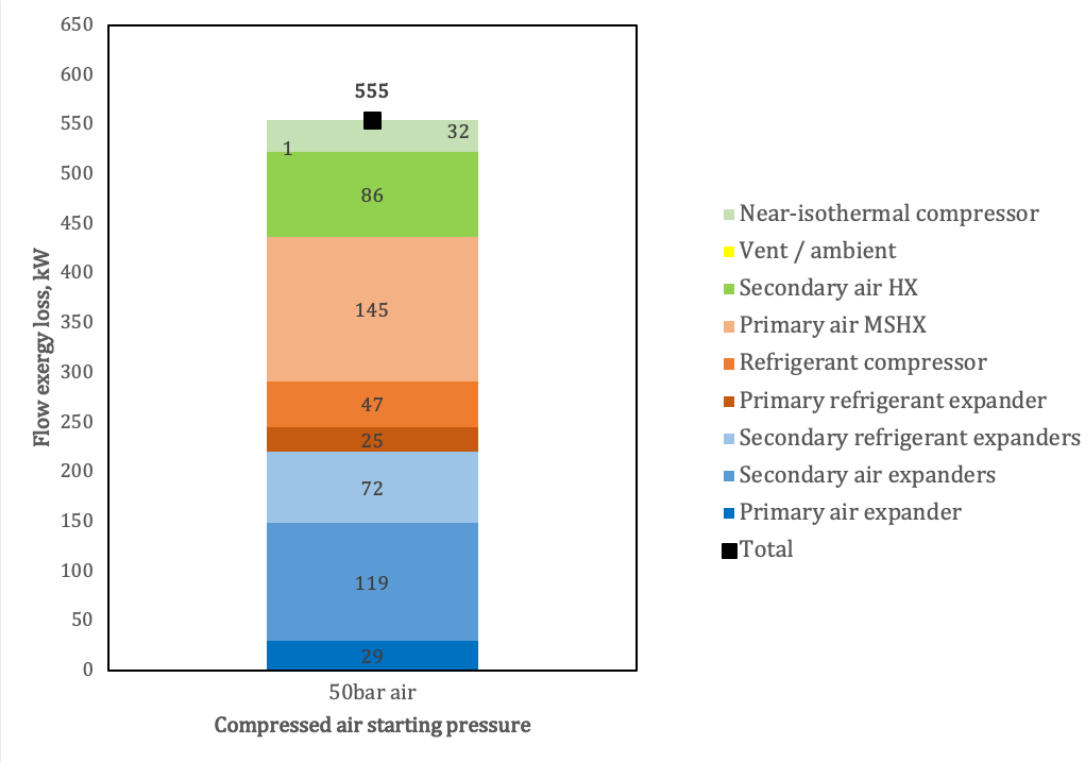


FIGURE 4.15: Distribution of component exergy loss in forward conversion system considered in the case study

the ability to withstand high pressures of fluids. Compact heat exchangers, such as the plate-fin type[107], are commonly employed in cryogenic processes where liquefaction is involved, or when there is a need for highly effective heat exchange with minimal exergy losses. In the present work, it will be assumed that the MSHX is of the plate-fin type. Finally, reversible compression-expansion devices, such as positive-displacement machines (screw/scroll type and reciprocating piston type), could be used in the proposed system. This idea is not new and has been investigated by a few parties in the past (see for e.g. Oralli et al.[116] and Mathie et al.[117]). With such equipment, operation can be carried out in both directions (i.e., compression as well as expansion), with fluid flow directions reversed and minimal modifications to the equipment. Therefore, as long as the number of stages of compression/expansion remain the same in both the forward and backward conversion processes, the same devices can be used for compressing and expanding fluids, which can be particularly advantageous because of savings realised in capital costs.

4.6.2 Sensitivity analysis

Central to the results presented in the analysis are the values chosen for the starting pressure of compressed air, the number of stages of refrigerant expanders and the number of stages of secondary air expanders (or equivalently compressors in the backward process). These affect losses in the expansion devices, the efficiency of heat exchange, and the mass flow of secondary air required.

Consider the set of refrigerant expanders in the forward conversion process. Increasing the number of stages of expansion reduces the pressure ratio, and so reduces the drop in outlet temperature, across each stage. Because of this, the specific work output per stage and thus the exergy loss per stage are also reduced. The refrigerant passes through the MSHX (after each expansion stage) effectively multiplying the heat capacity by the number of stages (for a given mass flow). An important point to note is that increasing the number of stages reduces the required refrigerant mass flow to provide the cooling needed for air liquefaction. However, the drop in required mass flow is not proportional to the increase in number of expansion stages, because the specific enthalpy difference across each heat exchanger stream reduces as the number of stages increases. Overall, since the required mass flow is reduced, the rate of work output from a multi-stage expander and, therefore, its exergy loss are also reduced compared to a single-stage expander.

This is clearly observed in Fig. 4.16., which shows that increasing the number of refrigerant expander stages from 1 to 3 (the first three columns from the left-hand-side of the figure to the right-hand-side of the same figure) reduces the overall exergy loss in the secondary refrigerant expanders. The exergy loss in the primary air expander is unchanged across these system configurations as the expansion process is single-stage throughout. However, whilst the secondary air expansion in the three leftmost columns remains one stage, the flow exergy loss reduces as the number of refrigerant expansion stages increases. This is because a greater number of refrigerant expansion stages implies lower required refrigerant mass flow, which in turn requires lower secondary air mass flow to provide cooling at the top section of the heat pump.

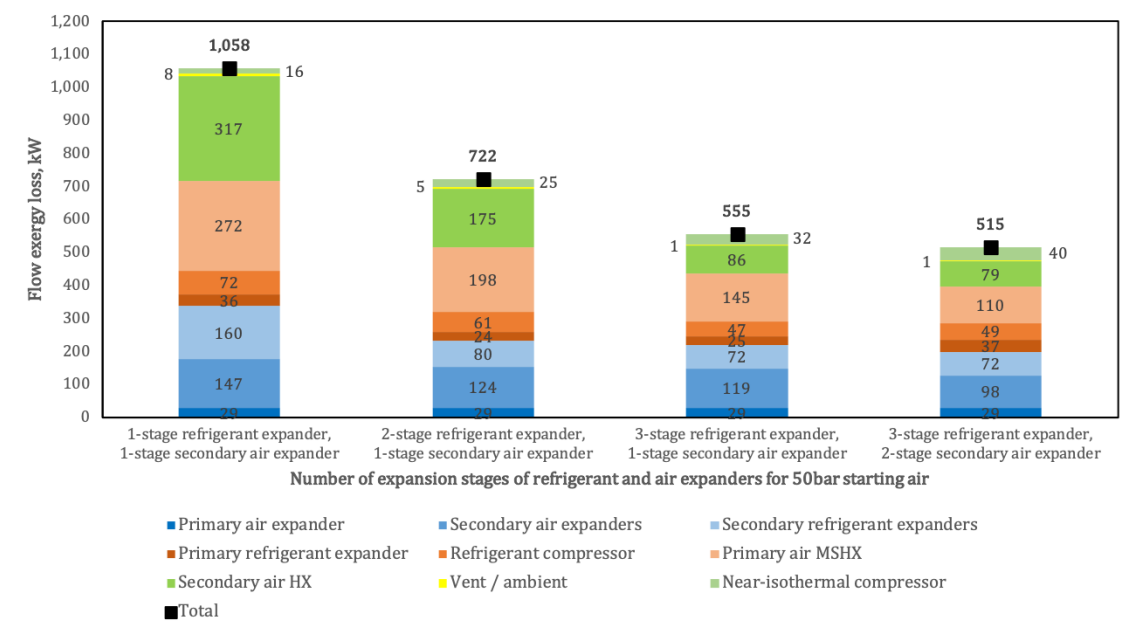


FIGURE 4.16: Sensitivity of exergy loss in forward conversion process to number of stages of expansion

Similarly, the number of stages of secondary air expansion can also be increased. The effect of doing so is shown in the fourth column (from the left-hand-side) of the figure, where a further decrease in overall exergy losses is observed.

The above trend in exergy loss reduction with the increase in the number of expansion stages translates to an increase in the efficiency of the forward conversion process. Similarly, in the backward conversion process, having the same number of stages of *compression* has a positive impact on the efficiency. The product of forward and backward conversion process efficiencies, defined here to the 'roundtrip' hybrid storage system efficiency, therefore increases. This is found to be 21% for a system with 1-stage refrigerant expansion and 1-stage secondary air expansion, increasing to 49% for a system with 3-stage refrigerant expansion and 2-stage secondary air expansion.

The sensitivity of system performance (both in terms of total exergy loss and efficiency) to starting pressure of compressed air in the tank is analysed next. Here, the system configuration comprises three secondary refrigerant expansion stages and two secondary air expansion stages (and all other equipments as in Fig. 4.11). As shown in Fig. 4.17,

beginning the process with a higher pressure of compressed air lowers the total exergy loss because it primarily relieves duty in the both the primary and secondary air MSHXs. Consequently, the *roundtrip* conversion efficiency increases from around 40% (20 [bar] starting air) to around 50% (80 [bar] starting air).

An important point to note is that in the present analysis an upper limit of 80 [bar] is set for the starting pressure of compressed air. A higher pressure would – via single-stage expansion at the assumed isentropic efficiency – would liquefy air at the expander outlet. Whilst this can be practically achieved via crogenic expanders, it creates additional problems such as cavitation damage in the expanders [114]. Furthermore, expanders capable of handling two-phase flow – whilst commercially available – are less mature and therefore cost relatively more than single-phase expanders [115]. A constraint on air expansion is therefore imposed to maintain a single-phase state at the outlet of the expanders.

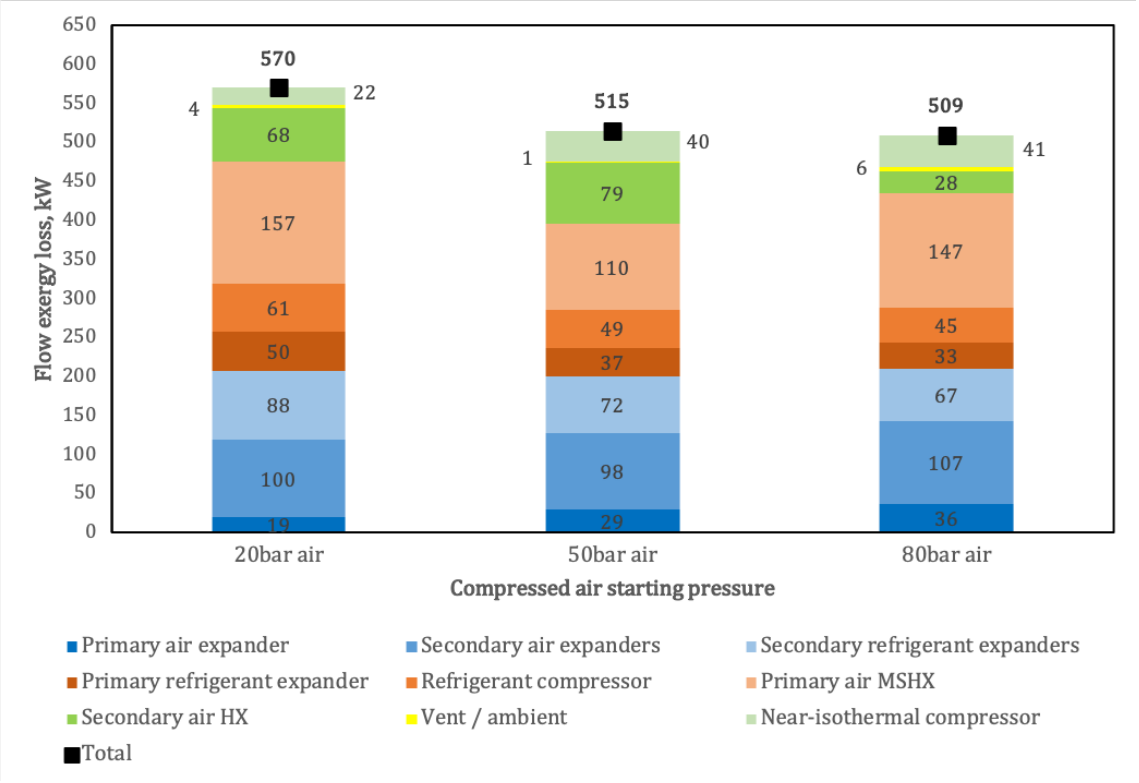


FIGURE 4.17: Sensitivity of exergy loss in forward conversion process to starting compressed air pressure

4.7 Conclusions

This chapter has presented the thermodynamic assessment of a new compressed air storage design supplemented with liquid air storage. Where geological constraints prevent the deployment of underground compressed air storage technologies, the energy storage capacity of relatively expensive aboveground steel-tank based compressed air schemes may be extended by the provision of liquid air storage. Liquid air possesses higher exergy storage density than compressed air, it does not require a pressurised vessel for storage and it is free from geological constraints. However, its power recovery efficiencies via various strategies, including the one presented in this chapter, are relatively lower than its compressed air counterpart. The system is therefore arranged such that all energy transactions with the grid occur via the compressed air store.

From the macro-level analysis presented here, it is observed that the roundtrip conversion efficiency for transforming ambient temperature compressed air at 50 [bar] to ambient pressure liquid air at a temperature just below its bubble point is approximately 44,[%]. However, by changing the system configuration to include more stages of expansion, multi-stream heat exchange, and a higher compressed air starting pressure (capped at 80 [bar] for reasons discussed in § 4.6.2), the roundtrip efficiency can be improved to around 50 [%].

Whilst the modelling and analysis carried out in this chapter avoids specifying detailed design of the system components involved, some commentary is provided to indicate the possible equipment type of heat exchangers, compressors and expanders that could be used in the proposed hybrid system. This also forms the basis of the capital costing exercise of this system (and the other compressed air storage methods investigated in this thesis) in Chapter 6.

Moreover, whilst sensitivity analysis has been carried out to test the impact of key parameters on overall system efficiency, the best solution (i.e., with the highest roundtrip efficiency) arrived at in this chapter cannot be guaranteed to be 'optimal' (e.g. in terms

of cost). In order to address the question on optimal system configuration, and so investigate the trade-off between cost and system efficiency whilst accounting for general design trends, so-called Pareto fronts must be generated. These fronts would comprise the leading-edge solutions with all other (suboptimal) system configurations lying either to the right or below the curve (i.e., the Pareto front). This is a complex area, out of scope of the present thesis, but an important query that is worth addressing in future research.

Further research could also look into determining the dynamic characteristics of this system to provide necessary insight for carrying out detailed engineering design efforts and tailoring it to local electricity market and regulatory mechanisms ultimately to maximise profits.

Chapter 5

Analysis of flexible and rigid vessels for underwater compressed air energy storage

5.1 Introduction

As discussed in Chapter 2, high pressure air is stored in reservoirs that exhibit one of two fundamentally different characteristics. One is constant volume, or *isochoric*, air storage where the volume occupied by the air in the vessel remains nearly constant irrespective of the total mass of stored air. This is an approximation of real behaviour of 'rigid' tanks or underground caverns where the change in volume of stored air between the extremum pressures is often so small that it is ignored. The other is constant pressure, or *isobaric*, air storage where the pressure inside the vessel is insensitive to the total mass of stored air and thus remains nearly constant. This, too, is an approximation of real behaviour where pressure variation within the store is negligibly small.

The useful work that is recoverable from an isochoric store is smaller than an equivalent isobaric store. This is because of some 'cushion gas' that remains in the isochoric vessel

when cycled between the maximum and minimum pressures, and because the last few grammes of air to leave the store emerges at a pressure significantly lower than the first few grammes. Moreover, in some CAES designs with isochoric stores, as is the case with existing CAES plants where the air is stored in underground salt caverns, the air pressure is reduced by throttling when exiting the cavern to the rated pressure of the expansion device. This further reduces the useful work that could be recovered. Although variable pressure operation during power recovery can avoid throttling losses, this necessitates the use of more complex machinery which inevitably incurs higher capital costs.

Isobaric vessels, on the other hand, can be optimised for operation at a design point by virtue of near identical pressure rating for the compression and expansion devices. As seen in Chapter 3, both pressure and temperature vary in isochoric containers giving rise to additional thermal stresses, thereby complicating their mechanical response. Isobaric containers avoid temperature fluctuations altogether and therefore typically experience relatively lower stress variations.

This chapter focuses on CAES systems that employ isobaric air stores by exploiting the hydrostatic pressure in underwater or deep sea environments. More specifically, this chapter deals with the structural behaviour of underwater storage vessels and it lays the groundwork for further analysis of underwater storage vessels with rigid walls. The load carrying requirements of underwater compressed air storage vessels are greatly reduced relative to air containments at the surface because the hydrostatic pressure counteracts the force exerted by the compressed air. Thus, the most important advantage of storing compressed air underwater is the simplified design of the storage vessel compared to that which stores pressurised air without the aid of hydrostatic pressure.

It should be noted that constant pressure characteristics for air storage can be achieved by various other means, for instance, via hydrostatic head between an underground cavern and a shuttle pond at the ground level[118] or via suitable fluid displacement mechanisms for aboveground pressurised air tanks[119]. However, these systems are not explored here.

We begin by discussing, briefly, the development of flexible vessels for underwater CAES. Based on the insights gained by researchers from the design of flexible vessels, structural analysis of rigid vessels for underwater CAES is performed, where it is shown that bending loads arise in the near-isobaric operation and that the resulting stress fields are non-trivial. Underwater, or deep sea, pumped hydroelectric storage is an alternative to underwater CAES technologies. Therefore, the rigid vessels for underwater pumped hydro storage technology is also briefly considered in the present chapter, and contrasted with the use of rigid vessels for underwater CAES. Finally, some conclusions are drawn.

5.2 Underwater compressed air energy storage

The storage of pressurised air in an underwater vessel greatly reduces the structural design requirements of that vessel, since this mechanism allows the water to provide additional support by reacting the pressure exerted by the compressed air on the inner wall of the vessel. These structural requirements are minimised when the pressure of the air inside the vessel is nearly the same as that in the surrounding water body, so that the structure carries only the forces due to net buoyancy and relatively small differential pressures across the wall of the vessel. Ultimately, the structural simplicity of the vessel presents the potential to achieve low costs of manufacture, installation and maintenance over its lifetime.

The amount of recoverable energy per unit of storage volume increases with depth, because the hydrostatic pressure – equal to the pressure of the stored air – increases with depth. Therefore, to maximise power recovery for a given volume of the vessel, it is beneficial to anchor the vessel as deep as practically possible. As seen from Fig. 5.1, the amount of energy that is recovered from compressed air depends strongly on the management of heat, i.e. whether the air is reheated before or during expansion; at a depth of 500 [m], the density of recoverable energy will be between approximately 5.6 [kWh/m^3] (for isothermal expansion) and 10.3 [kWh/m^3] (for adiabatic expansion where the final exhaust temperature is identical to that at ambient conditions).

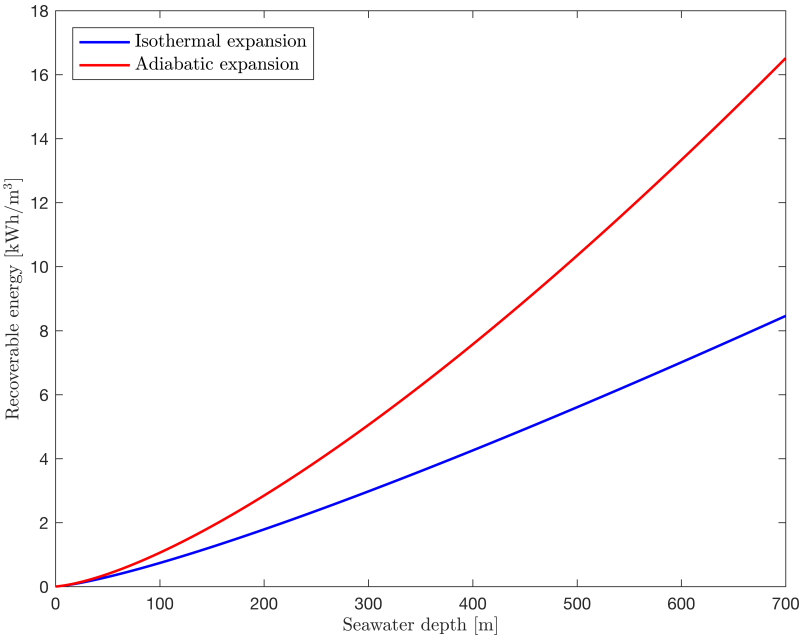


FIGURE 5.1: Recoverable energy from an underwater compressed air storage reservoir

On the other hand, the net buoyancy force on a vessel of given volume containing air within it can be considered to be independent of depth and the state of the surrounding water. This is calculated as:

$$f_{\text{buoyancy}} = V_{\text{vessel}} \left(\rho_{\text{water}} - \rho_{\text{air}}\right) g \tag{5.1}$$

where V_{vessel} is the volume of the vessel, ρ_{water} and ρ_{air} are the mean densities of surrounding water and air inside the vessel, respectively, and g is the acceleration due to gravity. Due to the higher compressibility of the air relative to the surrounding water, the net buoyancy force will decrease slightly with depth. This effect is disregarded in the present work due to its relatively minor impact on net buoyancy. It should also be noted that (5.1) ignores the mass and volume of the structural material.

Air storage vessels for underwater CAES are characterised by either flexible or rigid walls. Whilst flexible vessels for underwater CAES have been researched extensively [120]- [126], rigid vessels have received less attention. As will be discussed in a later section, depending on whether the vessels are open or closed at the bottom, water displacement mechanisms may be allowed. This is particularly advantageous in rigid vessels as it ensures

near-isobaric operation, and prevents any thermal contribution to the overall mechanical response. However, in both flexible and rigid vessels, the unintended build-up of water inside the vessel must be prevented as failure to do so will reduce the overall storage capacity. Moreover, a crucial requirement of any deep sea structure is to retain its structural integrity over long periods (e.g. 50 years), with little need for maintenance. Thus, the manufacture and deployment of underwater vessels require great care to ensure reliable operation over their lifetimes.

In the following, an overview of the analysis of flexible vessels for underwater CAES is presented first. Then, rigid vessels for underwater CAES are analysed.

5.2.1 Overview of flexible vessels for underwater compressed air energy storage

Whilst the first proposal for a flexible vessel, or *Energy Bag*, to store compressed air underwater can be traced back to 1989 by Laing[127], Pimm and Garvey[120]-[125] have studied Energy Bags since 2007 leading to the manufacture and testing of various prototypes. Energy Bags for underwater CAES are made of coated fabric material, which have structural reinforcements in the form of meridional straps to resist the net buoyancy force. A major advantage of these containers is that bending loads are non-existent, and the fabric carries all loads in tension. Fig. 5.2 shows two prototype designs of the flexible vessel proposed by Pimm and Garvey: Fig. 5.2(a) shows a 1.8 [m] diameter Energy Bag being tested at the University of Nottingham, and Fig. 5.2(b) shows a 5m diameter prototype that was tested at 25 [m] seawater depth at the European Marine Energy Centre in Orkney[123]. Pimm and Garvey's design of the Energy Bags involved attaching the air pipeline, for carrying compressed air between the vessel and power conversion devices, to the top of the vessel to minimise the risk of port blockage by unwanted entry of water into the vessel.

A detailed set of requirements for the commercial feasibility of flexible CAES vessels in grid-scale applications are described by Pimm and Garvey[123]; these include structural reliability and performance predictability at various scales, cost-effective manufacturing,



(a) 1.8m diameter prototype



(b) 5m diameter prototype

FIGURE 5.2: Energy Bag prototypes designed and tested by Pimm and Garvey [123]

installation, maintenance and decommissioning, and a tool which enables straightforward modelling and characterisation of the vessel architecture.

It is helpful to think of the Energy Bag architecture in terms of its two main components: an inflatable bladder, which acts as a separating surface between the stored air and the surrounding water; and a set of meridional tendons encompassing the bladder, which bears the overall buoyancy and pressure loads. The rationale behind separating the roles of the bladder material from that of the tendons lies in the enhanced flexibility of vessel design: the tendons can be optimised to resist the loads, and the bladder material can be optimised for effective air tightness.

Pimm and Garvey devise three strategies for obtaining the deformed shapes of an Energy Bag for various fill levels of compressed air. These are:

- a system of coupled ordinary differential equations (ODEs) to model an inextensible axisymmetric membrane
- finite element analysis to model the cross-section of an axisymmetric Energy Bag with cable elements
- three-dimensional finite element analysis to model a cable-reinforced membrane

Detailed description of the methods can be found in the doctoral thesis by Pimm [122]. We use the coupled ODE method to reproduce the deformed shapes of Energy Bags because of its relatively straightforward implementation. Fig. 5.3 shows the natural shape, i.e. purely meridional loading, of a bag fully filled with compressed air anchored at a depth of 500 [m]. The radius at the base is zero (the base is sealed), and the differential pressure at the base is also zero.

However, since the base of the bag is sealed, the bag can accommodate compressed air fill levels such that the differential pressure at the base is either negative (under-filled with air) or positive (over-filled with air). This is illustrated in Fig. 5.4. A bag with underpressurised base takes a taller, slender shape, whilst a bag with overpressurised base

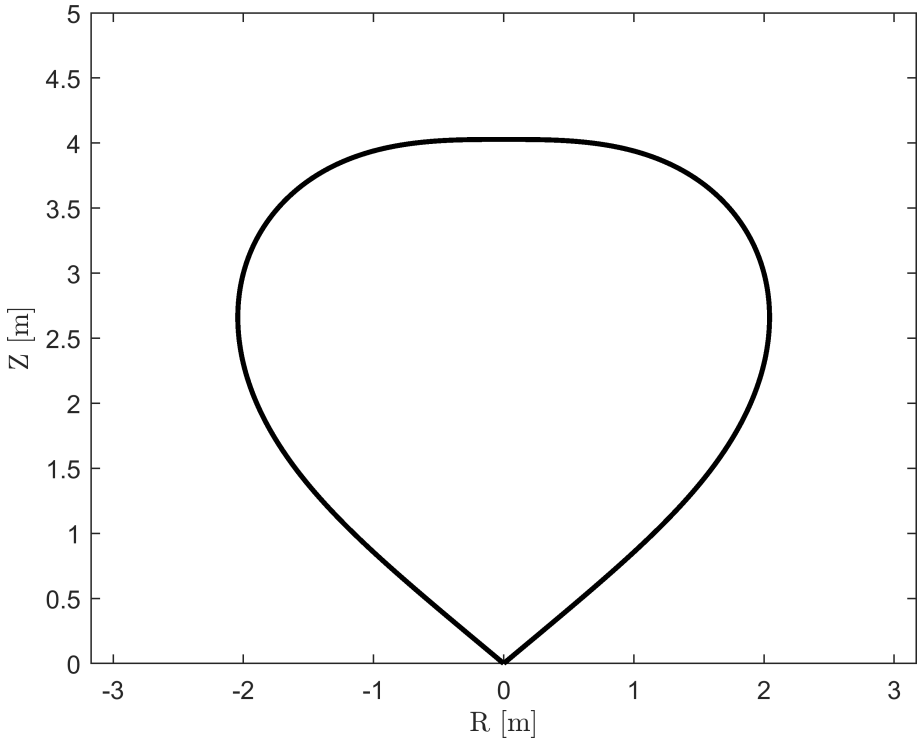


FIGURE 5.3: Energy Bag with single point of anchorage where differential pressure at the base is equal to zero

approaches a stubbier pumpkin shape. It should be noted that in an under-filled bag, the amount of air at the base of the bag is negligible. Therefore, the bag collapses to near-zero cross-section at locations where the differential pressure is not positive.

Energy Bags with non-zero base radius can also be modelled, as shown in Fig. 5.5. However, it is imperative that the bag is sealed against the seabed to maintain air (and water) tightness. A break in the seal will either cause the water to enter the bag and compress the contained air (in the case of underpressurised base), or the air to leak from the base until the differential pressure at the base reaches zero (in the case of overpressurised base).

Finally, Energy Bags with unsealed base are considered, as illustrated in Fig. 5.6. This configuration allows the surrounding water to enter and exit the base of the bag with the transaction of compressed air. Therefore, when the bag is not fully filled with air, it will contain water at the bottom with an air pocket above. To achieve static equilibrium, the pressure of the air will be equal to the hydrostatic pressure at the top of the water fill level (cf. red line in Fig. 5.6). Thus, the differential pressure across the membrane at all points

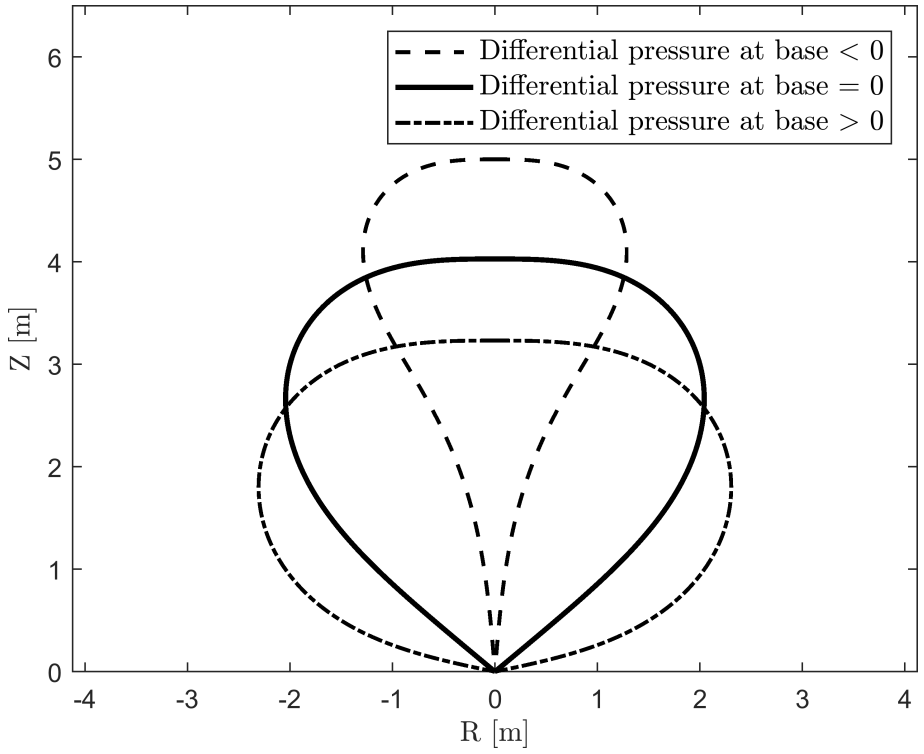


FIGURE 5.4: Deformed shapes of an Energy Bag with zero base radius and sealed base

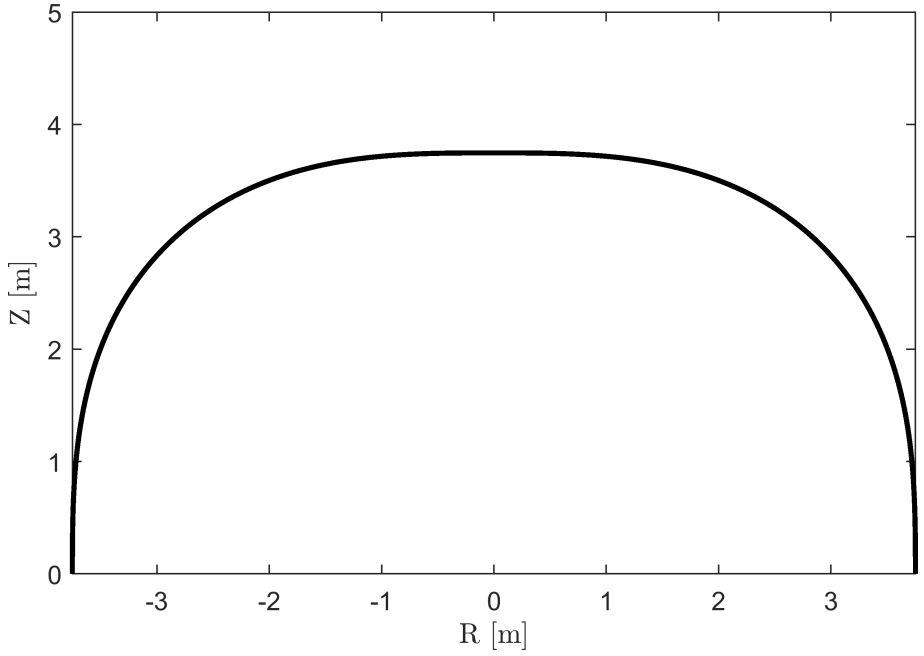


FIGURE 5.5: Energy Bag with non-zero base radius and sealed base. The differential pressure at the base is zero

below the bottom of the air pocket will be zero, resulting in straight sides as seen in the figure. It should be noted that when the unsealed bag in Fig. 5.6 is completely filled with air, its shape will be identical to that shown in Fig. 5.5.

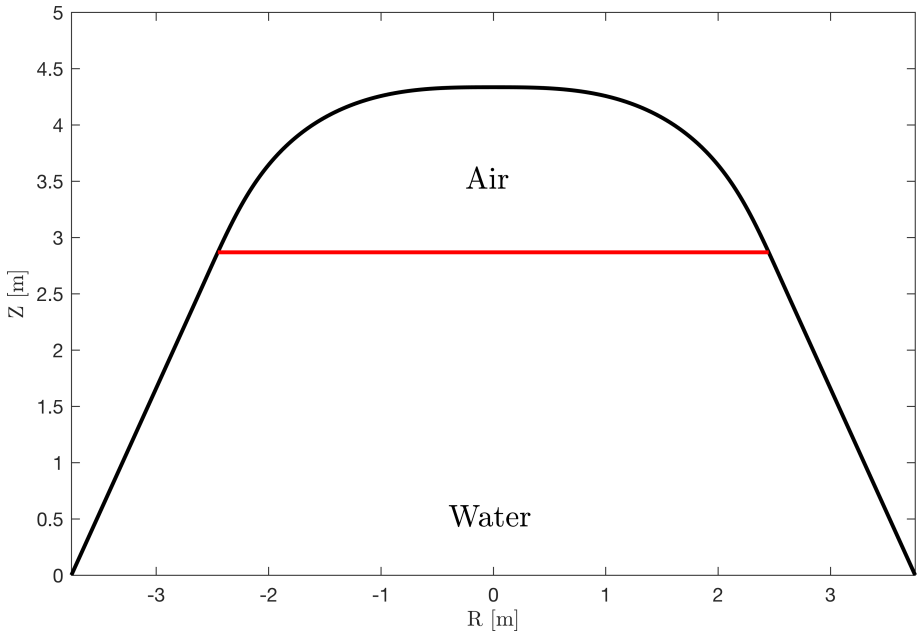


FIGURE 5.6: Energy Bag with non-zero base radius and unsealed base. The differential pressure at the base is zero

In terms of operation, sealed and unsealed Energy Bags are not very different, as observed in the pressure-volume curves in Fig. 5.7. The bag deforms to change its volume at various fill levels of air resulting in minimal pressure variation. This in turn enables more efficient use of compression-expansion devices. It should be noted that when a sealed-base bag is nearly full and approaching the pumpkin shape due to overpressurisation at the base as illustrated in Fig. 5.4, further increase in volume is smaller compared to that at lower fill levels, thereby causing a steep rise in the pressure-volume curve. This is shown in Fig. 5.8. Therefore, it is advantageous to maintain the internal air pressure at around the hydrostatic pressure at the base of the bag for near-isobaric operation.

The analysis of rigid vessels for underwater compressed air storage presented in § 5.2.2 employs an open bottom rigid container fixed on the seabed which allows water displacement within the vessel. The geometric dimensions of this rigid vessel are based on the optimum unsealed base natural shape Energy Bag, where the objective is to minimise the

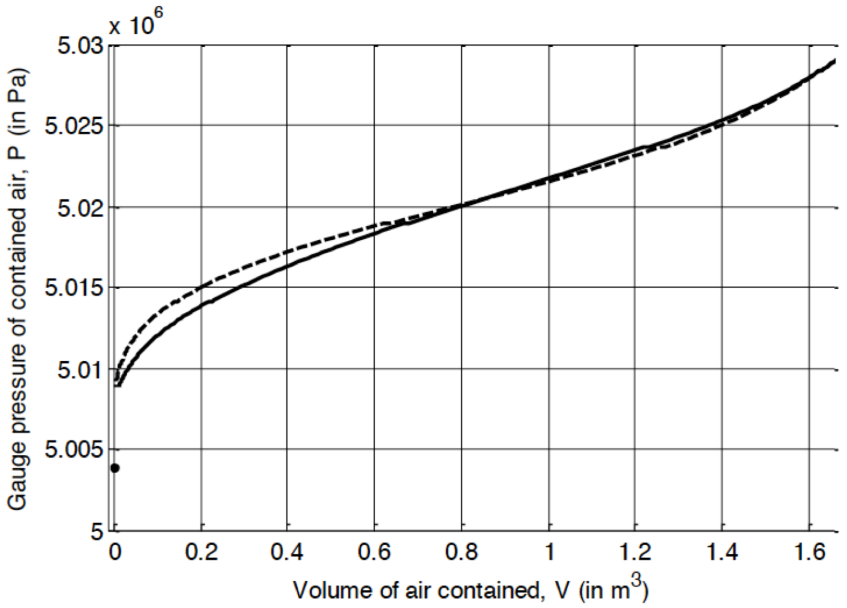


FIGURE 5.7: Pressure-volume curves for massless Energy Bags with sealed base (dashed black line) and unsealed base (solid black line). Adapted from Pimm [122]

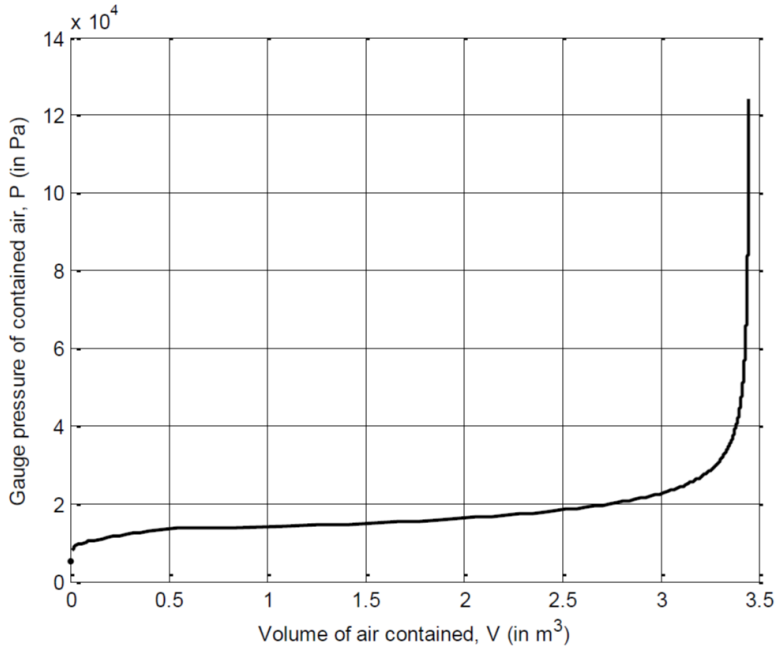


FIGURE 5.8: Pressure-volume curve for massless Energy Bags with sealed base. Adapted from Pimm [122]

capital cost per unit of energy storage capacity of the vessel. As demonstrated by Pimm and Garvey[120], the optimum natural shape bag with an unsealed base has a relatively wide base radius, and the sides of the bag meet the seabed at right angles to minimise the meridional tension required to balance the buoyancy force (see Fig. 5.5). By using the coupled ODE method and fixing the meridional length of the unsealed bag, the base radius of the bag can be found such that its sides meet the seabed at right angles.

5.2.2 Analysis of rigid vessels for underwater compressed air energy storage

An important advantage of rigid vessels is that its weight can act as ballast, potentially precluding the need for additional ballasting material to hold the vessel at the seabed. However, unlike flexible vessels, rigid vessels cannot change their shape with varying fill levels of compressed air and thus they carry loads in bending. It is because of this difference in structural behaviour, flexible vessels are considered to have the potential to cost less than their rigid counterparts. On the other hand, additional ballast is necessary for a flexible vessel to remain on the seabed, and the vessels are more prone to being damaged due to the nature of the structural material.

Nevertheless, rigid offshore structures, in general, have historically received some attention, mainly driven by the needs of the oil and gas industry[128;129]. For instance, storage of hydrocarbons in rigid vessels offshore have proven to be useful where production had begun prior to laying the transportation pipeline[130]. At remote locations where pipeline transportation may not be cost effective, rigid vessels can be used for temporary storage of hydrocarbons in close proximity to the production site. Some have also investigated using rigid vessels to store freshwater offshore, potentially integrated with a desalination plant, driven by scarcity of land and freshwater sources (e.g. islands)[148].

More recently, offshore energy storage in rigid vessels has been associated with either underwater CAES or underwater pumped hydroelectric storage (PHS). The former is discussed in what follows, and the latter in § 5.3.

Seymour[132] first proposed using rigid vessels for underwater compressed air storage. The scheme employed open-base tanks to allow water displacement; an illustration is shown in Fig. 5.9. Seymour described a notional 230 [MW]/10 [h] discharge duration system located at an underwater depth of 650 [m] off the cost of Carlsbad near San Diego, California, and calculated that a 16 [km] long, 1.2 [m] diameter air pipeline, running along a submarine canyon, would be needed to connect the underwater vessels and the onshore power plant.

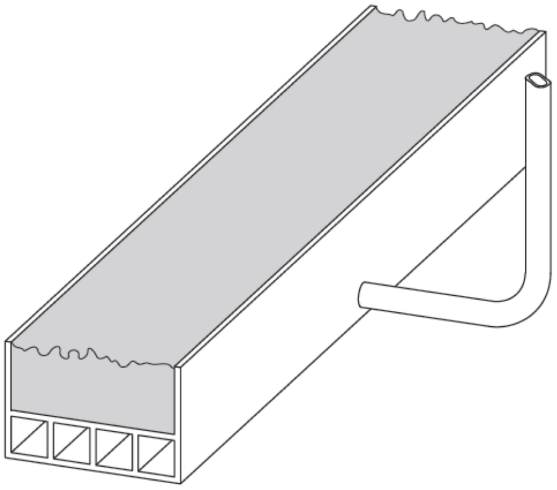


FIGURE 5.9: Rigid underwater vessel proposed by Seymour for CAES. Adapted from Pimm[123]

Fiaschi et al.[133] also proposed systems using rigid vessels at shallower depths of around 100 [m] to store the compressed air. The heat of compression was managed using rock bed thermal storage with further heat transfer enabled by the surrounding seawater.

Researchers at the University of Windsor, Canada, along with the Toronto-based company Hydrostor Inc., have studied structures for underwater CAES. In 2014, Hydrostor installed a 1.5 [MW]/750 [kWh] pilot plant comprising a mix of several rigid and flexible vessels at a depth of 80 [m], 3 [km] off the shore of Lake Ontario[134]. Marine salvage bags were used as the flexible vessels, and rigid vessels used in the pilot are shown in Fig. 5.10. Hydrostor then installed the first commercial underwater CAES plant off the coast of Aruba in 2016, and is now pushing for further commercialisation by targeting coastal cities[135].



FIGURE 5.10: Rigid underwater vessels used by Hydrostor in their pilot plant in Lake Ontario. Adapted from Van Walleghem [134]

Rigid underwater structures are employed not only in energy storage but also in many other areas that widely differ from each other. Several structural forms have been investigated in relation to these environments which include spheres, cylinders, combinations of spheres and cylinders, as well as toroids and ellipsoids [136]. The optimal shape is commonly the result of a trade-off between structural efficiency and cost. The choice of construction material depends on material strength to resist the various applied loads as well as corrosion in deep sea environments. In the analysis that follows, we consider *Lytag concrete* as the structural material. It is a marine grade cement that has been employed in the construction of underwater oil storage tanks in the North Sea and marine concrete bridges [137]. As concrete possesses poor tensile strength, reinforcement is often necessary (e.g. via rebar or post-tensioning cables), which has the effect of raising the materials cost. Although stainless steel and carbon steel are also commonly used by the offshore oil and gas industry and possess greater tensile strength than concrete, these are not considered here as they are relatively more expensive. Finally, we assume that the concrete is set underwater, which means that the initial state of stress of the vessel is zero.

We begin by assigning the optimal shape of the open-base flexible vessel from § 5.2.1 to the rigid vessel. Starting with a user-specified meridional length of around 6.2 [m], the base radius is calculated such that the base meets the seabed at right angles; the base radius is found to be around 3.8 [m]. Again, it is assumed that the vessel is anchored at a depth of 500 [m]. The minimum wall thickness is then calculated such that there is enough concrete to keep the vessel at the seabed when completely filled with compressed air at a pressure equal to the surrounding hydrostatic pressure. This is accomplished by balancing the net buoyancy of the storage chamber and the difference between the weight of the concrete and the buoyancy of the concrete.

The net buoyancy of the storage chamber is given by (5.1). The difference between the weight of the concrete and the buoyancy of the concrete is given by:

$$f_{\text{net,concrete}} = V_{\text{concrete}} \left(\rho_{\text{concrete}} - \rho_{\text{water}}\right) g \tag{5.2}$$

Assuming the density of concrete, $\rho_{\text{concrete}} = 2300\,[\text{kg/m}^3]$, density of water, $\rho_{\text{water}} = 1027\,[\text{kg/m}^3]$, pressure of air equal to the hydrostatic pressure at 500 [m] depth, and the temperature of air to be 5 [C], the volume of the chamber (internal volume), V_{chamber}, the volume of concrete, V_{concrete}, and the minimum thickness of concrete, t_{concrete}, are found to be 199.2 [m^3], 151.2 [m^3] and 0.75 [m], respectively. Therefore, the energy that can be recovered from this rigid underwater CAES reservoir will be between 1.1 [MWh] and 2.1 [MWh].

The idealised finite element geometry of the thickened up open-base rigid vessel, along with loading conditions, is shown in Fig. 5.11. Its structural behaviour is analysed by using the finite element method described in Chapter 3. However, owing to near-isobaric operation, temperature fluctuations of the air and the concrete material are negligible, and the response of the structure results from purely mechanical loads. Compressed air exerts pressure on the inner wall of the rigid vessel, and the surrounding water exerts pressure on the outer wall of the vessel. The movement of the bottom of the structure is constrained

in the vertical direction since the rigid vessel has sufficient ballasting weight to remain on the seabed.

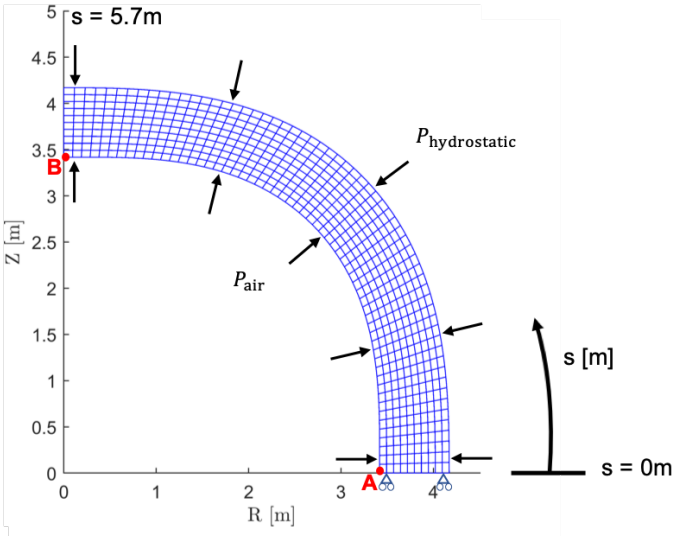


FIGURE 5.11: Schematic of the axisymmetric rigid vessel geometry derived from an open-base natural shape flexible vessel. A new parameter for measuring the distance along the meridian, s, is also defined.

The structural response of the vessel is presented for two extreme loading cases: when the container is completely filled with water (i.e. fully discharged state), and when the container is completely filled with compressed air (i.e. fully charged state).

Although the rigid and flexible vessels considered in the present underwater CAES application have the same shape, the structural response when subjected to pressure loads differs significantly. When the thickness of a pressure vessel is small compared with other dimensions, the vessel is termed a membrane structure. The resulting stresses due to applied pressure loads are then termed membrane stresses. The stresses across the wall of the vessel are assumed to be uniform, and the membrane offers no resistance to bending. The Energy Bag is a membrane structure and its behaviour is described by membrane action. On the other hand, the wall of the rigid vessel does offer resistance to bending and is thus a deviation from a true membrane shape. The stress field due to applied loading is more complex and is described by a combination of membrane and bending actions. In the following, the resultants of membrane and bending stresses – the force per unit length

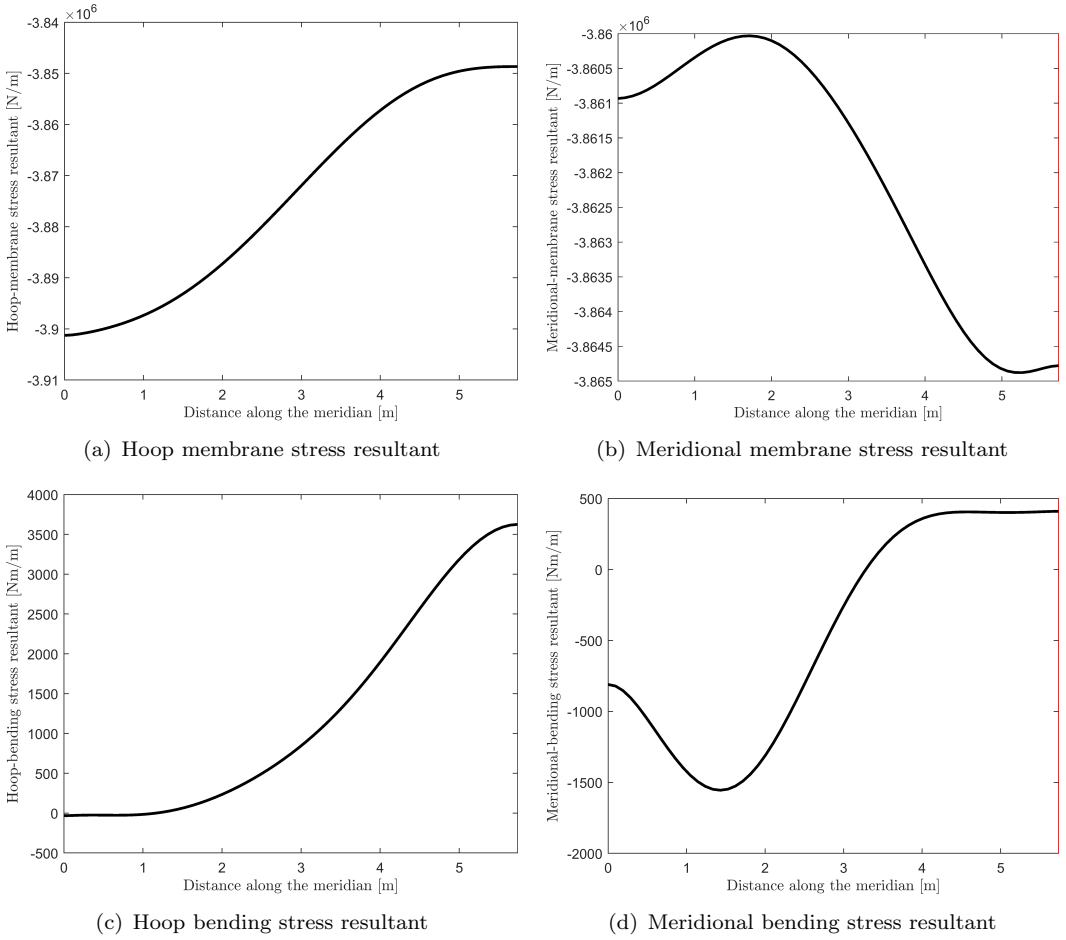
and bending moment per unit length, respectively – are presented for both the hoop and meridional directions.

If the variation of hydrostatic pressure with seawater depth is ignored, the vessel experiences uniform internal and external pressure when completely filled with water inside its volume. Due to the uniform internal and external applied pressure loading, (a) the hoop and meridional *membrane* stress resultant are both equal in magnitude to the product of applied pressure loading and the thickness of the vessel, and (b) the hoop and meridional *bending* stress resultants are zero, because the applied loading acts to uniformly deform the vessel by changing its volume without changing its shape (i.e., the shear stresses are zero).

However, when the dependence of hydrostatic pressure on seawater depth is considered, shear stresses arise because of the non-uniform applied pressure loading. This is shown in Fig. 5.12. Because the pressure now varies with seawater depth, slight variations are observed in the membrane stress resultants. The bending stress resultant in the hoop direction is zero at the base of the vessel increasing to a maximum at the top of the vessel, whereas that in the meridional direction reaches a maximum approximately 1.5 [m] from the base of the vessel along the meridian, before reducing to a minimum at around the mid-point and then increasing further.

When the vessel is completely filled with compressed air, the trends in stress resultant variation along the meridian are similar to that when completely filled with water. This is shown in Fig. 5.13. However, the magnitudes are much greater owing to larger differential pressures.

The variation of principal stresses with water fill level within the container is shown in Fig. 5.14 for point A near the base and point B near the top of the structure (cf. 5.11). Here, fill level is defined with respect to the height of the vessel. So, a 75 [%] water fill level implies that water is filled up to three-quarters of the height of the vessel. Whilst principal stresses are non-positive at all locations, the shear stresses are maximum when



(a) Hoop membrane stress resultant

(b) Meridional membrane stress resultant

(c) Hoop bending stress resultant

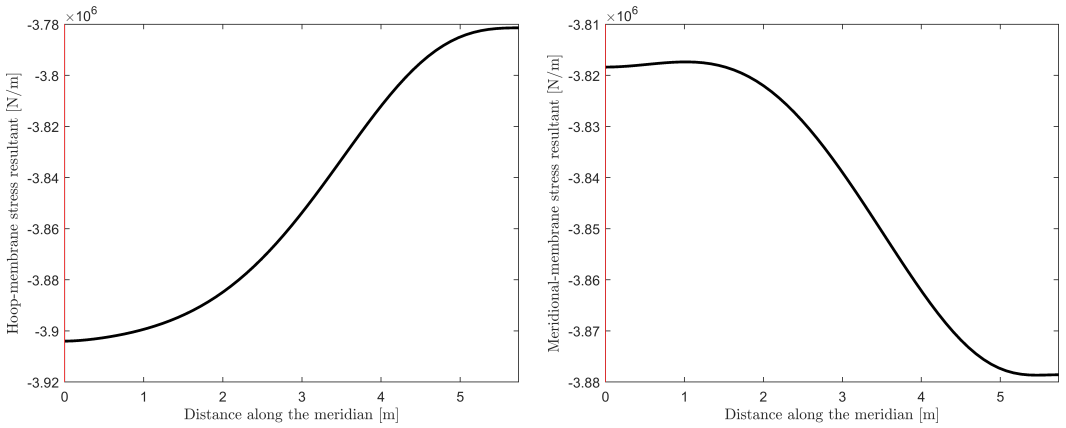
(d) Meridional bending stress resultant

FIGURE 5.12: Stress resultants in an underwater rigid vessel with non-uniform internal and external hydrostatic pressure. Distance along the meridian, s, is measured from the bottom of the vessel

the vessel is completely filled with compressed air, and the magnitudes are greater near the top of the vessel where the differential pressures are higher.

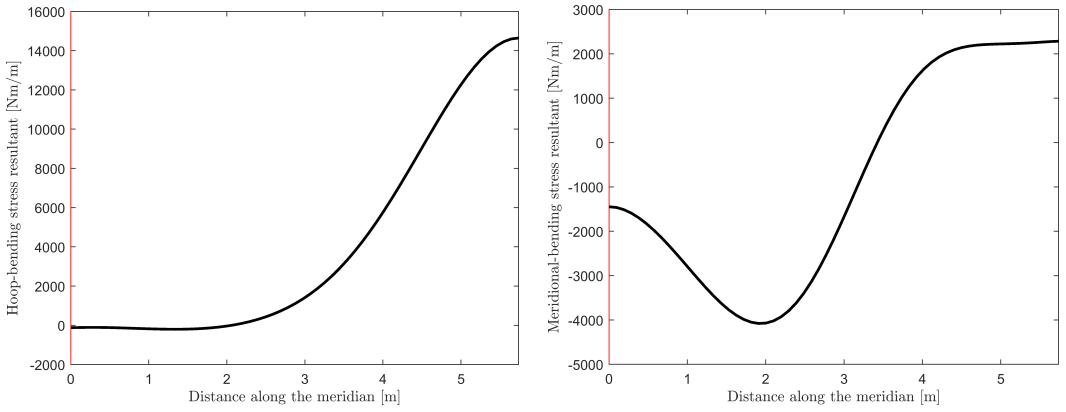
5.3 Underwater pumped hydro storage

The concept of underwater, or deep sea, pumped hydroelectric storage (PHS) is similar to land-based plants in that water is the carrier of energy. Large hollow spherical vessels located on the sea floor pump water out of the vessel during times of low energy prices using a pump-turbine device. This constitutes 'charging' of the energy store. During times of high energy prices, water flows back into the vessel driving the pump-turbine device



(a) Hoop membrane stress resultant

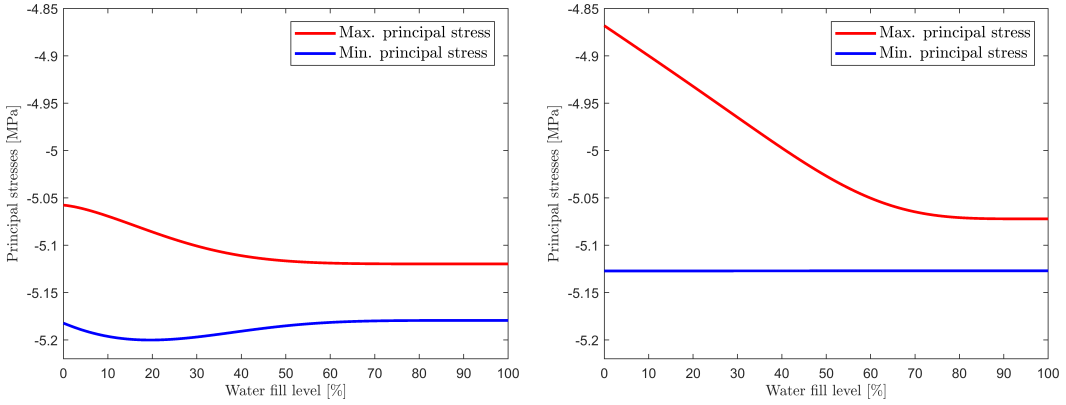
(b) Meridional membrane stress resultant



(c) Hoop bending stress resultant

(d) Meridional bending stress resultant

FIGURE 5.13: Stress resultants in an underwater rigid vessel completely filled with compressed air. Distance along the meridian, s, is measured from the bottom of the vessel



(a) Variation of principal stresses at point A near the base of the structure

(b) Variation of principal stresses at point B near the top of the structure

FIGURE 5.14: Variation of maximum and minimum principal stresses in an underwater rigid vessel with fill level of compressed air

in reverse mode to generate electricity. This constitutes 'discharging' of the energy store. Illustrations of this concept proposed by Slocum et al.[138] and Puchta et al.[139] are shown in Fig. 5.15 and 5.16, respectively.

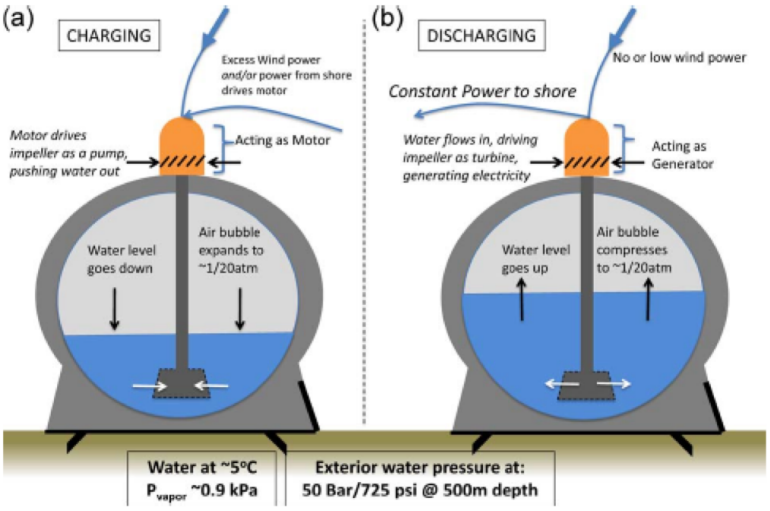


FIGURE 5.15: Underwater pumped hydro storage system proposed by Slocum et al.[138]

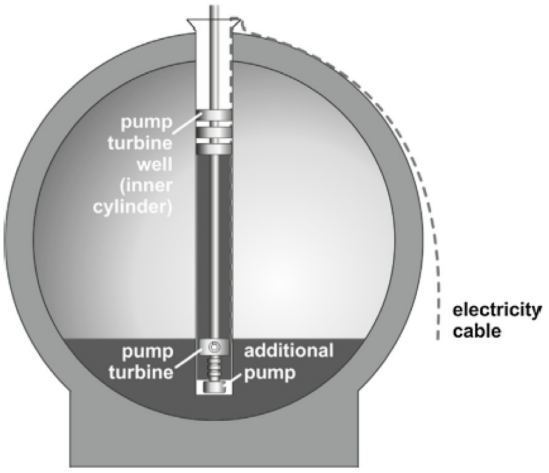


FIGURE 5.16: Underwater pumped hydro storage system proposed by Puchta et al.[139]

The recoverable energy from a rigid vessel used for underwater PHS is given by[138]:

$$E_{\text{recovered}}^{\text{UWPHS}} = V_{\text{chamber}}\, \rho_{\text{water}}\, g\, d\, \eta_{\text{turbine}} \tag{5.3}$$

The inner volume contains air which can be at atmospheric pressure (through provision of

a vent line from the vessel to the water surface) or below it (completely enclosed vessel). A major concern is the cavitation of the pump, especially when the vessel is completely enclosed. As reported by Fennel[140], when the water is pumped out of a fully enclosed vessel, i.e. when the vessel is charging, an air pocket expands twenty times from atmospheric pressure. This residual pressure helps to prevent pump cavitation. The air pocket is compressed back to atmospheric pressure during discharging. However, a vent line arrangement not only helps to reduce risk of pump cavitation by maintaining the inner volume at atmospheric pressure but also increases the energy storage capacity of the vessel.

In the previous section, the rigid vessel in the underwater CAES system found to have a chamber volume of 199.2 [m^3], wall thickness of 0.75 [m], concrete volume of 151.2 [m^3] recoverable energy between 1.1 [MWh] and 2.1 [MWh]. The energy that can be recovered from a rigid vessel in an underwater PHS system with the same chamber volume as the underwater CAES vessel is deployed, calculated from (5.3), will be 823 [MJ] or 0.24 [MWh], assuming this vessel is also located at 500 [m] depth and the efficiency of the turbine is 85 [%]. In other words, a rigid storage reservoir in an underwater CAES system stores between 4.6 and 8.5 times more energy than its equivalent reservoir in an underwater PHS system, depending on how that energy is recovered. Since the inner volume of the rigid spherical vessel under consideration is 199.2 [m^3], the inner radius, equal to 3.6 [m], can be calculated from:

$$r_{\text{inner}} = \sqrt[3]{\frac{3\,V_{\text{chamber}}}{4\,\pi}} \tag{5.4}$$

The minimum wall thickness of the vessel can be calculated by balancing the net buoyancy forces when the vessel is completely charged (i.e. empty of water) and assuming that the air inside the volume is at atmospheric pressure. At 500 [m] depth, the minimum wall thickness is 0.79 [m], and the volume of concrete required is therefore, 160.5 [m^3]. Thus, not only does the rigid vessel in an underwater PHS system store relatively lower amounts of energy, the cost of materials (i.e. concrete) will also be higher due to an increase in the volume of material used. Table 5.1 compares the various quantities of interest when

considering rigid wall vessels for underwater CAES and PHS systems.

TABLE 5.1: Rigid vessels in underwater CAES and PHS systems

	Underwater CAES	Underwater PHS
Vessel shape	Based on Energy Bag	Spherical
Depth	500 [m]	500 [m]
Chamber volume	199.2 [m^3]	199.2 [m^3]
Energy storage capacity	1.1-2.1 [MWh]	0.24 [MWh]
Minimum wall thickness	0.75 [m]	0.79 [m]
Volume of material	151.2 [m^3]	160.5 [m^3]

However, unlike underwater CAES systems, underwater PHS systems do not require any piping infrastructure to carry compressed air to and from the storage reservoir. Power conversion equipment is located on the storage reservoir (e.g. at the top), whereas in an underwater CAES system it is housed separately either onshore or offshore. Finally, methods of large-scale manufacture and deployment of the vessels play a significant role in overall cost-effectiveness of these energy storage systems – this is discussed briefly in the following section.

5.4 Discussion and conclusions

The location of the power conversion machinery and any additional system components (e.g. thermal energy stores) depends on the distance of the underwater vessel from the shore and the costs of transmitting compressed air through a high-pressure pipe versus laying electricity cables on the seabed. If the power conversion machinery is sited onshore, then compressed air is carried from the underwater vessel to the substation for power recovery. This allows easy station access for monitoring and maintenance. If, on the other hand, the power conversion machinery is located offshore, for instance on a floating platform, then compressed air would be transported between the vessel and the floating platform, and electricity cables would be transporting power to onshore locations. Since

compressed air travels shorter distances in the offshore substation arrangement, power recovery efficiency would increase due to decrease in pressure losses. However, maintenance of the plant is not straightforward since the substation will not be easy to access. Therefore, locating electrical substation onshore is generally preferred [141].

It can be inferred from the above discussion that the most suitable locations of underwater CAES would be those with deep water (e.g. 500 [m]) relatively close to shore. Pimm [124] investigated potential locations around the world considering the aforementioned criterion, and found that islands (e.g. Caribbean islands, Hawaii, Canary islands etc.) as well as coastal regions with high densities of population (e.g. Amalfi Coast, southern California) are extremely suitable for underwater CAES. Coincidentally, islands such as those in the Pacific Ocean are heavily reliant on diesel-fired power generation due to the obvious difficulty in importing natural gas via pipelines or coal via railway networks. Hawaii, for example, has plans to obtain 92 [%] of all its electricity from renewable sources by 2030 [142], and the island's suitability for underwater CAES can help support this transition by offering various electricity system services such as grid frequency regulation and reserve capacity.

The towing and deployment process of underwater vessels requires careful consideration. As discussed earlier, rigid vessels possess the significant advantage of structurally inbuilt ballast mass, and can therefore be designed to remain on the seabed without additional support. As noted by Slocum et al. [138], the most appropriate methods of deployment will likely use barges or buoyancy modules which can carry vessels from the shore to the desired location. If barges are used, the vessel would be lowered down into the water through a slot on the barge (e.g. a moon pool) by employing winch assembly mechanisms. With buoyancy modules, controlled descent mechanisms would be required for vessel installation. An illustrative example with barges for rigid vessel deployment is shown in Fig. 5.17.

Flexible vessels do not inherently have ballasting mass and must therefore be anchored to the seabed by large weights (i.e. gravity base anchors), piles (e.g. screw piles) or other suitable mechanisms. The extra ballasting mass, or deadweights, must be towed to the

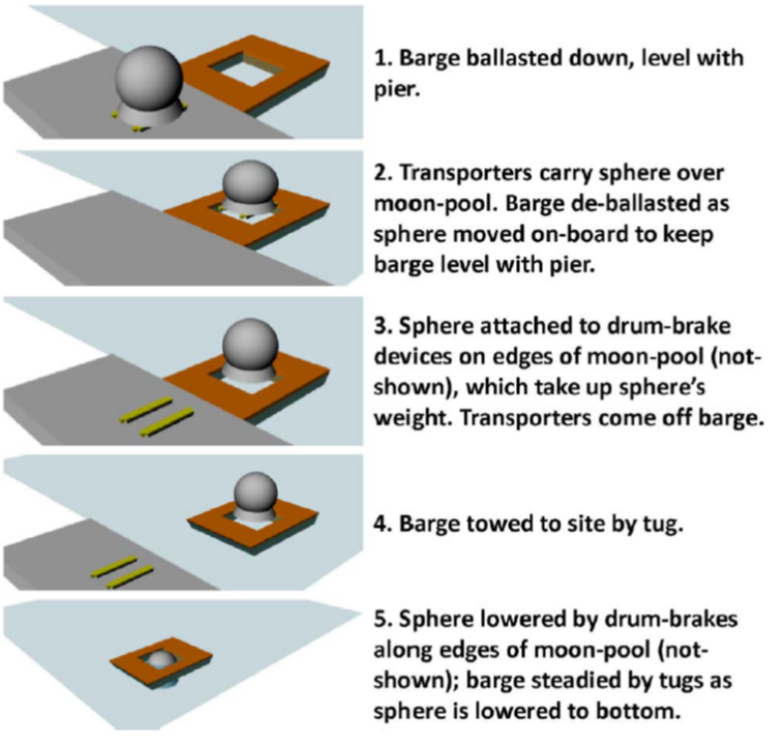
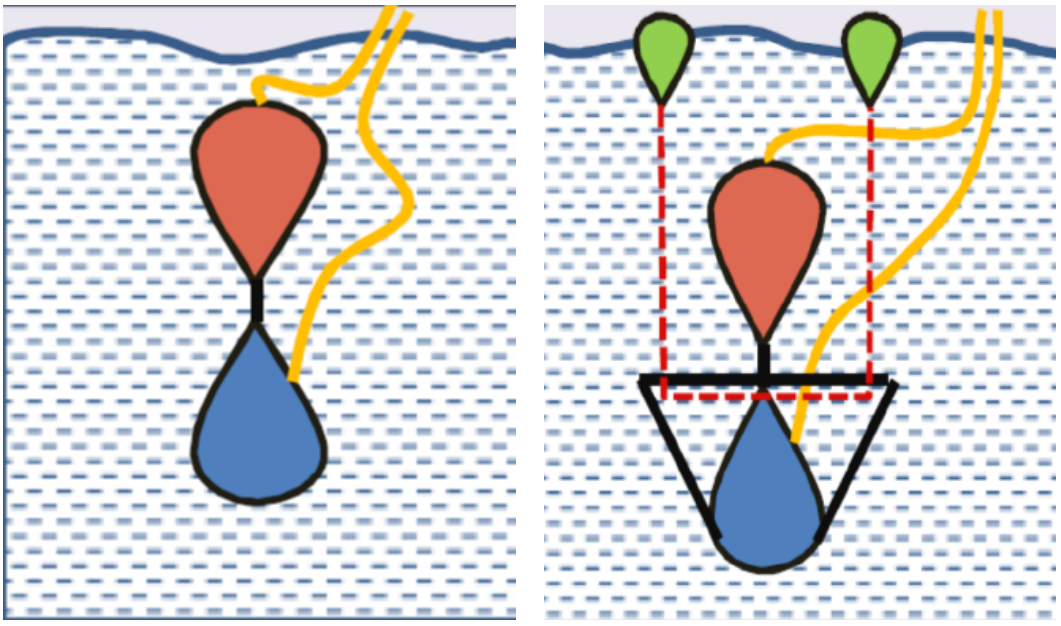


FIGURE 5.17: Deployment mechanism for rigid vessels proposed by Slocum et al.[138]

location of the vessel and can become a costly process at large plant scales[141]. Garvey et al.[125] propose two deployment mechanisms for an Energy Bag, as illustrated in Fig. 5.18. In Fig. 5.18(a), net buoyancy of the Energy Bag (coloured red) and the ballast unit (coloured blue) are adjusted continuously so as to enable controlled sinking of the components. Two separate air pipes (coloured yellow) associated with the Energy Bag and the ballast unit facilitate the correction of pressure relative to the surrounding water pressure. The alternative, shown in Fig. 5.18(b), is an external system comprising two floating buoys (coloured green) and a cable (dashed red lines) which allows controlled descent by adjusting the length of the cable. The deployment is made challenging by the fact that the combination of Energy Bag and ballast unit has neutral buoyancy for a given depth. Sinking slightly further than this equilibrium depth decreases the net buoyancy force and affects the the stability of the descent, which highlights the importance of active control mechanisms.

In conclusion, this chapter has documented and presented analysis on an alternative to



(a) Controlled descent of Energy Bag and ballast unit

(b) Controlled descent of Energy Bag and ballast unit with floating buoys and cable mechanism

FIGURE 5.18: Deployment mechanism for Energy Bags proposed by Garvey et al. [125]

conventional underground CAES technology where the compressed air is stored in deep sea environments. The main motivations are (a) less stringent structural requirements for the air storage vessel since the surrounding water body acts as a natural pressure restraint and (b) more efficient power recovery made possible by the near-isobaric operation of the store. Basic analysis was performed on the two main options for the storage vessel: flexible and rigid. Whilst past research has shown that flexible vessels have the potential to provide economic and efficient large-scale energy storage, experience from trials has shown that costs associated with deployment can be significant without proper control mechanisms. Whilst the deployment of rigid vessels can be more straightforward than flexible vessels, the former are structurally more complicated due to the bending loads that arise within the shell of the vessels, which this chapter has demonstrated. A large-scale underwater energy storage system, be that compressed air or pumped hydroelectric, not only requires cost-effectiveness in terms of mass manufacturing and efficient power recovery, but also in terms of offshore deployment methods.

Chapter 6

Cost comparison of underground, hybrid and underwater compressed air storage options

6.1 Introduction and overall approach

Engineering analysis of selected air storage methods within CAES strategies was the subject of the previous three chapters. This chapter focuses on their economics, i.e., the estimation of costs of those air storage methods by drawing on: (a) cost survey literature of similar systems, and (b) cost correlations of engineering system components. Crucially, it should be noted that the costing exercise performed here only addresses the air storage component, since the focus of this thesis is the various methods of energy storage via compressed air. The costs of a complete CAES system would depend on the costs of power conversion machinery that serves as the linking element between the electrical grid and the air storage component, whether or not heat from the compression of air is also stored, and other balance of system costs (such as civil works, pipework, valves, electrics, instrumentation, etc.).

The air storage methods investigated in this thesis comprise both mature (underground air storage in caverns) and novel (hybridised compressed air-liquid air storage and underwater air storage in rigid concrete structures) systems. The overall approach, thus, involves the use of existing cost data as well as bottom-up estimation using cost correlations of system components. Whilst costing components of mature technologies can be relatively easier because of the physical existence of similar projects and published cost data, costing new technologies or its components can involve significant uncertainties. Tenders or 'request for proposals' from manufacturers are usually necessary for more complete and accurate system costs. In this chapter, the objective is to arrive at a preliminary estimate of the costs of the three air storage methods investigated earlier in the thesis. The financial feasibility of the most cost-competitive system (i.e., the cheapest method of storing air per unit of useful energy stored) is then analysed in Chapter 7.

Ample cost data is available in the public domain for storing pressurised air in salt caverns; this is made use of in this chapter to derive estimates. However, cost data for systems similar to the proposed novel hybrid compressed air-liquid air storage system and the rigid (concrete-based) underwater air storage container are unavailable. Thus, where applicable, costs of the most important system components are determined individually and then summed to obtain a 'system-level' cost of air storage. In the case of the hybrid compressed air-liquid air system, the components include pressure vessels, compressors, expanders, and heat exchangers. In the case of the underwater air storage container, costs are estimated based published costs of a concrete structure operating in a corrosive environment; this is directly reported in § 6.3.

It is important to note that in this work, it is implicitly assumed that the cost correlations used can accurately capture costs of the system components. The hybrid compressed air-liquid air storage system, for instance, comprises many components that are available 'off-the-shelf'. Thus, the deviation of estimated costs from actual costs of the hybrid system may be relatively lower than, say, the estimated versus actual costs of a novel pumped thermal electricity storage system involving non-standard system components.

Finally, since the present chapter relies on cost correlations and historical cost literature and surveys, it is not only important to convert the cost estimates into the relevant currency (assumed to be GBP, £, herein), but also to account for inflation and adjust to current cost levels. This is done via cost indexing based on the Chemical Engineering Plant Cost Index[197].

6.2 Cost modelling of system components

In the following, cost correlation equations for components in the air storage methods proposed in this thesis – the underground, hybrid and underwater compressed air energy storage systems – are laid out. While every effort has been made to ensure their accuracy, the formulae are still subject to uncertainty, especially where costs pertain to 'first-of-a-kind' systems. Moreover, costs associated with electrical and structural 'balance of plant', labour, operation, equipment supplier margin, and sales tax have not been included.

6.2.1 Cavern

As discussed in § 3.1, solution mining of salt caverns for underground gas storage is technically mature and therefore of relatively low cost per unit of useful energy stored in high-pressure air. In general, the capital cost of a solution-mined salt cavern depends on the cost of the borehole well and the act of solution mining itself, which are in turn directly proportional to the depth of the cavern below ground surface. Furthermore, the cost of solution mining is proportional to the volume of the cavern, i.e., how much salt is excavated. Since the cavern depth is proportional to the maximum pressure experienced in the cavern[48], a simple linear cost relationship has been applied[198] based on salt cavern cost data from the McIntosh CAES plant:

$$C_{\text{cav}} = P_{\text{air,max}} \left(c_{\text{borehole}} + c_{\text{solution mining}} V_{\text{cav}} \right) \tag{6.1}$$

Here, C_{cav} is the cost of the solution-mined cavern in US$, $P_{\text{air,max}}$ is the maximum pressure experienced within the cavern, c_{borehole} and $c_{\text{solution mining}}$ are specific costs associated with drilling and solution mining the cavern, respectively, and V_{cav} is the volume of the cavern. Table 6.1 lists the parameters of equation (6.1): $P_{\text{air,max}}$ and V_{cav} are determined from the analysis in Chapter 3, whereas c_{borehole} and $c_{\text{solution mining}}$ are taken from Xue and White[198].

TABLE 6.1: Cavern cost parameters

c_{borehole}	41,275 [$/bar]
$c_{\text{solution mining}}$	0.11 [$/bar m^3]

6.2.2 Pressure vessel

From Turton et al.[199], the base cost of the pressure vessel, $C_{\text{PV,base}}$, is calculated in US$ from:

$$\log(C_{\text{PV,base}}) = K_1 + K_2 \log(A) + K_3 \left(\log(A)\right)^2 \tag{6.2}$$

Here, A is the volume of the pressure vessel in consideration. The parameters K_1, K_2 and K_3 (see Table 6.2) characterise the material which in this case is assumed to be carbon steel.

Next, the 'bare module' cost of the pressure vessel, $C_{\text{PV, BM}}$, is calculated to account for factors that cause the cost to deviate from base level (e.g. direct/indirect costs, installation and commissioning, etc.):

$$C_{\text{PV, BM}} = C_{\text{PV,base}} \left(B_1 + B_2 \, f_{\text{M}} \, f_{\text{P}}\right) \tag{6.3}$$

The constants B_1 and B_2 are cost correlation factors for the aboveground pressure vessel, f_{M} is a material factor which for this analysis is based on carbon steel, f_{P} is a pressure

factor (as the vessel is pressurised) calculated as shown below.

$$f_{\mathrm{P}} = \frac{1}{0.0063}\left(\frac{(P_{\mathrm{vessel}}+1)\ D_{\mathrm{vessel}}}{2\ (850-0.6\ (P_{\mathrm{vessel}}+1))}+0.00315\right) \tag{6.4}$$

TABLE 6.2: Aboveground pressure vessel cost parameters

K_1	3.4974
K_2	0.4485
K_3	0.1074
B_1	2.25
B_1	1.82

6.2.3 Compressor and expander

Based on Couper et al.[200], the capital costs of compressors and turbines are directly proportional to its power capacities Z (in horsepower), and parameters U_1 and U_2 which may vary according to the type of equipment chosen and its manufacturing material. The capital cost, $C_{\mathrm{comp/exp}}$, in US$ is calculated from:

$$C_{\mathrm{comp/exp}} = U_{1,\mathrm{comp/exp}}\, Z_{\mathrm{comp/exp}}^{U_{2,\mathrm{comp/exp}}} \tag{6.5}$$

Parameters in equation (6.5) listed in Table 6.3.

TABLE 6.3: Compressor and expander cost parameters

	Compressor	Expander
U_1	7190	378
U_2	0.61	0.81

6.2.4 Heat exchanger

The most common approach for estimating the cost of heat exchangers is by computing its surface area; this is because the heat exchanging area is directly proportional to material and fabrication cost. However, the computation of surface area can be a complex task depending on the type of heat exchanger, and may not be accurate especially if the analysis has not progressed to the detailed component design stage (as is the case in this thesis, see Chapter 4). Therefore, for a high-level cost estimate of the heat exchanger, the 'C-value' method[201] is employed which makes use of experimentally published costs in terms of heat exchanger duty and minimum temperature driving force (i.e., minimum approach temperature). In other words, published costs used here are per unit of watt per kelvin. Heat exchanger costs in this analysis, C_{hex}, in US$ are thus computed as:

$$C_{\text{hex}} = \text{UA}\, c_{\text{hex}} \tag{6.6}$$

Here, c_{hex} is the cost of the heat exchanger per unit of watt per kelvin, the product of U (the heat transfer coefficient) and A (the heat transfer area) is determined from previous analysis in Chapter 4. It is important to note that individually U and A are unknown because a detailed heat exchanger design is not part of the analysis. Once the heat exchanger type is specified based on suitability for the intended application and UA is determined, the cost information in Table 6.4, taken from Hewitt and Pugh[202], is used to logarithmically interpolate to obtain desired values.

TABLE 6.4: Heat exchanger cost parameters

Heat exchanger type	c_{hex} for UA $= 5,000$ [W/K]	c_{hex} for UA $= 100,000$ [W/K]
Shell and tube	0.91 [$/(W/K)]	0.134 [$/(W/K)]
Plate and fin	0.14 [$/(W/K)]	0.045 [$/(W/K)]

6.3 Results and discussion

Underground compressed air storage

In Chapter 3, the variation of temperature and pressure of air within the cavern was simulated over many charge-discharge cycles. The volume of the cavern chosen was 120,073 [m^3], and the maximum air pressure over the charge-discharge cycles was determined to be ca. 87 [bar]. Using this, and substituting parameters from Table 6.1 in equation (6.1), the cost of creating the cavern is calculated to be ca. £3.4m in nominal terms.

For this cost to be comparable to the costs of other air storage methods investigated in this thesis, the absolute cost is divided by the useful energy, or exergy, stored in the air containment. Exergy content (in kWh), B_{kWh}, in a mass of fluid, m_{f}, is determined by the following equation:

$$B_{\mathrm{kWh}} = \frac{m_{\mathrm{f}} \left[(h - h_0) - T_0 \ (s - s_0)\right]}{3.6 \times 10^6} \tag{6.7}$$

Here, h and s represent specific enthalpy and entropy of the fluid at the current state of the fluid (i.e. based on current fluid temperature, pressure, density); and h_0 and s_0 represent the same quantities at a reference state (where the temperature is T_0).

In an isochoric air storage vessel, such as the underground salt cavern, the temperature and pressure of the air inside that vessel vary with the fill level of the air. Therefore, to compute the *net* useful exergy stored over one charge-discharge cycle as defined in Chapter 3, equation (6.7) must be summed over the time-interval of that cycle. Since the analysis in Chapter 3 simulates one hundred such cycles, the net useful exergy stored is averaged over the total number of cycles. This is determined to be ca. 379,600 [kWh] per cycle.

The cost per unit of exergy stored in underground salt cavern-based compressed air storage is therefore ca. £9/kWh.

Hybrid compressed air and liquid air storage

In Chapter 4, it was determined that an upper limit of 80 [bar] would be set for compressed air stored aboveground in a steel tank so as to prevent the air from liquefying directly upon expansion. This would protect the expansion equipment from 'cold' wear and tear. Key output values from the analysis in Chapter 4 – summarised in Table 6.5 – are fed into cost equations described in § 6.2 to obtain cost estimates of individual components and, thus, the total cost.

Following the logic that the liquid air storage unit will contribute to a large proportion of the total energy storage capacity, it will be assumed that compressed air storage unit contributes 10% to total storage capacity, with the rest from liquid air storage. This is somewhat arbitrary, of course, and a sensitivity analysis can easily inform the optimal shares of component energy storage capacities. However, since the objective here is to minimise energy storage in compressed air, but still retain all power transaction capability with the grid through this unit, the 10-90 split between compressed air-liquid air storage capacities is a good starting point.

To estimate the cost of compressed air storage tanks, it is assumed that this sub-system comprises several industry-standard stainless steel pressure vessels: a typical example is a skid container with 12 CNG tubes each with major dimensions as shown in Table 6.5. Using the total tank volume, equation (6.7) is used to calculate total exergy stored in the steel tanks – this is determined to be 238 [kWh]. Therefore, the total exergy stored in liquid air tanks is 2,141 [kWh]. With this information, and that in Table 6.5, capital cost of each component in the hybrid storage system can be calculated. The total cost, i.e. the sum of costs of all components, is found to be £814k. From Fig. 6.1, it is clear that the single-stage refrigerant compressor followed by the liquid air tank contribute the largest shares to the overall cost. The heat exchanger parameters appear to be well-chosen since they contribute to lower shares of overall capital cost. This result implies that an incremental increase power capacity of the compressed air-to-liquid air conversion system

TABLE 6.5: Cost coefficients for the hybrid compressed air-liquid air storage system

Parameter	Value	Comment
Compressed air storage pressure	80 [bar]	Parameter from Ch. 4
Compressed air tank outer diameter	559 [mm]	Typical skid container dimension [208]
Compressed air tank shell thickness	14.8 [mm]	Typical skid container dimension [208]
Compressed air tank height	10,977 [mm]	Typical skid container dimension [208]
Compressed air tank density	7,700 [kg/m^3]	Typical skid container dimension [208]
Number of compressed air tanks	12	Typical minimum-buy package [208]
Liquid air tank cost	£133/kWh	Determined from Strahan [82] and Li et al. [98]
Primary air expander power	183 [kW]	Determined from Ch. 4
Secondary air expander power	688 [kW]	Determined from Ch. 4
Primary refrigerant expander power	234 [kW]	Determined from Ch. 4
Secondary refrigerant expander power	52 [kW]	Determined from Ch. 4
Refrigerant compressor power	653 [kW]	Determined from Ch. 4
Primary air MSHX thermal conductance	15,323 [W/K]	Determined from Ch. 4
Secondary air MSHX thermal conductance	180,425 [W/K]	Determined from Ch. 4

should justify a higher incremental benefit (e.g. increased revenue through energy market participation) compared to increasing the energy storage capacity.

The cost per unit of exergy stored in a hybrid system comprising a combination of (above-ground) compressed air storage and liquid air storage as proposed in this thesis is, therefore, ca. £342/kWh.

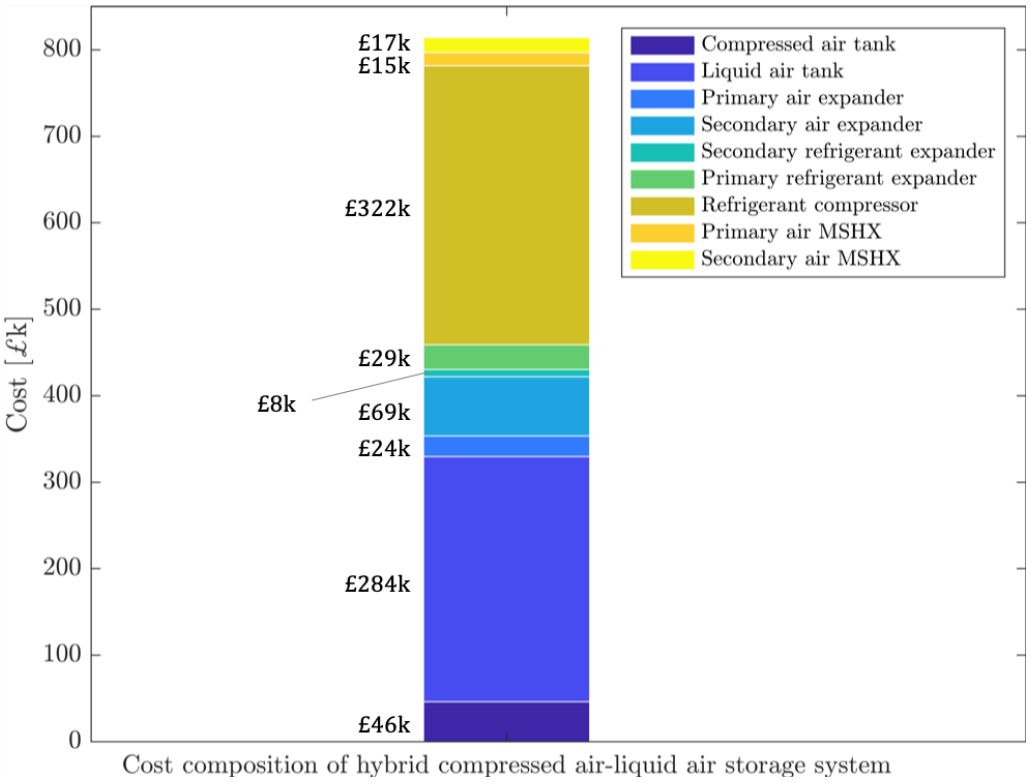


FIGURE 6.1: Component and total cost of the hybrid compressed air-liquid air storage system

Underwater compressed air storage

In Chapter 5, the rigid vessel for storing compressed air underwater was assumed to be constructed from corrosion-resistant concrete. Based on the dimensions of the optimal shape of the vessel (derived from Pimm[122]), the volume of concrete material required for the construction was estimated to be ca. 151 [m^3] (see Table 5.1).

Navarro et al.[203] have published unitary costs associated with the construction of corrosion-resistant concrete structures (see Table 6.6). Using this, and assuming the density of concrete to be 2300 [kg/m^3], the total cost of constructing the underwater rigid vessel can be calculated as the product of the density, volume and unitary costs of construction of the concrete structure. This is determined to be ca. £48k (nominal).

TABLE 6.6: Construction cost parameters for corrosion resistant concrete[203]

Cost parameter	Unit cost
Portland cement	87.8 [€/tonne]
Sand	14.0 [€/tonne]
Gravel	16.4 [€/tonne]
Fly ash	38.0 [€/tonne]
Silica fume	1.1 [€/kg]
Superplasticiser	1.4 [€/kg]
Steel reinforcement	5.3 [€/kg]
Hydrophobic surface treatment	19.0 [€/m^2]

Unlike underground compressed air storage, underwater vessels operate in isobaric mode which enables the pressure to remain constant over the entire range of fill level of compressed air inside the vessel; the temperature of the air also does not vary. Furthermore, this mechanism enables higher roundtrip efficiencies because operation of compression/-expansion machinery can be optimised for a single design point (see also § 5.1).

Assuming the rigid vessel to be anchored at a depth of 500 [m] underwater, the pressure of the air in the vessel, P_{chamber}, when completely filled is ca. 51 [bar][1]. Assuming, also, that air is at at ambient temperature, ideal gas laws can be applied in this case to estimate the

[1] Assuming density of water to be 1027 [kg/m^3]; acceleration due to gravity to be 9.81[m/s^2]; ambient pressure at surface of seawater to be 1.01325 [bar].

maximum exergy stored in the vessel, given by the following[2]:

$$B_{\mathrm{kWh,\,isobaric}} = \frac{P_0\, V_{\mathrm{chamber}} \left(\left(\frac{P_{\mathrm{chamber}}}{P_0} \right) \log \left(\frac{P_{\mathrm{chamber}}}{P_0} \right) - \left(\left(\frac{P_{\mathrm{chamber}}}{P_0} \right) - 1 \right) \right)}{3.6 \times 10^6} \tag{6.8}$$

$B_{\mathrm{kWh,\,isobaric}}$ is thus determined to be 838 [kWh] for the chosen underwater concrete vessel, which means that the cost per unit of exergy stored is ca. £58/kWh. For comparison, Pimm and Garvey[123] report that their flexible energy bag could cost around £20/kWh. As discussed in Chapter 5, flexible bags rely only on the surrounding hydrostatic pressure to store the air; therefore, the bag's function is to provide a separating membrane between the air and the water, significantly reducing its structural requirements compared to a rigid vessel. However, there are other important considerations for underwater energy storage, as discussed in the following, that may drive up overall system costs.

Discussion

In summary (see Table 6.7), whilst the absolute cost of air storage containment is highest in underground salt cavern-based CAES, it offers the lowest cost option per unit of useful energy stored because the technology is mature, most of the costs are fixed and the marginal cost for extending the air storage capacity is very low. The hybrid compressed air-liquid air system has the highest cost per unit of storage, whereas storing air in underwater rigid containers costs more than the underground option, but lower than the hybrid option, because the underwater vessel is made of relatively low cost materials.

It is important to comment on the (expected) sizes of the three air storage systems investigated herein, *relative* to each other, and their impact on the cost of energy storage.

Underground salt caverns can accommodate several hundred thousand cubic meters of air volume and so store energy in the range of hundreds of MWh to tens of GWh, depending on the geology and useful cavern volume. Underground compressed air storage, thus,

[2]Derived from equation (6.7) by substituting ideal gas formulae for changes in enthalpy and entropy w.r.t. ambient conditions.

TABLE 6.7: Absolute and specific costs of exergy storage in air underground, hybridised with liquid air, and rigid underwater containers

Air storage option	Absolute cost, £k	Exergy stored, kWh	Cost per unit of stored exergy, £/kWh
Underground salt cavern compressed air storage	3,428	379,600	**9**
Hybrid compressed air and liquid air storage	814	2,379	**342**
Underwater compressed air storage, rigid vessel	48	838	**58**

truly belongs to the bulk energy storage application category. Since the storage method is technically mature and cost correlations used are based on actual cost data, the calculated volume, stored energy and cost derived here are representative of a real-world system.

The hybrid compressed air-liquid air storage system employs aboveground steel tanks for storing pressurised air and non-pressurised, thermally well-insulated tanks for storing liquid air. Over the years, several parties have considered building commercial aboveground CAES plants – notable examples are EPRI-led designs of a 15 [MWh] capacity plant [206] that is able to discharge for 1 [h] at full power (developed for ESPC Inc.), and a 41 [MWh] capacity plant [207] that is able to discharge at full power for 4.5 [h] (developed for New York Power Authority). However, aboveground compressed air-only systems are limited in its energy storage capacity (no more than a few tens of MWh at scale) as storing large volumes of high pressure air in steel tanks is cost-prohibitive: the cost of storage scales with pressure (of the air) times volume (of the steel tank). Because of this reason, aboveground CAES systems are more suited for distributed generation or smart grid type of applications. Integrating liquid air storage can provide relief to standalone aboveground CAES systems by (a) lowering the cost of air storage in steel tanks and (b) increasing the time duration over which energy can be stored and discharged at the same level of power. However, the hybrid arrangement as proposed in this thesis significantly lowers roundtrip efficiency because of the component exergy losses during the transformation of compressed air to and from liquid air – bearing in mind that a further transformation

to and from electricity is needed, thus incurring more losses. While the cost per unit of energy stored of this system is higher compared the underground and underwater storage options, it does not suffer from locatability issues[3], and can possess significantly lower lead times (i.e., time from construction date to commercial operations date) than underground or underwater CAES systems. Furthermore, the cost calculated here is for a system that is new and therefore has scope for reduction through further system design optimisation and technological learning.

Underwater energy storage – either via compressed air or 'reverse' pumped hydro systems – is intended to be a bulk storage application. For instance, Pimm and Garvey [123] envisage a commercially deployed energy bag to contain around 200 [MWh] of exergy[4]. At suitable locations, multiple energy bags can be deployed to increase the energy storage capacity to the GWh-regime. Similarly, StenSea's commercial target for underwater pumped hydro storage in concrete spheres is 20 [MWh] of energy storage per sphere [205], scalable to multi-GWh storage at suitable underwater topographies. However, to achieve cost effective large-scale energy storage underwater, the capability to bulk-manufacture storage vessels and suitable deep water locations that are relatively close to shore are absolutely critical. Whilst the former has a direct effect on the cost of vessel per unit of energy stored, the latter influences the costs of vessel deployment, installing electrical (and compressed air transport pipe systems), and operating and maintaining the vessel during its lifetime, which therefore affects total system cost. In general, the further away from the shore the system is, the greater the costs of electrical and other 'balance of plant' as well as maintenance cost (even if this maintenance is infrequent, e.g. once every few years). Thus, the calculated volume, stored energy and cost are perhaps representative of a prototype first-of-a-kind system intended for technology demonstration. The cost of energy stored will be relatively higher at this stage with expected reductions in future due to economies of scale in manufacturing, technological learning and innovative deployment techniques such as that discussed in § 5.4.

[3] It is worth noting that state-of-the-art lithium-ion battery cells (including racks and DC components), which are also highly locatable, currently cost ca. £168/kWh [204] – around 50% lower than the proposed hybrid storage system.

[4] For an energy bag with dimensions 40 [m] height, 40 [m] maximum diameter, anchored at 500 [m] depth.

6.4 Conclusions

This chapter has devised capital cost models for the three air storage containments analysed earlier in the thesis. Whilst the underground and hybrid air storage options are analysed at their intended energy storage capacities for commercial application, the underwater air storage method has significantly lower capacity. This is because of the resulting accuracy of cost estimates: at large capacities economies of scale would lower the costs of underwater storage, although there is no information/learning from actual systems at present that captures this benefit. With this in mind, the results show that the underground option is the most cost competitive in terms of cost per unit of exergy stored in the air, whereas the hybrid option is the least competitive. However, both hybrid and underwater air storage options are novel and their competitiveness can be expected to improve as their technological maturity and readiness levels develop. Furthermore, although the hybrid option has the highest unitary cost, it can be deployed in locations where its competitors cannot function. It is here that comparison against costs of other highly locatable technologies – such as battery storage, whose upfront energy storage costs are currently lower but of the same order of magnitude – and their relative learning rates become relevant. Therefore, immediate future work could investigate cost learning curves applicable to the hybrid option, which will depend of course on the room for improvement of each system component in terms of technical performance as well as cost. It is also important, in this vein, to account for whole system costs, i.e., the costs of power conversion machinery, electrical and structural balance of plant and other auxiliary components.

Chapter 7

Value of energy storage integrated behind-the-meter with renewable generators

7.1 Introduction and context

Drawing on the conclusion of the previous chapter – namely, that underground CAES enables the cheapest form of air storage amongst the options considered in this thesis – this chapter focuses on a broader theme by seeking to examine economic and financial value of integrating underground CAES with wind power generation.

It was discussed previously that the rate of deployment of renewable power generation technologies around the globe – especially solar PV and wind energy – is increasing. It was also discussed that renewable energy sources are widely recognised to have great potential to reduce fossil fuel dependency in the electric sector. However, unlike conventional sources of power generation currently supplying the largest fraction of electricity, both solar and wind are characterised by variable and uncertain output. These characteristics have raised concerns about the reliability of an electric grid with high renewable penetration, and

the affordability of integrating large amounts of zero carbon power sources onto the grid. Moreover, from the point of view of the renewable site operator (RSO), the uncertainty and variability of output translate into high-risk premiums when participating in competitive power markets. In other words, a RSO may incur negative cash flows to compensate the renewable generator's intrinsic deviations from their predicted outputs, which may lead to an undesirable, imbalanced, operation of the network.

The error associated with predicting the output of renewable sources increases with the forecast time horizon. Therefore, updating the output forecast closer to real-time operation improves its accuracy. Thus, a rolling dispatch framework provides one way to address the inherent uncertainty of the renewable source. For instance, Tuohy et al. [143] investigate such an approach and the benefits associated with it, whereby unit commitment is performed in a rolling-planning framework. Renewable power variability can be better predicted closer to real-time and in some cases minimised by diversifying the renewable resource (e.g. wind). However, additional reserves are required to mitigate lost revenue; examples of this include lull periods when the renewable source suddenly becomes unavailable or due to an underutilised grid connection at low capacity factors.

In recent years, many efforts have been made from a mathematical point of view to improve forecast models of renewable output, especially in the context of wind energy [165;166]. Regardless of the particular model adopted, the error associated with predicting the output of renewable sources increases with the forecast time horizon. Hence, changes to the current regulatory framework to allow updating the forecast closer to real-time operation would improve the accuracy of the forecast. A rolling dispatch framework provides an effective solution to address the inherent uncertainty of the renewable source. For instance, some authors [143;157] investigated the benefits of such approach, whereby unit commitment is performed in a rolling fashion. However, whilst the accuracy of forecast of power outputs could be improved by applying the aforementioned techniques or adopting more favourable regulatory frameworks, additional reserves are required to mitigate lost revenue due to the output variability. For example, during lull periods when the renewable source suddenly

becomes unavailable (or exhibits reduced output capability) the RSO would miss the opportunity of generating revenues. If these periods coincide with times of high electricity prices on the wholesale energy market, the value of lost opportunity would be significant. Similarly, to avoid high grid connection charges and/or large cost associated with other equipment (e.g. inverters), the RSO may set the export limit of the renewable site to a value lower than the maximum. This would lead to local curtailment in those time intervals characterised by large energy availability. Consequently, a second way to reduce the uncertainty as well as variability of the renewable output is to combine the operation of the renewable site with an energy storage asset.

Integrating energy storage to fill this gap would: (a) enable better control over dispatch by time-shifting energy and reduce the exposure of wind power errors to imbalance penalties; (b) allow better utilisation of the grid connection to the renewable source; (c) reduce curtailment of renewable energy; and (d) offer environmental benefits by precluding fossil fuel usage (which might be used for balancing purposes if renewables would be left without the possibility to regulate their output e.g.[144]). The co-location of energy storage with renewables can be categorised in two ways[145]. The first is an embedded arrangement whereby the energy store is located behind-the-meter with the renewable site. Here, the store is unable to charge from the grid and the collective system only exports energy via the meter . The second is a parallel arrangement whereby the energy store is equipped with its own energy meter, and it only shares the grid connection capacity of the renewable generator. Since the store is also able to charge from the grid in the parallel metering arrangement, there is a possibility of 'brown power' being sold as 'green power', thus putting operators at risk of losing renewable subsidies. With embedded metering, this issue is essentially circumvented. Embedded metering also enables the renewables operator to retain the identity of the site thereby creating savings on additional grid connection capacity costs [14]. It is worth pointing out that the focus of this paper is an energy storage unit connected behind-the-meter with a renewable generator.

Previous works[146;147] discussed the effectiveness of pumped hydro storage units to time-shift energy as well as manage energy imbalance of wind farms via stochastic programming methods. The pumped storage unit can transact power with the grid, and both positive imbalances (actual output larger than forecast) and negative imbalances (actual output smaller than forecast) are penalised, at costs which are obtained by scaling the wholesale energy prices (in the paper by multiplying all wholesale prices by 1.5). Castronuovo et al.[148] proposed whereby a pumped storage unit is used solely to compensate for energy deviations of a wind farm's commitments on the day-ahead market. Ding et al.[149] presented an extension of this strategy where both energy arbitrage and imbalance management capabilities of the system, within a mixed integer non-linear optimisation framework, for specific imbalance market mechanisms. The methodology for managing imbalance here also penalises the absolute value of the difference between actual and predicted output at scaled wholesale energy prices; the impact of any negative market/imbalance prices is not discussed. Zucker and Hinchcliffe[150] investigated the value derived by solar PV installations integrated with battery storage (lead-acid and lithium-ion technologies) via a mixed integer linear optimisation model. Here the value is derived from arbitraging on the wholesale market as well as avoiding curtailment of generation. It should be noted that the 'curtailment avoidance' scheme investigated by the authors is essentially a behind-the-meter configuration where storage charges from solar PV only, but the ability of the store to time-shift energy is not considered. Moreover, self-discharging and energy capacity fade (typical characteristics of electrochemical batteries) are ignored. A similar analysis within a linear optimisation framework is performed by Gill et al.[151]. The authors modified the methodology to a heuristic optimisation framework[152] to include the effect of self-discharge, where the heuristics approach is justified by stating the inability of a linear optimisation framework to account for self-discharge.

The main contribution of this paper is the development of a detailed business case for an energy store connected behind-the-meter with renewable source based on a novel optimal scheduling model. Four sources of revenue are considered:

- Energy arbitrage realised on the wholesale energy market (including renewable obligation incentives[187])
- A novel imbalance management mechanism of the combined system based on real-time imbalance prices. We note that not all energy deviations are penalised; since the imbalance price (positive or negative) reflects the needs of the grid during real-time operation, the proposed system responds to this price by re-adjusting its delivery compared to its commitment (cleared market schedule) as the optimisation rolls over the time-horizon[188]
- Reduction of peak-demand use-of-system or network charges based on Triad charges[189]
- Participation in the Capacity Market[190]

Another important contribution relates to the development of a purely linear optimisation framework to maximise profits, executed on a rolling-plan basis, whilst considering the effects of self-discharge on the short-term optimal operation as well as long-term investment plan. The model can also account for capacity degradation of the storage unit, although both degradation and self-discharge are negligible in CAES systems (versus lithium ion battery storage systems, for example). From a set of historical data of wind energy availability and system imbalance prices we derived several statistically-similar scenarios to improve the robustness of the results. Moreover, a simple but effective wind error forecast model based on random walk technique is developed to simulate time-increasing mismatches between actual wind energy and predicted values. Results demonstrate that given current market conditions, the business case for an underground salt cavern-based CAES system integrated with a wind farm is non-existent. This may change in the future when renewable capacity installed on the grid is expected to increase dramatically, thereby creating relatively more volatile energy price signals (i.e. larger differences between peak and off-peak prices). However, results show instrumental findings regarding the ability to reduce the cycling (and therefore mitigate wear and tear) of the storage unit when it performs the proposed imbalance management mechanism.

It is assumed that the renewable generator is installed and already in operation and the investment case is analysed for retrofitting a storage unit onto the renewable generator. It is also assumed that the renewable energy storage system is a price-taker, i.e. the system has no influence on electricity market prices.

We begin by introducing the problem and describing the sources of revenue considered. Next, the method for modelling energy storage dynamics is presented along with discussion of the methodology adopted for generating a number of scenarios for wind availability and system imbalance prices, starting from historical data. The main characteristics of a simple but effective wind error forecast model are then introduced. This is followed by formulation of the optimisation model highlighting the optimal allocation of the revenue streams within the rolling optimisation framework. A detailed financial model is also presented in this section. Finally, the results are presented and discussed, and conclusions are drawn.

7.2 Problem description

The schematic representation of a storage asset connected behind-the-meter with a renewable site is shown in Fig. 7.1. Note that the energy output of the whole site is the sum of the energy outputs of individual generators (e.g. single wind turbines for the case of a wind farm). Since we are interested in the high-level energy transactions between the site, the storage unit and the grid, we considered the renewable site as a single, large equivalent generator. In this work, we focused on a particular embedded arrangement, which involves the storage unit absorbing energy from the renewable source only. This choice enables the integrated site to remain an exporter of renewable energy and therefore retain accreditation of subsidy schemes such as, in the Great Britain (GB) regulatory framework, the Renewables Obligation (RO), Feed-in-Tariff, etc..

It is worth pointing out that the proposed scheme and developed algorithm can be applied to several different implementations, without major changes. In fact, the present storage

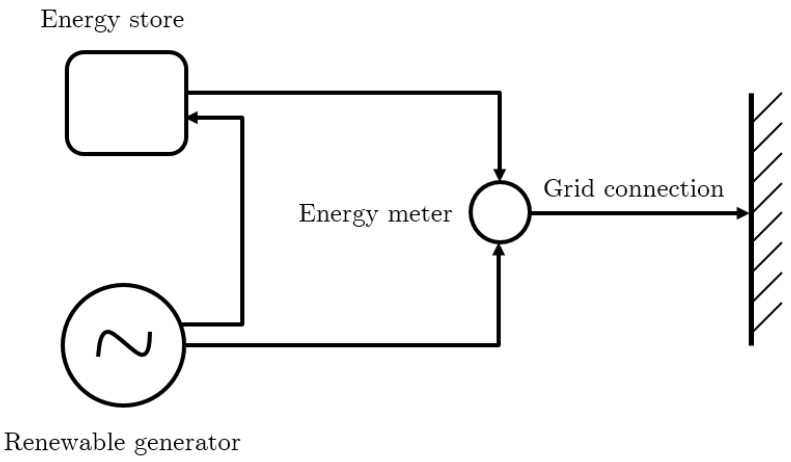


FIGURE 7.1: An energy storage unit embedded within a renewable site

unit can represent chemical energy storage (e.g. batteries, fuel cells), mechanical energy storage (e.g. pumped hydro, flywheel), or thermomechanical energy storage (compressed air, liquid air) systems. Similarly, the renewable generator may represent wind farms, photovoltaic (PV) farms, etc. Without loss of generality, in the remainder of this paper we will consider a lithium-ion battery storage unit embedded behind the meter with a wind farm.

The main objective for a storage unit, when integrated with a renewable site, is to increase the net revenues by reducing the costs faced due to the intrinsic variability and limited foresight of wind power output. The revenue opportunities considered in this work reflect the current regulatory framework in GB. However, the extension of the proposed model to other regulation schemes is not a major challenge as many countries have already in place similar schemes, i.e., a wholesale energy market, a payment/reward scheme to account for renewable deviations from declared positions and embedded benefits [146;148].

7.2.1 Sources of revenue

This chapter does not consider revenue streams associated with the provision of frequency response services by CAES systems – faster-responding storage systems (such as batteries or flywheels) are better suited for this application. The proposed study instead determine

the viability of a profitable business case almost entirely based on merchant revenues (i.e. wholesale energy market, imbalance management and Triad mechanism) which in turn may require a more aggressive cyclic operation compared to frequency response. In particular, we considered four types of revenue sources. First, the storage unit of the Renewable Energy Storage System (RESS) can engage in an arbitrage by absorbing energy from the wind farm at periods of relatively low prices on the wholesale market and sell it back at periods of higher prices. Note that these prices would include the top up represented by the Renewable Obligation (RO) subsidy, i.e., a fixed sum added to the wholesale market prices.

Second, over the winter months, the storage unit can add value by targeting embedded benefits associated with Triads, which correspond to three half-hour electricity trading periods called the Settlement Periods (SP), during November to February, when electricity demand is highest on the entire GB transmission network [30]. The assets happening to be generating during Triads events receive a further remuneration on top of the revenues collected on the wholesale market. More detail on the Triad mechanism and its inclusion in the optimal decision-making process to operate the RESS are discussed in § 7.2.2.

Third, the RESS can participate to the GB Capacity Market (CM) and derive revenue for its contracted capacity. In the recently announced five-year review of CM regulations [31], Ofgem (i.e. the GB regulator) intends allow renewables and its hybrid arrangements with storage to actively bid for CM contracts. The System Operator (SO) procures capacity for sustained power delivery at maximum contracted levels to cope with stress events on the power system. Notifications of the potential occurrence of these events are sent to CM contract holders 4h ahead in time of actual delivery. Note that the notification may not necessarily be followed by an actual delivery of the service. In fact, if system conditions have changed over the 4h interval, the SO may decide to relieve CM contract holders of the actual service provision. Furthermore, the SO considers such a notice period long enough to allow a CM asset to trade and deliver other services on other markets (e.g. the wholesale

market). CM providers are rewarded with monthly payments for their obligation at the auction clearing price[191].

It is worth noting that from the moment when a grid stress event is notified, the RESS (as in Fig. 1) may not be able to inject power into the grid at contracted levels by the 4h notice interval (provided that the stress event is confirmed). This could be due to low availability or total unavailability of wind during the stress event, and/or the storage unit not being able to charge up to its rated storage capacity during the 4h notice period to then discharge at maximum power. The occurrence of stress events is hard to forecast. However, such events have been historically rare[192]. Hence, in this paper we have not considered the actual realisations of stress events. This allowed us to neglect checking whether (rare) actual stress events may coincide with (rare) prolonged unavailability for the RESS to generate[1].

Moreover, the remuneration for storage units depends strongly on their minimum discharge durations to be guaranteed throughout the duration of the contract. For the same maximum power output, a storage unit that can discharge at full power for a longer duration will receive more revenue than that for a shorter duration. For this reason, so-called de-rating factors (published by National Grid) state that for a storage unit with 4h (and above) minimum discharge duration has its capacity rated at approximately 96% of maximum output, whilst a 0.5h discharge duration storage unit is rated at around 21% of maximum power output. If the energy capacity of the storage degrades, then depending on the remaining energy storage capacity a different derating factor may apply. A fourth-order polynomial function (blue curve in Fig. 7.2) has been fit to the published de-rating factors (red circles in Fig. 7.2) to facilitate the calculation of revenues in the present application. This is not an issue with the present analysis as underground salt-cavern based compressed air storage systems undergo minimal capacity degradation over time.

[1]The longest wind lull period of the historical data of actual wind output considered in this analysis is 3h. This implies that RESS's comprising storage units of minimum discharge durations greater than 1h will not be able to fully charge itself from wind if the stress event warning period coincides with the lull. In reality, however, the grid connection of the wind farm site will allow electricity to be imported (e.g. for powering up the wind turbine, cooling, etc.). Therefore, it is possible to ensure that the storage unit is fully charged before the stress event in the case of a long wind lull (e.g. 3h) even if the storage duration is greater than 1h.

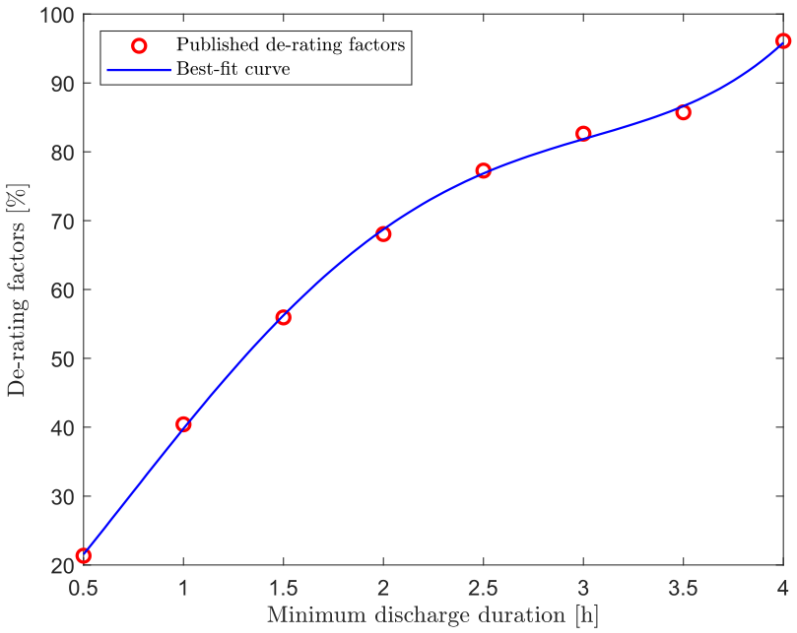


FIGURE 7.2: Published values are in red circles, blue curve represents the 4th order polynomial fitting function $\mathrm{f}(x) = 1.1\,x^4 - 8.5\,x^3 + 14.8\,x^2 + 27.1\,x + 5.3$

Previous GB CM auctions have demonstrated the inclination of storage unit operators to favour short-term (annual) contracts[192]. We have assumed in the present application that the RESS bids into the CM year by year. Moreover, the revenues from CM are assumed to be independent from the optimal day-by-day scheduling problem. In other words, the revenue for a year contract first requires the assessment of the minimum discharge duration and the associated de-rating factor at the end of each operational year. Finally, CM revenues are calculated by multiplying the de-rating factor by the discharge power capacity and the auction price of the CM. We assumed that the RESS operator perfectly forecasts the amount of remaining energy capacity (at the end of each year) so that the RESS would be able to fulfil the contracted CM position if actually required (rare events).

The fourth and final source of revenue is concerned with capturing value from system imbalance prices. These prices reflect the position of the system i.e. its power mismatch. The system will assume a long position if the actual generation exceeds the system demand. On the contrary, the system will be in a short position when the demand is greater than the generation. Many factors contribute to alter the perfect balanced position of the system such as imperfect forecast of system demand, imperfect forecast of RES outputs,

etc. The positive or negative power mismatch is called Net Imbalance Volume (NIV), which is employed by the SO to determine, at each SP, a negative or positive imbalance price.

Renewable generation operators, like other market participants, contract to either generate (or consume in the case of load) an amount of energy for each SP. This is initially notified to the SO as a Physical Notification (PN), but may be updated to a final value before market closure, referred to as the Final Physical Notification (FPN), exactly one hour ahead of time of each SP, called the Gate Closure. Therefore, the single wind farm could happen to be in a long or short local position (energy measured at the meter of the site is greater/lower than the committed FPN) when the system is in a long or short position.

The imbalance prices are used by the SO to reward/penalise assets that happen to be in a local position opposite/in line to the one of the system. However, a wind farm in a standalone configuration, i.e. not equipped with a battery storage, is exposed to the uncertainty of possible combinations of 'local vs. system positions' without any degree of controllability. Instead, considering the RESS configuration in Fig. 7.1, the storage behind-the-meter with the wind farm can be employed to conveniently manage the imbalance positions of the wind farm. We distinguish between two schemes of active imbalance management for the renewable site, to be compared to the non-active case, where the storage is only employed for energy arbitrage purposes on the wholesale market.

One approach measures the mismatch between the FPN and actual output of the renewable generator in an SP and it instructs the storage unit to absorb or release appropriate amounts of energy to compensate for the excess or shortfall of renewable energy output, allowing for local balancing of the site. We shall refer to this strategy as Imbalance Volume Minimisation. Cash flows arising from mismatches between forecasted and actual output are computed as the actual volume delivered to the market minus the scheduled (or committed) output multiplied by the imbalance price.

Another approach to manage the intrinsic imbalance of the renewable site is to elicit profit by adjusting actual delivery of energy from the site during real-time operation relative to

the scheduled amount in this period. Thus, a positive imbalance price may incentivise the provision of an amount of energy relatively larger than the scheduled one (i.e. the FPN). Per contra, delivering relatively lower amounts of energy to the market compared to the FPN if the imbalance price is negative, also results in a revenue for the site operator. Since the imbalance price is inextricably linked to the NIV of the electricity system [156], we shall refer to this strategy as NIV chasing.

By way of example, consider Fig. 7.3 where the renewable energy storage system (RESS) commits 10 [MWh] for a SP in the future, with 7 [MWh] from the renewable source and 3 [MWh] from storage. It is also assumed that the store can discharge a maximum of 14 [MWh] in this period. During real-time operation, the actual output from the renewable source (1 [MWh]) is less than what had been forecasted for this period.

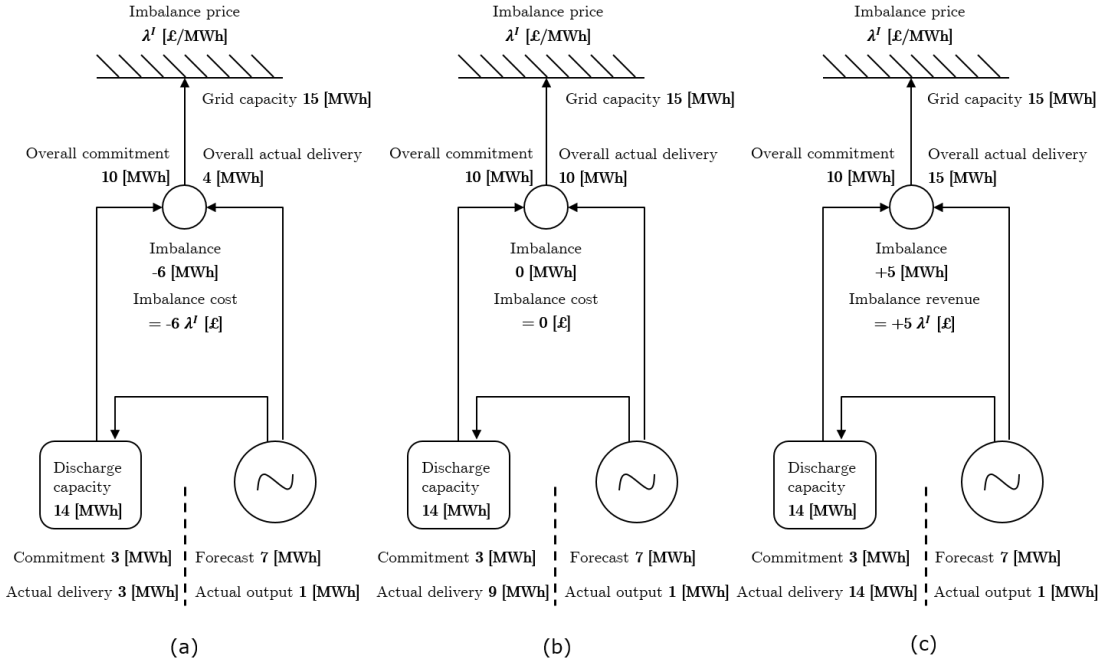


FIGURE 7.3: The mechanisms of imbalance management of a renewable generator

Assuming the imbalance price λ^{I} [£/MWh] to be positive, there are three possibilities:

- Without imbalance management, the RESS incurs a negative imbalance volume of 6 [MWh] in this case and, therefore, a penalty $p = -6\lambda^{\mathrm{I}}$ [£]

- *Imbalance volume minimisation*: the store can compensate for the imbalance by readjusting its delivery to 9 [MWh], thereby reducing the penalty of the system to zero; namely, $p = 0$ [£], as shown in Fig. 7.3(b)

- *NIV chasing*: with this strategy, the system can also earn profits of $p = 5\lambda^{\mathrm{I}}$ [£] by discharging a further 5 [MWh] as shown in Fig. 7.3(c). In other words, the output at the meter of the system is not limited to the final (or scheduled) energy position submitted at market closure

7.2.2 Mechanics of optimal allocation

This section summarises the main assumptions and features of the proposed optimisation problem for the operation of a RESS. The mechanics of the core optimisation algorithm are illustrated in Fig. 7.4. Note that the optimal operation of the RESS is analysed over a 24 [h] period formed by $n = 48$ SPs of 30 [min] each. The simulations to determine the optimal operation of the RESS are carried out with the rolling-planning approach [157], performing a complete calculation with a 24 [h] horizon in half-hourly time steps $i = \{1, \ldots, n\}$ and discarding all decisions beyond the first SP. This strategy is particularly beneficial due to the time-increasing nature of the forecast error of renewable output forming the RESS. As time approaches the instant of physical delivery of electricity, improved forecasts become available. A rolling-plan optimisation allows for accommodating changes to the optimal path and therefore intrinsically reducing the uncertainty in renewable output. At each optimisation roll $j = \{1, \ldots, N\}$, the underlying assumption is that the RESS is able to re-trade its positions (with the exception of the FPNs) at the relative wholesale electricity prices $\Lambda^{\mathrm{M}}_{\mathrm{j}} = \{\lambda^{\mathrm{M}}_{1}, \ldots, \lambda^{\mathrm{M}}_{\mathrm{n}}\}_{\mathrm{j}}$.

At a generic optimisation roll j, the set of n wholesale electricity prices and a single imbalance price $\lambda^{\mathrm{I}}_{1,\mathrm{j}}$ (relative to $SP_{1,\mathrm{j}}$), are known. In general, the imbalance price is not known until closer to real-time delivery of electricity and depends on bids and offers accepted by the SO on post-Gate Closure actions called the Balancing Mechanism (BM). Due to the typical poor knowledge of bids and offers, their accepted values and NIV

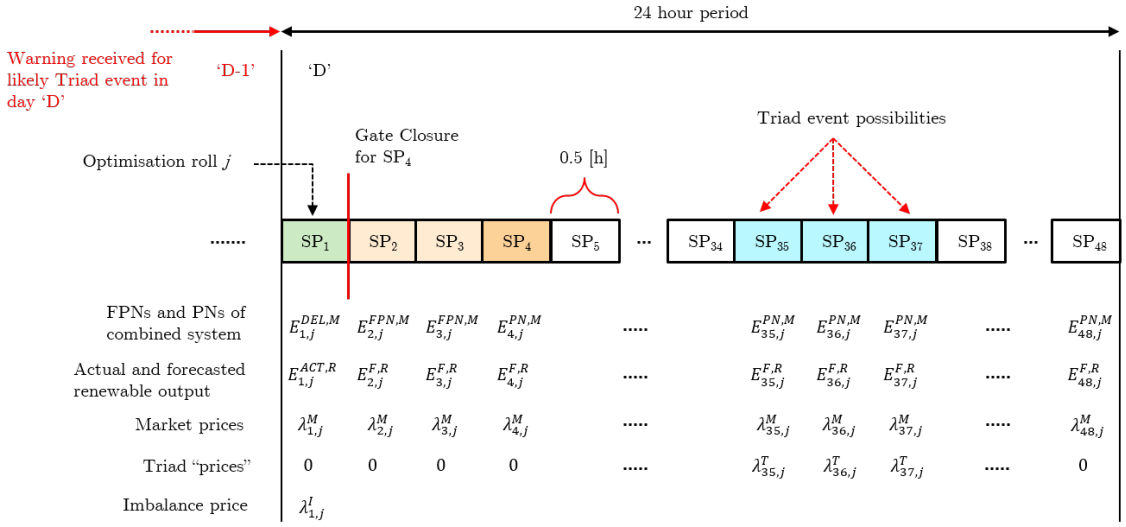


FIGURE 7.4: The rolling-planning optimisation framework for generic days $D-1$ and D

ahead in time[156;158], it is assumed that only one imbalance price is known (with perfect knowledge) per optimisation roll. By the end of a physical day, the RSO may receive warnings announcing the occurrence of Triad events for the day after. These alerts are sent out by various energy suppliers and third party intermediaries to companies over the Triad season (November to February). The SO then confirms the actual Triad events; namely, the day and SP of three periods of highest demand, usually in March[159]. In this model, Triad events were only expected during 5-6:30pm; namely, during three SPs. Moreover, the Triad price signal $\lambda^{\mathrm{T}}_{\mathrm{i,j}}$ is divided by three (assuming equal probabilities) and simply added to the wholesale prices in the objective as the energy content associated with these prices are one and the same. Clearly, because there are no triad possibilities associated with the rest of the SPs, the price signal for these periods is zero.

When the optimisation roll is in $SP_{1,\mathrm{j}}$, actual renewable energy output in this SP, $E^{\mathrm{ACT,R}}_{1,\mathrm{j}}$, is known as it can be measured. Forecasts of renewable energy output $E^{\mathrm{F,R}}_{\mathrm{i,j}}$ for SPs $i = \{2, \ldots, n\}$ (which may be updated) are also known. It is possible that the delivery of energy from the system to the market in the first SP, $E^{\mathrm{DEL,M}}_{1,\mathrm{j}}$, is different to the FPN associated with it due to the revelation of the imbalance price. The Gate Closure for $SP_{4,\mathrm{j}}$ is towards the end of $SP_{1,\mathrm{j}}$, which means that the FPN of the combined system for $SP_{4,j}$

must submitted latest by the end of this SP. The FPNs for $SP_{2,j}$ and $SP_{3,j}$ would have been submitted at previous Gate Closures.

7.3 Modelling wind power and price scenarios, wind power forecast error and energy storage dynamics

The time horizon chosen in this paper to evaluate the investment in a storage unit located behind the meter of a wind farm is $Y = 20$ years. We have assumed that the annual sets of market prices, imbalance prices and the available wind energy (with 30 min granularity) are repeated year by year over the entire investment horizon. To improve the robustness of the results, proposed model has been run for $K = 50$ different prices/wind availability scenarios. This allows the consideration of more favourable or adverse (in terms of total annual revenues) combinations of actual prices and wind energy availability. In particular, the scenarios differ from each other by the actual wind energy availability and actual imbalance prices.

7.3.1 Generation of wind energy and price scenarios

This section deals with the procedure to create K 'credible' scenarios for actual wind output, energy market prices and system imbalance prices. The approach we use here is based on a generalised probabilistic methodology to generate time-coupled patterns presented by Sajjad et al.[160] and de Quevedo et al.[161]. Three sets of historical data from 1 November 2015 to 31 October 2016 of 30 [min] granularity are considered as the initial data set for actual wind power output[162], market prices and system imbalance prices, respectively. These data are shown in Fig. 7.5 via their empirical Cumulative Distribution Functions (CDFs).

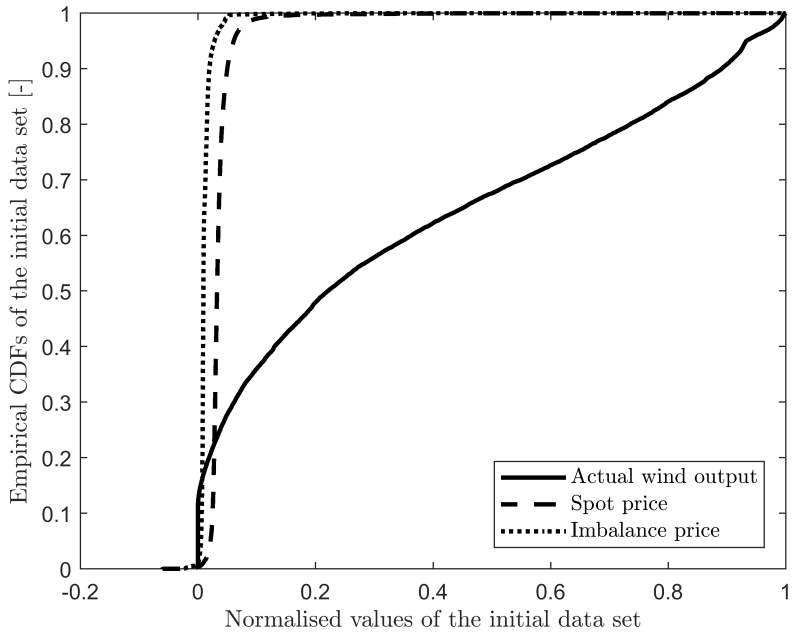


FIGURE 7.5: Empirical CDFs for normalised values from the initial data set comprising actual wind power output, spot prices and system imbalance prices of half-hourly granularity over one year

We refer the reader to § 2.1 of de Quevedo et al.[161] for a step-by-step description of the methodology adopted. However, the effectiveness of the aforementioned procedure is demonstrated in Fig. 7.6.

The initial (historical) data of wind output (black solid line) are shown together with the calculated data of two patterns (red and blue dashed lines) constructed for the same one-year duration with 30 [min] time steps. It is easily observed that the calculated patterns are close to the sequences of historical data. This also holds true for patterns calculated for the initial spot price and imbalance price data set. Hence, this procedure guarantees that the full statistical characteristics of the initial data are preserved. Finally, note that for a generic day in the year, the half-hourly values recorded for each scenario may differ, in general, from the corresponding values in the historical set of data; see Fig. 7.7 for a demonstration involving 48 half-hourly actual wind output data on a typical day from the initial data set and its two associated patterns.

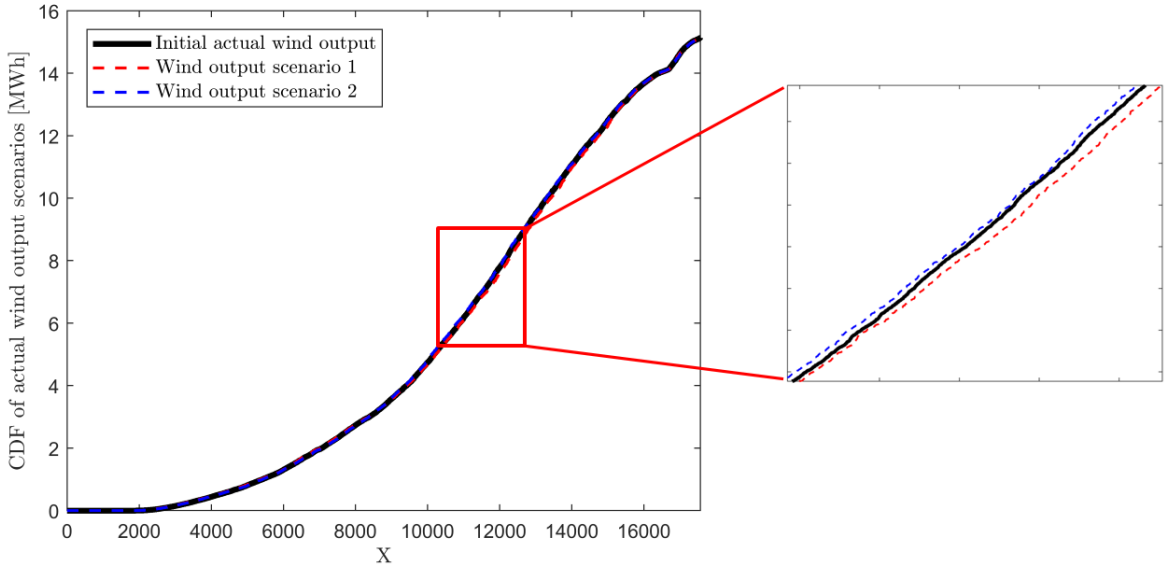


FIGURE 7.6: Sorted values of actual wind power output for the initial data as well as two associated scenarios. Inset shows magnified region of the plot to demonstrate that patterns are statistically similar, but not identical

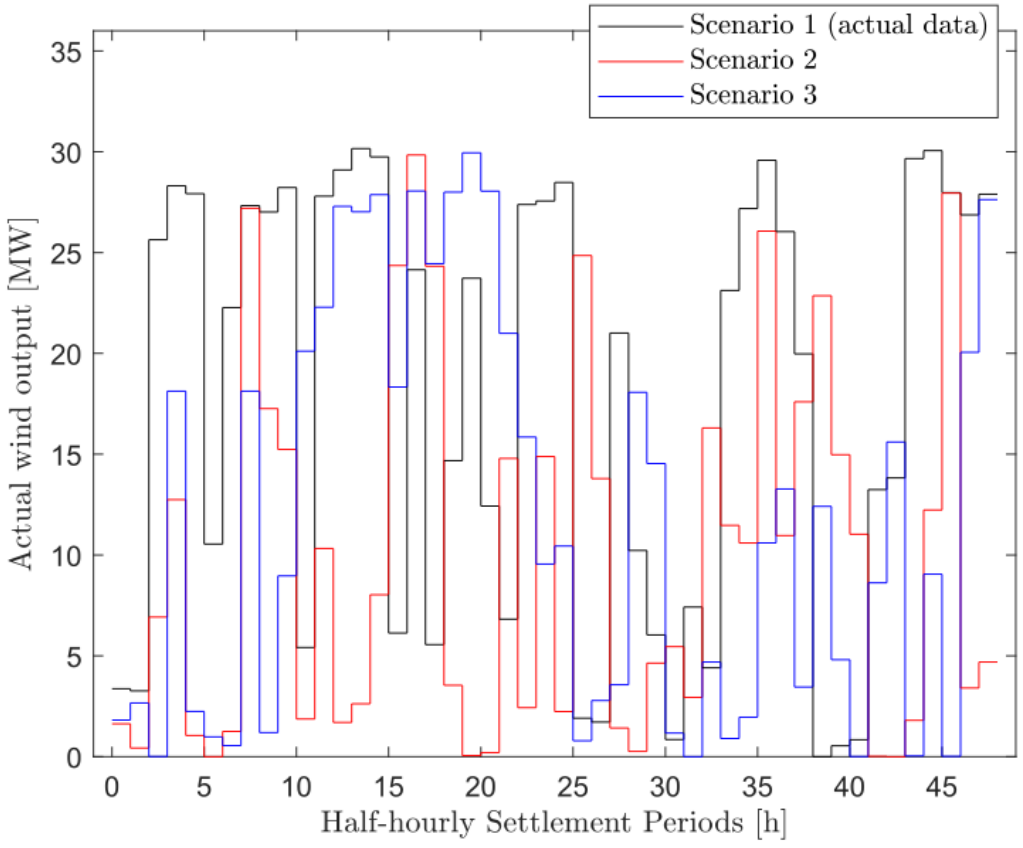


FIGURE 7.7: Actual wind output over 48 half-hours for the initial data as well as the two scenarios

7.3.2 Modelling wind forecast error

In this work, we are interested in wind power errors defined as the difference between the actual power at a certain time and the value of the power forecasted for the same interval. The errors, in fact, determine the optimal operation of a battery performing NIV chasing. Based on general characterizations of wind power forecast errors, we derived a simple but effective methodology to generate these quantities for each of the K wind scenarios.

Wind power forecast error has been usually assumed to have a Gaussian[165] (or quasi-Gaussian[196]) distribution. IDoherty and O'Malley[165] show that, for an individual farm, the mean value μ of the distribution is considered to be zero and the variance, $\bar{\sigma}^2$, of wind power forecast error – per unit of installed capacity – increases in a linear fashion with the forecast horizon. Hence, to compute wind errors, we employed the random walk, a stochastic process that represents the cumulative sum of Independent and Identically Distributed (IID) random variables. From Gauss' theory of statistical error, the sum of a large number of small disturbances, or random values, approximate the normal distribution[195]. Therefore, wind power forecast errors can be modelled by applying the random walk process. The forecast error time-series, Z, is thus defined as a Gaussian random walk process:

$$Z = \sum_{\mathrm{i}=1}^{\mathrm{n}} X_{\mathrm{i}} \tag{7.1}$$

with $X_{\mathrm{i}} = N\left(\mu_{\mathrm{i}}, \sigma_{\mathrm{i}}^2\right)$. Moreover, if as in this case $\bar{\mu} = [\mu_1, \ldots, \mu\mathrm{i}] = 0$ and $\sigma_{\mathrm{i}}^2 = \bar{\sigma}^2 \ \forall i = \{1, \ldots, n\}$[165], where $\bar{\sigma}^2 = 0.0085$ in the present work to match the findings in [7], the forecast error time-series, Z, belongs to a normal distribution:

$$Z \sim N\left(0, n\,\bar{\sigma}^2\right) \tag{7.2}$$

Hence, the random-walk process allows to compute a sequence of wind forecast errors described by a Gaussian distribution with a zero-mean value and a linearly time-increasing

variance. At a generic optimisation roll j, the forecasts of wind power output for the next $n = 48$ half-hour SPs are computed as the difference between the actual wind power output and the wind power forecast error, where the error is calculated by using (7.1) and scaled up by the installed capacity of the wind farm. An example of the back-calculated wind power forecasts, with the time-increasing nature of forecast errors for the initial data set of actual wind output is shown in Fig. 7.8.

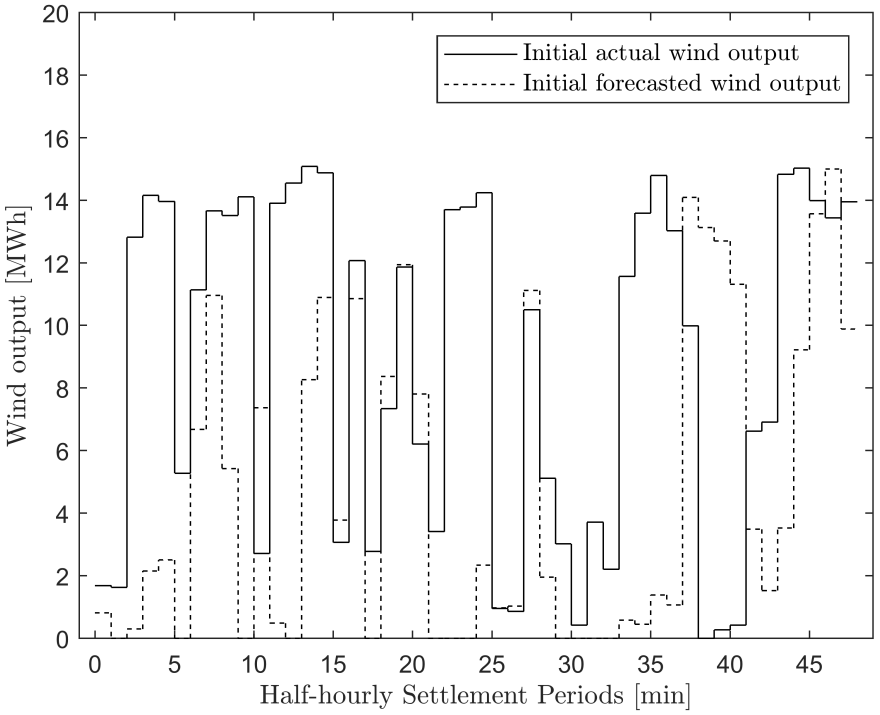


FIGURE 7.8: Actual and forecasted wind power output over 48 half-hours for the initial data set

7.3.3 Energy storage model

The energy store is modelled as an energy conversion unit, where transactions occur via charging and discharging. Limitations on the maximum/minimum State of Charge (SoC) are coupled to maximum/minimum power constraints. Depending on the type of storage technology, further constraints apply which have a non-trivial impact on the operation of

the energy store. In this work, we focus on CAES systems and ZEBRA battery technologies by choosing model parameters that best represent their respective techno-economic characteristics. It is important, especially for energy storage in batteries, to account for self-discharge effects whereby energy in the store gradually leaks due to internal dissipations[167]. Furthermore, energy transactions are characterised by inefficiencies resulting in higher energy consumptions whilst charging. Conversely, in discharging mode, the store would release slightly less energy due to the same losses[168].

Taking these characteristics into account, the relationship between the state of charge and transaction of power for the store may be written as shown in (7.3)[169]. The energy that is lost from the store due to an inherent leakage term τ is either refilled by variable power consumption $P^{\mathrm{C}}(t)$ or compounded by variable power discharge $P^{\mathrm{D}}(t)$. To reflect the fundamental fact that charging and discharging processes are inefficient, the power terms in equation (7.3) account for the respective energy transaction efficiencies. The roundtrip efficiency is defined as the product of efficiencies η_{C} and η_{D}, associated with charging and discharging energy, respectively.

$$\frac{\mathrm{d}S(t)}{\mathrm{d}t} = \frac{-1}{\tau} S(t) + \left(\eta_{\mathrm{C}} P^{\mathrm{C}}(t) - \frac{P^{\mathrm{D}}(t)}{\eta_{\mathrm{D}}} \right) \tag{7.3}$$

We are now interested in a time-discrete solution of (7.3) to be integrated in the optimisation problem presented in § 7.4. Considering a generic interval i of length Δt [min] and a constant charging/discharging power across the entire interval, the solution is given by (7.4):

$$\begin{aligned} S_{\mathrm{t}+1} &= \gamma S_{\mathrm{t}} + \beta \left(\eta_{\mathrm{C}} P_{\mathrm{t}}^{\mathrm{C}} - \frac{P_{\mathrm{t}}^{\mathrm{D}}}{\eta_{\mathrm{D}}} \right) \Delta t \\ \gamma &= e^{-\Delta t/\tau}, \ \beta = \left(1 - e^{-\Delta t/\tau}\right) \left(\frac{\tau}{\Delta t}\right) \end{aligned} \tag{7.4}$$

Note that S_{t} and $S_{\mathrm{t}+1}$ are states of charge at the beginning and the end of interval Δt. This is also shown schematically in Fig. 7.9.

In this work, the self-discharge effect is expressed through a time constant τ. This is

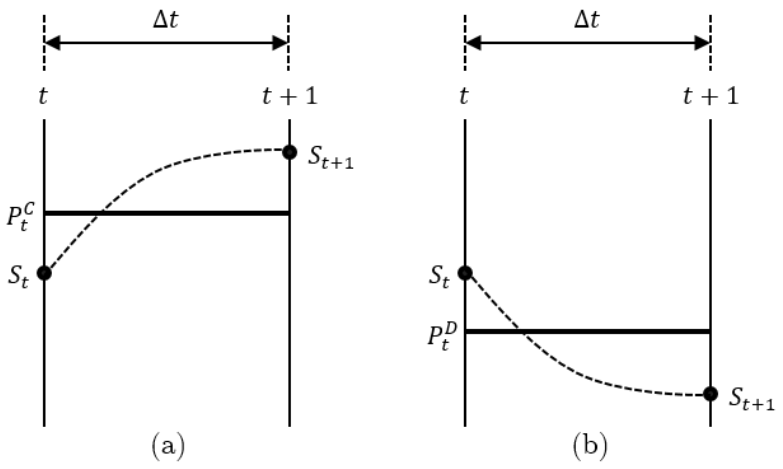


FIGURE 7.9: Evolution of State of Charge in an energy storage unit whilst (a) charging energy and (b) discharging energy

computed by rearranging (7.4) so that the power terms are set to zero, and the SoC at the end of an appropriate time-interval (e.g. one day) is set to a value published in manufacturers' catalogues. This is not materially relevant for the CAES system considered in this analysis.

Another important issue associated with the real operation of storage units, especially electrochemical batteries (e.g. lithium ion battery storage), is the degradation, or fading, of the maximum energy storage capacity. This irreversible loss occurs during (a) operational cycling, termed the cyclic life loss; and (b) idle operation, termed the calendric life loss[171]. The rate of degradation depends on how the battery is operated through the charging/discharging actions (i.e., how the battery cycles), its chemistry and ambient conditions. Battery degradation has two main physical manifestations: energy capacity fade (which limits the amount of energy stored), and power capacity fade (which limits the power transaction capability). Whilst degradation is also not materially relevant for the CAES system considered in this analysis, functionality has nonetheless been built in to the optimisation tool to cater for a variety of storage units with differing technical characteristics.

The degradation profile is based on recent experimental results conducted on lithium-titanate hydrates. Wang et al.[194] measured the energy capacity loss of electrodes with

progressive battery ageing cycles; these are shown as red squares in Fig. 7.10. The battery can cycle about 10,500 times before degrading to 20% of its original capacity (the marker for end-of-life of the battery, i.e., all battery cells need to be replaced by brand new ones). A third-order polynomial function has been fit to this data (blue curve in Fig. 7.10) – which can be used to compute the energy capacity fade of the battery if considered in the analysis.

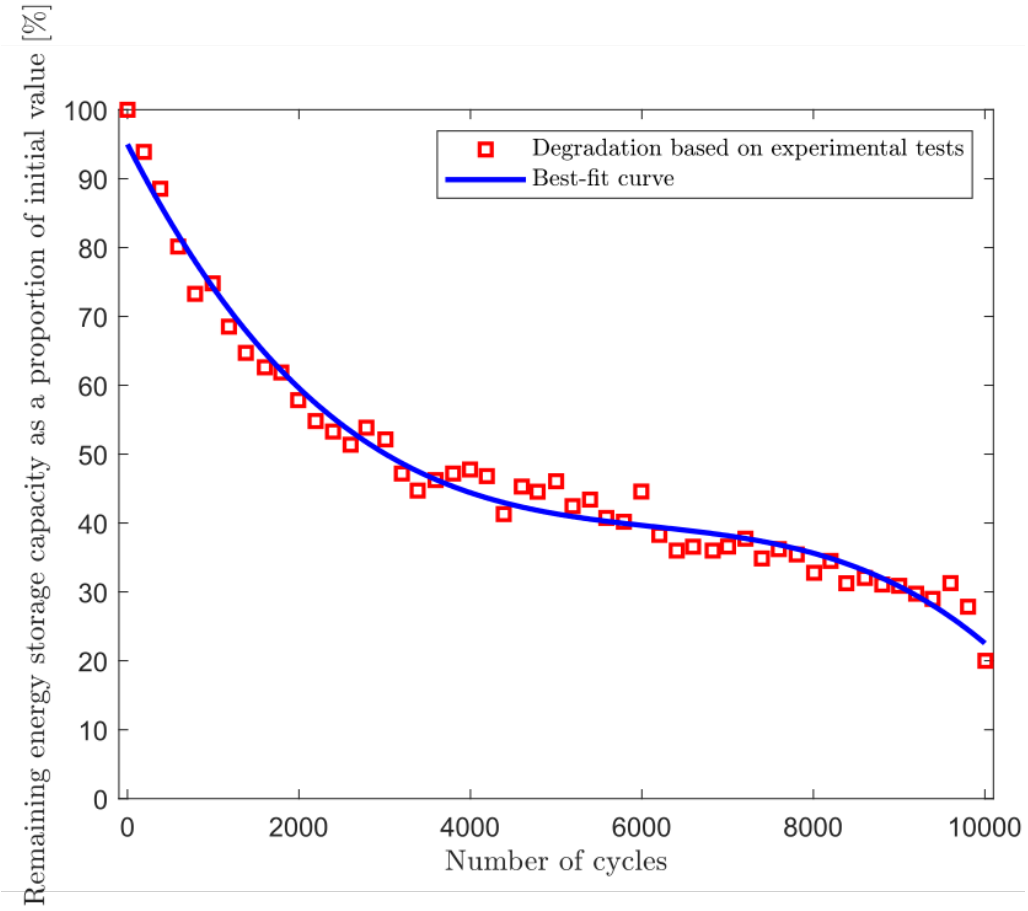


FIGURE 7.10: Cycling performance of lithium titanate hydrates in lithium ion batteries. The figure shows experimental data (red squares) and the third-order polynomial fitting function $\mathrm{f}(x) = -5.4\,x^3 + 6.2\,x^2 - 6.5\,x + 41.3$ (blue curve)

7.4 Optimisation model

With respect to the energy storage unit, the SoCs are chosen as the decision variables of the optimisation problem. To do this, two sets of variables $\mathcal{S}^{\mathrm{C}} = \left\{S_{\mathrm{i}}^{\mathrm{C}}\right\}_{\mathrm{i}=1}^{\mathrm{n}+1}$ and $\mathrm{S}^{\mathrm{D}} = \left\{S_{\mathrm{i}}^{\mathrm{D}}\right\}_{\mathrm{i}=1}^{\mathrm{n}+1}$

define the operation of two fictitious storage units: one only absorbs energy and the other only releases energy. At any point in time, the SoC of the real store S_{i} may be expressed as the sum of SoC of the fictitious stores, $S_{\mathrm{i}}^{\mathrm{C}}$ and $S_{\mathrm{i}}^{\mathrm{D}}$, as shown in (7.5):

$$S_{\mathrm{i}} = S_{\mathrm{i}}^{\mathrm{C}} + S_{\mathrm{i}}^{\mathrm{D}} \tag{7.5}$$

Thus, the charging and discharging energies, $E_{\mathrm{i}}^{\mathrm{C}}$ and $E_{\mathrm{i}}^{\mathrm{D}}$, are defined based on the decoupled states of charge as shown in (7.6) and (7.7).

$$E_{\mathrm{i}}^{\mathrm{C}} = \frac{\left(S_{\mathrm{i+1}}^{\mathrm{C}} - S_{\mathrm{i}}^{\mathrm{C}}\,\gamma\right)}{\eta_{\mathrm{C}}\,\beta} \tag{7.6}$$

$$E_{\mathrm{i}}^{\mathrm{D}} = \frac{-\eta_{\mathrm{D}}\,\left(S_{\mathrm{i+1}}^{\mathrm{D}} - S_{\mathrm{i}}^{\mathrm{D}}\,\gamma\right)}{\beta} \tag{7.7}$$

It is worth pointing out that this framework is in line with the rolling optimisation approach as it allows to calculate the optimal initial SoC without adding a cost function on the initial energy state. In addition, it leads to the same optimal solution where the decision variables are the charging/discharging powers, instead of the SoCs, and the first SoC is fixed.

The optimisation takes the form of a revenue maximisation problem, since the RESS is also assumed to be a price-taker. Furthermore, all prices are known when each optimisation roll is performed. Besides the sets of SoC defining the storage operation $\left(\mathcal{S}^{\mathrm{C}},\ \mathcal{S}^{\mathrm{D}}\right)$, $\varepsilon^{\mathrm{R,M}} = \left\{E_{\mathrm{i}}^{\mathrm{R,M}}\right\}_{\mathrm{i=1}}^{\mathrm{n}}$ is the set of decision variables relative to the proportion of renewable energy directly injected to the market and not passed to the energy store. As mentioned in previous sections, the optimal schedule for the RESS is determined over a typical year by employing a rolling-plan optimisation method over 24 hours of 48 time-intervals. The objective function is shown in (7.8).

$$f = \max_{\mathcal{S}^{\mathrm{C}},\,\mathcal{S}^{\mathrm{D}},\,\varepsilon^{\mathrm{R,M}}} \left\{ \sum_{\mathrm{j=1}}^{\mathrm{N}} \left[\left(\sum_{\mathrm{i=1}}^{\mathrm{n}} \left(E_{\mathrm{i}}^{\mathrm{D}}\,\lambda_{\mathrm{i}}^{\mathrm{M}} + E_{\mathrm{i}}^{\mathrm{R,M}}\,\lambda_{\mathrm{i}}^{\mathrm{M}} - E_{\mathrm{i}}^{\mathrm{C}}\,\lambda_{\mathrm{i}}^{\mathrm{W}} \right) + \left(E_{\mathrm{i}}^{\mathrm{D}} + E_{\mathrm{i}}^{\mathrm{R,M}} \right)\,\lambda_{\mathrm{i}}^{\mathrm{T}} \right)_{\mathrm{j}} \right.\right. \\ \left.\left. + \left(E_{\mathrm{j}}^{\mathrm{DEL,M}} - E_{\mathrm{j}}^{\mathrm{COM,M}} \right)\,\lambda_{\mathrm{j}}^{\mathrm{I}} \right] \right\} \tag{7.8}$$

The price that the store is exposed to while charging, $\lambda^{\mathrm{W}}_{\mathrm{i,j}}$, is set to zero, i.e., the store effectively buys energy for free. This reflects the reasoning that the RSO might choose to divert 'wrong time' renewable energy to the store for later use, thereby avoiding either curtailment or selling at low market prices.

The energy delivered to the market, $E^{\mathrm{DEL,M}}_{\mathrm{j}}$, measured at the meter of the RESS, is the sum of energy discharged from the store and renewable energy that is not fed to the store; (7.9) describes this:

$$E^{\mathrm{DEL,M}}_{\mathrm{j}} = E^{\mathrm{D}}_{1,\mathrm{j}} + E^{\mathrm{R,M}}_{1,\mathrm{j}} \quad \forall j = \{1, \ldots, N\} \tag{7.9}$$

The energy committed by the RESS to the market, $E^{\mathrm{COM,M}}_{\mathrm{j}}$, is equal to its FPN submitted according to Gate Closure rules.

The constraints to the objective comprise different parts. Equations (7.10)-(7.13) deal with the energy store only: (7.10) and (7.11) set the maximum and minimum charging and discharging powers, respectively, and (7.12) sets the bounds on SoC levels. Since we generate the optimal operation of the system over a typical year and assume that the number of years in the investment horizon thereafter repeat with the same characteristic trends, ideally a constraint would be imposed such that state of charge of the store at the beginning of the year is equal to that at the end of the year. However, this constraint may not always be satisfied if the error between the actual and forecasted output is significant thereby rendering the energy store unable to meet its pre-set state of charge. Thus, (7.13) in part imposes that the SoC at the end of the optimisation horizon is as close as possible to that at the beginning. (7.14) and (7.15) represent constraints due to the availability of the renewable generation: (7.14) sets the bounds on the green energy that can be sold to the market, whereas (7.15) includes the possibility of renewable energy being spilled or curtailed. Finally, (7.16) represents the network constraint and sets the maximum grid (export) capacity.

$$0 \leq E^{\mathrm{C}}_{\mathrm{i}} \leq \left(P^{\mathrm{C}}_{\mathrm{max}}\, \Delta t\right) \quad \forall i = \{1, \ldots, n\} \tag{7.10}$$

$$0 \leq E^{\mathrm{D}}_{\mathrm{i}} \leq \left(P^{\mathrm{D}}_{\mathrm{max}}\, \Delta t\right) \quad \forall i = \{1, \ldots, n\} \tag{7.11}$$

$$0 \leq S_{\mathrm{i}} \leq S_{\max} \quad \forall i = \{1, \ldots, n\} \tag{7.12}$$

$$S_1 \leq S_{\mathrm{N}} \tag{7.13}$$

$$0 \leq E_{\mathrm{i}}^{\mathrm{R,M}} \leq \left(P_{\mathrm{i}}^{\mathrm{R}}\, \Delta t\right) \quad \forall i = \{1, \ldots, n\} \tag{7.14}$$

$$E_{\mathrm{i}}^{\mathrm{C}} + E_{\mathrm{i}}^{\mathrm{R,M}} \leq \left(P_{\mathrm{i}}^{\mathrm{R}}\, \Delta t\right) \quad \forall i = \{1, \ldots, n\} \tag{7.15}$$

$$E_{\mathrm{i}}^{\mathrm{D}} + E_{\mathrm{i}}^{\mathrm{R,M}} \leq \left(P^{\mathrm{G}}\, \Delta t\right) \quad \forall i = \{1, \ldots, n\} \tag{7.16}$$

(7.8)-(7.16) together provide the full definition of the linear optimisation problem, which generates an optimal policy.

7.5 Financial model

The optimisation problem, when entirely solved, returns the short-term revenues of the RESS over the horizon Y, for each scenario K. A discounted cash-flow analysis is performed over this planning horizon to quantify the financial viability of such a project. The most commonly used performance metric to measure financial desirability of a project is its Net Present Value (NPV), which is the sum of net annual discounted cash-flows associated with the project. The NPV can be computed by employing the formula shown in (7.17), where the net revenue R and costs C of a project over the investment timeline are considered, and the cost of capital (or discount rate) r is applied to give preference to cash-flows of the present or near future over those of the more distant future. A return on investment is made if the NPV of the project is positive.

$$\mathrm{NPV} = \sum_{\mathrm{k}=0}^{\mathrm{Y}} \frac{R_{\mathrm{k}} - C_{\mathrm{k}}}{(1+r)^{\mathrm{k}}} \tag{7.17}$$

Another useful performance metric is the Internal Rate of Return (IRR). Mathematically, the IRR is the discount rate for which the NPV is equal to zero and its calculation relies on the same formula as the NPV. Put another way, the IRR is the highest cost of capital the project can bear whilst breaking even.

Since the objective of this work is to investigate the financial performance of retrofitting an energy storage unit onto a renewable site, net revenue R equals the difference between the short-term revenue of the integrated system over the investment timeline and that of the renewable generator on its own, whilst costs C include the initial capital investment and yearly operating costs associated with the energy store. It is assumed that the renewable site is in existence and in operation, and the timing of the decision to invest in an energy storage unit to add on to the site does not affect its optimal operation [173]. In this sense, together with the assumption on repeatability of input signals (wind power, prices, etc.) each year over the investment horizon, the solution generated will be an open-loop one.

7.6 Results and discussion

As explained in § 7.3.1, based on the initial data set comprising historical actual wind power output data, wholesale energy prices and system imbalance prices, 50 statistically similar scenarios are generated ($K = 50$). Then, for each scenario, forecasts of wind power output are back-calculated based on the methodology described in § 7.3.2. It should be noted that the frequency for updating wind power output forecasts is chosen, initially, to be once per day.

We analyse the optimal operation and financial feasibility of a storage unit integrated with a wind farm of 30 [MW] installed capacity over a project horizon of 10 years ($Y = 10$), considering the technical and economic characteristics of a salt cavern-based CAES plant. As the grid export and installed capacities of the wind farm are 30 [MW], the power rating of the store is set to this value to avoid underutilisation of grid connection capacity. The minimum discharging time is set to 2 [h], i.e., a maximum energy storage capacity of 60 [MWh]. Furthermore, we consider the capital costs of an energy storage unit to be split between that associated with power conversion, CapEx_P, and with storing energy, CapEx_E; the fixed operating costs are accounted for via OpEx.

The services that large-scale CAES can provide to the grid, which include energy arbitrage, reserve capacity and renewable power integration, have been researched extensively[174;175;176]. We take these abilities for granted and do not explore the plant characteristics necessary for providing such services. A CAES plant has a lifetime significantly greater than the project horizon considered in the present work, and therefore has associated benefits. However, economic and financial analysis over longer-term horizons (e.g. 50 years) would be meaningless under the assumption of constant trends of energy prices assumed herein. Thus, we do not explore this further. Analysis from Chapter 6 has determined the cost of storing energy in salt caverns via compressed air is around £9/kWh. However, other underground CAES plant costs – such power conversion system and operating costs – were not explored in Chapter 6 since it required considering a fuller system with various components that are out of scope of the present thesis. Therefore, such costs are taken from Zakeri and Syri[177], and listed in Table 7.1.

We neglect capital expenditure associated with decommissioning the project, variable operating costs, and assume zero price inflation as well as corporation tax rate.

For a particular scenario, the net annual short-term revenue of the wind farm along with the components of revenue for the first year of operation are shown in the waterfall plot in Fig. 7.11. It is seen that the power sold to the wholesale energy market (*Wholesale market*) and its associated Renewables Obligations revenue (*RO revenue*) account for the largest shares of total revenue. Because of the discrepancies between actual and forecasted wind power output, the wind farm in this case incurs imbalance costs (*Self-imbalance cashflow*). The wind farm exports power during the Triad periods and hence accumulates some revenue (*Triad revenue*); however, this is not the maximum possible value, which is derived from the maximum exportable power from the site during the three Triad periods: $3 \times 30\,[\text{MW}] \times 5\,[\text{£/kW}] = 0.45\,[\text{£m}]$.

In the following, to show the effect of imbalance management, as defined in the *NIV chasing* strategy, on the added value of storage, results are presented for two operation modes: (a) the store is used only to arbitrage on energy prices and manage Triad periods,

TABLE 7.1: System parameters for the RESS including those specific to the energy storage process

Common system parameters	
Installed wind farm capacity	30 [MW]
Grid connection (export) capacity	30 [MW]
Renewables Obligations revenue	48.1 [£/MWh]
Triad revenue, λ^{T}	5 [£/kW]
Investment horizon, Y	10 years
Discount rate, r	6.5 [%]
CAES parameters	
Charge/discharge capacity	30 [MW]
Maximum energy storage capacity	60 [MWh]
Roundtrip efficiency	75 [%]
$\mathrm{CapEx_P}$[2]	843 [€/kW]
$\mathrm{CapEx_E}$	9 [£/kWh] (see Chapter 6)
OpEx	3.9 [€/kW-year]

[2]It is assumed that €1 is equal to £0.89

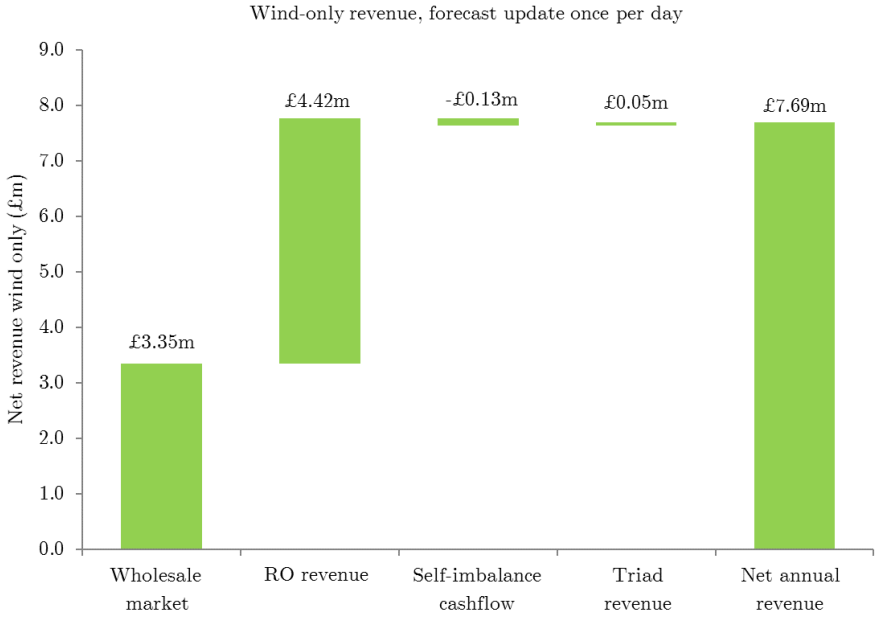
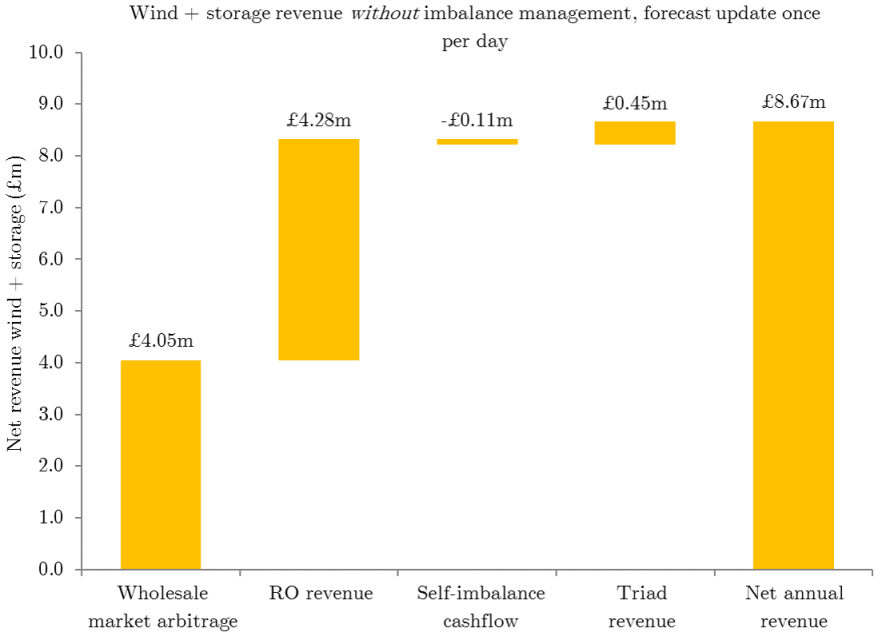


FIGURE 7.11: Short-term revenue distribution for the wind farm operating on its own; wind power forecasts updated once every 48 half-hours

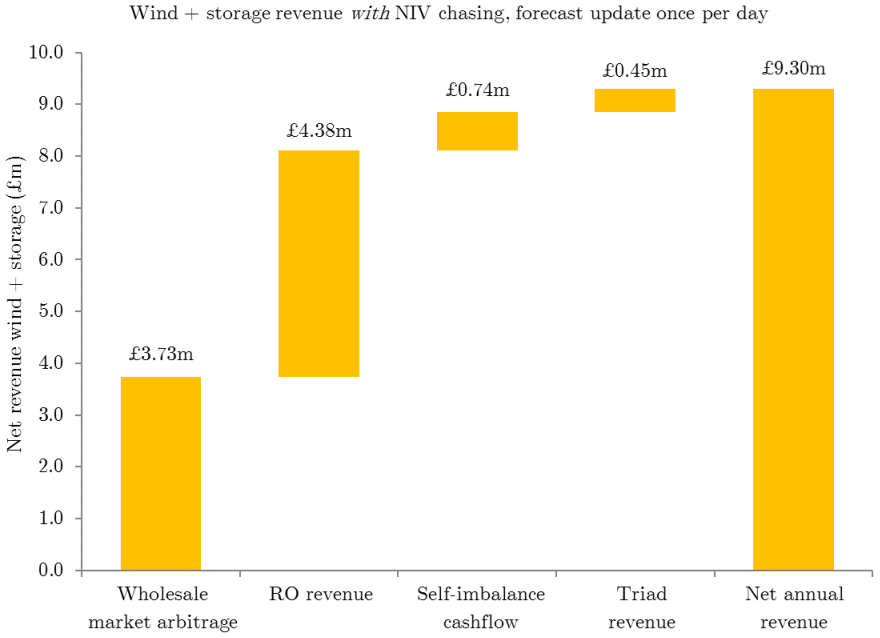
but not the imbalance of the wind farm, which we shall refer to as *Mode I*; and (b) the store is used to manage imbalance of the wind farm in addition to energy arbitrage and Triad management, which we shall refer to as *Mode II*.

When the storage technology is CAES, the short-term revenue of the RESS in the first year for *Mode I* is shown in Fig. 7.12(a). It can be observed that arbitrage and RO revenue still form the majority contributors to the total revenue. However, the imbalance cost to the collective site is decreased compared to the wind farm on its own due to the reduction in uncertainty over delivery of energy brought about by the integration of the storage unit. Since the operation is optimised and warnings for Triad periods are received in advance, the strategy outlined in this work results in the RESS recovering the maximum Triad revenue.

However, employing the store to manage the imbalance of the wind farm has clear benefits, as seen in Fig. 7.12(b). Whilst the share of revenue from energy arbitrage decreases and maximum Triad revenue is still recovered, the cashflow from self-imbalance of the collective site is no longer negative. This can be attributed to the fact that system imbalance prices are in general more volatile than wholesale energy prices, as seen in Fig. 7.13. Furthermore, the peaks of imbalance prices have values that are significantly higher than their wholesale energy price counterparts: values of wholesale energy prices range between $-61\,[£/\text{MWh}]$ and $1000\,[£/\text{MWh}]$, compared with $-154\,[£/\text{MWh}]$ and $3000\,[£/\text{MWh}]$ for imbalance prices. Therefore, an optimal policy which targets energy delivery for relatively higher positive imbalance prices inevitably earns higher revenue. When imbalance prices are negative, the RESS delivers less energy than it had scheduled for this period, thereby earning revenue. Optimising operation for energy arbitrage alone implies capturing value between price differentials across time – noting that price for charging energy is always zero in the present work. However, when the optimal policy also includes *NIV chasing*, the store adjusts its delivery relative to the FPN when a single imbalance price is revealed at each optimisation roll to capture the value in the infrequently occurring, but extreme values of, imbalance prices.



(a) Waterfall revenue plot for *Mode I* with CAES



(b) Waterfall revenue plot for *Mode II* with CAES

FIGURE 7.12: Short-term revenue distribution for the RESS in the first year of operation in *Mode I* and *Mode II* with CAES; wind power forecasts updated once every 48 half-hours

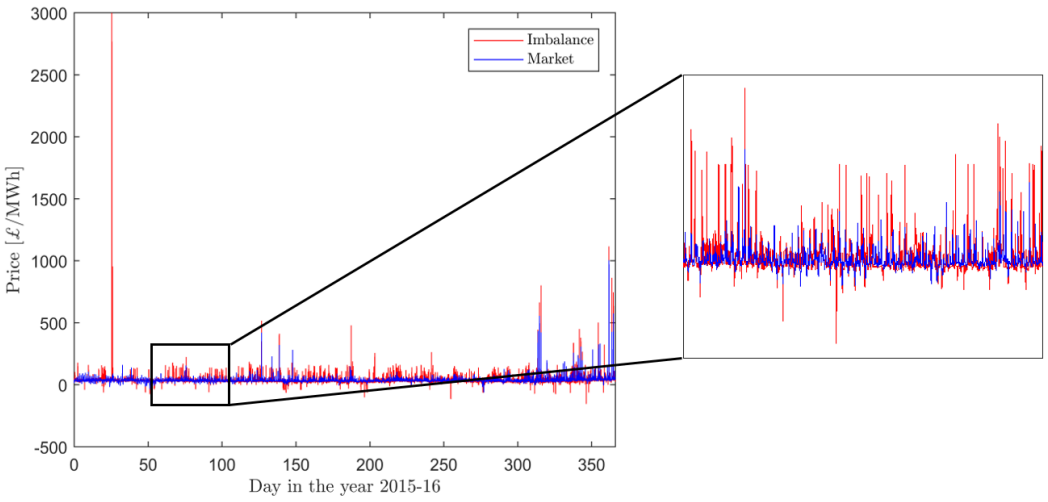
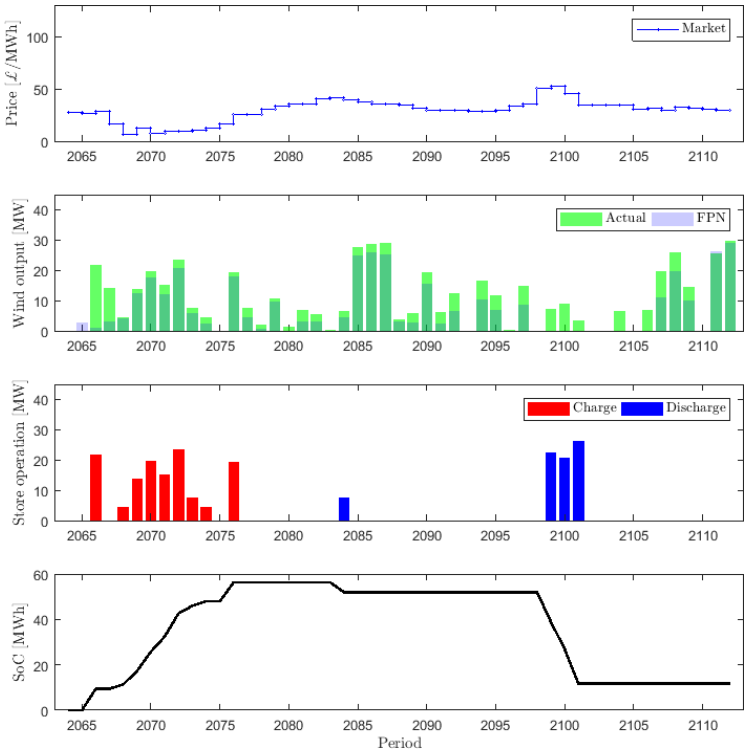


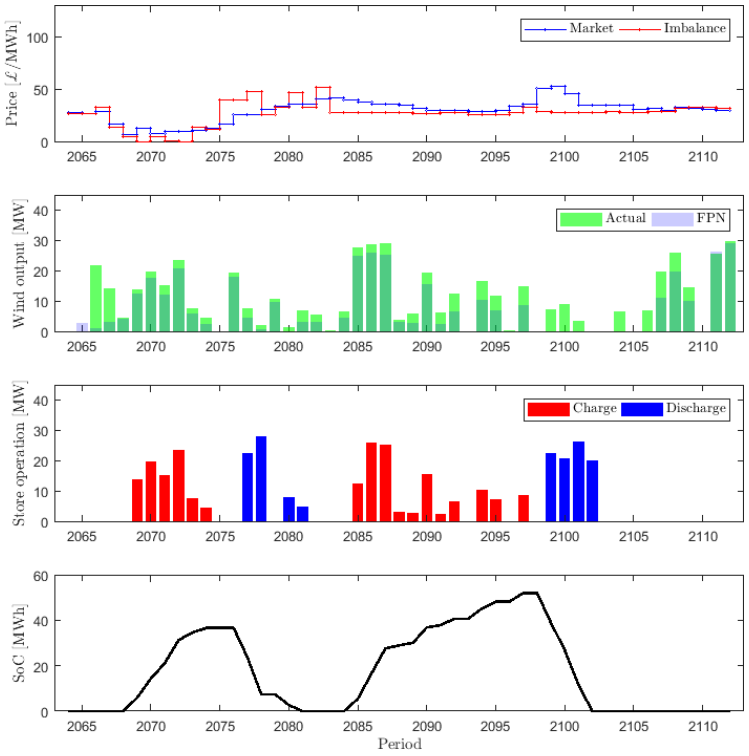
FIGURE 7.13: Volatility of system imbalance prices relative to the wholesale energy prices in the GB market for the year 2015-16

The optimal schedule for a typical day across *Mode I* and *Mode II* is shown in Fig. 7.14. It can be observed that for *Mode I*, shown in Fig. 7.14(a), the store absorbs excess wind during low energy price periods and delivers it at high energy price periods, which in this case coincide with low wind periods. The change in operation of the store in *Mode II* is evident in Fig. 7.14(b), where the store discharges additionally during periods of relatively high imbalance prices in order to earn revenue. This is followed by subsequent charging so as to capture value by discharging at high energy prices as before. Due to these reasons, there is an increase in total revenue of the RESS in *Mode II* relative to *Mode I* of operation.

Previous results proved the economic advantages of performing NIV chasing when operating the battery storage within the RESS. The second important effect of the NIV chasing strategy is the reduction of the overall cycling of the storage unit, which results in the storage unit having a longer operational lifetime compared to that without NIV chasing. If, as in the present work, energy arbitrage across time and/or markets is the main or only source of revenue, then the storage unit utilises almost the entire bandwidth of its capacity for energy transactions. Fig. 7.15 provides an illustration of the annual number of cycles of the battery with and without NIV chasing; most cycles occur in the 90-100%



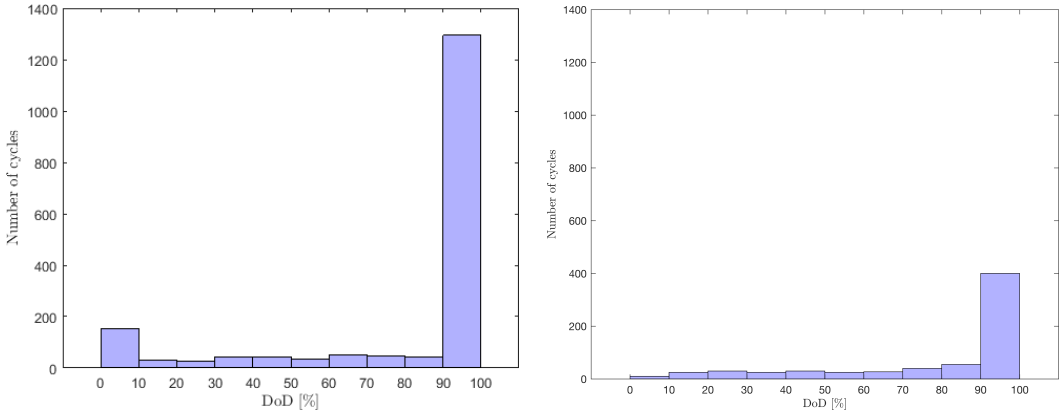
(a) Wind and storage optimal schedules in *Mode I* of operation



(b) Wind and storage optimal schedules in *Mode II* of operation

FIGURE 7.14: Wholesale energy and imbalance prices, actual and forecasted wind power output and schedule of storage for a typical day in *Mode I* and *Mode II* of operation

depth-of-discharge range. More importantly, it can be observed that cycling is more pronounced when the primary source of revenue is energy arbitrage across time (i.e. without NIV chasing) – approximately three times more – than that with NIV chasing as part of the revenue stream (see Fig. 11ab). Thus, besides the short term economic advantages of NIV chasing (thereby increasing the added value of storage), it indirectly helps prolong the life of the storage unit by reducing the number of lifetime cycles performed.

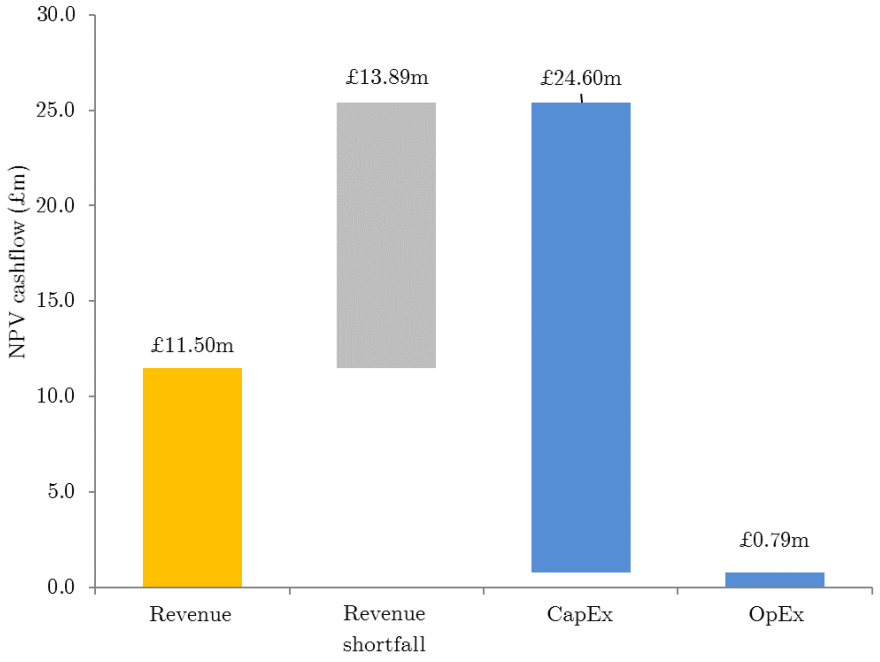


(a) Cycling of CAES in *Mode I*

(b) Cycling of CAES in *Mode II*

FIGURE 7.15: Cycling CAES

The cashflows associated with NPV of the project in *Mode II* with CAES is shown in Fig. 7.16(a). It can be observed that the NPV, termed *Revenue shortfall* in the figure, is negative, implying that the project is unprofitable. This is due to that fact that net operational revenues are not able to recover the upfront costs of the storage unit quickly enough within the considered investment horizon. However, if the RESS were able to participate in other markets or provide additional grid services, there could be enough revenues to make the business case profitable. Consider the Capacity Market mechanism in the GB electricity market, which was introduced to ensure security of energy supply. It commenced in the year 2018, and operates in conjunction with the current energy market [179]. This mechanism is part of the broader government scheme to reliably deliver low-carbon electricity, whilst minimising consumer costs. The SO, National Grid, procures capacity from flexible generation and demand participants, usually under long-term contractual framework (>10 years) and remuneration in [£/kW/year], with the expectation of sustained power delivery

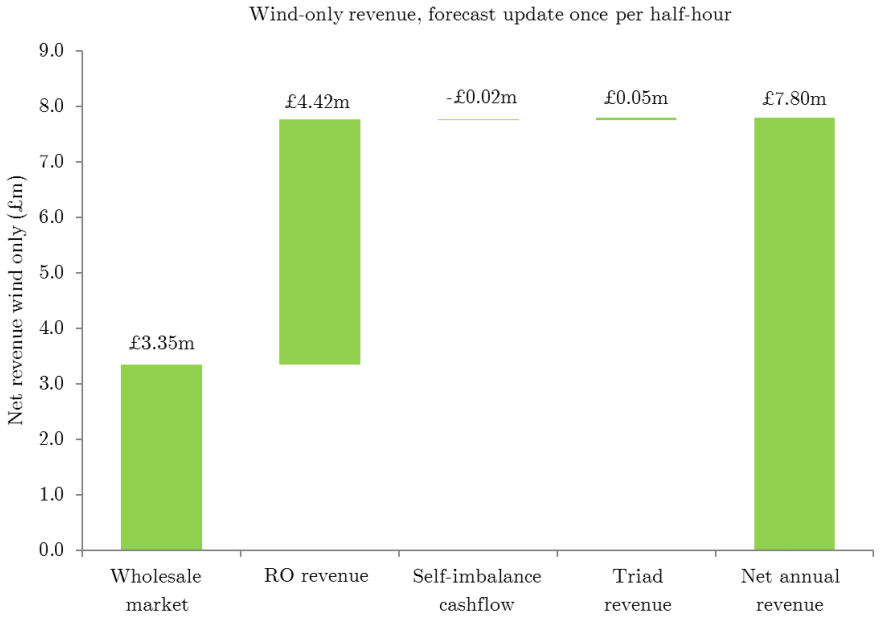


(a) NPV waterfall of RESS with CAES as the energy storage unit

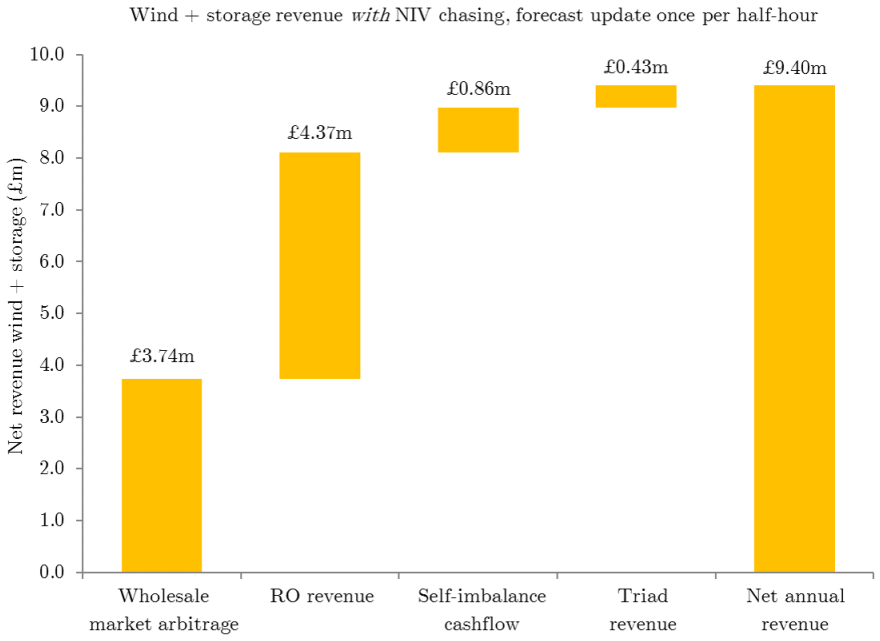
FIGURE 7.16: NPV cash-flow split between revenue and expenditure for *Mode II* of operation, and a wind power forecast update frequency of once per day

at maximum levels during electricity grid stress events. Large-scale long-life energy storage units such as CAES systems are suitably placed to participate in this mechanism. If the project lifetime for the CAES unit considered in the present analysis is 25 years, and it is assumed that all input signals to the optimiser remain unchanged over this period, additional revenue in the form of capacity payments of 20 [£/kW/year] will result in the project breaking even. In other words, an IRR is achieved that is equal to the discount rate $r = 6.5\,[\%]$.

The analysis of this chapter has largely ignored the regulatory and commercial barriers for energy storage and associated hybridised arrangements. Issues surrounding the asset class definition for storage, double charging for energy transactions, and revenue stacking when storage operators participate in the Capacity Market are not well-established [183]. Hybrid storage systems, especially with renewable generators, trigger a re-accreditation process whereby the continued payment of low-carbon subsidies to stakeholders is reviewed on a



(a) Revenue distribution for the wind farm alone in its first year of operation



(b) Revenue distribution for the RESS in the first year of operation

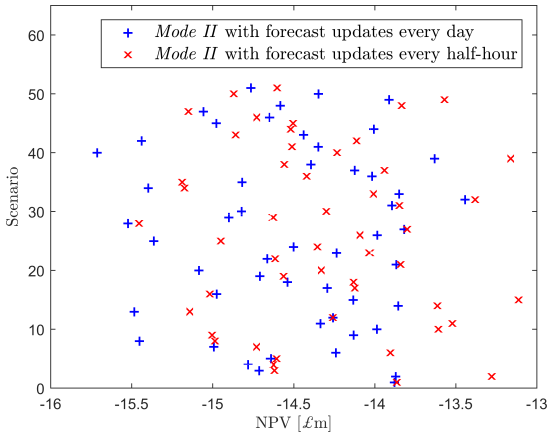
FIGURE 7.17: Short-term revenue distributions for wind-only and wind plus storage systems operating in *Mode II* with CAES, where wind power forecasts are updated once every half-hour

case-by-case basis[184]. In the specific case of the embedded arrangement discussed in this work, *NIV chasing* may not be allowed by the SO if the storage unit is sufficiently large in installed capacity; generators classed as 'large' according to the GB Grid Code (>100MW in England and Wales), are not allowed to deviate from their physical notifications for 'excessive benefits'[185]. Moreover, hybrid arrangements may mandate the existing operator of the site to apply for expansion of grid connection capacity (known as *Transmission Entry Capacity*), which places them on an often-long list of developers seeking approval for connecting to the grid[186].

In the analysis thus far, wind power forecasts were updated once per day. If this frequency is increased to once every half-hour, the imbalance costs of the wind farm over one year is reduced (cf. Fig. 7.17(a)) compared to that with lower-frequency forecast updates (cf. Fig. 7.11). Although the short-term revenue of the RESS in this case also increases – cf. Figs. 7.17 and 7.12(b) – the value of storage remains on similar levels. This is further demonstrated in Fig. 7.18(a) which shows the NPVs of 50 statistically similar scenarios for the two wind power forecast update frequencies. The NPV of the RESS with CAES system averaged -14.51 [£m], with standard deviation 0.56 [£m], for forecast updates every day; and an average of -14.32 [£m], with standard deviation 0.57 [£m], for forecast updates every half-hour. Thus, updating wind power forecasts in the present case has a positive effect, although only marginally.

7.7 Conclusions

This chapter has presented the workings of a flexible tool to analyse the financial effectiveness of energy storage systems connected behind-the-meter with renewable generators. A rolling-planning optimal scheduling algorithm was developed to account for the error associated with forecasting wind power output as well as the half-hourly revelation of system imbalance prices. The business case for a wind farm coupled with CAES was analysed under various scenarios, with a detailed storage model considering self-discharge and degradation, all under a purely linear optimisation framework.



(a) Scatter plot of NPV with CAES

FIGURE 7.18: Distribution of NPVs across all 50 scenarios for RESS with CAES as the storage unit; two extreme frequencies for updating wind power forecasts – once per day and once per half-hour – are considered

It was observed that managing imbalance of the renewable generator via the *NIV chasing* strategy captures significant value, and stacking revenue sources increases the overall short-term revenue of the system. The *NIV chasing* strategy also has the effect of reducing cycling of the storage system, thereby prolonging its lifetime.

Updating wind power forecasts more frequently increases the added value of storage only marginally, since the overall revenues of both the renewable source (if operating on its own) and the RESS proportionally increase with the frequency of wind power forecast update.

An important point to note is the assumption that market participants can reschedule their energy delivery at every optimisation roll, or every half-hour. In reality, a distinction should be made between 'forward' and 'close-to-real-time' markets. Consequently, the integration of day-ahead and intra-day energy market participation in the optimisation framework described here can form part of further research.

The behind-the-meter configuration of storage with wind farms can access only a limited number of revenue sources; thus, this business model may not always constitute an effective business case. In this particular case study, it was discussed that a stable long-term source of revenue for providing peaking capacity (e.g. Capacity Market in the UK) would be

needed to make the business case profitable. Nonetheless, the tool presented here can facilitate a first evaluation of hybrid renewable energy storage systems and can be modified easily to accommodate various other system configurations: parallel-metered renewable energy storage systems, integration with other forms of generation, standalone storage systems, etc..

Chapter 8

Conclusions and future work

8.1 Thesis summary

Powering the future in a clean and sustainable manner remains one of the most formidable challenges faced by mankind today. In achieving this goal, if large amounts of electricity are supplied by renewable energy sources, then it is likely that large amounts of additional energy storage are also needed. In order to aid this broader transition, this thesis has explored one such class of energy storage technologies called compressed air energy storage (CAES) with a focus on the methods of air storage. The thesis has looked at three of the most promising air storage methods comprising one existing, mature, method (underground salt cavern compressed air storage) and two novel methods (hybrid above-ground compressed air-liquid air storage and underwater compressed air storage). The investigations have focused on detailed technical assessments from thermo-mechanical and structural standpoints. However, the appraisals have been complemented with detailed discussions from economic as well as financial standpoints, investigating the cost competitiveness of the air storage methods explored and the ways in which a full CAES system (i.e., including power conversion machinery and other system components) may be integrated with renewable generation to participate in the (current) deregulated GB electricity market.

In what follows, a brief summary of contributions to science arising from this thesis is outlined. Then, key conclusions by chapter are discussed, and finally, some directions for further research are outlined.

8.2 Summary of contributions to engineering science

The thesis has created new knowledge, and therefore contributed to the science of engineering, in the following four ways:

- Formulation of the coupling of thermodynamic and mechanical responses of an underground salt cavern subject to rapid air injection and withdrawal cycles
- Hybridisation of an aboveground steel tank-based compressed air storage system with liquid air storage for enhancing energy storage density and locatability of the system, and minimising the marginal cost of energy storage capacity
- Derivation and demonstration of non-trivial bending stresses in a thin-shelled rigid structure storing pressurised fluids underwater
- Formulation of a purely linear optimisation framework for managing energy imbalance of renewable power generators integrated with compressed air energy storage

8.3 Key chapter conclusions

In Chapter 3, a quasi-static thermodynamic model was built and implemented via the finite element method to predict variations in temperature and pressure resulting from frequent transactions of compressed air into and out of a large underground salt cavern formation operating in an isochoric fashion. Using the theory of thermoelasticity, the capability of the finite element model to predict stress fields in the rock particles was developed. Salt rock particles operating in unsafe stress regimes were identified, and their propensity fo fail at these high-risk locations was investigated by using two stress-based failure criteria. It

was found that the susceptibility of rock particles to failure is increased when the internal air pressure is at a minimum and the change in temperature is maximum. Finally, the importance of choosing the most appropriate material failure criterion for the design of the cavern was also highlighted.

In Chapter 4, a CAES system where the energy storage capacity of the air store is extended by supplementing with liquid air storage was proposed and analysed. General motivations for this hybridised arrangement stem from the geological constraints of underground CAES and relatively high capital expenditure associated with aboveground tank-based compressed air storage, which could be addressed by highly locatable, energy dense and relatively cheaper liquid air storage. Whilst roundtrip efficiency was estimated for a single operating point of the combined system, it was found to be comparable to existing pure LAES schemes, even with the relatively low starting pressure of compressed air considered.

In Chapter 5, preliminary structural analysis of rigid-wall vessels for underwater compressed air storage is carried out. The basic motivation here was the reduction in load carrying requirements of the air storage reservoir due to the natural resistance to compressed air offered by hydrostatic pressure in deep sea environments. This in turn simplifies the structural design and costs of the air storage reservoir. A comparison was made with the relatively more well-established flexible-wall vessels for underwater CAES. Whilst flexible vessels can change their shape with varying fill levels of compressed and thereby avoid bending loads in the structure, rigid vessels do experience bending loads in the shell and may lead to material failure if not managed properly. However, flexible vessels require additional ballasting material to be anchored to the sea floor whereas rigid vessels can be designed with inherent ballast. A comparison was also made with rigid-wall vessels for underwater PHS, where it was noted that rigid vessels in underwater CAES systems store at least ~ 5 times more energy than their PHS counterparts, and cost less from a materials cost standpoint. However, it was also noted that cost-effectiveness is required not only

in terms of power recovery, materials and manufacturing methods but also in terms of offshore deployment methods of these vessels, especially at large scales.

In Chapter 6, the capital costs of the air storage containments were estimated and compared with each other. Here, both existing cost literature as well as bottom-up methods (via cost correlations) were used in deriving the costs of air storage. It was found that the underground air storage vessel has the lowest cost (£9/kWh), followed by the underwater air storage vessel (£58/kWh) and then the hybrid air storage system (£342/kWh). The two novel methods of the three options may realise cost reductions in the future due to 'learning by doing' and it is suggested as an area for future research. Nonetheless, the options possess different characteristics – most notably in terms of intended physical size and system rating and geographical locatability – and so the higher cost methods may be deployed in locations where lower cost methods cannot possibly be realised.

Finally, in Chapter 7, a rolling-planning optimal dispatch algorithm was developed to maximise the short-term revenue of an energy storage unit embedded with a renewable power generator, where the rolling-planning framework incorporates the time-increasing nature of the error associated with forecasting wind power output as well as energy prices which are revealed closer to real-time power delivery. The business for a wind farm coupled with a large-scale underground CAES system was analysed under various scenarios, with a detailed storage model considering self-discharge and degradation, all under a purely linear optimisation framework. It was found that 'active' usage of the energy storage unit to manage the imbalance of the wind farm not only captures significant value but also reduces the cycling of the storage system, thereby prolonging its operational lifetime. It was also found that stacking multiple revenue sources further increases the overall short-term revenue of the combined renewable energy storage system.

8.4 Suggested future work

Underground compressed air storage

It was discussed in Chapter 3 that the dynamic behaviour of rock salt plays a significant role in the chosen pattern of air compression and decompression cycles. Accounting for the creeping behaviour of rock salt and other rate-dependent parameters in the constitutive material model would be a clear next step in obtaining a more accurate mechanical response of rock salt.

Coupling the thermal and mechanical parts of the model by taking into account the dependence between the temperature and strain fields would be another area of investigation.

Hybrid compressed air-liquid air storage

Chapter 4 highlighted the importance of high-efficiency two-phase heat exchangers for the transformation between compressed air and liquid air. An improvement in the modelling of system components would incorporate pressure losses in heat exchangers as well as axial heat conduction.

More importantly, in order to arrive at the optimal system configuration (for a given application), and so investigate the trade-off between cost and system efficiency whilst accounting for general design trends, generating the so-called Pareto fronts could form part of future work. These fronts would comprise the leading-edge solutions with all other (suboptimal) system configurations lying either to the right or below the curve (i.e., the Pareto front). Further research could also look into determining the dynamic characteristics of this system to provide necessary insight for carrying out detailed engineering design efforts and tailoring it to local electricity market and regulatory mechanisms ultimately to maximise profits.

Underwater compressed air storage

Techno-economic parametric studies can be conducted to determine the optimal size of the rigid vessel for underwater CAES for specified economic performance. Furthermore, model tests of the rigid vessel can be carried out to gain experience in practical aspects: manufacturing, handling and longer-term operation of the vessel.

Compressed air storage costs

Future work should include the investigation of learning rates of the novel air storage methods investigated in this thesis, which will depend on the room for technological and cost improvement of each system component. This should be followed by the costing of complete systems, i.e., power conversion machinery, electrical equipment, civil works, etc. Finally, comparison against costs of other mature energy storage technologies could also be part of further work.

Value of renewable energy storage

A first extension to Chapter 7 could be the use of the tool to model other configurations, for instance an energy storage unit integrated with a renewable power generator with bi-directional power flows. However, it should be noted that configurations such as the aforementioned will necessitate mixed integer programming and extend the algorithm execution time.

The financial effectiveness of retrofitting a storage unit onto a renewable power generator could be compared against a 'greenfield' investment of wind/solar farm with energy storage.

In configurations with bi-directional power flows for the storage unit, system services such as frequency regulation and reserve capacity could also be modelled for further revenue stacking.

Bibliography

[1] Rajendra K. Pachauri, Andy Reisinger, et al. "Climate Change 2007: Synthesis Report. Contribution of working groups I, II and III to the fourth assessment report of the Intergovernmental Panel on Climate Change". Technical report, Intergovernmental Panel on Climate Change, 2007. Available online at: `https://www.ipcc.ch/report/ar4/syr/`, Last accessed 25 December 2017.

[2] BEIS, "Digest of United Kingdom energy statistics 2017", July 2017. Available online at: `https://www.gov.uk/government/uploads/system/uploads/attachment_data/file/643414/DUKES_2017.pdf`, Last accessed 25 December 2017.

[3] Ottmar Edenhofer, Ramon Pichs-Madruga, et al. "Renewable Energy Sources and Climate Change Mitigation: Special report of the Intergovernmental Panel on Climate Change". Cambridge University Press, 2011. `http://ipcc.ch/report/srren/`, Last accessed 25 December 2017.

[4] European Commission, "EU Directive 2009/28/EC", 2008. Available online at: `http://eur-lex.europa.eu/legal-content/EN/ALL/?uri=celex%3A32009L0028`, Last accessed 25 December 2017.

[5] BEIS, "UK energy in brief 2017", July 2017. Available online at: `https://www.gov.uk/government/uploads/system/uploads/attachment_data/file/631146/UK_Energy_in_Brief_2017.pdf`, Last accessed 25 December 2017.

[6] American Physical Society, "Integrating renewable electricity on the grid", 2010. Available online at: `https://www.aps.org/policy/reports/popa-reports/upload/integratingelec.pdf`, Last accessed 25 December 2017.

[7] A. Mullane and M. O'Malley, "The inertial response of induction machine based wind turbines", *IEEE Transactions on Power Systems*, **20**(3), 1496-1503, 2005.

[8] National Grid, "National electricity transmission system security and quality of supply standard", 2017. Available online at: `https://www.nationalgrid.com/sites/default/files/documents/NETS%20SQSS%20V2.3.pdf`, Last accessed 25 December 2017.

[9] Institution of Mechanical Engineers, "Closure of UK coal and nuclear plants to create electricity supply gap of up to 55 [%] by 2025", 26 Jan 2016. Available online at: https://tinyurl.com/jn7y3gg, Last accessed 25 December 2017.

[10] European Commission, "Vision and Strategy for European Electricity Networks of the Future", 2006. Available online at: http://ec.europa.eu/research/energy/pdf/smartgrids_en.pdf, Last accessed 25 December 2017.

[11] B. Silva, C. L. Moreira, L. Seca, Y. Phulpin and J. A. Peas Lopes, "Provision of inertial and primary frequency control services using offshore multiterminal HVDC networks", *IEEE Transactions on Sustainable Energy*, **3**(4), 800-808, 2012.

[12] M. Aunedi, P-Aristidis Kountouriotis, J. E. Ortega Calderon, D. Angeli and G. Strbac, "Economic and environmental impact of dynamic demand in providing frequency regulation", *IEEE Transactions on Smart Grid*, **4**(4), 2036-2048, 2013.

[13] R. Moreno, R. Moreira and G. Strbac, "A MILP model for optimising multi-service portfolios of distributed energy storage", *Applied Energy*, **137**, 554-566, 2015.

[14] S. Garvey et al., "On generation-integrated energy storage", *Energy Policy*, Short Communication, 544-551, 2015.

[15] G. Strbac, I. Konstantelos, M. Aunedi, M. Pollitt and R. Green, "Delivering future-proof energy infrastructure", Report for National Infrastructure Commission, 2016. Available online at: https://www.nic.org.uk/wp-content/uploads/Delivering-future-proof-energy-infrastructure-Goran-Strbac-et-al.pdf, Last accessed 25 December 2017.

[16] Carbon Trust, "Compressed air equipment", 2012. Available online at: https://www.gov.uk/government/uploads/system/uploads/attachment_data/file/376180/ECA760_Compressed_Air_Equipment.pdf, Last accessed 31 December 2017.

[17] T. Kitchener, "CAES", The Future of Compressed Air Energy Storage event, The Shard, London, UK, 2016. Available online at: https://warwick.ac.uk/fac/sci/eng/research/grouplist/electricalpower/images/members/shared/theshard/presentations/pressure_gap_ak.pdf, Last accessed 31 December 2017.

[18] F. W. Gay, "Means for storing fluids for power generation", US Patent 2,433,896; 1948.

[19] M. Budt, D. Wolf, R. Span and J. Yan, "A review on compressed air energy storage: Basic principles, past milestones and recent developments", *Applied Energy*, **170**, 250-268, 2016.

[20] RWE Power, "ADELE - Adiabatic compressed air energy storage for electricity supply", 2012. Available online at: https://www.rwe.com/web/cms/mediablob/en/391748/data/364260/1/rwe-power-ag/innovations/Brochure-ADELE.pdf, Last accessed 2 February 2019.

[21] Energy Research Knowledge Centre, "Compressed air storage system: follow-up project (ADELE-ING)", Available online at: https://setis.ec.europa.eu/energy-research/project/adiabater-druckluftspeicher-f%C3%BCr-die-elektrizit%C3%A4tsversorgung-nachfolgeprojekt-adele-ing, Last accessed 2 February 2019.

[22] S. Zunft, "Adiabatic CAES: The ADELE-ING project", SCCER Heat & Electricity Storage Symposium, PSI, Villigen (CH), May 5, 2015. Available online at: http://www.sccer-hae.ch/resources/SymposiumMay2015/Talks/SCCER2015-AdiabaticCAES-Zunft.pdf, Last accessed 2 February 2019.

[23] S. Zunft et al., "Electricity storage with adiabatic compressed air energy storage: Results of the BMWi-project ADELE-ING", International ETG Congress 2017, November 28-29, Bonn, Germany, 2017.

[24] D. Haugen, "Scrapped Iowa project leaves energy storage lessons", Available online at: https://energynews.us/2012/01/19/midwest/scrapped-iowa-project-leaves-energy-storage-lessons/, Last accessed 2 February 2019.

[25] R. Schulte, N. Critelli, K. Holst, G. Huff, "Lessons from Iowa: Development of a 270 Megawatt Compressed Air Energy Storage Project in Midwest Independent System Operator ", Sandia National Laboratories, 2012. Available online at: https://www.sandia.gov/ess-ssl/publications/120388.pdf, Last accessed 02 February 2019.

[26] S. Linden, "Review of CAES systems development and current innovations that could bring commercialisation to fruition", Proceedings of Electrical Energy Storage Applications and Technology Conference, San Francisco, 2007.

[27] J. Funk, "First Energy postpones project to generate electricity with compressed air", Available online at: https://www.cleveland.com/business/index.ssf/2013/07/firstenergy_postpones_project.html, Last accessed 02 February 2019.

[28] General Compression, "General Compression Signs Agreement with ConocoPhillips to Develop Compressed Air Energy Storage Projects", Available online at: https://www.prnewswire.com/news-releases/general-compression-signs-agreement-with-conocophillips-to-develop-compressed-air-e
html, Last accessed 2 February 2019.

[29] D. Fong, "Insights by Danielle Fong", 2012. Last accessed 2 February 2019.

[30] B. Yirka, "SustainX builds 1.5 MW isotherm compressed air energy storage system", Available online at: https://phys.org/news/2013-09-sustainx-mw-isotherm-compressed-air.html, Last accessed 2 February 2019.

[31] P. K. Nag, "Basic and applied engineering thermodynamics", Tata McGraw Hill, 2012.

[32] J. Spector, "LightSail Energy Enters 'Hibernation' as Quest for Game-Changing Energy Storage Runs Out of Cash", 2017. Available online at: https://www.greentechmedia.com/articles/read/lightsail-energy-cheap-compressed-air-storage-hibernation#gs.3wJm7KyX, Last accessed 2 February 2019.

[33] J. John, "SustainX to Merge With General Compression, Abandon Above-Ground CAES Ambitions", 2015. Available online at: https://www.greentechmedia.com/articles/read/sustainx-to-merge-with-general-compression-abandon-above-ground-caes-ambiti#gs.RWfC9LVc, Last accessed 2 February 2019.

[34] J. Barel, "Build Interest Deliverable 5.3: National Event Report FRANCE", 2017. Available online at: https://www.buildinterest.community/wp-content/uploads/2018/08/Event-report-FR-1.pdf, Last accessed 2 February 2019.

[35] A. Klochko, available online at: https://www.f6s.com/andreiklochko, Last accessed 2 February 2019.

[36] Bine Information Services, "Compressed air energy storage power plants", 2007. http://www.bine.info/fileadmin/content/Publikationen/Englische_Infos/projekt_0507_engl_internetx.pdf, Last accessed 31 December 2017.

[37] E. Ingersoll and D. R. Marcus, "Wind turbine system", Patent Application US20080050234-A1, 2008.

[38] S. Garvey, "Structural capacity and the 20MW wind turbine", Proceedings of the Institution of Mechanical Engineers, *Part A: Journal of Power and Energy*, **224**(8), 1083-1115.

[39] J. Sieber, "Wave energy accumulator", Patent Application US2009226331-A1, 2009.

[40] O. Fumio, "Transducer for the conversion of tidal current energy", Patent Application US4071305-A, 1978.

[41] A. G. Southcombe, "Wave or tidal power harnessing apparatus", Patent Application GB2267128-A, 1992.

[42] S. Garvey, "Compressed air energy storage: performance and affordability", Marcus Evans Biannual Energy Storage Conference, Amsterdam, December 2010. https://app.box.com/s/afdfc8e2bc451647f8be, Last accessed 31 December 2017.

[43] Black and Veatch, "Cost and performance data for power generation technologies", Prepared for NREL, 2012. Available online at: https://www.bv.com/docs/reports-studies/nrel-cost-report.pdf, Last accessed 31 December 2017.

[44] D. Wolf, "Methods for Design and Application of Adiabatic Compressed Air Energy Storage Based on Dynamic Modeling", PhD thesis, 2011. Available online at: http://publica.fraunhofer.de/eprints/urn˙nbn˙de˙0011-n-1546519.pdf, Last accessed 31 December 2017.

[45] C. Jakiel, S. Zunft and A. Nowi, "Adiabatic compressed air energy storage plants for efficient peak load power supply from wind energy: the European project AA-CAES", *International Journal of Energy Technology and Policy*, **3**(5), 2007.

[46] S. Zunft, "Adiabatic CAES: The ADELE-ING project", SCCER Heat & Electricity Storage Symposium, PSI, Villigen (CH), May 5, 2015. Available online at: http://www.sccer-hae.ch/resources/SymposiumMay2015/Talks/SCCER2015-AdiabaticCAES-Zunft.pdf, Last accessed 31 December 2017.

[47] ALACAES. Available online at: https://alacaes.com/aa-caes-technology/, Last accessed 31 December 2017.

[48] P. Berest and B. Brouard, "Safety of Salt Caverns Used for Underground Storage", *Oil & Gas Science and Technology*, **58**, 361-384, 2003.

[49] S. Folga et al., "US natural gas storage: risk-based ranking methodology and results", Argonne National Laboratory, 2016. Available online at: https://publications.anl.gov/anlpubs/2016/12/132436.pdf, Last accessed 02 February 2019.

[50] T. Barron, "Regulatory, technical pressures prompt more US salt cavern gas storage", Oil & Gas Journal Digital Magazine, 1994. Available online at: https://www.ogj.com/articles/print/volume-92/issue-37/in-this-issue/general-interest/regulatory-technical-pressures-prompt-more-us-salt-cavern-gas-storage.html, Last accessed 02 February 2019.

[51] P. Berest, B. Brouard, M. K. Jafari and L. V. Sambeek, "Underground Compressed Air Storage Facility for CAES-G/T Power Plant Utilizing Air-tight Lining", *International Society of Rock Mechanics News Journal*, 17-21, 1997.

[52] M. Nakata, H. Yamachi, A. Nakayama, S. Sakurai, T. Shidahara, "THERMODYNAMICAL APPROACH TO COMPRESSED AIR ENERGY STORAGE SYSTEM", *Doboku Gakkai Ronbunshu*, 31-42, 1998.

[53] P. Berest, B. Brouard, M. K. Jafari and L. V. Sambeek, "Transient behaviour of salt caverns – interpretation of mechanical integrity tests", *International Journal of Rock Mechanics and Mining Sciences*, **44**, 767-786, 2007.

[54] M. K. Jafari, B. Brouard and P. Berest, "Multicycle gas storage in salt caverns", *SMRI conference*, York, UK, October 2011.

[55] B. Brouard, A. Frangi and P. Berest, "Mechanical stability of a cavern submitted to high-frequency cycles", *SMRI conference*, Texas, USA, April 2011.

[56] H. M. Kim, J. Rutqvist, D. W. Ryu, B. H. Choi, C. Sunwoo and W. K. Song, "Exploring the concept of compressed air energy storage (CAES) in lined rock caverns at shallow depth: A modelling study of air tightness and energy balance", *Applied Energy*, **92**, 653-667, 2012.

[57] T. Wang, X. Yan, H. Yang, X. Yang, T. Jiang and S. Zhao, "A new shape design method of salt cavern used as underground gas storage", *Applied Energy*, **104**, 50-61, 2015.

[58] C. S. Desai and A. Varadarajan, "A Constitutive model for quasi-static behaviour of rock salt", *Journal of Geophysical Research*, **92**(811), 11445-11456, 1987.

[59] J. L. Ratingan, L. V. Sambeek, K. L. DeVries and J. D. Nieland, "The influence of seal design on the development of the disturbed rock zone in the WIPP Alcove seal tests", Report RSI-0400, RESPEC, 1991.

[60] U. E. Hunsche, "Failure behaviour of rock around underground cavities", *Proceedings of the 7th symposium on salt*, Kyoto, Japan, **1**, 59-65, 1993.

[61] K. L. DeVries, K. D. Mellegard, G. D. Callahan and W. M. Goodman, "Cavern roof stability for natural gas storage in bedded salt", Report RSI-1829, RESPEC, 2005.

[62] E. J. Langham, "The underground storage of compressed air for gas turbines: a dynamic study on an analogue computer", *The Computer Journal*, **8**(3), 216-224, 1965.

[63] M. Raju and S. K. Khaitan, "Modelling and simulation of compressed air storage in caverns: A case study of the Huntorf plant", *Applied Energy.* **89**, 474-481, 2012.

[64] R. Kushnir, A. Dayan and A. Ullmann, "Temperature and pressure variations within compressed air energy storage caverns", *International Journal of Heat and Mass Transfer*, **55**, 5616-5630, 2012.

[65] P. Quast and F. Crotogino, "Initial experience with the compressed air storage project of Nordwestdeutsche Kraftwerke AG (NWK) at Huntorf/West Germany, *Erdoel Erdgas Zeitschrift*, **95**(9), 310-314, 1979.

[66] M. Nakhamkin, E. Swensen, R. Schainker and B. Mehta, "CAES plant performance and economics as a function of underground salt dome storage transient processes", ASME paper No. 89-GT-143, 1-5, 1989.

[67] K. W. John, "Evaporites: sediments, resources and hydrocarbons", Springer, 893–943, 2006.

[68] Y. Huang et al. "Techno-economic study of compressed air energy storage systems for the grid integration of wind power", *International Journal of Energy Research*, **42**, 559-569, 2018.

[69] P. Berest, B. Brouard, H. Djizanne and G. Hevin, "Thermomechanical effects of a rapid depressurisation in a gas cavern", *Acta Geotech*, **9**(1), 181-186, 2013.

[70] P. Berest, "Thermomechanical aspects of high frequency cycling in salt storage caverns", *International Gas Union Research Conference*, Seoul, South Korea, October 2011.

[71] J. L. Urai and C. J. Spiers, "The effect of grain boundary water on deformation mechanisms and rheology of rock salt during long-term deformation", *Proceedings of the 6th conference on mechanical behaviour of salt, SaltMech6*, Hannover, Germany, May 2007.

[72] Z. Hou, "Mechanical hydraulic behaviour of rock salt in the excavation disturbed zone around underground facilities", International Journal of Rock Mechanics and Mining Sciences, **40**, 725-738, 2003.

[73] N. D. Critescu, "A general constitutive equation for transient and stationary creep of rock salt", *International Journal of Rock Mechanics and Mining Sciences and Geomechanics Abstracts*, **30**(2), 125-140, 1993.

[74] B. F. Shorr, "Thermal integrity in mechanics and engineering", Springer-Verlag Berlin Heidelberg, 2015.

[75] F. P. Beer, E. R. Johnston, J. T. DeWolf and D. F. Mazurek, "Mechanics of materials", McGraw Hill 6th Ed., 2012.

[76] J. N. Reddy, "An introduction to continuum mechanics", Cambridge University Press 2nd Ed., 2013.

[77] K. J. Bathe, "Finite Element Procedures", 2nd Ed., 2014. Available online at: `http://web.mit.edu/kjb/www/Books/FEP_2nd_Edition_4th_Printing.pdf`, Last accessed 7 November 2017.

[78] P. E. van Keken, C. J. Spiers, A. P. van den Berg and E. J. Muyzert, "The effective viscosity of rock salt: implementation of stead-state creep laws in numerical models of salt diapirism", *Tectonophysics*, **225**, 457-476, 1993.

[79] K. Serbin, J. Slizowski, K. Urbanczyk, S. Nagy, "The influence of thermodynamic effects on gas storage cavern convergence", *International Journal of Rock Mechanics and Mining Sciences*, **79**, 166-171, 2015.

[80] R. Schainker, "Compressed Air Energy Storage System Cost Analysis", EPRI Technical Update: 1016004, 2008.

[81] D. Evans et al., "Geological storage of energy – comments on UK CAES potential", The British Geological Survey, 2017. Available online at: `https://warwick.ac.uk/fac/sci/eng/research/grouplist/electricalpower/images/members/shared/theshard/presentations/bgs_shard_dje_v3_website.pdf`, Last accessed 2 February 2019.

[82] D. Strahan (Ed.), "Liquid air in the energy and transport systems. Opportunities for industry and innovation in the UK", *Centre For Low Carbon Futures, UK*, Report Number 021, 2013. Available online at: `http://liquidair.org.uk/files/full-report.pdf`, Last accessed 8 October 2017.

[83] E. M. Smith, "Storage of electrical energy using supercritical liquid air", *Proceedings of IMechE*, 289-298, 1977.

[84] K. Chino and H. Araki, "Evaluation of energy storage method using liquid air", *Heat Transfer – Asian Research*, **29**(5), 347-257, 2000.

[85] H. Araki, M. Nakabaru and K. Chino, "Simulation of heat transfer in the cool storage unit of a liquid-air energy storage system", *Heat Transfer – Asian Research*, **31**(4), 284-296, 2002.

[86] H. Chen, Y. Ding, T. Peters and F. Berger, "A method of storing energy and a cryogenic energy storage system", Patent Number WO 20070966565 A1.

[87] Highview Power Storage, Available online at: `http://www.highview-power.com/pilot-demonstrator-january-2010-february-2011/`, Last accessed 8 October 2017.

[88] R. Morgan, S. Nelmes, E. Gibson and G. Brett, "Liquid air energy storage – analysis and first results from a pilot scale demonstration plant", *Applied Energy*, **137**, 845-853.

[89] Highview Power Storage, Available online at: `http://www.highview-power.com/pre-commercial-laes-technology-demonstrator/`, Last accessed 8 October 2017.

[90] D. Kaye, Personal communication with Bharath Kantharaj, London, UK, 2017.

[91] H. S. Chen, T. N. Cong, W. Yang, C. Q. Tan, Y. L. Li and Y. L. Ding, "Progress in electrical energy storage system: a critical review", *Progress in Natural Science*, **19**, 291-312, 2009.

[92] Air Products, Available online at: `http://www.airproducts.com/industries/Energy/Power/Power-Technologies/energy-storage`, Last accessed 8 October 2017.

[93] Linde Group, Available online at: `http://www.the-linde-group.com/en/clean_technology/clean_technology_portfolio/energy_storage/liquid_air_energy_storage/index.html`, Last accessed 8 October 2017.

[94] B. Ameel, C. T'Joen, K. De Kerpel, P. De Jaeger, H. Huisseune, M. Van Belleghem and M. De Paepe, "Thermodynamic analysis of energy storage with a liquid air Rankine cycle", *Applied Thermal Engineering*, **49**(6), 941-949, 2013.

[95] Y. Li, Y. Jin, H. Chen, C. Tan and Y. L. Ding, "An integrated system for thermal power generation, electrical energy storage and CO_2 capture", *Applied Thermal Engineering*, **35**, 1158-1167, 2011.

[96] R. Morgan, S. Nelmes, E. Gibson and G. Brett, "An analysis of a large-scale liquid air energy storage system", *Proceedings of the Institution of Civil Engineers*, 1-10, 2015.

[97] Y. Li, H. Cao, S. Wang, Y. Jin, D. Li, X. Wang, Y. L. Ding, "Load shifting of nuclear power plants using cryogenic energy storage technology", *Applied Energy*, **113**, 1710-1716, 2014.

[98] Y. Li, X. Wang, Y. L. Ding, "A cryogen-based peak shaving technology: systematic approach and techno-economic analysis", *International Journal of Energy Research*, **37**, 547-557, 2013.

[99] J. Szargut, "Exergy Method: Technical and Ecological Applications", *WIT Press*, 2005.

[100] E. W. Lemmon, R. T. Jacobsen, S. G. Penoncello and D. G. Friend, "Thermodynamic properties of air and mixtures of nitrogen, argon, and oxygen from 60 to 2000K at pressures upto 2000MPa", *Journal of Physical and Chemical Reference Data*, **29**, 331, 2000.

[101] E. W. Lemmon and R. T. Jacobsen, "Viscosity and thermal conductivity equations for nitrogen, oxygen, argon and air", *International Journal of Thermophysics*, **25**(1), 21-69, 2004.

[102] B. Gido, E. Friedler and D. M. Broday, "Assessment of atmospheric moisture harvesting by direct cooling", Atmospheric Research, *182*, 156-162, 2016.

[103] J. W. Leachman, R. T. Jacobsen, S. G. Penoncello and E. W. Lemmon, "Fundamental Equations of State for Parahydrogen, Normal Hydrogen, and Orthohydrogen", *Journal of Physical and Chemical Reference Data*, **38**, 721, 2009.

[104] M. J. Assael, S. Mixafendi and W. A. Wakeham, "The viscosity and thermal conductivity of normal hydrogen in the limit of zero density", *Journal of Physical and Chemical Reference Data*, **14**(4), 1315-1324, 1986.

[105] W. M. Rohsenow, J. P. Hartnett and E. N. Ganic, "Handbook of heat transfer applications", *McGraw Hill*, 2nd ed., 1985.

[106] J. W. Westwater, "Boiling heat transfer in compact and finned heat exchangers", *Advances in two-phase flow and heat transfer*, Springer Netherlands, 827-857, 1983.

[107] M. M. Hasan, I. A. Karimi and H. E. Alfadala, "Modeling Phase Change in Heat Exchanger Network Synthesis", *18th European Symposium on Computer Aided Process Engineering*, Lyon, 2008.

[108] T. M. Flynn, "Cryogenic Engineering", 2nd ed., New York: Marcel Dekker, 2005.

[109] Watson et al., "Multistream Heat Exchanger Modeling and Design", *American Institute of Chemical Engineers*, **61**(10), 3390-3403, 2015.

[110] H. A. J. Watson an P. I. Barton, "Modelling phase changes in multi-stream heat exchangers", *International Journal of Heat and Mass Transfer*, **105**, 207-219, 2017.

[111] , Grossman et al., "A rigorous disjunctive optimisation model for simultaneous flowsheet optimisation and heat integration", *Comput. Chem. Eng.*, **22**(98), 157-164, 1998.

[112] Kamath et al., "Modelling multistream heat exchangers with and without phase changes for simultaneous optimisation and heat integration", *American Institute of Chemical Engineer*, **55**(1), 190-204, 2012.

[113] Bell et al., "Pure and Pseudo-pure Fluid Thermophysical Property Evaluation and the Open-Source Thermophysical Property Library CoolProp", *Ind. Eng. Chem. Res.*, **53**(6), 2498–2508, 2014.

[114] Song et al., "Swirling and cavitating flow suppression in a cryogenic liquid turbine expander through geometric optimization", *Proceedings of the Institution of Mechanical Engineers, Part A: Journal of Power and Energy*, 2015.

[115] Oil % Gas Journal, "Two-phase expanders manage feed-gas changes", Available online at: `https://www.ogj.com/articles/print/volume-112/issue-3/processing/two-phase-expanders-manage-feed-gas-changes.html`, Last accessed 23 March 2019.

[116] Oralli et al., "A study on scroll compressor conversion into expander for Rankine cycles", *International Journal of Low Carbon Technologies*, **6**(3), 200-206, 2011.

[117] Mathie et al., "A Framework for the Analysis of Thermal Losses in Reciprocating Compressors and Expanders", *Heat Transfer Engineering*, **35**, 2014.

[118] L. Nielsen and R. Leithner, "Dynamic Simulation of an Innovative Compressed Air Energy Storage Plant - Detailed Modelling of the Storage Cavern", *WSEAS Transactions on Power Systems*, **4**(8), 253-263, 2009.

[119] NYSERDA, "Mini-Compressed Air Energy Storage for transmission congestion relief and wind shaping applications", Final Report 08-05, 2008.

[120] A. Pimm and S. Garvey, "Analysis of flexible fabric structures for large-scale subsea compressed air energy storage", *Journal of Physics: Conference Series*, **181** 012049, 2009.

[121] A. Pimm, S. Garvey and R. Drew, "Shape and cost analysis for pressurised fabric structures for subsea compressed air energy storage", *Proceedings of IMechE*, Part C: Journal of Mechanical Engineering Science, **225**, 2017-1043, 2011.

[122] A. Pimm, "Analysis of flexible fabric structures", PhD Thesis, University of Nottingham, 2011.

[123] A. Pimm, S. Garvey and M. de Jong, "Design and testing of Energy Bags for underwater compressed air energy storage", *Energy*, **66**, 496-508, 2014.

[124] A. Pimm and S. Garvey, "Potential locations for underwater compressed air energy storage in Europe and North America", *Proceedings of the 2014 Offshore Energy Storage Symposium (OSES)*, Windsor, Canada, July 10-11, 2014.

[125] S. Garvey, M. Chee and A. Pimm, "Deployment methods for flexible air containments in deep water far offshore", *Proceedings of the 2017 Offshore Energy Storage Symposium (OSES)*, Boston, USA, July 12-14, 2017.

[126] J. Mas and J. M. Rezola, "Tubular design for underwater compressed air energy storage", *Journal of Energy Storage*, **8**, 27-34, 2016.

[127] O. Laing and J. L. N. Laing, "Energy storage for off-peak electricity", USA Patent US4873828, 31 March 1989.

[128] R. Royles and J. M. Llambias, "Buckling behavior of an underwater storage vessel", *Experimental Mechanics*, **25**(4), 421-428, 1985.

[129] W. Davis and J. Madary, "Offshore oil storage structure with submergence shell", US Patent US3738113 A, 1973.

[130] D. Bushnell, "Plastic buckling of various shells", Journal of Pressure Vessel Technology, **104**, 51-72, 1982.

[131] F. Castro, "Apparatus for storing and conveying fresh water within the sea", US Patent US3230967 A, 1966.

[132] R. J. Seymour, "Undersea pumped storage for load levelling", *In: California and the World's Oceans*, San Diego, 1997.

[133] D. Fiaschi, G. Manfrida, R. Secchi and D. Tempesti, "A versatile system for offshore energy conversion including diversified storage", *Energy*, **48**, 566-576, 2012.

[134] C. Van Walleghem, "Concept to construction: the world's first grid connected UW-CAES facility", *Proceedings of the 2014 Offshore Energy Storage Symposium (OSES)*, Windsor, Canada, July 10-11, 2014.

[135] Hydrostor Inc., Projects, Available online at: `https://hydrostor.ca/`, Last accessed 14 January 2018.

[136] J. M. Llambias, "Response of an underwater structure of optimum shape to general loading", PhD thesis, University of Edinburgh, 1985.

[137] Lytag Structural Concrete, Lytag. Available online at: `http://www.lytag.com/applications/structural-concrete`, Last accessed 14 January 2018.

[138] A. Slocum, G. Fennell, G. Dundar, B. Hodder, J. Meredith and M. Sager, "Ocean Renewable Energy Storage system: Analysis of an undersea energy storage concept", *Proceedings of the IEEE*, **101**(4), 906-924, 2013.

[139] M. Puchta, J. Bard, C. Dick, D. Hau, B Krautkremer, F. Thalemann, H. Hahn, "Development and testing of a novel offshore pumped storage concept for storing energy at sea – Stensea", *Journal of Energy Storage*, **14**(2), 271-275, 2017.

[140] G. Fennell, "System design and manufacturability of concrete spheres for undersea pumped hydro energy or hydrocarbon storage", Masters thesis, Massachusetts Institute of Technology, 2011.

[141] A. Pimm and S. Garvey, "Chapter 7: Underwater Compressed Air Energy Storage", *Storing Energy: With Special Reference to Renewable Energy Sources*, Ed. T. Letcher, 2016.

[142] T. Hunt, "Can the big island of Hawaii get all its electricity from renewables?", 2014, Available online at: `https://www.greentechmedia.com/articles/read/can-the-big-island-of-hawaii-get-all-of-its-electricity-from-renewables#gs.v_NbOW8`, Last accessed 14 January 2018.

[143] A. Tuohy, E. Denny and M. O'Malley, "Rolling unit commitment for systems with significant installed wind capacity", *Proceedings of the 2007 IEEE Power Tech Conference*, Lausanne, Switzerland, 2007.

[144] S. Tewari and N. Mohan, "Value of NAS Energy Storage Toward Integrating Wind: Results From the Wind to Battery Project", *IEEE Transactions On Power Systems*, **28**(1), 532-541, 2013.

[145] A. Lahnaoui, P. Stenzel and J. Lissen, "Techno-economic analysis of photovoltaic battery system configuration andlocation," *Applied Energy*, **227**, 497-505, 2018.

[146] J. G. Gonzalez, R. M. R. I. Muela, L. M. Santos and A. M. Gonzalez, "Stochastic joint optimisation of wind generation and pumped storage units in an electricity market", *IEEE Transactions On Power Systems*, **23**(2), 460-469, 2008.

[147] Y. Yuan, Q. Li and W. Wang, "Optimal operation strategy of energy storage unit in wind power integration based on stochastic programming", *IET Renewable Power Generation*, **5**(2), 194-201, 2011.

[148] E. D. Castronuovo, J. Usaola, R. Bessa, M. Matos, I. C. Costa, L. Bremermann, J. Lugaro and G. Kariniotakis, "An integrated approach for optimal coordination of wind power and hydro pumping storage", *Wind Energy*, **17**(1), 163-172, 2016.

[149] H. Ding, P. Pinson, Z. Hu and Y. Song, "Integrated bidding and operating strategies for wind-storage systems", *IEEE Transactions on Sustainable Energy*, **7**(1), 163-172, 2016.

[150] A. Zucker and T. Hinchcliffe, "Optimum sizing of PV-attached electricity storage according to power signals - a case study for Germany and Italy", *Applied Energy*, **127**, 141-155, 2014.

[151] S. Gill, G. W. Ault and I. Kockar, "The optimal operation of energy storage in a wind power curtailment scheme", *IEEE Power and Energy Society General Meeting*, San Diego, CA, USA, 2012.

[152] S. Gill, E. Barbour, I. A. G. Wilson and D. Infield, "Maximising revenue for non-firm distributed wind generation wit energy storage in an active management scheme", *IET Renewable Power Generation*, **7**(5), 421-430, 2013.

[153] J. Rittershausen and M. McDonagh, "Moving energy storage from concept to reality: Southern California Edison's approach to evaluating energy storage", 2010. Available online at: `https://www.edison.com/content/dam/eix/documents/innovation/smart-grids/Energy-Storage-Concept-to-Reality-Edison.pdf`. Last accessed 23 November 2017.

[154] J. E. Shigley, C. R¿ Mischke and R. G. Budynas, "Mechanical Engineering Design", London: McGraw Hill, 2004.

[155] National Grid, "Introduction to Triads", 2015. Available online at: `www2.nationalgrid.com/WorkArea/DownloadAsset.aspx?id=44940`. Last accessed 23 November 2017.

[156] Elexon, "Imbalance Pricing Guidance", 2016. Available online at: https://www.elexon.co.uk/wp-content/uploads/2016/10/Imbalance_Pricing_guidance_v11.0.pdf. Last accessed 23 November 2017.

[157] F. Teng, V. Trovato and G. Strbac, "Stochastic scheduling with inertia-dependent fast frequency response requirements", *IEEE Transactions on Power Systems*, **31**(2), 1557-1566, 2016.

[158] Elexon BM Reports, "System Buy and System Sell Prices", Available online at: https://www.bmreports.com/bmrs/?q=balancing/systemsellbuyprices. Last accessed 23 November 2017.

[159] B. Coyne, "National Grid confirms Triad dates", 27 March 2017/ Available online at: https://theenergyst.com/national-grid-confirms-triad-dates/. Last accessed 23 November 2017.

[160] I. A. Sajjad, G. Chicco and R. Napoli, "Probabilistic generation of time-coupled aggregate residential demand patterns", *IET Generation, Transmission and Distribution*, **9**(9), 789-797, 2015.

[161] P. M. de Quevedo, J. Allahdadian, J. Contreras and G. Chicco, "Islanding in distribution systems considering wind power and storage", *Sustainable Energy, Grids and Networks*, **5**, 156-166, 2016.

[162] B. Kantharaj, Wind power output data from November 2015-November 2016 provided by EDF Energy during B. Kantharaj's industrial work placement at EDF Energy R&D, 2016.

[163] R. Watson and L. Landberg, "Evaluation of prediktor wind power forecasting system in Ireland", *Wind Energy Association Conference*, Madrid, Spain, June 2003.

[164] G. N. Kariniotakis and P. Pinson, "Evaluation of the MORE-CARE wind power prediction platform. Performance of the fuzzy logic based models", *Wind Energy Association Conference*, Madrid, Spain, June 2003.

[165] R. Doherty and M. O'Malley, "A new approach to quantify reserve demand in systems with significant installed wind capacity", *IEEE Transactions on Power Systems*, **20**(2), 587-595, 2005.

[166] Z. Wang, C. Shen and F. Liu, "A conditional model of wind power forecast errors and its application in scenario generation", *Applied Energy*, **212**, 771-785, 2018.

[167] A. H. Zimmerman, "Self-discharge losses in lithium-ion cells", *IEEE AESS Systems Magazine*, 19-24, 2004.

[168] E. M. Krieger and C. B. Arnold, "Effects of undercharge and internal loss on the rate dependence of battery charge storage efficiency", *Journal of Power Sources*, **210**, 286-291, 2012.

[169] V. Trovato, S. H. Tindemans and G. Strbac, "Leaky storage model for optimal multi-service allocation of thermostatic loads", *IET Generation, Transmission and Distribution*, **10**(3), 1-9, 2015.

[170] M. H. Chang, H. P. Huang and S. W. Chang, "A new state of charge estimation method for $LiFePO_4$ battery packs used in robots", *Energies*, **6**, 2007-2030, 2013.

[171] O. Erdinc, B. Vural and M. Uzunoglu, "A dynamic lithium-ion battery model considering the effects of temperature and capacity fading", *International Conference on Clean Electrical Power*, Capri, Italy, 9-11 June 2009.

[172] P. Ramadass, B. Haran, R. White and B. N. Popov, "Mathematical modelling of the capacity fade of Li-ion cells", *Journal of Power Sources*, **123**, 230-240, 2003.

[173] M. Zugno, J. M. Morales, P. Pinson and H. Madsen, "Pool strategy of a price-maker wind power producer", **28**(3), 3440-3450, 2013.

[174] H. Lund and G. Salgi, "The role of CAES in future sustainable energy systems", *Energy Conversion and Management*, *50*(5), 1172-1179, 2009.

[175] E. Drury, P. Denholm and R. Sioshansi, "The value of compressed air energy storage in energy and reserve markets", *Energy*, **36**(8), 4959-4973, 2011.

[176] D. Wolf, A. Kannigeisser, M. Budt and C. Doetsch, "Adiabatic compressed air energy storage co-located with wind energy – multifunctional storage commitment optimisation for the German market using GOMES", *Energy Systems*, **3**(2), 181-208, 2012.

[177] B. Zakeri and S. Syri, "Electrical energy storage systems: A comparative life cycle cost analysis", *Renewable and Sustainable Energy Reviews*, *42*, 569-596, 2015.

[178] B. L. Ellis and L. F. Nazar, "Sodium and sodium-ion energy storage batteries", *Current Opinion in Solid State and Materials Science*, *16*(4), 168-177, 2012.

[179] Ofgem, "Annual Report on the Operation of the Capacity Market in 2016/17", 7 June 2017. Available online at: `https://www.ofgem.gov.uk/system/files/`

docs/2017/06/annual_report_on_the_operation_of_the_capacity_market_in_2016-17.pdf. Last accessed 23 November 2017.

[180] National Grid, "Rewards for businesses switching on to DSR", 2 March 2016. Available online at: http://nationalgridconnecting.com/rewards-for-businesses-switching-on-to-dsr/. Last accessed 23 November 2017.

[181] National Grid, "Monthly Balancing Services Summary", September 2017. Available online at: http://www2.nationalgrid.com/WorkArea/DownloadAsset.aspx?id=8589942888. Last accessed 23 November 2017.

[182] National Grid, "Enhanced Frequency Response 2016", 2016. Available online at: www2.nationalgrid.com/WorkArea/DownloadAsset.aspx?id=8589937157. Last accessed 23 November 2017.

[183] House of Commons, "The energy revolution and future challenges for UK energy and climate change policy", 13 October 2016. Available online at: https://www.publications.parliament.uk/pa/cm201617/cmselect/cmenergy/.../705.pdf. Last accessed 23 November 2017.

[184] Regen, "Ofgem announcement regarding storage and the Renewables Obligation", 14 September 2017. Available online at: https://tinyurl.com/y749whoq. Last accessed 23 November 2017.

[185] Ofgem, "Transmission Constraint Licence Condition Guidance", 29 October 2012. Available online at: https://www.ofgem.gov.uk/ofgem-publications/40377/tclc-guidance-pdf. Last accessed 23 November 2017.

[186] B. Kantharaj. Personal communication with George Harris, EDF Energy Renewables, May 2017.

[187] Ofgem, "About RO". Available online at: https://www.ofgem.gov.uk/environmental-programmes/ro/about-ro. Last accessed 04 March 2019.

[188] Elexon, "System Buy and Sell prices". Available online at: https://www.bmreports.com/bmrs/?q=balancing/systemsellbuyprices. Last accessed 04 March 2019.

[189] National Grid, "Forecast TNUoS tariffs". Available online at: https://www.nationalgrid.com/sites/default/files/documents/October%20Forecast%20TNUoS%20Tariffs%20for%20201819%20Report.pdf. Last accessed 04 March 2019.

[190] Everoze, "UK Capacity Market", Available online at: http://everoze.com/uk-cm/. Last accessed 04 March 2019.

[191] Ofgem, "Five year review of the CM rules". Available online at: https://www.ofgem.gov.uk/system/files/docs/2018/09/capacity_market_rules_five_year_review_open_letter_2018_1.pdf. Last accessed 04 March 2019.

[192] National Grid, "Frequently asked questions". Available online at: https://gbcmn.nationalgrid.co.uk/faq/system-stress-events/how-many-system-stress-events-can-be-expected-each-year. Last accessed 04 March 2019.

[193] National Grid, "Duration limited storage de-rating factor assessment". Available online at: https://www.emrdeliverybody.com/Lists/Latest%20News/Attachments/150/Duration%20Limited%20Storage%20De-Rating%20Factor%20Assessment%20-%20Final.pdf. Last accessed 04 March 2019.

[194] S. Wang et al., "Lithium titanate hydrates with superfast and stable cycling in lithium ion batteries", *Nature Communications*, pp. 1-8, 2017.

[195] M. Hill, "Approximating the random walk using the central limit theorem", 23 August 2011. Available online at: http://www.math.uchicago.edu/~may/VIGRE/VIGRE2011/REUPapers/Hill.pdf. Last accessed 04 March 2019.

[196] H. Bludszuweit, J.A. Domínguez-Navarro, and A. Llombart, "Statistical Analysis of Wind Power Forecast Error", *IEEE Transactions on Power Systems*, **23**(3), 983-991, 2008.

[197] S. Jenkins, "Economic indicators: Chemical engineering essentials for the CPI professional". Available online at: https://www.chemengonline.com/economic-indicators-cepci/, Last accessed 09 March 2019.

[198] H. Xue and A. White, "A comparative study of liquid, solid and hybrid adiabatic compressed air energy storage systems", *Journal of Energy Storage*, **18**, 349-359, 2018.

[199] R. Turton et al. "Analysis, synthesis and design of chemical processes", 4th ed. London (UK), Pearson Education International, 2013.

[200] J. Couper et al., "Chemical process equipment: selection and design", 2nd ed. MA (USA), Butterworth-Heinemann, Elsevier Inc., 2010.

[201] R. Shah and D. Sekulic, "Fundamentals of heat exchanger design", John Wiley and Sons Inc., 2003.

[202] G. F. Hewitt and S. J. Pugh, "Approximate design and costing methods for heat exchangers", *Proc. Int. Conf. Heat Exchangers for Sustainable Development*, June 14–18, Lisbon, Portugal, 801–820, 1998.

[203] I. J. Navarro et al., "Life Cycle Cost Assessment of Preventive Strategies Applied to Prestressed Concrete Bridges Exposed to Chlorides", *Sustainability*, **10**, 845-860, 2018.

[204] R. Fu, T. Remo and R. Margolis, "2018 U.S. Utility-Scale Photovoltaics-Plus-Energy Storage System Costs Benchmark", NREL report PR-6A20-72401, 2018.

[205] C. Lay and J. Bard, "StenSea – Stored energy in the sea", *7th International Renewable Energy and Storage Conference and Exhibition*, 2012.

[206] ESPC Inc., "15 MW CAES Plant with Above Ground Storage – Distributed Generation", Available online at: `http://www.espcinc.com/library/15_MW_CAES_Project_with_Above_ground_Storage.pdf`, Last accessed 23 March 2019.

[207] New York Power Authority, "Above Ground Compressed Air Energy Storage System - Phase One Economic Analysis", Available online at: `https://www.nyserda.ny.gov/Researchers-and-Policymakers/Research-Project/Research-Projects/Research-Project-Search-Results/Project-Information?p=9133`, Last accessed 23 March 2019.

[208] ISO11120 12 tube CNG skid containers, Alibaba.com, Available online at: `https://www.alibaba.com/product-detail/LUXI-CNG-12-tube-skid-container_60116613715.html?spm=a2700.7724838.0.0.PSpFWc`, Last accessed 23 March 2019.